Electrochemical Sodium Storage in Non-Graphitizing Carbons – Insights into Mechanisms and Synthetic Approaches towards High-Energy Density Materials

Univ. Diss. zur Erlangung des Titels
"Doctor rerum naturalium"
(Dr. rer. nat.)
in der Wissenschaftsdisziplin "Anorganische Chemie"

eingereicht von

Konstantin Schutjajew

an der
Mathematisch-Naturwissenschaftlichen Fakultät
Institut für Chemie der Universität Potsdam
und dem
Max-Planck-Institut für Kolloid- und Grenzflächenforschung

am
14. Oktober 2021

Erstgutachter:
Prof. Dr. Martin Oschatz

Zweitgutachter:
Prof. Dr. Dr. h. c. Markus Antonietti

Hauptbetreuer: Prof. Dr. Martin Oschatz

Weitere Betreuer: Prof. Dr. Dr. h. c. Markus Antonietti

Weitere Gutachter*innen: Prof. Dr. Andrea Balducci

Ort und Datum der Disputation: Potsdam, 22.02.2022

Dissertation, Universität Potsdam, 2022

Published online on the
Publication Server of the University of Potsdam:
https://doi.org/10.25932/publishup-54189
https://nbn-resolving.org/urn:nbn:de:kobv:517-opus4-541894

Danksagung

Ich bedanke mich herzlich bei Prof. Dr. Martin Oschatz für die Gelegenheit, meine Arbeit in seiner Gruppe anfertigen zu dürfen. Ihm gebührt darüber hinaus großer Dank für seine Rolle als beispielhafter Mentor und Ratgeber in meiner wissenschaftlichen und professionellen Entwicklung. Prof. Dr. Dr. h. c. Markus Antonietti danke ich dafür, dass er es mir ermöglichte, meine Forschung in seiner Abteilung am Max-Planck-Institut für Kolloid- und Grenzflächenforschung durchzuführen.
Ich danke auch meinen Freunden und Kollegen, denn ohne sie wäre diese Arbeit in der Form nicht möglich gewesen. Dazu zählen, unter Anderen, Runyu Yan, Ralf Walczak, Milena Perović, Ivan Ilic, Paolo Giusto, Francesco Brandi, Baris Kumru, Jonas Pampel, und Erik Troschke. An all die anderen, namentlich nicht genannten Wegbegleiter aus dem Chez Briel geht nicht minder Dank für die vielen langen Abende in bester Gesellschaft. Besonders zu erwähnen sind außerdem Tim Tichter, Jonathan Schneider und Marcus Gebhard. Mit ihnen verbrachte ich mit die besten Stunden in Labor und Büro, doch auch sonst war auf die drei immer Verlass.
Dr. Nadja Tarakina und Dr. Eneli Monerjan danke ich für aufschlussreiche Gespräche über Elektronenmikroskopie und Röntgenstreuung.
Ich bedanke mich bei den Technikerinnen und Technikern des MPI, der Uni Potsdam und der Uni Jena, welche durch ihre sorgfältigen Messungen und Experimente zu dieser Arbeit beitrugen, besonders bei Ines Below-Lutz, Antje Völkel, Daniel Werner, Heike Runge, Bolortuya Badamdorj und Beate Fähndrich.
Auch meine Studenten sollen in diesem Abschnitt nicht zu kurz kommen. Ich danke Marcus Pieper, Cevin Braksch, und Sebastian Witt für ihren Einsatz und wünsche ihnen für ihren eigenen Weg alles Gute.
Zu guter Letzt bedanke ich mich bei meiner Familie, insbesondere bei meiner Mutter Elena und meinem Vater Dmitrij, meiner Oma Erna, meiner Schwester Anastasia und meinem Onkel Kirill, die stets an mich glaubten und mich unterstützten wo sie es nur konnten.

Contents

List of Figures

List of Tables

1. Motivation

Besides other distinct traits such as upright walking, language, and the utilization of tools, mankind stands out from other species by the ability to control fire. And probably since the first bonfire intentionally lit by one of our ancestors, carbon has always been a constant and indispensable companion for every civilization. It enabled warm shelters, hot food, and durable tools, just to name a few examples. Finally, with the invention of the first steam engine and the resulting industrialization, carbon occurring as the main component of coal, later also in the constituents of oil and gas, became a source of energy for all imaginable applications, on top. Unable or unwilling to anticipate the consequences, mankind interfered with the natural carbon cycle, in search of comfort and wealth. Over millennia, solar energy was harvested by bacterial and vegetational autotrophs to convert carbon dioxide into biomolecules, passing through the food chain, just to find themselves decomposing aerobically again to carbon dioxide, or anaerobically to valuable for humans fossil fuels like coal, gas, or oil. Driven out of equilibrium by anthropogenic intervention, the cycle could not follow the ever increasing energy demand, so that by the beginning 21st century we find ourselves facing depleting natural resources and increasing atmospheric carbon dioxide concentration.[1]

Regardless of recent efforts to reduce our energy consumption, the demand for electrical energy in particular is ever rising, so that it is expected to triple by the end of this century, compared to the early 2000s.[2,3] The only way to ensure a stable and sustainable energy supply is to focus on the development and exploitation of renewable energy sources, especially solar, wind, and hydroelectrical ones. These sources, however, strongly fluctuate depending on daytime, season, and weather conditions, so that their availability hardly matches peak consumption hours. Therefore, electricity must be collected during the peak activity of renewable production and allocated when it is needed, which can only be done by means of electrical energy storage systems. A plethora of technological solutions was proposed and, each to a different extent, implemented into the grid.[4–6] Besides mechanical storage solutions, such as pressure accumulators and reservoirs, which have strict geological requirements, and power-to-gas approaches, which are associated with high infrastructural

investments, secondary batteries of different types offer a relatively facile and scalable way of storing electrical energy.[7] Among them, redox flow batteries (RFBs) either require high initial investments or contain highly toxic components, depending on the particular cell chemistry, while traditional lead-acid batteries are cheap but lag behind regarding energy density.[8–10] With its high gravimetric and volumetric energy density, the lithium ion battery (LIB) meets the criteria for efficient EES on grid scale. Unfortunately, it is not only subject to significant price fluctuations, depending on demand and request, but also the present lithium resources in the Earth's crust will most likely not be enough to provide sufficient storage capacities.[11] Due to its effectively infinite availability, and the common development history, sodium ion batteries (SIBs) returned into the focus of research around ten years ago.[9,12] The two storage systems share basic operating principles and cell chemistries so that vital components such as cathode material classes and electrolytes can be adapted from LIBs to SIBs. However, the most frequently used LIB anode material, graphite, which stands out due to its abundance, low cost, and a favorable charge storage behavior, cannot be adapted to the SIB, as only negligible amounts of sodium can intercalate into this carbon modification.[13] For this reason, state-of-the-art anodes for SIBs are made of hard carbon (HC), a carbon allotrope, which consists of turbostratically disordered, bent graphene layers. Regions of extended parallel stacking as well as cavities, which can be regarded as closed pores, formed by diverging graphene layers are two main structural features of this special material.[14,15] While it is clear that the formation of LiC_6 is the reason for the pronounced, low-potential capacity plateau in the common LIB, the structural feature required for efficient, low-potential energy storage in SIBs was subject to substantial debates in the scientific community. The first, comprehensive in situ studies on sodiated hard carbon by Stevens and Dahn were indicating a deposition of sodium in the closed pores, a unique feature of hard carbon.[16–18] More and more studies are emerging, which provide evidence that it is exactly the closed pore, which is able to accomodate sodium in a so-called quasimetallic state, a condition in which electron density is back-donated into the alkali metal orbitals, decreasing the formal oxidation state, according to nuclear magnetic resonance (NMR) studies.[19]
While literature correlating the existence of closed pores with low-potential sodium storage is ubiquitous, investigation on the effects of pore size, shape and chemical nature of the carbon on the sodium deposition mechanism is still in its early stages. To shed light on these relationships is the scope of the present thesis. By synthesizing model materials of precisely known morphology, porosity, and chemical nature, the required attributes, like heteroatom content and porosity are derived. Electrochemical impedance spectroscopy analysis is additionally established as a highly valuable technique to monitor different modes of sodium

storage. Further evidence for the necessity of closed pores is demonstrated by selective pore closing and filling. Finally, the acquired knowledge is transferred towards the synthesis of precisely tailored materials, which are capable of storing sodium at potentials close to that of metallic sodium. Hence, this thesis contributes to the development of efficient negative SIB electrodes by providing mechanistic knowledge on sodium storage in different stages and utilizes the obtained insights to present synthetic approaches to obtain materials with desirable properties for the use in low-potential sodium-ion anodes. The collected insights of the present work will therefore hopefully serve as guidelines for the future design of efficient anodes used in high-energy sodium ion batteries.

2. Introduction

2.1. Energy storage systems

2.1.1. Fundamentals, definitons, and characteristics

Energy storage and management is closely related to human evolution. Even far before the industrial revolution, steam engines, and electricity, people had to come up with solutions for problems like cooking warm food or heating their commodities. In a broader sense, energy storage is accomplished by preparing or gathering a substance of higher inner energy, be it thermal, chemical, electrical or other. This substance should come in a convenient physical appearance, in order to be able to stockpile and consume it whenever it is required. To stick to the above example, the perhaps earliest form of energy storage is the collection and burning of wood. Solar energy is converted by trees into chemical energy via photosynthesis and the resultant lignocellulosic mass (i.e. wood) is reacted with atmospheric oxygen by people, in order to transform the chemical energy into heat.[7] An analogous reasoning can be applied to any other fuel, however in modern society a definition of energy storage and particularly of energy storage systems not only must encompass a wider range of energy sources, means of storage, and applications, but also needs to include aspects such as sustainability and geopolitical interests.

An energy storage system is generally defined as a technical appliance capable of fulfilling the three fundamental processes of energy uptake, storage, and release in one cycle. It forms a unit of components such as the energy converter, reservoir, as well as all auxiliary elements, required to accomplish the aforementioned cycle.[7] The respective segments do not necessarily have to be localized at the same place, neither are they bound to a certain component, but the overall efficiency, defined as the ratio between energy stored to energy released, will depend on their amount and design. Energy storage systems can be classified according to several different criteria. If an energy storage system can only be charged and discharged once, it is considered a primary, if it is designed for multiple charge-storage-discharge cycles it is termed a secondary storage. All fossil fuels, such as gas, oil, and coal are therefore

primary sources and the terminology can be extended to batteries by regarding single-use batteries as primary, and rechargeable ones (i.e. accumulators) as secondary batteries. The physical state of the energy stored is another important aspect, with consequences on the properties and possible applications of an energy storage system. Most commonly, categories like electrical, chemical, mechanical, and thermal energy are used. Purely electrical storage can be accomplished only in capacitors, where charges are separated from each other to form an electrochemical double layer. Chemical storage is usually realized by employing other types of energy in order to create chemical bonds and synthesize a compound of high internal energy. The ease of transportation of the created medium distinguishes this type of storage against the others, but it requires the transformation of different forms of energy into each other during charging and discharging, hence lowering the overall efficiency. Classical fossil fuels are typical representatives of chemical storage, technological implementations are often referred to as "power-to-X". Mechanical storage can be again subdivided into potential energy (*e.g* storage reservoirs), kinematic energy (e.g. flywheels), and pressure storage (*e.g* caverns). Thermal storage is generally affected by inherent dissipation of heat and requires insulation. By this way, usually no long term storage can be accomplished, but thermal storage can contribute to the overall efficiency of a process, if implemented *e.g* in the heating of architecture or the supply of hot water.[7]

As a combination of electrical and chemical processes, electrochemical energy storage (EES) constitutes a special and particularly promising type of energy storage. Here, the application of an electrical potential causes an electron current, which results in the equivalent amount of a chemical substance to react towards a product with a higher internal energy. In the reverse process, the compound can react to the initial form, enabling the withdrawal of the previously stored electrical energy. EES in principle does not need transformation of one form of energy into another, because an electrical current is used to both charge and discharge the system, and therefore proceeds with high efficiency. Additionally, electricity is arguably the most versatile appearance of energy and can be easily conducted over relatively long distances and utilized on-site.[7]

Before continuing to the further discussion and classification of the presented energy storage systems with respect to time and amount of energy stored, some important characteristic quantities need to be defined. They can be conveniently viewed as connected to the physical quantities power and energy, with the units W (Watt) and Wh (Watt hour), respectively. The term energy W is the absolute energy content of a particular energy storage system, additionally setting it into a relationship with the time required to charge or discharge, yields the physical quantity power P. In order to be able to compare different technologies, it is use-

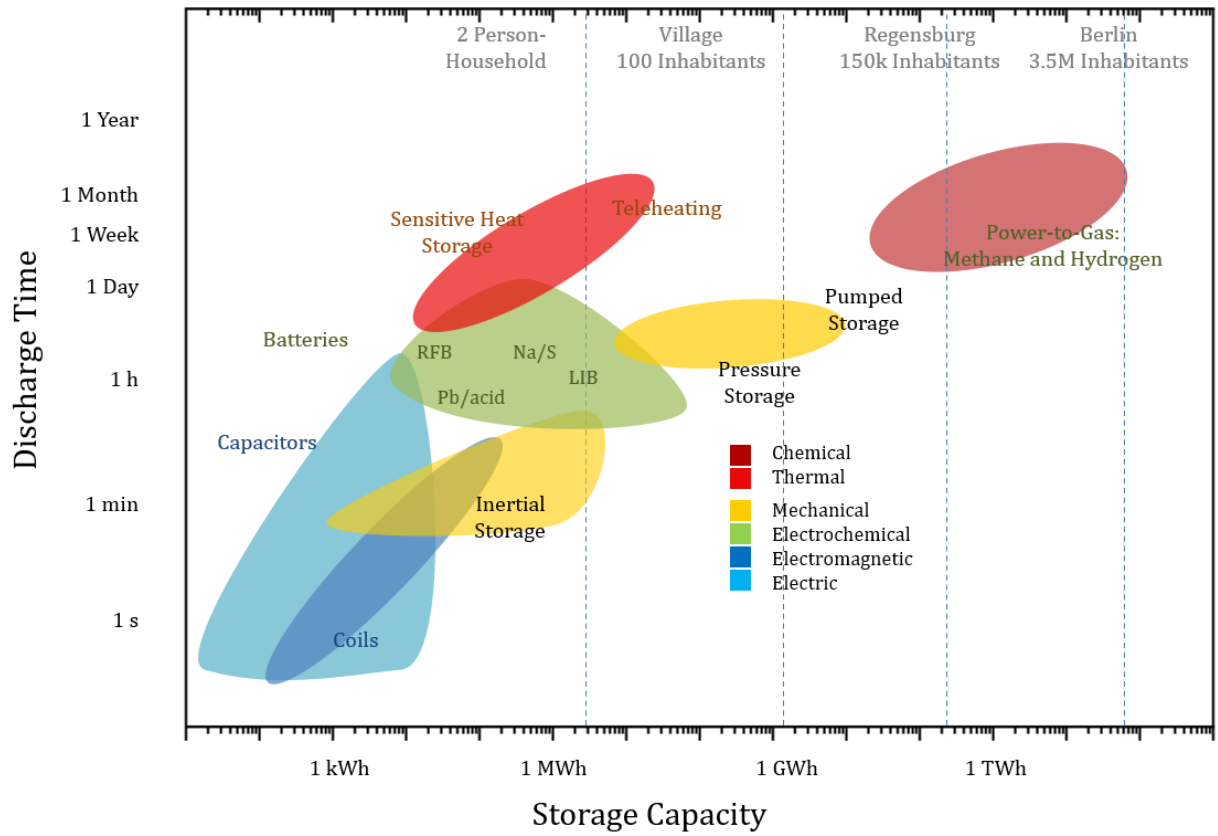

Figure 2.1.: Ragone plot of different energy storage systems, classified by energy type. Typical, technologically implementable storage capacities are plotted on the abscissa, and discharge times on the ordinate, instead of energy density and power density, respectively. Reproduced after Sterner et al..[7]

ful to normalize power and energy to the mass or the volume of the system, respectively.[7] The resulting quantities are the gravimetric or volumetric energy/power density (alternatively often called "volume/mass specific energy/power"), which is an information about the energy content or power output of a unit mass or volume of the particular energy storage type. Frequently, the term "capacity" is used in the discussion of energies or energy densities. This is not to be confused with the physical capacitance, a quantity often used in capacitor research, and will be used depending on the context within this work, henceforth. High energy and power densities are particularly important for mobile energy storage for the application in e.g. consumer electronic, communication, and transportation, whereas they can be sacrificed in favour of other factors like low cost or operational safety, when larger scale storage is concerned. In most cases energy and power density behave antiproportional to each other, meaning that usually a storage system capable of storing large amounts of en-

ergy per unit mass or volume will only be able to be charged or discharged over longer times, resulting in a low power density. This dilemma is often termed as the "Ragone-conflict" and can be visualized in a double-logarithmic plot of power vs. energy (density), the Ragone-diagram, exemplary presented in figure 2.1 with the "power"-axis replaced by the equivalent quantity "discharge time". It is evident from this plot that the power/energy characteristics of an energy storage system predetermines its application to the greatest extent and finally leads to temporal and size-classification of energy storage. Capacitors or coils can typically store only low amounts of energy, while being capable of discharging within seconds or minutes. This renders them ideal for temporary buffers of energy peaks or other applications, where short bursts of power have to be dealt with. Electrochemical storage offers higher storage capacities in trade of longer discharge times and is therefore suitable for equalizing the energy profile of a single, renewably powered household.[7] At the current state of development to supply the energy demand of entire cities is only possible by means of chemical storage, due to energy density limitations. This reasoning underlines the importance of the diversification of energy storage devices and the design of systems, which efficiently serve the purpose targeted by the application field. Stability is another important factor, when talking about safety and long term economy of a storage technology. Two types must be distinguished in this context, where on the one hand cycling stability describes the number of charge-store-discharge cycles an energy storage system can undergo before the end of life is reached and on the other hand the calendric stability means the time such a system can be left unexploited without suffering a loss of capacity or other properties. For every desired field of application a suitable energy storage system has to be selected, based on the presented above but also on other parameters, relating to sustainability aspects, as energy storage becomes particularly important when it comes to the implementation of renewable sources into the energy supply of entire societies.[7]

2.1.2. Energy storage and renewable energy sources

The global need for energy is currently increasing and also is expected to rise in the future, as not only human population is growing, but with steadily ascending life standards in developing and emerging market countries also the energy consumption per capita is on the rise, as evident from figure 2.2.[20] In order to be able to provide more and more people with an ever improving and energy-intensive lifestyle, more energy must be produced. In figure 2.2 a) it is demonstrated that at today's state of technological development, this energy demand would be vastly covered by the burning of fossil fuels, which would only

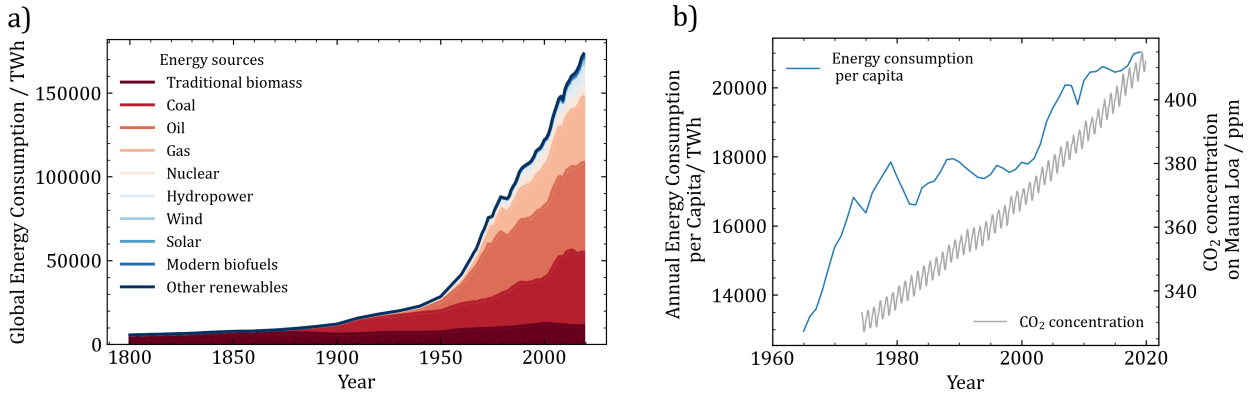

Figure 2.2.: Global energy consumption a) by source and b) per capita. From Smil[4] and BP Statistical Review of World Energy,[5] published online in OurWorldInData.org, retrieved from 'https://ourworldindata.org/energy-production-consumption'. CO_2 concentration from Thoning et al.,[6] retrieved from 'https://gml.noaa.gov/aftp/data/trace_gases/co2/in-situ/surface/'.

accelerate the continuous trend of accumulation of carbon dioxide in the atmosphere, shown in figure 2.2 b).[4,5] Carbon dioxide is a greenhouse gas and therefore contributes to global warming and further resultant problems, such as extreme weather conditions, droughts, and the expansion of deserts and infertile lands. Even if this anthropogenic global warming is dismissed or mitigated, despite the evaluation of the international panel on climate change (IPCC) of human impact on global warming as likely to very likely,[21] it is undeniably true that too high of an atmospheric carbon dioxide concentration will have a significant impact on the metabolism of many species in the food chain as well as on the respiratory system of animals, leading to a direct or indirect impact on human health.[22–24] Furthermore, carbon dioxide is only one aspect of environmental pollution caused by the combustion of oil, gas, and coal. Even though the problem was foreseen by Arrhenius and others already in the late 19$^{\text{th}}$ century[25,26] only in the last few decades the results of humanity's reckless action are starting to materialize, forcing the development of a truly sustainable energy economy.

According to the report on pathways to sustainable energy by the united nations economic comission for europe, sustainable energy rests on three pillars, namely energy security, environmental aspects, and the impact on the quality of life on involved individuals.[27] Energy security is concerned with national energy supplies from an economic and political point of view, while with respect to quality of life, sustainable energy must be accessible and affordable to the broad society and at the same time must cause as little risks as possible for the public health. This includes acute hazard due to failure but also long term harms due to

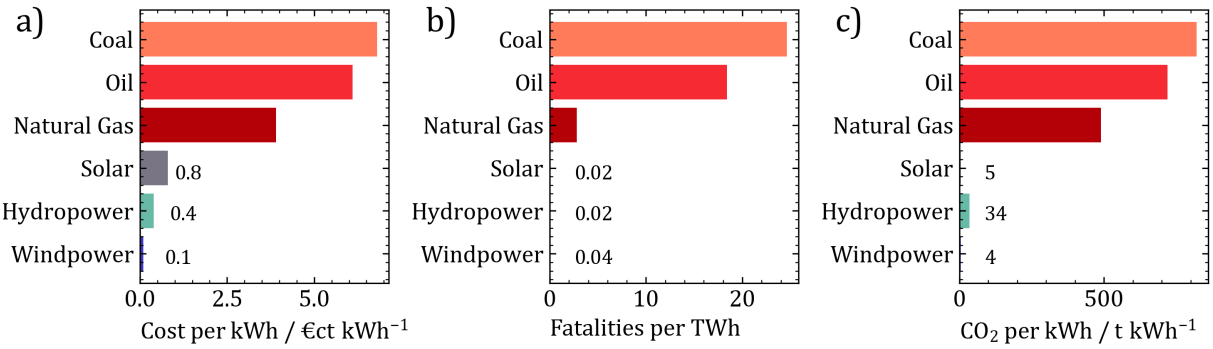

Figure 2.3.: Cost, fatalities, and CO_2 emissions per unit energy by source. Costs adapted from Wesselak et al.,[28] fatalities from Markandya and Wilkinson,[29] and Sovacool et al.,[30] and CO_2 emissions from Turconi et al.[31] and Pehl et al.[32]

pollution of the surrounding. Finally, the environmental aspect aims at protecting humanity from risks arising from the energy economy on the environment, overlapping with the former field regarding protection from pollution, but mainly dealing with the consequences of climate change, with special focus on the reduction of CO_2 emissions as a major contributor to the greenhouse effect.[27] While a reduction of energy need and an overall more efficient utilization of it is necessary, it will be inevitable to shift energy production towards renewable sources. An evaluation of currently available energy sources in figure 2.3 clearly shows that traditional fossil fuels lag behind modern renewables regarding all three, safety, CO_2 emissions, as well as cost per kWh of energy produced.[28–32][1]

Turning away from fossil fuels towards the electrification of the most influential energy sectors – grid electricity, transportation, the chemical industry, and heating – would require an entire reorganization of the present energy supply structure. In an executive summary published by the Federal Environment Agency of Germany from 2010 a roadmap for the shift towards renewable energies by the year 2050 is outlined.[33] There, it is expected that the higher efficiency reached by the direct production of electricity from renewable sources as compared to the classical combustion/transformation technology will cause a reduction in primary energy consumption, i.e. the gross energy use including losses by conversion efficiency factor, in the electrical grid from 515 TWh to 390 TWh. Assuming a constant passenger and a growing freight traffic, the electrification of the transportation sector will also reduce the energy need due to increased efficiencies of electric powertrains. The newly

[1] Nuclear energy is disregarded in this discussion deliberately, as the issues with this technology, mainly waste disposal and proneness to terrorism and proliferation, are beyond the subject of sustainability, but rather fall into the realm of politics and ethics, to the opinion of the author.

emerged electromobility will, however, have to be supplied by the electric grid and therefore burdens its primary consumption with another 150 TWh. A similar effect is forecast in the heating sector, where at lower percentages of renewable consumption the power-heat-coupling will increase the efficiency, but when approaching a fully renewable economy heat will have to be generated from electricity, which finally adds around 95 TWh to the energy demand from the grid.[7,33] The bottom line of this breakdown is that the future energy market as a whole will massively depend on electrical energy from renewable sources and that the load must be distributed evenly on a local as well as a temporal scale, as these systems are highly fluctuating in their electricity output. Expansion and upgrade of the electric grid can solve this problem to some extent but it is unavoidable to store the generated electrical energy, especially when fully turning to renewable sources. As of 2015, only 1 % of the energy consumed worldwide could be stored at all, 98 % of which was stored through pumped hydroelectricity, which is obviously insufficient.[20,34] This underlines the importance of research dedicated to energy storage systems on the entire range of size and timescales for the further advance of sustainable energy supply.
As it was partially introduced in section 2.1.1 a large variety of energy storage systems exists, each with different advantages and disadvantages. However, as was already pointed out, the leading future energy type will be electric, therefore it is reasonable to invoke as less transformation steps as possible and take electrochemical energy storage into closer consideration, as it offers the best trade-off between high efficiency and energy and power density, while being versatile and independent of geographical conditions. The fundamentals of EES will be explained together with some practical aspects in the following section.

2.1.3. Electrochemical energy storage

In EES an electrical current is used to drive a reversible redox reaction and the energy is stored in the chemical bonds of the formed species. This approach allows high efficiencies close to 100 %, because the Carnot-cycle, which usually limits the efficiency of energy transformers, does not apply here. In this discussion, the limitation of a closed system is explicitly pointed out, so that mainly batteries fall under the definition, whereas energy conversion and power-to-X systems like fuel cells, or physical storage devices like (super)capacitors are disregarded, although all of the mentioned technologies share some similarities with each other. During the charging process electrical energy is expended to force an endergonic reaction, which is released in the discharge step, when the redox reaction (ideally) is proceeding backwards to form the starting compounds, causing an electrical current. Physically, this current

flow can be expressed as charge (in Coulomb) per unit time (in seconds) and therefore has the dimension of current with the SI unit Ampere (A).[35]

$$I = \frac{dQ}{dt} \qquad [I] = \frac{C}{s} = A \tag{2.1}$$

The electron flow is related to the progress of the chemical reaction via Faraday's laws. If one transferred electron corresponds to the flow of the elementary charge $e = 1.602 \cdot 10^{-19}$ C, then the charge of a mole of electrons is equal to the elementary charge multiplied by Avogadro's number $N_A = 6.022 \cdot 10^{23}$, which yields Faraday's constant, $F = e \cdot N_A = 96485$ C mol^{-1}. Taking into account that one formula conversion can include more than one electron by considering their number as z_e, Faraday's law can be formulated as:

$$Q = z_e \cdot F \tag{2.2}$$

The electrochemical reaction is typically conducted in an electrochemical cell, consisting of two electrodes connected via an external electrical circuit, where the electrical current is led through, as well as an ion-conducting medium, which ensures the mass transport and charge balance between the two electrodes, termed electrolyte. The electrolyte can be liquid or solid, in the former case it is common to separate the half cell compartments by density, diaphragms, or separators.[35] A full electrochemical cell always consists of two half cells, where on one side the reduced species loses an electron and is hence oxidized, and on the other side an oxidized compound takes up an electron and becomes the reduced species. The electrode where the oxidation takes place is called the anode, the one where reduction occurs is called the cathode, so that this nomenclature depends on whether the exergonic or the endergonic process is regarded. Additionally, the distinction between negative and positive electrode exists, where the positive electrode is the one with the higher electrochemical potential, irrespectively of the process under consideration.[35] The electrochemical potential of one half cell at a constant temperature and pressure is described by $\Delta_R G = -z_e F \Delta E$, directly resulting in the general form of the Nernst equation 2.4, if referred to the expression for the Gibbs free energy, equation 2.3.[36]

$$\Delta_R G = \Delta_R G^0 + RT \ln \prod_{i=1}^{k} a_i^{\nu i} \tag{2.3}$$

$$\Delta E = \Delta E^0 + \frac{RT}{z_e F} \ln \prod_{i=1}^{k} a_i^{\nu i} \tag{2.4}$$

The potential of the combination of both half cells in the full cell, i.e. the measured open circuit voltage, is defined as the potential difference between the anode and the cathode.

$$\Delta E = E_{\text{Cathode}} - E_{\text{Anode}} \tag{2.5}$$

As the terms "anode" and "cathode" depend on whether the charge or the discharge is concerned, the sign of the potential varies. Furthermore, the measurement of potentials is always carried out relative to a defined standard electrode system, to mention the most important examples, the standard hydrogen electrode, or several second-type electrodes such as the saturated calomel or silver/silver chloride electrode.
Some important considerations for the conceptualization of an electrochemical cell can be made here. First of all, according to the basic physical definition of power $P = E \cdot I$ or energy $W = E \cdot Q$ (with P, the power, E, the voltage, I the electrical current, and W the energy), the energy density depends on two parameters, the potential difference of the half cells and the number of chemical reactions that can take place per unit mass or volume of the cell. In practice, this means that the potential difference should be chosen as large as possible, favoring more noble compounds for the positive electrode and less noble for the negative electrode.[36] Regarding the charge density, likely the most important setscrew for practical applications is the number of charge carriers exchanged per unit mass or volume of the material, depending on whether the gravimetric or volumetric energy density is considered. For the full battery other cell components, like current collectors, separators, housings, or battery management systems (BMS) must be regarded as well, as they constitute vital parts of the full energy storage system, so that the importance of the characteristics of the pure active electrode material fades away when moving to a more technical scale.
The efficiency metrics of an EES must be discussed separately. Besides energy efficiency loss due to overpotentials caused by ohmic resistances or electrode kinetics, side reactions are the major source of efficiency loss. They can be manifold and depend not only on the battery type, but also on the state of charge, the life cycle of the battery, and the applied currents and general parameters of utilization. The ratio of capacity input to output is commonly termed as the coulombic efficiency and is an important measure for the occurrence of parasitic side reactions. As EES are typically built as a closed system, only in some cases allowing access to the interior or gas exchange, like in lead-acid batteries, a low coulombic efficiency can severely limit the lifetime of an EES.[7] From a simple estimate it is evident, that a coulombic efficiency of >99.9 % is required to operate a battery for more than 200 cycles, if the end of life is defined at 80 % capacity retention.

Nowadays the most widespread battery types on the market are lead-acid batteries, which find their application in starter batteries and outside of the consumer market are often used as stationary storage, and LIBs, which are frequently found in all areas that require high energy density, such as transportation and consumer electronics.[7,37] However, many more potential cell chemistries exist, out of which most are suitable for stationary storage, while only a selection can be applied for electric vehicles due to significantly different performance requirements.[38] According to Wadia et al.,[38] only redox couples based on Li have the potential to operate in high energy density applications such as electromobility, while for stationary EES a variety of couples can be exploited. The authors calculated an "energy storage potential" for several possible battery types, based on the annual production of the required elements, projecting that apart from LIBs and the lead-acid system, sodium based chemistries like Na/S, or Na/$NiCl_2$ have been identified as having an energy storage potential, capable of keeping pace with energy production, while meeting government-projected price requirements. Alkali-ion batteries based on lithium, sodium, or others will play a significant role in future energy storage. Considering the ubiquity and versatility of the wider class of alkali-ion batteries, it is reasonable to discuss this array of systems in more detail.

2.2. Alkali-ion batteries - state of the art

2.2.1. Common origins

The rising development and spread of various types of portable electronic devices in the 1980s drove the development of more and more powerful secondary batteries. Starting with rechargeable NiCd cells of different formats, soon the environmetally and safety-concerning Cd was replaced by metal hydrides in the NiMH battery. However, the energy density soon reached its limits and severe drawbacks like the memory effect or the lazy battery effect initiated research on alkaline secondary cells. Lithium primary batteries, where a metallic lithium anode was combined with a metal-oxide cathode, were known since the early 20th century and were commercially available since the seventies of the same century.[39] Their high mass-specific capacity in the range of 300 Wh kg^{-1}, the low self-discharge, and robustness with respect to operational temperature inspired the research of rechargeable lithium secondary batteries in contrast to primary ones. Cells in which metallic lithium anodes are employed are inherently impossible to recharge, because dendritic lithium deposits after only a few cycles, causing shortcuts by piercing of the separator, finally resulting in a failure of the battery and a thermal runaway in the worst case. Therefore, a lithium storing compound

had to be found, capable of storing as much lithium as possible with respect to the mass of the compound itself, without undergoing irreversible chemical side reactions or sacrificing the low electrochemical potential. Among alloying and conversion electrodes, carbonaceous materials turned out to be useful for this application.[40] Graphite in particular was subject to great research interest, ever since the existence and formation of binary graphite intercalation compounds was demonstrated by Guerard and Herold in 1975.[41] Its incompatibility with the most prominent electrolyte solvent during that time, propylene carbonate (PC) together with the lack of solid electrolytes with sufficient for application conductivities, moved the focus of academic and especially industrial research efforts towards the exploration of the related, though considerably less ordered materials nowadays mostly referred to as soft and hard carbon.[40,42] The structure of these classes of carbon shall be treated in more detail in later sections of the thesis, but it should serve as a first approximation that soft carbons consist of turbostratically disordered, but mostly parallel layers of graphene, and therefore will adapt a graphitic structure upon reaching their respective graphitization temperature, typically around 2300°C. Hard carbons on the opposite have domains of pronounced graphitic stacking as well as such where carbon atoms are arranged rather randomly. These materials will keep their disordered structure even upon exceeding the graphitization temperature and rather transform into a glassy carbon.[14,15] Accordingly, Rosalind Franklin termed these materials *graphitizable* and *non-graphitizable* carbons in her pioneering work from 1951.[43] Soft carbons exhibit similar lithium storage characteristics to graphite while at the same time being stable in the state-of-the-art electrolyte of that time, PC. As a result of extensive optimization work on precursors and temperature treatment, the first commercially available LIB was introduced by Sony in 1991, using an elaborately treated soft carbon on the anode and $LiCoO_2$ on the cathode.[40] Non-graphitizable, or hard carbon anodes were used in second generation LIBs, while advances in electrolyte development and the switch to mixtures based on ethylene carbonate (EC), dimethyl carbonate (DMC), and diethyl carbonate (DEC) finally enabled the operation and widespread triumph of the graphite/$LiCoO_2$ LIB, which is to the present date outweighing other cell compositions on the market, measured in units of produced energy density of these batteries.[40,44] Even though it often seems like the LIB was determined and designed to dominate from its early days on, cell systems based on the other alkaline metals, in particular on sodium, were pursued just as insistently and until the breakthrough of $LiCoO_2$ were even on par with LIB research.[44–47] Working with sodium was however difficult at the end of the 20^{th} century, as the quality of battery materials and gloveboxes was often insufficient to safely handle the more reactive metal.[48] Finally, the main reasons why SIB research was mostly discontinued in the late 1980s is that high

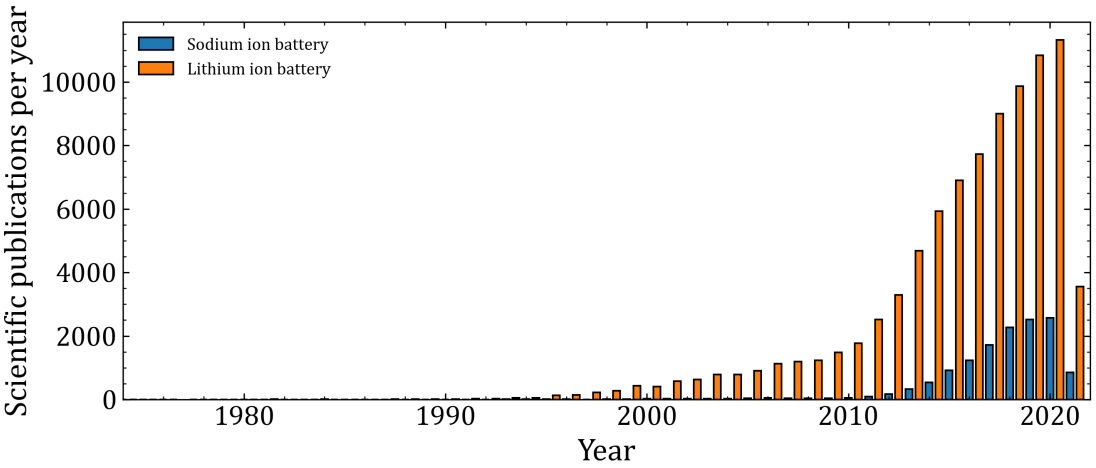

Figure 2.4.: Scientific publications related to LIBs and SIBs according to a web of science search in July 2021 for the terms "lithium ion battery" and "sodium ion battery", respectively.

energy densities were readily available using comparably simple materials such as $LiCoO_2$ on the cathode and diverese carbons and even graphite on the anode side.[40,44] Contrary to its lithium analog, $NaCoO_2$ exhibits a complex sodiation and desodiation curve, see figure 2.9a) with a voltage difference between charged and discharged state of more than one Volt, rendering practical application rather difficult.[44] Even more severe limitations were encountered on the negative side, where disordered carbons and later graphite were known and used for Li-insertion. Only few studies about SIB anode materials were available before 1990[49–51] and moreover sodium was found incompatible with graphite, as no thermodynamically stable binary intercalation compounds are formed.[44] As a result of the success in development of LIBs from simple and abundant components and the difficulties encountered in SIB research, the interest in the latter technology soon stalled and, except for few but important research inputs, e.g. from Stevens and Dahn,[16–18,52] was not rediscovered until the early 2010s. This can be seen from figure 2.4, where the majority of research on SIBs begins only after 2010, while papers on LIBs constantly contribute to the publication output. However, it should not be overseen in this context that a large amount of investigation on alkali ion batteries was and is being performed in industrial laboratories, e.g. by Sony, and therefore is not represented by scientific articles but is rather manifested in patent applications.[39,40]
The reason for the recent revival of SIB research interest is that due to the prospect of declining LIB resources, more abundant energy storage technologies must be explored.[53] In order to achieve an understanding of the benefits and drawbacks of LIBs and the challenges

encountered in the attempt to replace them by SIBs in certain energy storage applications, the fundamental operating mechanism of both systems will be discussed in detail. The current LIB and SIB technology in application-oriented as well as academic research will be presented in the following sections and their market potential will be briefly addressed with respect to availability of the required resources and related costs.

2.2.2. Fundamental operating principle and components

The term "alkali ion battery" encompasses a wide array of cell chemistries, in particular Li, Na, and K ion batteries are in the focus of research.[44,54,55] Each of the named alkali metals has to be paired with suitable reaction partners on positive and negative sides, in order to design a functioning cell. The fundamental operating principle of an SIB is shown in figure 2.5 and is basically valid also for other types of alkali ion batteries, if the electrode materials are replaced. The anode serves as a host for an electropositive alkali metal species, be it an alloy, or a graphitic, or carbonaceous intercalaction compound. A hard carbon anode is shown in figure 2.5. Upon discharge, the compound on the negative side is oxidized and releases alkali ions, which migrate through the electrolyte and are finally accommodated in the active material of the positive electrode.[56] The cathode material is often a metal oxide, where the metal center undergoes a redox-reaction upon alkali-ion uptake.[57] Of course different concepts than the ones mentioned here exist also for the cathode material and the battery is usually termed according to the compound employed on the positive side. The name "alkali-ion battery" is reserved to materials, where alkali ions do not undergo further reactions in the active material of the cathode, these are commonly transition metal oxides, phosphates, coordination polymers, or polyanionic compounds.[57] They are opposed by the special class of alkali-sulfur batteries, where typically a carbon-sulfur composite is employed as the positive electrode and the ions form (poly-) sulfides upon discharge, the transfer of anode materials to this technology is non-trivial and requires the solution of several sulfur-specific problems.[37,58] Organic battery components constitute another field of research, serving different applications with their own specific challenges, so that they will not be covered by this work, neither.[59,60]

Cathode materials

In all alkali-ion batteries capacity and voltage, and hence the energy density, are strongly dependent on the cathode chemistry. For LIBs, the benchmark system among alkali-ion batteries, the most important and most frequently investigated group of materials are metal

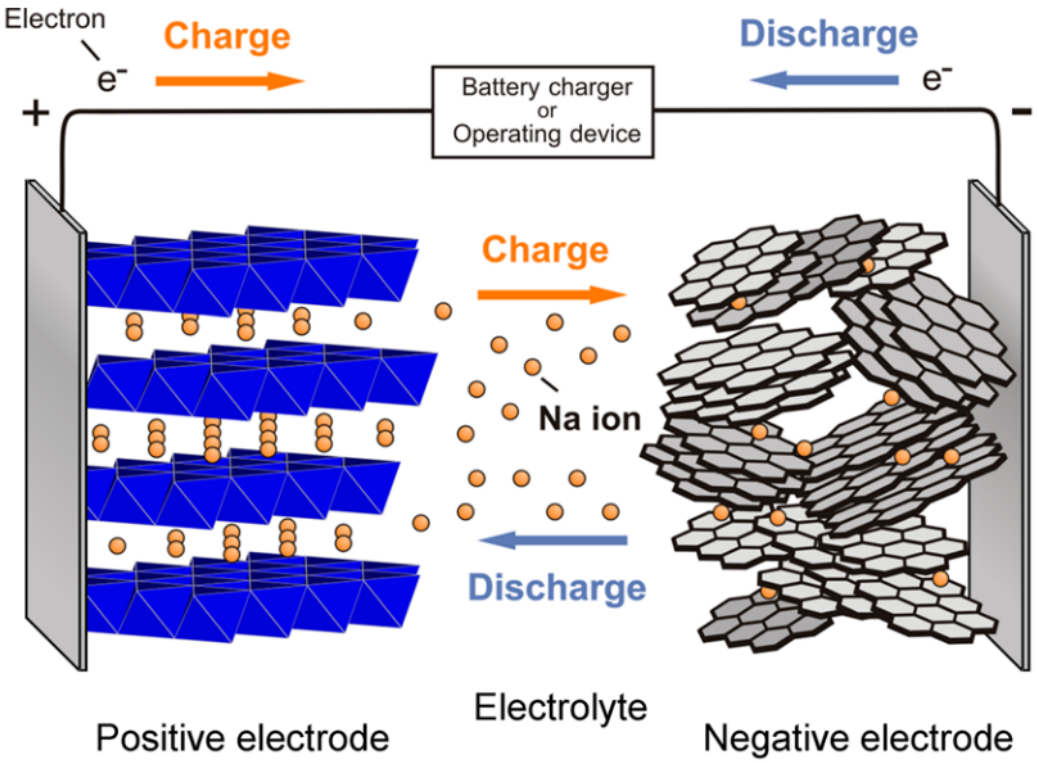

Figure 2.5.: Schematic representation of the operating principle of a SIB. Reprinted with permission from Yabuuchi et al., *Chemical Reviews*, **2014**, *114*, 11636-11682. Copyright 2014, American Chemical Society.

oxides with a layered structure of the α-$NaFeO_2$ type with the general formula $LiMO_2$, where M can be Co, Ni, or Al, also in mixed stoichiometries, see figure 2.6a). In the first commercialized material, lithium cobalt oxide (LCO, $LiCoO_2$), lithium can be intercalated and deintercalated utilizing the redox couple Co^{4+}/Co^{3+} at potentials around 4.0 V vs. Li/Li^+.[40] Formally, the stoichiometry could yield 274 mAh g^{-1}, but due to the collapse of the structure at Li-contents lower than 30 % only 140-150 mAh g^{-1} can be utilized at a cut-off voltage of 4.2 V vs. Li/Li^+, as shown in the voltage profile in figure 2.6b).[57,61,62] Although the energy density of LCO with 624 Wh kg^{-1} is among the highest of all metal oxides, it has severe drawbacks regarding safety and stability.[57] Exceeding the voltage limit of 4.6 V vs. Li/Li^+ for example, causes the evolution of oxygen, which in turn can react with the flammable organic electrolyte causing a thermal runaway.[63–65] These problems can be solved by electronic control circuits, so that for mobile and automotive applications the advantages of such a material outweigh its drawbacks. However, particularly for stationary applications, where volume and mass limits are less restrictive, it is rational to sacrifice energy and power

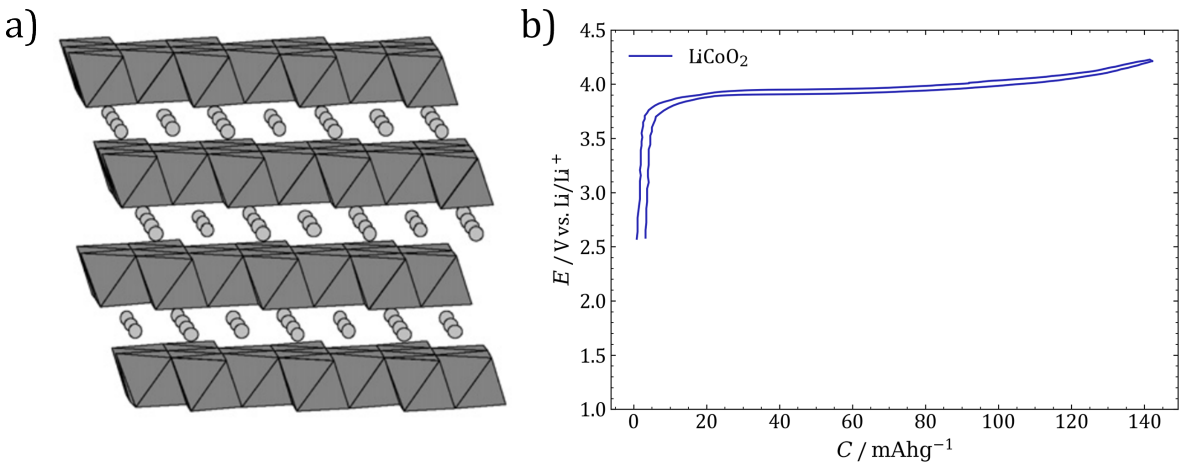

Figure 2.6.: a) Crystal structure of LCO with MO_6 octahedra shown in dark grey and Li-ions as spheres. Reprinted from figure 5a) in *Journal of Power Sources*, *174*, Ohzuku et al., "An overview of positive-electrode materials for advanced lithium-ion batteries", 449-456, Copyright 2007, with permission from Elsevier. b) Charge-discharge curve of LCO, data digitized and reproduced from Ohzuku et al. 2007.[62]

density in favor of a stable long-term operation and explore alternative compounds. Furthermore, the scarcity of Co, the Earth's crust contains only 30 ppm of it, together with the uneven distribution with large deposits in politically and socially unstable areas like Central Africa additionally advocate against the use of Co-containing materials in EES.[57,66,67] In order to resolve the problem of scarcity and resource conservation, the structurally closely related compound lithium nickel oxide (LNO, $LiNiO_2$), where all Co is replaced by cheaper Ni, can be used. Ni containing metal oxides generally can release more Li from their crystal structure, without compromising their stability and therefore this material can achieve a higher reversible capacity of around 200 mAh g^{-1} at lower cost.[57,68] Yet, it raises the same concerns with its Co-analogue regarding oxygen evolution and additionally shows a faster capacity fade due to Li-ion mobility within the crystal lattice, an effect often termed lithium nickel disorder.[57,69,70] $LiMnO_2$ constitutes the third single-metal layered oxide, however its thermodynamically stable structure shows unfavourable electrochemical properties, while the electrochemically active α-$NaFeO_2$ phase is difficult to synthesize and undergoes an irreversible structural transformation into spinel type $LiMn_2O_4$ (LMO) during delithiation.[71,72] Spinels are to some extent an own material class and will be briefly introduced at later stage. A successfully employed concept to tune the properties of the cathode materials is the synthesis of mixed crystals. The proneness of LCO or LNO to form oxygen upon exceeding the discharge voltage limit for example can be easily alleviated by incorporating Ni, Co, and

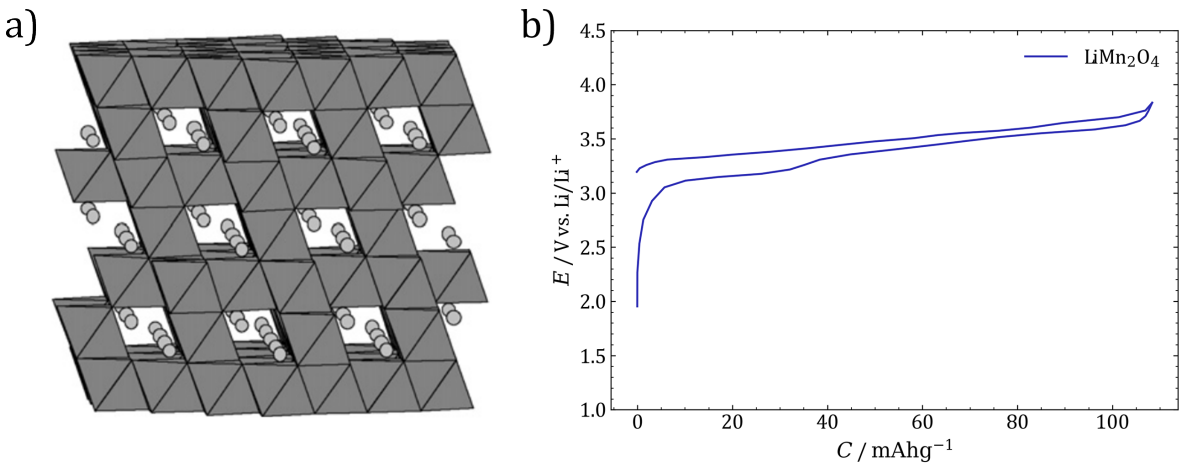

Figure 2.7.: a) Crystal structure of LMO with MO_6 octahedra shown in dark grey and Li-ions as spheres. Reprinted from figure 5b) in *Journal of Power Sources*, *174*, Ohzuku et al., "An overview of positive-electrode materials for advanced lithium-ion batteries", 449-456, Copyright 2007, with permission from Elsevier. b) Charge-discharge curve of LMO, data digitized and reproduced from Korthauer et al. 2007.[62]

Al ions, yielding the commercially available crystal lithium nickel cobalt aluminium oxide (NCA, $Li(Ni_{0.8}Co_{0.15}Al_{0.05})O_2$).[57,73] A mixed crystal structure with a good trade-off between energy density, power density, safety, and cyclability, lithium nickel manganese cobalt oxide (NMC, $Li(Ni_{0.33}Mn_{0.33}Co_{0.33})O_2$), is frequently applied in commercial cells. As usual, Co contributes to a high electrical conductivity, while Ni serves as an affordable means for the reduction of the Co content. Mn stabilizes the lattice against decomposition due to oxygen loss, however negatively influences the conductivity. 160 mAh g^{-1} can be used reversibly at a operational voltage of 3.7 V, resulting in an energy density of 592 Wh kg^{-1}.[57,74,75]
Spinels are another type of metal oxides employed as cathode active materials in LIBs, with the general formula LiM_2O_4, where M is typically Mn or Ni. LMO is one of the oldest known and utilized representative of this class, with a typical capacity of 100 mAh g^{-1} at 4.1 V.[76] The structure is shown along a typical charge/discharge curve in figure 2.7. Typically, this compound has a poor cycle stability, due to the intrinsic Jahn-Teller instability of its crystal structure and is therefore highly sensitive towards water and acids, which cause the dissolution of Mn^{2+} ions.[77–80] These Mn^{2+} ions can deposit on both, anode and cathode as MnO, causing capacity loss or even cell damage.[81] However, the class of spinels is gaining increased research attention as mixed spinel crystals can reach operating voltages of 4.7 V or even 5.1 V in some examples, already reaching the oxidative stability limit of the electrolyte.[76,82] Finally, another important material class employed as LIB cathodes are

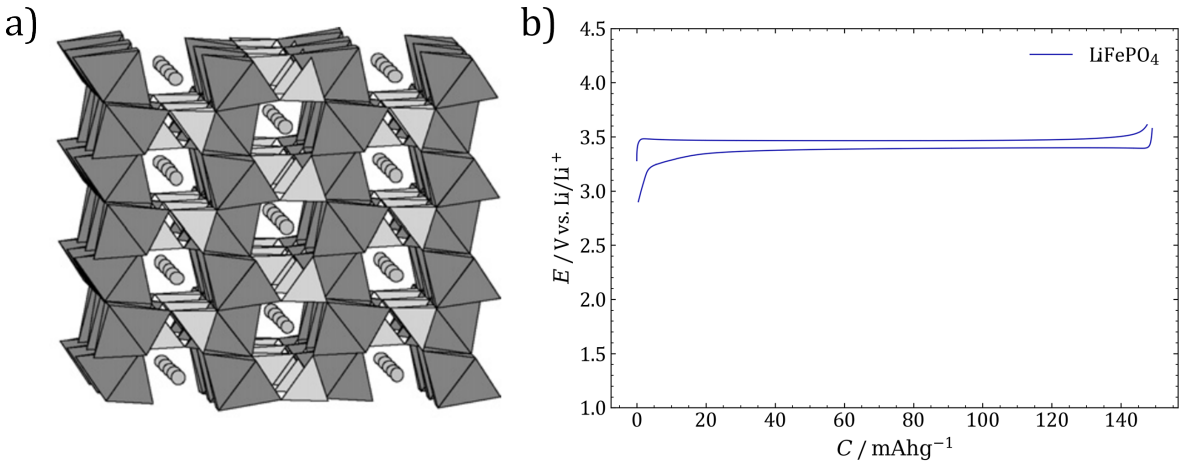

Figure 2.8.: a) Crystal structure of LFP with MO_6 octahedra shown in dark grey, PO_4 tetrahedra in light grey and Li-ions as spheres. Reprinted from figure 5c) in *Journal of Power Sources*, *174*, Ohzuku et al., "An overview of positive-electrode materials for advanced lithium-ion batteries", 449-456, Copyright 2007, with permission from Elsevier. b) Charge-discharge curve of LFP.

metal phosphates, $LiMPO_4$ where M can be Fe, Mn, Co, or Ni, which are often referred to as olivines, as they crystallize in the respective structure, see figure 2.8a). The most widely known substance among this class is lithium iron phosphate (LFP, $LiFePO_4$), in which approximately 160 mAh g^{-1} of Li equivalent can be stored at an operating voltage of 3.4 V, as shown in figure 2.8b). LFP exhibits a series of outstanding characteristics, such as an exceptionally flat charge and discharge plateau and virtually no structural distortion during operation, leading to a high cycle life, and finally the ability to be charged and discharged at up to 20 C.[83–85] On the downside, the low ion and electrical conductivity require the manufacturing of submicron sized particles or even carbon coating, in order to compensate this drawback, yet up to 97 % of the theoretical capacity can be reached with these techniques. Incorporation of Mn into the structure leads to a higher working voltage, however reduces the conductivity even further, so that an optimum is found in commercial applications around 60 % of Mn. Using Co or Ni phosphates, high voltage LIBs can be realized with discharge plateaus around 5.0 V vs. Li/Li^+.[57,83,86,87]

The replacement of Li by Na is a viable and important approach to enable affordable and environmentally reasonable EES on the grid, but also mobile scale. The first and most obvious reason is the ubiquity of Na, which is about 1000 times more abundant than Li.[44] At the first glance, the concern of an intrinsically lowered energy density arises, due to the higher molar mass of Na compared to Li (23.0 vs. 6.9 g mol^{-1}), however this is only substan-

tial, if metal electrodes are concerned outside the context of the remaining components and compounds required. Approximately a half of the mass of a cell originates from the cathode material, about a quarter is due to the anode side, and the remaining quarter is contributed by inactive components, such as separators, current collectors, etc. On a battery pack level the impact of active materials becomes even less.[38,88,89] Considering the formula mass of the typical layered oxide $LiCoO_2$ and comparing it to its Na analogue $NaCoO_2$, the contribution of the bare alkali ion is illustrated. In the case of Li, a theoretical capacity of 274 mAh g^{-1} is calculated, while the value of 235 mAh g^{-1} for Na is only by 15 % lower, not to mention that the theoretical capacity rarely coincides with the practically useful one, as was discussed in the previous paragraphs. Another limitation that is encountered in the transition from Li to Na is the lower operating voltage on cell level, which is a result of a less negative redox potential of Na compared to Li and even the other alkali metals. This cannot be explained solely by the standard electrode potential, which is strictly valid only for aqueous solutions, but the solvation energy of the ion in the respective solvent has to be regarded as well. By doing so in a simple Born-Haber-cycle, the cohesion, the ionization, and the solvation energies must be considered.[36] Without the solvation energy, Li shows the lowest energy for the reaction of the metallic species to the bare ion ($A(s) \rightarrow A(g) + e^-$) by far, this is reasonable considering the small ion radius, leading to the hard ion character, compared to the heavier alkali metals. This same small ion radius however, leads to the exceptionally low standard electrode potential of Li/Li^+, as the solvation (in the case of standard potentials, hydration) is generally more exothermic with smaller ion radii.[36] However, the cell voltage is not affected by the solvation energy thermodynamically, whatsoever, as a liberated ion is solvated and again de-solvated upon accommodation in the respective host matrix, hence occurs on both sides of the equation.[90] Yet, a lower solvation and desolvation barrier might improve the kinetics at the electrode/electrolyte interface and the lower solvation energy of the Na-ion causes the higher ion conductivity in Na-based electrolytes, both positively influencing the suitability of SIBs for high power applications.[44,91–93] In most cases, the cell voltage is due to the cathodic energy gain, from incorporating alkali-ions into the host structure, therefore a brief comparison of cathode materials for LIBs and SIBs is necessary. The transition from Na to Li is not as straightforward as it may seem from literature and a one-by-one replacement is definitely not possible.[94,95] Layered oxides are an important class of cathode materials for SIBs just as for LIBs. As mentioned previously, $NaCoO_2$ cannot be effectively used due to the distinct potential difference between its two voltage plateaus. Like in many other mainly Co and Ni based layered oxides known from LIB research investigated for sodium storage, phase transitions induced by a shift in stacking order of the layers of

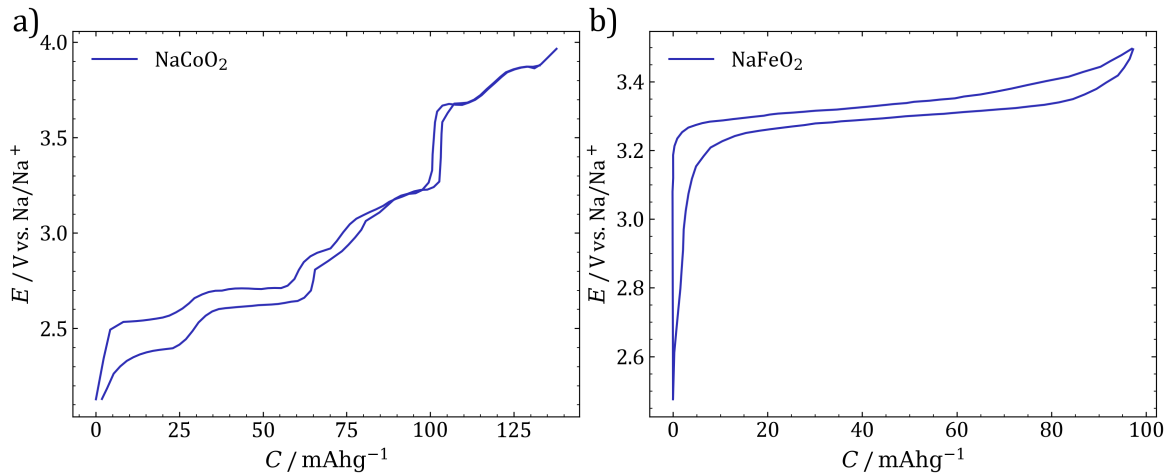

Figure 2.9.: Voltage profiles of $NaCoO_2$ and $NaFeO_2$. Data digitized and reproduced from Yoshida et al.[96]

metal oxide octahedra upon extraction of the relatively large Na-ion are the reason for the change in energy of the sodium sites, which in turn causes a complicated voltage profile, rendering these materials challenging to employ in practice.[44] α-$NaFeO_2$ is a typical sodium ion host, storing more than 90 mAh g^{-1} of sodium at a cut-off potential of 3.4 V vs. Na/Na^+ at a relatively flat voltage plateau, oppositely to $NaCoO_2$ in figure 2.9a).[96] A higher discharge than about 0.3 mol Na per formula unit however, leads to an irreversible phase transition and hence to the deterioration of the material, so that the material delivers an energy density of 300 Wh kg^{-1}, about half the amount of a typical Li-layered oxide cathode.[97] Using the analogous Mn species, it is possible, depending on the polymorph, to reversibly extract 120-130 mAh g^{-1} of Na from the structure. Unfortunately, the cycling stability of these materials is significantly lower and the voltage profile becomes less flat. Further, the Mn^{2+}/Mn^{3+} couple is limited to a potential of less than 3 V vs. Na/Na^+. Therefore, similar to LIB layered oxides, it becomes viable to replace only parts of the metal in the host structure, in order to combine favourable properties. Energy densities in the order of 520 Wh kg^{-1} can be achieved that way, notably using only abundant and non-toxic materials.[44] Layered oxides of the α-$NaFeO_2$ type can be prepared with many different 3d-transition metals, ranging over Ni, Cr, V, and Co, each in different polymorphs, reaching similar maximum capacities of up to 160 mAh g^{-1}, but the vast majority of these materials suffers from very inconsistent voltage profiles upon sodium insertion/extraction.[44,94,95] The chemistry of polyanionic compounds is by far more rich for Na than it is for Li and therefore holds the biggest promise to bring forth a suitable material for the positive electrode of SIBs.[44,95] $NaFePO_4$, the Na

counterpart to the popularly used LFP, exhibits a similar cycling behaviour with a flat voltage plateau during the sodiation, and two voltage plateaus during desodiation at 2.9 and 3.0 V vs. Na/Na^+ in its electrochemically active triphylite structure.[98,99] Just like in LFP, almost the entire theoretical capacity can be utilized here. Mn-based phosphates behave similar to Fe-based ones, but studies investigating this material class remain rare. On the downside, the drawbacks such as the low conductivity and the resulting need to further treatment of the particles are shared with LFP, as well.[44,94,95] Replacing the phosphate by the pyrophosphate anion to obtain $Na_2MP_2O_7$ energy density is sacrificed in favor of a higher reversibility and power density, as the diffusion channels grow by the use of a larger structure-determining anion. Fe and Mn are mainly the metals of choice for this materials class, where Mn pyrophosphates even yield cell voltages up to 3.6 V. Again, mixtures of phosphates and pyrophosphates were prepared in the endeavor to achieve a high energy density material with good rate capability. As a result of anion-optimization, fluorine-doped Na_2FePO_4F deserves particular attention. It can deliver up to 110 mAh g^{-1} of reversible capacity in practice and shows two voltage plateaus, close enough to each other for practical application at 3.06 V and 2.91 V vs. Na/Na^+.[44,94,95] NASICON-strctured vanadium phosphates with the formula $Na_3(V_2(PO_4))_3$ were found to exhibit reversible capacities of up to 120 mAh g^{-1} in a voltage window of 2.3-3.9 V vs. Na/Na^+ at a flat plateau with low polarization during sodiation and desodiation.[44,100,101] Their main advantage is their extremely high Na-conductivity (hence the name **Na S**uper **I**onic **Con**ductor), enabling a capacity retention of 50 % even at 40 C current during sodiation in the case of $Na_3(V_2(PO_4))_3$.[102] Also here, the properties can be tuned by the previously presented approaches, namely replacement of metal ions or anions.[44,94,95] The last viable material class in this overview are metal hexacyanometallates, also frequently termed prussian blue or white analogues, with the name derived from the parent complex. These materials consist of $Fe(CN)_6$ octahedra with alternating Fe^{II} and Fe^{III} centers, as shown in figure 2.10a). They are capable of accommodating Na ions in their octahedral vacancies at two voltage plateaus at 3.6 and 2.9 V vs. Na/Na^+, reaching 120 mAh g^{-1} in the case of $Na[FeFe(CN)_6]$, at a capacity retention of 87 % over 500 cycles, where the typical sodiation/desodiation curve looks like in figure 2.10.[44,103] Using Mn, higher capacities can be reached at the cost of operating voltage, conductivity, and cycling stability, enabling optimization by preparing mixed metal prussian whites.[104,105] This literature overview demonstrates that a selection of viable materials exists for the SIB positive electrode, however it cannot be overseen that their capacities, operating voltages, and hence also their energy densities are lagging behind LIB cathodes, hampering the application of SIBs in fields, where already the LIB leaves room for improvement in terms of

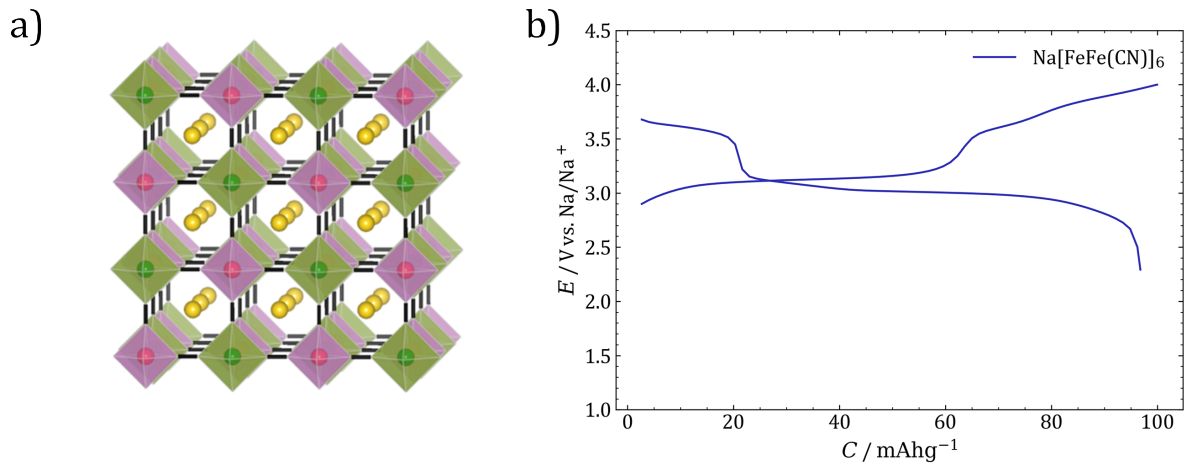

Figure 2.10.: a) Crystal structure of $Na[FeFe(CN)_6]$ with $FeCN_6$ octahedra shown in purple and green, representing the two oxidation states of iron. Reprinted with permission from figure 24b) in Yabuuchi et al., *Chemical Reviews*, **2014**, *114*, 11636-11682. Copyright 2014, American Chemical Society. b) Charge-discharge curve of $FeCN_6$.

energy density, such as electric transportation. However, the properties of the presented materials render the SIB suitable for application in cheap and sustainable large scale EES systems.

Non-electrode components

The electrolyte plays an important role in any type of EES, which is to conduct ions between the electrodes, thereby closing the electrical circuit of the cell by enabling mass transport. In alkali-ion batteries another crucial function is executed by the electrolyte, which is the formation of a solid-electrolyte interphase (SEI), a layer of polymers and salts forming mainly at the negative electrode, due to the reductive decomposition of electrolyte components, protecting the electrode from undergoing further side reactions.[106]
Generally, the same requirements as for LIBs hold for SIB electrolytes, which are chemical, electrochemical, and thermal stability, ionic conductivity, and electrical insulation. At the same time, especially in view of sustainability and economy, these compounds must be sourced from sustainable and abundant resources, be of low toxicity, and a low cost. The electrolyte must not react with any of the cell components, in particular active materials, current collectors, cell housings, or separators. The electrochemical window should cover the charge and discharge voltages of the materials chosen; a highly reductive environment is present at the negative electrode and oxidative conditions are found at the positive one, especially in the case of high-voltage cells.[94] While the latter point is less vital in SIBs, as

in general lower potentials are present on the positive side, reductive decomposition must be prevented or at least restricted to well known and controllable reactions. Thermal stability encompasses, besides a wide liquidus range, resistance against thermal decomposition, as well as the maintenance of constant properties throughout the entire temperature range. Ionic conductivity enables the fast ion transport and therefore a lower cell resistance and hence higher power densities, while electronic insulation is necessary for a stable and safe operation with low self-discharge rates. The electrolyte can be seen from the point of view of its components, which are mainly the solvent or solvent mixture, the sodium salt, and possible additives.[106] As a major part of the electrolyte, the alkali-salt plays an important role for the performance of the final system. Generally, in alkali-ion electrolytes the transference number of the anion is always higher than that of the cation due to its larger diameter and hence its weaker solvation shell, resulting in the majority of the mass transfer and charge being carried by the anion of the salt. Therefore, the power is finally often limited by the diffusivity of the cation, which, due to the smaller ratio of charge to radius puts Na ions in favour over Li ions.[106] The choice of salts is determined by parameters such as solubility in typical solvents and a suitable electrochemical stability window, in addition to the factors mentioned above, whereby basically analogous salts qualify for SIBs as for LIBs. The decomposition of alkali salts typically occurs as an anodic process, therefore anions are usually constructed with electron withdrawing atoms around the central atom, to yield weakly coordinating anions, such as $ClO4^-$, BF_4^-, PF_6^-, $CF_3SO_3^-$ (OTf), $[N(FSO_2)_2]^-$ (FSI), and $[N(CF_3SO_2)_2]^-$ (TFSI). Among these salts there is no optimal candidate and each option requires a trade-off between the discussed properties.[106,107] Due to cost and safety reasons, $ClO4^-$ is not viable for practical application and is only a choice for academic research. BF_4^- and OTf both produce less conductive electrolytes, where OTf additionally contributes to the corrosion of Al current collectors. This is also a problem for TFSI and possibly even for FSI, the use of which would normally comprise a cost advantage for SIBs.[108,109] PF_6^- offers the best intermediate between conductive electrolytes, suitable stability, and sufficient safety, only limited by sensitivity to moisture and elevated temperatures.[106]

When discussing electrolyte stability and salt solubility, the solvent deserves at least as much attention as the salt. Contrary to the salt, the expedient electrolytes are further prone to reductive decomposition and the by-products formed thereby are adding another level of complexity to the system, which is the SEI. The general requirements for the solvent where already named previously and are equal for SIBs and for LIBs. Today, most research is conducted using polar, aprotic solvents, organic carbonate esters and glycol ethers being the most prominent compound classes among these organic-based electrolytes. Here the latter

category is specifically interesting in academic research, regarding the use of graphite as anode material for SIBs or even metallic anodes, which is why their role will be discussed at a later stage together with the anodic sodium storage mechanism. Although no single solvent can fulfill the requirements sufficiently, cyclic carbonates such as EC and PC are advantageous due to their high dielectric constant and both, electrochemical and chemical stability under cell conditions.[110] When graphite is used as an anode, PC will cointercalate into the structure together with Li-ions, leading to step-wise exfoliation of graphene layers and the deterioration of cell performance upon cycling, a similar problem in a lesser extent occurs also in hard carbon anodes. Additionally, PC appears to be unstable in combination with HC anodes, leading to a furthermore pronounced SEI growth with each subsequent cycle. EC does not show this behavior, even oppositely, it forms a stable, protective SEI-layer upon reductive decomposition. However, it is not possible to use EC alone, as its melting point is found at 36°C, so that it is necessary to switch to binary or even ternary solvent mixtures. Linear carbonates, such as dimethyl carbonate, ethyl-methyl carbonate, and diethyl carbonate, are well miscible, have a sufficient liquidus range and most importantly in their role as co-solvents for EC, have a low viscosity, so that an optimized solvent system can be developed. Typical mixtures for SIBs are EC/DEC in a ratio around 1:1, in LIBs EC/DMC or EC/DMC/DEC are used, where in general it can be observed that binary mixtures of EC with DMC yield higher ionic conductivities, while addition of linear carbonates with larger alkyl-residues results in a more flexible, organic SEI layer, which is why DEC is often preferred as a co-solvent particularly in SIBs.[107] Some works, however, find that the impact of the solvent on the cell performance is rather low in Na electrolytes, as compared to their Li counterparts, suggesting future development work to focus on the optimization of the SEI buildup, rather than solvent/ion interactions in SIBs.[111]

An interesting phenomenon was observed by the group of Adelhelm, when using NaOTf in glycol ether solvents as the electrolyte, combined with graphite negative electrodes.[112] They found that the solvent is capable of solvating the Na-ion in a way that a co-intercalation into the graphite interlayers becomes possible. In this way they reached a capacity of nearly 100 mAh g^{-1}.

Some research is also centered around the use of room-temperature ionic liquids (RTILs) as electrolytes for LIBs and SIBs. These molten organic salts consist only of ions, which results in some interesting properties, such as low volatility, thermal stability, and a rather wide electrochemical stability window. On the other side, RTILs are highly viscous and lack ionic conductivity. Several examples of operational half and full cells exist, yet the practical relevance of RTIL electrolytes remains arguably low, considering the synthetic effort and hence

high cost, connected with their utilization. On top, RTIL-based systems usually require the operation at elevated temperatures, lowering their overall energy efficiency.[106,107,113]
Solid electrolytes are another, increasingly important field of research. Sodium and lithium conducting solids are capable of transporting ions selectively, without a solvation shell, with ion conductivities approaching those of liquid electrolytes, especially for Na. Further they show a higher thermal stability and less proneness to dendrite-induced shortcuts. However, no system comes without limitation. Solid electrolytes cannot be easily adapted from one electrode system to the other, impeding research activities, and furthermore still show a high temperature dependence of ion conductivity. Hence, more investigation will have to be carried out, in order to enter a practically relevant stage. Finally, the mechanism and overall operating principle of all-solid-state batteries differs from that of typical liquid-based systems and hence will not be covered in this work in further detail.[114]
As stated at an earlier instance, the SEI is of utmost importance in alkali-ion battery anodes, and its composition and properties substantially differ between LIB and SIB systems.[107,115] The concept of an SEI was already proposed and supported in 1979 by Peled, when he studied the concurring electrodeposition of alkali and alkaline earth metals and aluminium in different electrolytes.[116] From the observation that in some electrolytes alkali and alkaline earth metals are deposited before alumnium, he correctly deducted that the cathode is covered with a thin layer of ion-conducting, but electronically insulating layer immediately upon contact with the metal, and the thickness of this layer is governed by the tunneling distance of the electrons through the film. As these are properties of a solid electrolyte and the layer is located between metal and the actual electrolyte, the phenomenon was termed the solid electrolyte interphase.[116] The formation of this layer is crucial for the operational stability of a cell, but as electrolyte is consumed upon its buildup and to a varying extent also during operation, it negatively impacts the energy density and the cycle life of a battery. Therefore, the formation mechanism and the structure must be considered in more detail. While the SEIs in both, SIBs and LIBs, consist mainly of an inhomogeneous precipitate of organic and inorganic carbonates, the SEI of LIBs contains more alkyl carbonates and other organic compounds, as opposed to a more inorganic SEI in SIBs.[117] It is mainly the distinct reactivity of the two alkali metals with the carbonate ester electrolytes that causes the different SEI composition in the respective cells.[109] While the main SEI formation step happens around 0.2-0.3 V vs. Li/LI^+ in Li/graphite cells, the same reaction in Na/HC cells is obviously not possible due to the higher half cell potential of the latter, overall leading to a lower SEI stability in Na/HC anodes.[109] The inorganic constituents undergo degradation by reaction and deposition over soluble intermediate species and hence cause a faster aging

of Na half cells, as compared to Li half cells, where the organic SEI would grow only upon current flow during the first few cycles.[118,119] Moreover, the SEI in Na-systems was shown to be more porous and inhomogeneous than in Li-cells, again leading to a proneness to earlier mechanical cracking and constant decomposition.[120,121]
Different methods have been proposed to inhibit the growth of the SEI or at least to control the growth process in order to achieve a compact and durable structure. The simplest and arguably the most viable approach in practical cells is the preparation of electrolytes with SEI-forming additives, such as fluoroethylene carbonate (FEC), vinylene carbonate (VC), or others, but their benefits are often limited to specific anode systems and are not always profitable. Some design aspects for anodes show correlations with the extent of SEI formation. Larger specific surface areas generally lead to lower capacities and higher irreversible first-cycle capacities in both, LIB and SIB anodes.[122–125] Note, that the reduction of surface area effectively mitigates the inefficiency in the first cycle due to electrolyte decomposition, but inefficiency sources such as Na-ion trapping cannot be addressed in such a way.[126] In an extended sense also the post-synthetic reduction of surface area can be regarded as the synthesis of an artificial SEI or at least knowledge can be transferred from this field. This is an approach broadly employed in the venture of utilizing Li or Na metal anodes, but can be also useful for the preparation of closed-porous materials, as will be discussed in the section of anodic sodium storage.[127–129]

Anode materials

The ideal negative electrode in terms of energy density would obviously be a bare metal anode, but as the anodic dissolution of the alkali metals is irreversible in the sense that the smooth metal surface is not re-formed upon reduction, alkali metal storing compounds have to be designed and employed. In reference to previous discussion, a good alkali-storing material must have properties such as low atomic weight and a constant working potential close to that of the bare metal, in order to account for a high energy density. Of course, both, chemical and electrochemical stability over time and cycle life are fundamental requirements to an anode material, just as the usual aspects, like cost efficiency, environmental benignity, and safety.[130] Different storage concepts can be distinguished, such as insertion, alloying, and conversion material. The energy density increases along this series, whereas the (cycling) stability and safety diminishes, in a first, rough approximation. The term "insertion" encompasses the process intercalation and generally is reserved for procedures, where the structure of the host material undergoes no or only minor changes upon uptake of the guest species. Typically, carbonaceous materials are regarded as insertion hosts, but also Ti(IV)-

oxide or titanates fall under this category, and capacities in the range of 300 mAh g^{-1} can be reached in this way.[57,131,132] A brief comparison of sodium and lithium storage in different carbonaceous materials was already given in section 2.2.1 and a whole chapter will be dedicated to sodium and also lithium storage in hard carbons, as this is the main subject of this thesis. An overview over the most important anode materials apart from carbon will follow hereinafter. Titanium-based anodes encompass a range of oxides, utilizing the Ti^{4+}/Ti^{3+} redox couple as the charge compensation reaction during alkali metal uptake. Generally, for most titanium oxide and titanate anode materials, a lithiation potential of around 1.5 V vs. Li/Li^+ can be measured, while the sodiation takes place in a potential window of 0.5-1.0 V vs. Na/Na^+. Hence, using Ti-based anodes in LIBs will result in lower energy densities. For SIBs on the other hand, the voltage is low enough to keep the energy density high, while providing a reliable end-of-charge voltage for safe and metal plating-free operation.[132,133] Titanium dioxide, including its polymorphs as well as its amorphous appearances, can store considerable amounts of both, Li and Na, however, the potential at which the reaction takes place is significantly lower in the case of Na. In a voltage window between 3 and 0 V vs. Na/Na^+, up to 160 mAh g^{-1} of sodium equivalent can be accommodated, at a constantly declining voltage profile.[134,135] Conductivity is a tremendous issue in TiO_2, which can be tackled by similar techniques as in LFP cathodes, i.e. nanosizing and carbon coating of the particles. If these aspects are minded, the majority of the capacity can be retained even at high current densities.[134] Layered titanium oxides have a similar structure as the layered transition metal oxides, described in the previous section on cathodes 2.2.2. As their tetravalent state is stabilized, their sodium intercalation/deintercalation potential is lower than that of the other transition metal oxides and hence it was studied as an anode material for the first time in 1983. An extended structural transition was observed so that only an stoichiometric range of $0.7 \leqslant x \leqslant 1.0$ in Na_xTiO_2 can be effectively used, corresponding to 78 mAh g^{-1}, according to the original publication.[136] Partial replacement of the Ti atoms by Li, Cr, Co, or Ni enables the control over the utilizable Na stoichiometry, cycling stability, and power density.[133] Titanates are arguably the most important insertion anode material besides carbons, in both, LIBs and SIBs. They occur in similar crystal structures, where among a variety of other modifications and compositions the most prominent LIB-oriented formulas are $Li_4Ti_5O_{12}$ and $Li_2Ti_3O_7$. The Li versions of both are basically "zero-strain" materials, where the volume expansion upon Li uptake is below 1 %, and therefore exhibit a good long term cyclability.[137,138] $Li_4Ti_5O_{12}$ shows a relatively flat voltage below 1.55 vs. Li/Li^+ and intercalates up to 3 Li equivalents per formula unit, resulting in a specific capacity of 175 mAh g^{-1}. $Li_2Ti_3O_7$ promises a higher ionic conductivity, however its high capacity

of 235 mAh g^{-1} is only available at a sloping voltage profile.[132] $Li_4Ti_5O_{12}$ can even serve as a host for Na ion storage, where only Na ions are selectively (de)intercalated at 1.0 V vs. Na/Na^+, reaching capacities of 145 mAh g^{-1}.[137] However, generally, due to the larger ionic radius, the electrochemistry of Na based titanates and hence the preferred compositions differ from those based on Li and since Na is also heavier than Li, Na-rich structures are lower in energy density and hence they are unfavoured. $Na_2Ti_6O_{13}$ is a typical sodium titanate used for anodes, with high possible power density and cycle stability, but low capacity. Compared to Li, the operating voltage is lower, similar to TiO_2 materials.[138,139] Tuning the structure and composition, the voltage profile of the anode can be changed to have a rather sloping or plateau-like behaviour and the rate capability can be adjusted, however the intrinsic problem of low capacity and low electrical conductivities remain for the titanate-based anode class.[140]

A series of fourth and fifth main group elements can form binary compounds with Li and Na, where even several Li or Na atoms can appear per formula unit, promising theoretical capacities of up to thousands of mAh g^{-1}. The formation of a clearly defined compound has a great advantage in terms of a constant reaction potential, but the process of alloy formation usually is connected with significant volume changes, causing a rapid capacity loss via mechanical failure of the anode, which must be managed by suitable compositing techniques.[131,141,142] Si is arguably the most studied and well understood alloy anode for Li, due to its high capacity of 4200 mAh g^{-1} at $Li_{22}Si_5$ and the abundance of Si. While the electrochemical lithiation of Si follows a strict sequence of compounds along the Li-Si phase diagram at 415°C, the reaction at room temperature results in the formation of an amorphous alloy, which is furthermore strongly dependent on the Si particle size.[142,143] In an X-ray diffraction study, where Si anodes were lithiated to different extents, it turns out that below 50 mV vs. Li/Li^+ the alloy undergoes a crystallization to form the Li-Si alloy with the highest Li-content at room temperature, $Li_{15}Si_4$. By setting such a lower voltage limit, the material can be cycled more reversibly only within the amorphous range, allowing for less mechanical stress on the grains.[144,145] Despite the high theoretical capacity of Si anodes for Na storage of 725 mAh g^{-1}, no significant alloy formation was observed in practice.[131,146,147] Sb alloys have more distinct phases and hence voltage plateaus, and can alloy with Li to store 600 mAh g^{-1} of capacity at a delithiation potential of 1.0 V vs. Li/Li^+, but the well known problem of volume expansion limits the cycle stability to a few tens of cycles.[142,148] Sb forms alloys with Na as well, however the intermediate species do not follow the phase diagram and appear to be amorphous, which provides a volume-buffering effect and is presumably why the cycling stability of Sb anodes with Na is higher than with Li.[149]

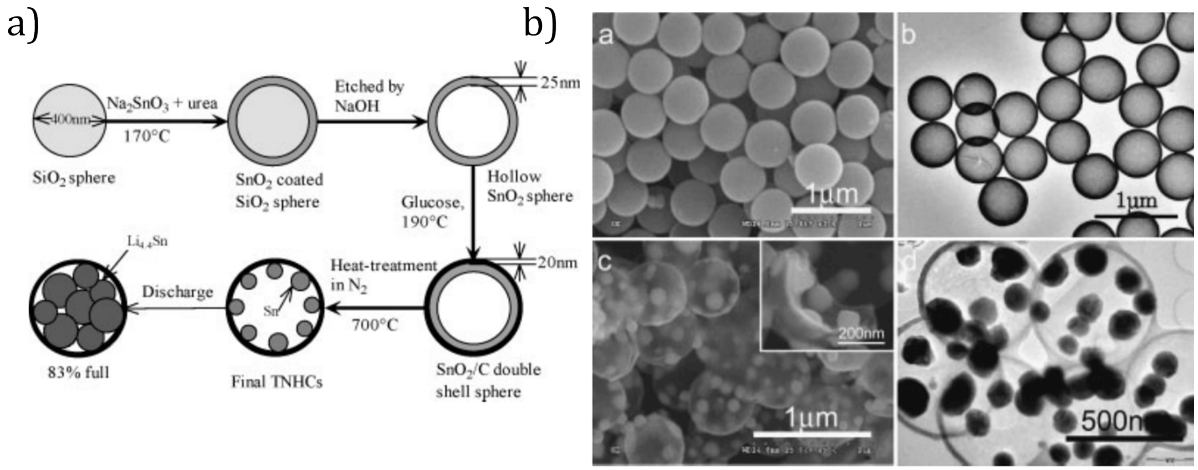

Figure 2.11.: Encapsulation approach for the stabilization of Sn-alloy anodes. a) Synthetic scheme and b) TEM images for the synthesis of carbon-encapsulated of Sn nanoparticles. Reprinted with permission from Zhang et al., *Advanced Materials*, **2008**, *20*, 1160-1165. Copyright 2008, Wiley-VCH Verlag GmbH & Co KGaA, Weinheim.

For Sn anodes in LIBs one can observe the full stoichiometric range from Sn at 0.66 V vs. Li/Li^+ to $Li_{22}Sn_5$ at 0.31 V vs. Li/Li^+, however not all the reactions are manifested as solid voltage plateaus, depending on the phase transition mechanism. This results in capacities in the order of 800 mAh g^{-1}.[142] A very similar behaviour is observed in SIB anodes.[150] Some further materials can be used for LIB alloy anodes, such as Al or Mg, but the problems of volumetric expansion and low stability remain the same.[142] As an interesting class of SIB anode materials, phosphorus shows some remarkable properties, undergoing reactions that are filed between alloying and conversion in the literature.[150] The redox potential of the formation of Na_3P is found at 0.4 V vs. Na/Na^+, whereas the different modifications of P show different characteristics. White P is highly toxic and pyrophoric, red P is abundant and chemically stable, while black P has a high electrical conductivity.[150] Black P has a layered structure, somewhat similar to graphite, and up to 0.25 Na atoms per P can be incorporated between the layers, before P-P bond cleavage and hence expansion and pulverization set in.[151] As similar as the problems of all alloy materials are, as similar are the proposed attempts to solve them. They involve the composition with amorphous and conductive materials, like conductive carbon additives, mechanically ductile particles, in order to make up for the low conductivity and alleviate the expansion issue. A particularly creative, however arguably difficult to realize method is to encapsulate the alloying compound into a hollow, conductive carbon hull and hence to stabilize the grown alloy phase, as illustrated in figure 2.11.[131,142,145,152–154] By this way the authors enabled a size-limited growth

of nanoparticles in order to stabilize the active phase. This approach is furthermore inspiring for the synthesis of hard carbon based anodes, where the forming quasimetallic sodium is as well directed by the surrounding closed pore. Finally, conversion anodes usually employ metal oxides or sulfides as the active materials, which undergo a chemical reaction with Na upon reduction, leading to the formation of a new metal compound and, in many cases, NaO_2. Typically, these reactions happen at relatively high potentials vs. Na/Na^+ but high capacities, even beyond those of alloying anodes, can be achieved.[131,154] However, due to the complexity of the involved reaction, the instability of many compounds over long times, low conductivity, and side reactions, conversion materials rarely exceed cycle numbers of a few tens, or at most 100 cycles without significant deterioration of performance.[155] From this summary on the state-of-the-art of SIB and LIB anodes, its is evident that carbonaceous materials offer the best combination of properties, such as (electro)chemical stability, tuneable structure and properties and relatively high energy and power densities. Therefore, alkali metal storage mechanism in such materials will be discussed in the further section, with a special focus on Na, as carbon materials, especially hard carbons, are particularly promising in this case. Finally, the goal of this work, the elucidation of the nature of the interaction between Na and hard carbon and the synthesis of advanced carbon-based anode materials for SIBs, will be introduced and the chosen approach will be explained.

2.3. Sodium and lithium storage in hard carbons

2.3.1. Structure of disordered carbons

Graphite is the most prevalent sp^2 carbon allotrope and consists of stacked layers of hexagonally arranged, sp^2-hybridized carbon, often referred to as graphene sheets. The X-ray diffraction pattern of graphite in figure 2.13 shows two main reflexes among others, which are the (002) reflex, representing the distance of the graphene layers to each other, and the (100) reflex, arising from diffraction at the plane spanning between carbon atoms within a graphene sheet. The (100) signal could in principle be resolved even further, revealing graphene polytypes with different stacking sequences, ABAB in the case of hexagonal 2H graphite and ABCA in rhombohedral 3R graphite, figure 2.12. In a defect-free graphite crystal the respective graphene layers are arranged parallel to each other and oriented into the same direction.[15] The length of coherently stacked graphene layers orthogonally to the reticular plane is here given by the term L_c, while the size of the layer within plane direction is represented by L_a. L_c and L_a are typically obtained from Raman measurements or

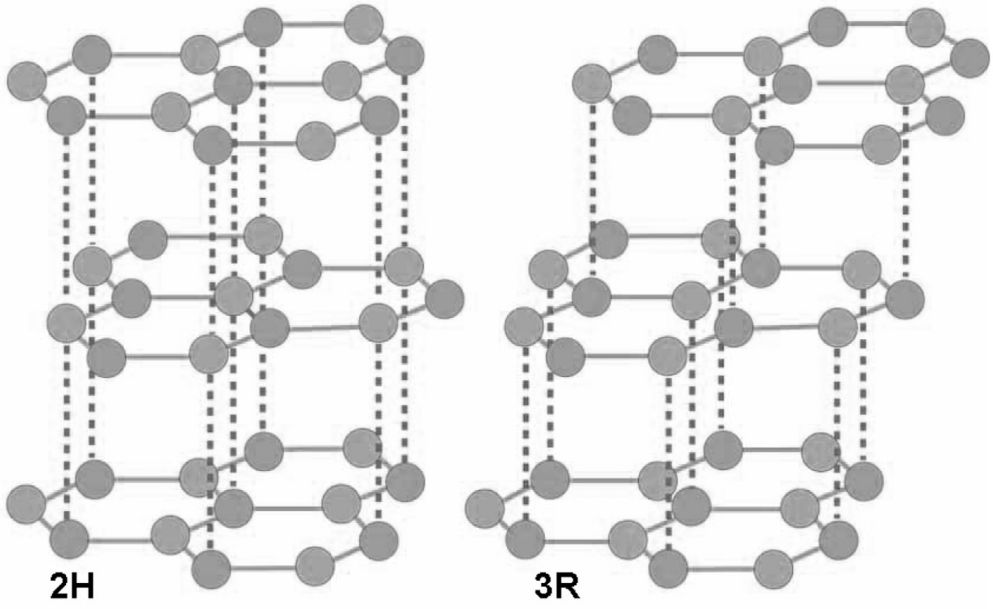

Figure 2.12.: Crystal Structure of 2H and 3R graphite. ABAB stacking pattern in hexagonal 2H, and ABCABC pattern in rhombohedral 3R graphite. Reprinted from Carbon, *95*, Seehra et al., "Detection and quantification of 2H and 3R phases in commercial graphene-based materials", 818-823, Copyright 2015, with permission from Elsevier.

XRD-patterns. The distances d_{002} and d_{100} are accessible via the position of the respective reflexes in the XRD-pattern.[15]

As it was already mentioned previously, graphite is currently the most widespread commercial negative electrode material in LIBs. Upon full lithiation the graphene layers shift to achieve an AAAA stacking motif and form the intercalation compound LiC_6. This reaction corresponds to a theoretical gravimetric capacity of 372 mAh g^{-1} and occurs at potentials close to 0 V vs. Li/Li^+.[122] Disordered carbon materials were also investigated and even employed in commercial LIBs, because they promise higher lithiation capacities, but usually show completely different voltage profiles upon Li uptake and generally hold other challenges for practical application, such as deviating first-cycle efficiencies and incompatibility with cell components. Yet, the most important reason, why disordered carbons are gaining research interest is their ability to store significant amounts of sodium reversibly and at suitable potentials.[15,40] The reason for this behaviour are of course their special structural features, originating from a unique combination of defects and disorder. Disordered carbons can be synthesized from a variety of carbon-rich precursors of natural and synthetic origins, pure organic compounds, but also biomass derived precursors, most prominently by heat treatment at suitable temperature programs.[156–158] During the process of heat treatment,

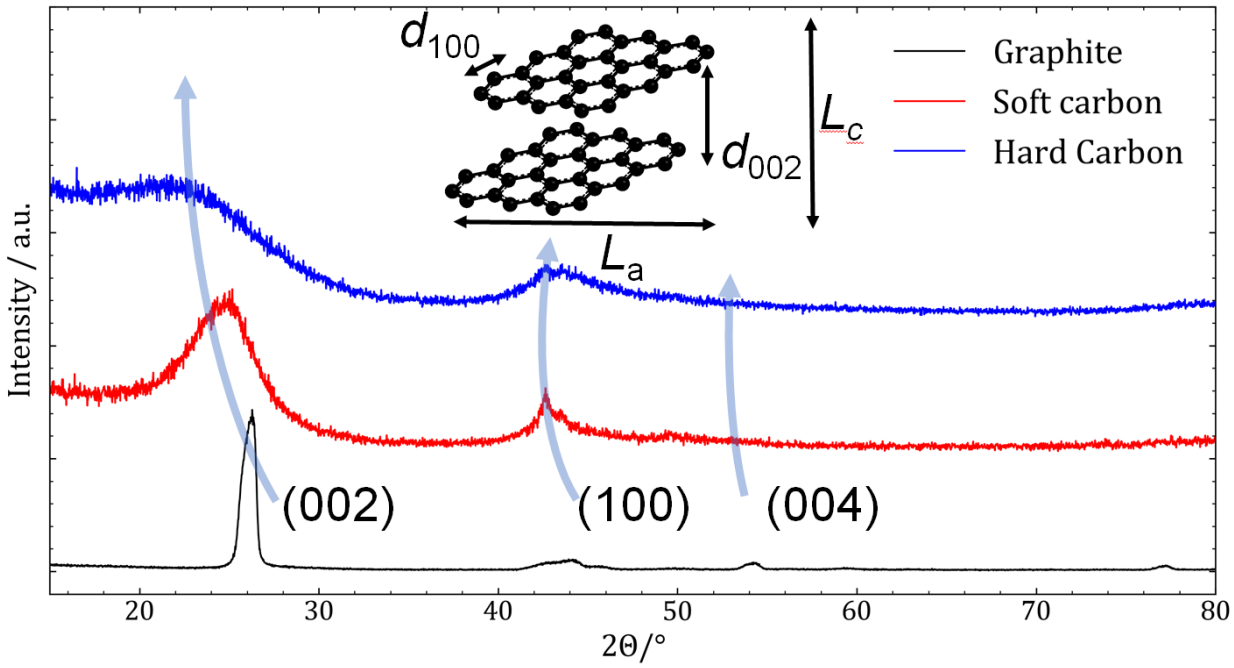

Figure 2.13.: X-ray diffraction patterns of graphite, soft carbon and hard carbon with assignment to most important reflexes. Inset scheme shows relevant characteristics of a crystallite, L_c the crystalline coherency length in stacking direction and L_a, in reticular plane direction.

volatile compounds such as N_2, H_2O, and CO_2 leave the precursor matrix and the fraction of carbon in the resulting product increases, inheriting the name "carbonisation" to this process. Upon heat treatment up to 1000°C, depending on the precursor, a considerable share of closed and open porosity is generated so that surface areas of up to thousands of $m^2\ g^{-1}$ and particle densities of 1.4-1.8 g cm^{-3} are reached.[157,159] At temperatures higher than 1200°C the material undergoes rearrangements of the carbon framework, a loss of hydrogen content, connected with an increase of the amount of sp^2 carbon and carbon six rings, leading to a collapse of external porosity, to yield carbons with gas-detectable specific surface areas (SSAs) lower than 50 $m^2\ g^{-1}$ showing more abundant and larger internal pores with increasing heat treatment temperature.[156,159,160] The processes occuring beyond this temperature and hence also the structure of the resulting product is highly dependent on the precursor employed. This point immediately leads to the distinction between soft and hard carbons.

Soft carbons are carbons derived from precursors such as coal pitch, petroleum pitch, polyvinyl chloride or similar, treated below their graphitization temperature, which is usually found between 2300 and 2500°C.[14] Upon applying this temperature to this type of carbon precur-

sor, they transform into synthetic graphite and hence are also called graphitizing carbons. These carbons have relatively large ordered graphene layers in both parallel and perpendicular directions where the interlayer distance is that of graphite, 0.3354 nm, interrupted by graphene sheets, which are twisted or rotated against each other and are hence called turbostratically disordered, adapting an interlayer distance of 0.3440 nm.[161] In this way, tens to hundreds of layers are stacked on top of each other, with graphite-like zones of up to 60 nm in diameter. The disorder is manifested in a broadening and shift towards low angles of the (002) reflex, see figure 2.13, red line. Upon heat treatment of a graphitizing carbon, the graphitic regions grow in both directions, while the mean interlayer distance decreases and approaches values known for graphite.[43,162,163] Furthermore, the layers are not perfectly flat, but due to point defects within the graphene sheets some extent of curvature is observed. The weak forces holding the layers together result in graphitizing carbons usually being mechanically soft.[15,156] Contrary to soft carbons, hard carbons do not attain a graphitic structure, even if treated at temperatures above 3000°C, and hence are called non-graphitizing carbons, synonymously.[156] It is important to make a distinction between graphitizing or graphitizable and graphitic carbons, as even a graphitizable carbon synthesized below its graphitization temperature is not graphitic yet. Further, both soft and hard carbons, cannot be called amorphous, as they still show some local order and anisotropy, whereas the term "amorphous" is reserved to materials with localized π orbitals.[164–167] Hard carbons are typically derived from cross-linked polymeric precursors like carbohydrates, phenolic resins, but also different types of biomass. Oppositely to soft carbon precursors, which are thermoplastic and often even undergo liquefaction during temperature treatment, thus facilitating the rearrangement of graphene layers towards a parallel and in the end graphitic structure, hard carbon precursors are thermosetting, leading to the inheritance of the macromolecular structure of the parent compound to the resulting carbon. Therefore, the synthesis of hard carbons can be regarded as a solid state carbonization. Within this process, carbon atoms possess a limited mobility with a motion range of up to 1 nm, enabling the formation of a stable, six-ring-based structure, but restricting the structural changes to a minimum, hence maintaining the overall precursor morphology on a larger scale.[156] The void space, formerly occupied by carbon atoms is left behind, resulting in a low density due to a significant share of internal pores, which are particularly important for electrochemical alkali-ion storage.[156,165,168] These features influence the XRD-pattern of a typical hard carbon in two ways, as is exemplarily visualized in figure 2.13. Firstly, the lower interlayer coherence causes a broadening and diminishing of the (002) reflection, which in addition is overlayed by incoherent background scattering caused by micropores.[162,169,170] The main feature of hard

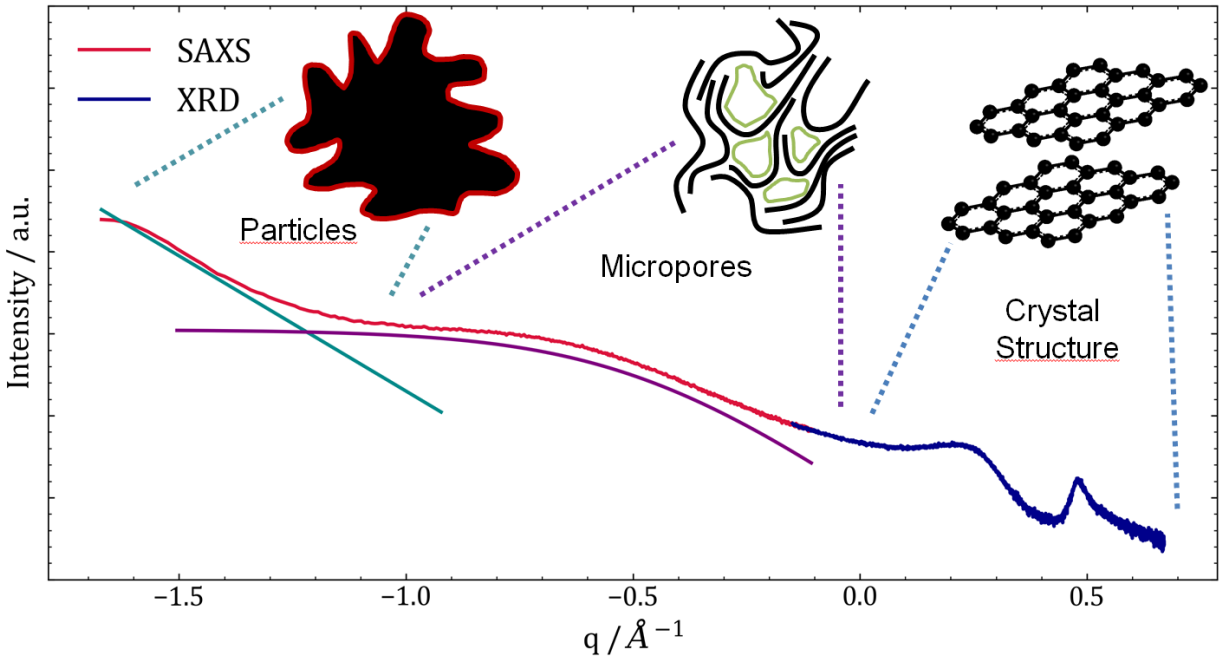

Figure 2.14.: Exemplary X-ray scattering of a hard carbon in a 2Θ or q range covered by SAXS (red line) and XRD (blue line), with the structures, responsible for scattering highlighted. Linear Porod behavior shown in dark cyan, micropore scattering in purple line. Reproduced after Saurel et al..[15]

carbon materials is therefore the (100) reflection of carbon atoms within the reticular plane. The investigation of the microstructure of carbons beyond their crystallinity by small-angle X-ray scattering (SAXS) experiments, also considering their microporosity, dates back to the middle of the 20$^{\text{th}}$ century and nowadays SAXS is an established technique to study carbonaceous materials with inhomogeneous electron density.[156,166] It is in principle an X-ray scattering experiment at very small 2Θ typically below 10° until down to hundredths of a degree. Further details will be discussed in the methods section of this work. Using this approach, it is possible to investigate structures (i.e. phase contrasts) in the size range of roughly one to several tens of nanometers, hence information about meso- and micropores becomes accessible.[171] A representative SAXS pattern of a hard carbon is depicted in figure 2.14. The angular range 2Θ is transformed into dimensions of a scattering vector q using the relationship $q = 4\pi sin(\Theta/\lambda)$, and both axes are typically shown in double logarithmic scaling. At small q the scattering declines with q^{-4}, indicative of a Porod behaviour due to scattering at defined interfaces of large objects. Information about the surface area related to particle grain boundaries can be extracted from this portion of the SAXS curve.[156,172–174] With intermediate q values ($0.1\mathring{A} \leq q \leq 1\mathring{A}$) the scale of investigated structures becomes

smaller, and scattering at micropores now dominates the scattering, resulting in a declining plateau in the SAXS pattern. Finally, at higher q the relationship to an XRD experiment becomes evident, as the incoherent scattering transitions into Bragg diffraction at interatomic, periodic structures and the (100) and (200) reflexes due to atomic carbon-carbon interactions.[156,171] One of the first models comprehensively describing the structure of hard carbons, with the mechanism of lithium and sodium storage in mind, was proposed on the basis of the presented properties as well as on the analysis of SAXS patterns by Dahn et al. in 1997 and is widely known as the "falling cards" model.[171,175] In a series of papers the group measured and analyzed SAXS patterns of pyrolyzed carbohydrates, mainly sugars, but also cellulose, starch, and biomass, which allowed them to draw conclusions on the structural evolution of common hard carbon precursors upon heat treatment between 800°C and 2100°C. They applied a simplified model, which accounted for the linear Porod-part, the plateau-like micropore part, as well as the low-q part of the (002) reflex, and hence could follow the evolution of the radius of gyration of the micropores, and both the macropore and micropore surface areas, respectively. This model is still popular even in recent publications, as it is capable of describing systems with low amounts of lateral imperfections and defects fairly well, using only four parameters.[176,177] They found the macropore surface area to remain constant throughout the temperature series, indicating a negligible impact on the particle size, while the micropore surface area declined until temperatures about 1100°C and remained constant above. The radius of gyration, a measure for the diameter of the closed pore, assuming a spherical geometry, increased linearly with rising heat treatment temperature. The authors concluded upon these data that as the pore surface area remained the same, while their diameter increased, the number of micropores had to decrease, implying a coalescence of micropores into larger pores with bigger correlation lengths into stacking, as well as lateral directions, i.e. increasing L_c and L_a values. They further regarded the evolution of the gyration radius and the stacking height of graphene layers, to derive the actual falling card model, which describes the carbon structure as a house of cards, where each card represents a graphene layer. Upon heat treatment, enough thermal energy is provided to break single sheets of graphene out of their framework and realign parallel to another adjacent sheet, see figure 2.15b). This process explains the growth of seemingly coherent carbon layers and the increase of the pore radius even semiquantitatively within their dataset.[160,171,175] Even though this method explains many features of hard carbons obtained at different pyrolysis conditions, it contains some oversimplifications. Both Franklins early model and the falling cards model, essentially built upon it, describe the hard carbon structure basically as sp^2 domains of certain size, connected by amorphous sp^3

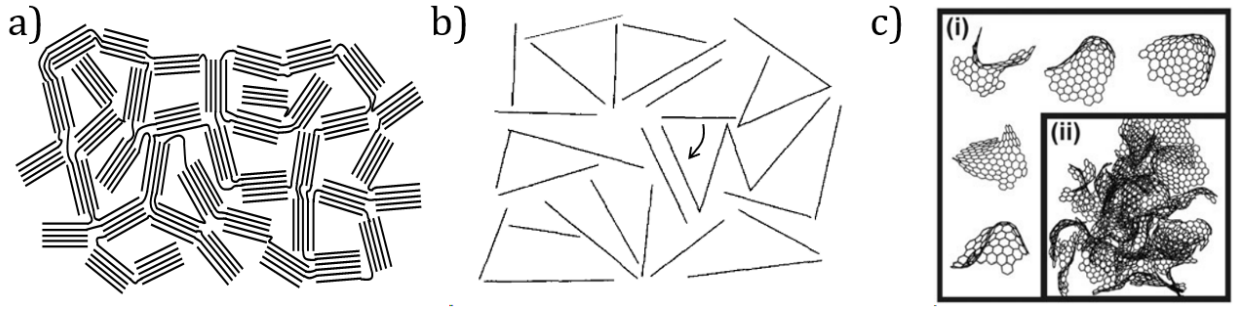

Figure 2.15.: Development of the models of the structure of non-graphitizing carbons. a) Isolated sp^2 fragments connected by sp^3 regions, after Franklin 1951[166] b) "Falling cards" model of the structural evolution upon heat treatment. Reprinted from figure 4a) in *Carbon*, *174*, Dahn et al., "The "falling cards model" for the structure of microporous carbons", 825-830, Copyright 1997, with permission from Elsevier.[175] c) More recent model including curved graphene layers. Republished with permission of Royal Society of Chemistry, from *Physical chemistry chemical physics*, Terzyk et al., *9*, 5919, copyright 2007; permission conveyed through Copyright Clearance Center, Inc.[178]

hybridized patches, as depicted in figure 2.15.[166] This view fails to accurately describe the crosslinks between the more graphitic areas of the carbon framework. These crosslinks would have to be exceptionally, almost unrealistically stable, in order to be able to prevent sp^2 hybridization and consequent graphitization at temperatures beyond 2500°C. Furthermore, the proposed sp^3 fragments connecting the sp^2 zones, are not stable at such high temperatures, rendering their role in the structure of non-graphitizing carbons unlikely.[161,179] Furthermore, structural features like layer curvature, lateral imperfections, and finite size of the carbon layers, present in non-graphitizing carbons, can cause deviations from the $I \propto q^{-4}$ behaviour at low q as well as an overestimation of microporosity from the convex part of the scattering curve.[180–184] Inspired by the structure of fullerenes and related structures, more recent models aim to involve the layer curvature in their description of the hard carbon structure, as shown in figure 2.15 c). Contrary to earlier models, the graphene layers are assumed to be built up from five, six, and seven membered rings, with both sp^2 and sp^3-type bonds between them, even fullerene-like regions were proposed to be part of the structure of non-graphitizing carbons.[161,185] This allows for a better description of the interconnectivity of the layers, the structural development during heat treatment, and hence the formation mechanism of closed pores. Finally, also the interpretation of alkali-ion diffusion through the carbon lattice requires the assumption of extended, curved graphene layers.[186,187] The open porosity of hard carbons, as studied by gas sorption techniques, shows a very distinct development during heat treatment, as well.

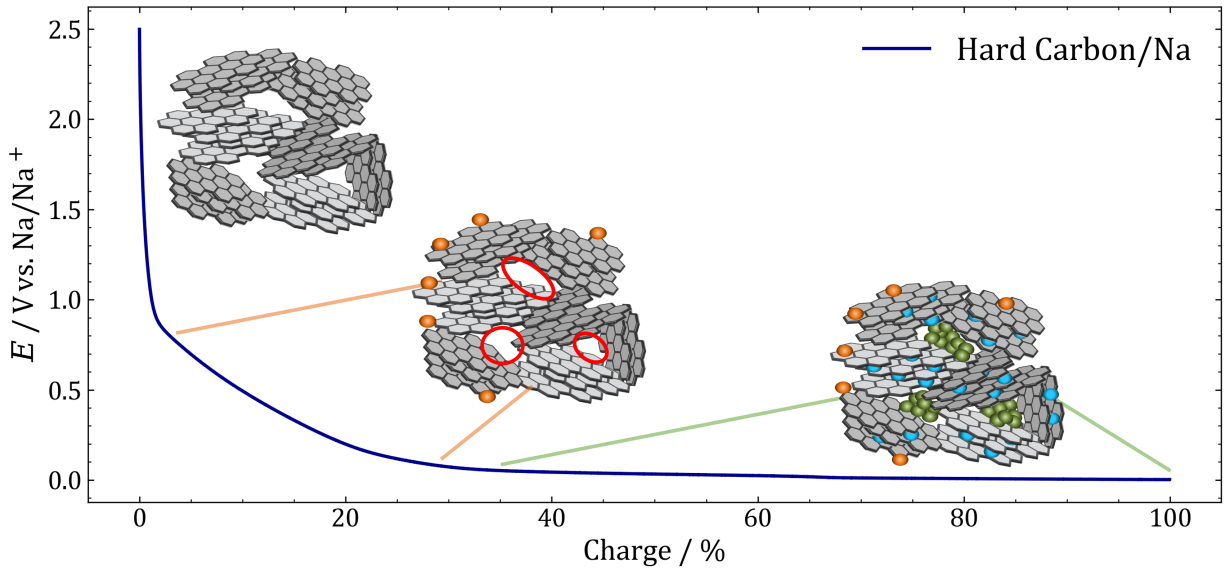

Figure 2.16.: Model sodiation curve of a non-graphitizing carbon. Insets show illustrations of mechanistic steps occuring during the key steps of the curve. Orange spheres represent Na atoms adsorbed to high-energy sites of the carbon, blue spheres show Na intercalated into expanded graphitic regions, green spheres symbolize the formation of Na clusters at a low-potential plateau. Excerpts reprinted with permission from Yabuuchi et al., *Chemical Reviews*, **2014**, *114*, 11636-11682. Copyright 2014, American Chemical Society.

2.3.2. Mechanism of sodium storage in hard carbons

The sodium storage mechanism in non-graphitizing carbons is dictated by the characteristic structure of these materials and significantly differs from that in graphitizing ones and graphite itself. Over the last decades it was investigated by a variety of techniques, but still remains somewhat riddling. Yet, for the conduction of efficient and target oriented research, the detailed understanding of the sodiation process and of the requirements towards the carbon material structure is indispensable. As sodium and lithium (and even potassium) share some of the subprocesses during insertion into the carbon host, insights from studies dedicated to both metals can be used to deduct a mechanism, but the discussion will be carried out with respect to sodium.[18,168,188,189] The typical galvanostatic sodiation curve of a hard carbon is exemplarily shown in figure 2.16. Two distinct regions can be identified with the unaided eye, one with a constantly declining voltage, above approximately 0.1 V vs. Na/Na^+, usually called *sloping region*, and a prolonged phase with a relatively constant potential over a large part of the capacity below 0.1 V vs. Na/Na^+, termed *plateau region*. The former one is usually ascribed to the reversible adsorption of Na to H-terminated graphene

edges, defects, functional groups, and heteroatoms.[52,190–193] The sloping shape of the voltage profile is typically explained by the wide energy distribution of the involved adsorption sites,[193] but a possible explanation is also a single-phase insertion of Na into the carbon framework resulting in a solid-solution type of reaction, which would also result in such a curve shape.[142,143,194,195]

Meanwhile for the plateau region it is clear from fundamental electrochemical considerations that a single, well defined process involving at least partial electron transfer must be the reason for this portion of capacity. However, the assignment of processes and the associated locations of the carbon framework to the plateau region is still subject to discussion. Commonly proposed and sometimes competitively discussed processes are intercalation into regions of expanded d-spacing[196,197] and nanopore filling by sodium clusters.[16,159,191] The first systematic study of the mechanism of sodium storage in non-graphitizing carbons was carried out by Stevens and Dahn in 2000, using in situ SAXS.[16] They designed an in situ SAXS cell, in which HC was sodiated and desodiated to different extents, and as SAXS is sensitive to changes in scattering contrast, the insertion and accumulation of Na could be followed by this method. They could show that during the sloping region of the sodiation no significant change in microporosity took place, which is well in line with the explanation of adsorption to high-energy sites, yet was explained by the intercalation into expanded graphitic regions by the authors.[16] During the sodiation plateau however, a part of the microporosity vanished and reappeared when the sodium was extracted in the desodiation plateau. As of the impact of the intercalation of Na into expanded graphite layers, the matter was studied in detail by Qiu et al.[192] They investigated a typical temperature series of carbohydrate derived hard carbons in order to develop a relationship between lattice parameters derived from XRD and Raman spectroscopy, specific surface area as measured from sorption experiments and the sodium storage at sloping and plateau phases, respectively. While the authors came to a similar conclusion regarding the sloping region, it was claimed that the plateau phase occurs solely due to the intercalation of Na into expanded graphene interlayers. They presented a calculation, analogous to typical approaches from gas physisorption, which states that the ideal, most stabilizing interlayer distance for Na intercalation is located between 0.37 nm and 0.47 nm, with more narrow spacings providing insufficient space for Na accommodation and too wide regions resulting in weaker surface adsorption to the layers, which cannot be counted as intercalation anymore. Consequently, they described the sodiation mechanism as the adsorption to high energy sites, followed by intercalation, and finally surface coverage of graphene layers. While the idea of describing the interaction between Na and graphene is in principle very meaningful, the authors assumed defect-free graphene sheets and not Na-Na

interaction, which both play an important role in pore filling by Na clusters. They further completely ruled out effects due to open porosity and also did not regard internal porosity in their discussion. The authors came up with an energetic consideration of sodium storage in their article. Na-ions are firstly bound to sites with high affinity to cations, which are most likely the previously described defects. Subsequently, sites providing the next highest level of stabilization are occupied, which obviously are those, where Na ions are surrounded by two stabilizing surfaces, resulting in a process that could be described as intercalation. Only after that sodium deposits at sites stabilized by only one surface, but due to the low interaction forces between graphene and Na, this process already competes with metallic sodium deposition.[192] Relying solely on gas sorption techniques can lead to misguiding conclusions, as with these methods only gas accessible surface area and porosity can be investigated and the presence of closed porosity is therefore completely disregarded, no matter how small or diffusive the probe gas is. Matei Ghimbeu et al. drew convincing conclusions on the presence of functional groups using temperature programmed desorption (TPD), but did not find a relationship to porosity measured by physisorption with N_2, CO_2 and Kr, from which they ruled out the possibility of accumulation of sodium in pores in general.[198] In 2015 Bommier et al. published an article, bringing kinetics into play by studying the diffusivity of Na during sodiation using the galvanostatic intermittent titration technique.[196] A high apparent diffusion was found during the sloping region, declining during the plateau phase, and again rising when the potential approached 0 V vs. Na/Na^+. The slow diffusion during the plateau region was explained in terms of a lower accessibility of graphitic interlayers and the blocking of diffusion pathways by similarly charged atoms. According to the authors, the change in diffusivity indicated the onset of another storage mechanism, which was attributed to adsorption to graphene layers. The latter process could be the onset of further pore filling, given a suitable internal pore structure.[196] Arguably one of the most comprehensive works on sodium storage in the familiar temperature-treated hard carbon series was presented in 2020 by Morikawa et al.[197] The authors presented an in situ small and wide angle X-ray scattering (SAXS and WAXS) study under the rigorous absence of air, moisture, and CO_2. The development of the interlayer distance was followed by the (002) signal in the WAXS patterns, showing that the expansion of the interlayer distance only proceeded until a certain point of the sodiation plateau. At sodium amounts exceeding this point, a new signal was observed at approximately 29° in the WAXS pattern shown in figure 2.17a), which was complementary to micropore-related scattering in SAXS and was finally attributed to the correlation of sodium in small clusters. The micropore scattering contribution in the SAXS pattern depicted in figure 2.17b) is furthermore reducing in the course of sodiation. From

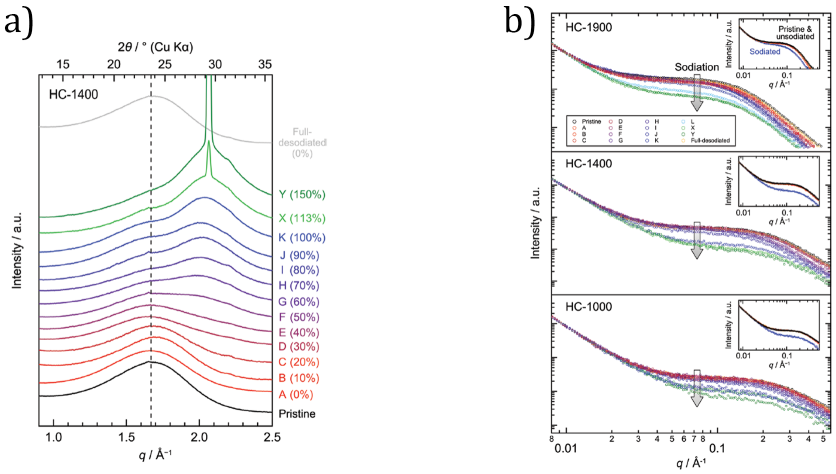

Figure 2.17.: WAXS and SAXS patterns of HCs during sodiation. a) Signal at approx. 29° in the WAXS pattern appearing during plateau storage mechanism. b) SAXS pattern of a HC temperature series shows reducing micropore scattering contribution upon increasing sodiation. Reprinted with permission from Morikawa et al., *Advanced Energy Materials*, **2019**, *10*, 1903176. Copyright 2019, Wiley-VCH Verlag GmbH & Co KGaA, Weinheim.

the charge transferred and the SAXS pore volume they derived the density of these clusters to be in the range of 16-25 atoms nm^{-3}, well in line with the bulk *bcc* crystal structure of Na. Hence, all three mechanisms play an important role in hard carbon sodium storage. The sloping contribution declines with increasing order in the carbon material. In a temperature range between 1100°C and 1500°C, the expanded graphitic domains significantly contribute to sodium storage and finally, when these interlayers become too narrow, clustering of Na in the closed pores becomes the mechanism contributing to the carbon's sodium storage capacity the most.[197]

The electronic environment of sodium and hence its chemical binding situation is an important complementary information to the structural insights presented. Both nuclei, ^{7}Li and ^{23}Na, have a non-zero nuclear spin and hence can be effectively studied using solid state NMR spectroscopy.[199] The first in situ NMR spectroscopic studies on hard carbon were dedicated to the investigation of the lithiation process. Upon increasing degree of lithiation, two characteristic signals are measured, one with a minor intensity around 0-17 ppm and one with a major intensity between 80-120 ppm. The former one is attributed to intercalated lithium, while the latter one, with a lower chemical shift, is due to lithium clusters forming inside the closed nanopores of the hard carbon.[19,200,201] The shift is explained by the increased shielding of the nuclear spin due to growing electronic contributions on the Li-nuclei themselves.[202,203] The low-field peak occurs analogously in ^{23}Na experiments, and can be

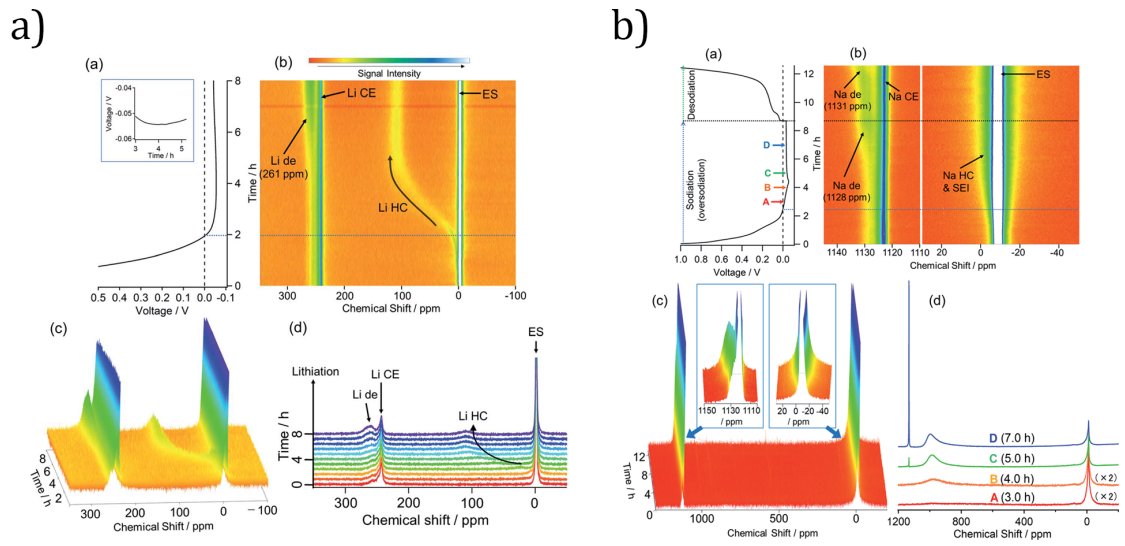

Figure 2.18.: in situ NMR spectra of a) the lithiation and b) the sodiation processes of HC. Top left subpanel shows voltage profiles recorded during the NMR experiment. Top right and bottom left panels represent waterfall plots of NMR spectra recorded during the sodiation. Bottom right panels depict *ex situ* NMR spectra after indicated alkalimetallation time. Republished with permission of Royal Society of Chemistry, from *Advanced Energy Materials*, Gotoh et al., *10*, 1903176, copyright 2020; permission conveyed through Copyright Clearance Center, Inc.

further resolved into three sub-peaks under conditions of magic-angle spinning (MAS). Here, the Na ion from the salt is found around -10 ppm, and two broader peaks between 5 ppm and -15 ppm are further measured. The latter two were attributed to Na intercalated between graphene sheets and pore filling to different extents, respectively.[193,202,204] When trying to reproduce a similar study for ^{23}Na, the high-field signal was initially not observed for several possible reasons,[205] until Stratford et al.[191] measured the occurrence of a signal at chemical shifts >700 ppm, as compared to metallic sodium around 1200 ppm, which was attributed to the formation of Na clusters in internal pores. A dependence of the chemical shift and hence the metallic character of the deposited sodium on the carbonization as well as pretreatment conditions was observed, where sodiated carbons prepared at 2000°C showed a ^{23}Na shift at 1114 ppm, almost coinciding with that of metallic Na.[177]

More recently, in situ or even operando solid-state NMR experiments became feasible and more popular in mechanism oriented research. Except for a recent study on Li/graphite,[206] experiments are usually conducted in static cells without MAS, due to the easier realization of the contact between potentiostat and NMR cell, hence the chemical shifts differ quantitatively and the signals are generally broader. In trade, unbiased information about the alkali

species is obtained even under non-equilibrium conditions.[189] In a Li-half cell setup, a clear and distinct signal at approximately 110 ppm is found forming concomitantly with the voltage plateau, which could be attributed to quasimetallic lithium, well differentiated against lithium intercalated in graphite, as well as dendritic lithium, see figure 2.18 a), top right panel. The Li-cluster peak is observed in both static and MAS experiments and disappeared in a reversed manner during delithiation. On the other hand in sodium, static NMR measurements only yield electrolyte signals in the low field, alongside with the metal peak from the counter electrode at approximately 1100 ppm, as well as depositing metallic sodium upon oversodiation, as shown in figure 2.18b), top right panel. The quasimetal signal could only be observed in MAS NMR experiments, as depicted in the lower right panel of figure 2.18b) at 900-1000 ppm. For both alkali metals the quasimetal formation peak occurred below 0 V vs. the respective metal and before the onset of dendrite formation.[189] These findings clearly indicate that the alkali metal deposited in pores is not only of a somewhat metallic nature, but also its reactivity and chemical potential is close to that of the bulk element. However, this very similarity is problematic, as the deposition in pores occurs at similar potentials like the irreversible metal plating. In an operating cell, this induces a competition between the two processes, of which only the former one is desired. The undesired metal formation is further favored at higher current densities, where the cell is more polarized due to internal resistances, causing the bulk metal growth to occur earlier.

2.4. Theoretical background of some important methods

2.4.1. Electrochemical techniques

Galvanostatic charging and discharging

Galvanostatic cycling is perhaps the most important and most frequently used method for the investigation of battery systems. As the term *galvanostatic* already implies, the current is held constant throughout such an experiment and the electrode potential is recorded as a function of time. The time is then multiplied by the current flow to yield the charge, which from Faraday's fundamental laws is equivalent to the amount of electroactive species reacted. Usually, the charge is plotted on the abscissa, while the potential is found on the ordinate. The method is well-suited for the distinction of different processes occurring at an electrode, but even more interesting, especially for battery electrodes, is the possibility to quantify the amount of charge stored, related to a process within a particular potential window. By inverting the current, statements about the chemical reversibility and coulombic

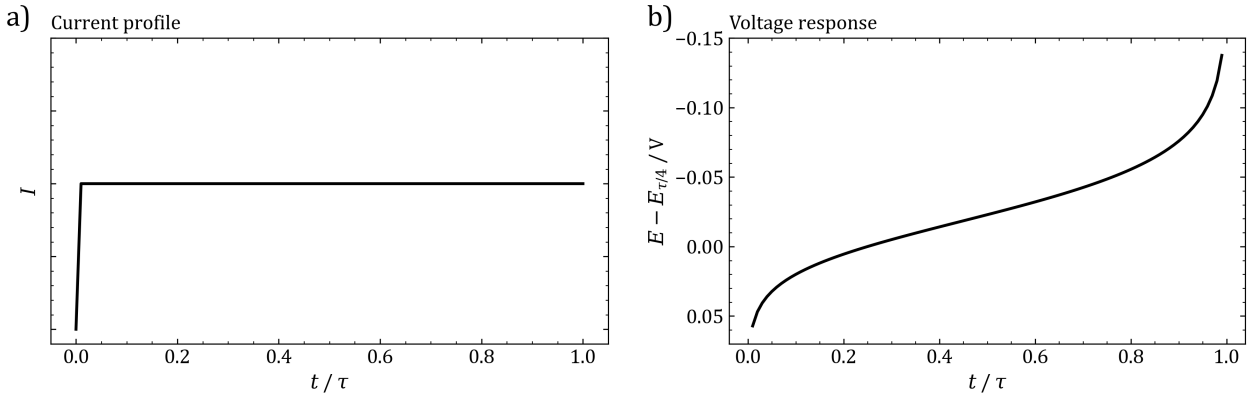

Figure 2.19.: a) Current applied and b) potential measured during a simulated galvanostatic experiment with semi-infinite diffusion at a planar electrode.

efficiency become accessible. The coulombic efficiency is then defined as the ratio between charge flown during the backward, to that of the forward reaction.
For a first approximation, an exemplary reduction like $A + e^- \rightarrow A^-$ at a semi-infinite diffusion gradient and a planar electrode surface without double layer capacity can be considered. A defined electrical current is then applied, hence the mass flux at the electrode surface is constant and well-known. The species A is reduced at a steady rate and the measured potential corresponds to the electrochemical potential of the redox couple, including Nernstian concentration and overpotential contributions. Exemplary current and voltage profiles are depicted in figure 2.19 in a realistic scale. Over time, the concentration of A at the electrode surface depletes and a concentration gradient is established, which is on the one hand maintained by the surface reaction and on the other hand counterbalanced by diffusion. This results in a somewhat curved shape of the potential-time diagram. Obviously, the magnitude of the applied current has a crucial impact on the concentration gradient and hence on the shape of the chronopotentiogram. As the concentration of the electroactive species is reduced, the measured potential rapidly decreases.[2] Theoretically, if no other electroactive compound is available, the current flow must cease at this point, but practically, there is always another species A' present, even if it is the electrolyte or other cell components being electrolyzed. In this case, the voltage jumps to the value characteristic for the respective potential of $A' + e^- \rightarrow A'^-$.[35] Although the fundamental findings of this simplified consideration in principle hold true for porous, solid-state intercalation electrodes, applied as LIB

[2]Throughout this work, the IUPAC convention is followed, according to which oxidative currents have a positive, and reductive currents a negative sign. The term "charge" is reserved to the endothermic process, while "discharge" describes voluntary electrochemical reactions.

and SIB anodes, as well, some special aspects and arising deviations must be considered. The reaction product, instead of being transported off the electrode surface, as is the case in the first approximation, enters the bulk of the electrode and is further transported through solid-state diffusion processes, which introduces another potentially rate determining step. The intercalation process itself can be compared to a dissolution of a guest species M in the host species H and the process of intercalation strongly depends on the type of host-guest interactions, especially on the number of phases before and after.[194] As already stated, the time axis can be easily converted into a capacity axis and by normalizing to the mass or stoichiometry of the host material, the potentiogram can be effectively viewed as a phase diagram for the insertion of the guest compound into the host structure. The shape of the phase diagram is dependent on the amount of phases formed during the respective reaction and can be described using Gibbs' phase rule for closed systems at equilibrium, $f = C - P$, where f is the number of degrees of freedom, C is the number of components, and P is the number of phases. For perfectly non-stoichiometric compounds, where the insertion of the guest species does not involve a phase change and happens gradually, the number of components is two and the number of phases is one, therefore one degree of freedom exists along the composition axis, during which the number of phases stays the same. Therefore, the potential depends on the degree of occupancy, $y = x/x_{max}$, and as such shows a curved or sloping shape.[195] If on the contrary the reaction involves the formation of a new phase, the amount of components is equal to that of phases and therefore all intensive quantities including the chemical potential are fixed and therefore the voltage at which such a reaction occurs is constant during the stoichiometric composition range at which the respective phase is present. Contrary to the former one-phase reactions, this type of insertion has a more favorable voltage profile but often is less reversible due to the kinetic hindrances caused by formation and dissolution of a new phase.[194,195]

Charge-discharge curves are crucial for the evaluation of the performance of battery electrodes and hence are found in virtually every study concerned with new electrode materials. In the case of SIB and LIB anodes, the most widespread setup consists of a sodium or lithium metal counter electrode and a hard carbon working electrode, ionically connected via an electrolyte-soaked separator. The metal counter electrode at the same time functions as a reference electrode. While this type of two-electrode setup is usually avoided in other branches of electrochemistry, its application is legitimate in this case for several reasons. The reference electrode should not conduct any current in an ideal case, as it would induce polarization effects and the working electrode potential could hence be measured incorrectly. Furthermore, the reaction against which the working potential is referenced must be well-

defined and time-invariant. In SIB and LIB two-electrode half cell setups, the metal counter electrode usually is electrically conductive and the currents are low enough that polarization effects can be neglected. Also, the only reaction that can effectively happen at such an electrode is the dissolution and deposition of alkali metal, hence the criterion of a defined reaction is fulfilled as well. Finally, working battery cells are almost always constructed in two-electrode assembly, which is why this setup is practically more relevant.
Typical charge-discharge protocols for SIBs (and LIBs as well) consist of a discharge step (sodiation) of the hard carbon electrode at a constant current (CC), until the lower voltage limit of 0 V vs. Na/Na^+ is reached. Due to electrode polarization, this voltage might be reached earlier than the full sodiation capacity of the working electrode is exploited. Two different approaches exist, to correctly assess the material's sodium storage capacity. A constant voltage step can be applied, when the cell arrives at the lower voltage limit, holding the cell at 0 V vs Na/Na^+ until the current depletes to a certain value. This method can be used to reliably evaluate conventional electrode materials and due to the ease of realization is frequently applied in research close to application.[57,189] However, especially in hard carbon negative electrodes, significant amounts of charge stored are observed at potentials below 0 V vs. Na/Na^+, which requires an alternative approach. The beginning of bulk sodium plating is usually manifested in a voltage minimum, a few tens of Millivolts in height, which is due to a crystallization overpotential. This was already proved by in situ XRD and NMR experiments.[189,207] In a first step, the capacity of the bulk sodium plating onset is determined, by oversodiating a set of cells and observing the nucleation peak. Once bulk sodium has formed, in the following cycles the plating will be facilitated, hence these cells are to be disposed thereafter. Subsequent cells would then be cycled with a capacity limit of a fraction of the bulk sodiation capacity, e.g. 90 % of it. While this method requires more initial effort, it allows the utilization of otherwise underestimated capacity and appears more suitable to evaluate the "true", material-intrinsic sodiation capacity, as compared to experiments with voltage limitation.

Cyclic Voltammetry

In contrast to galvanostatic charging and discharging, in cyclic voltammetry (CV) the potential of the working electrode is controlled versus the reference electrode and the resulting current is measured. A constant voltage ramp is imposed on the cell, called the scan rate ν, starting from the initial voltage E_i and ending at the final voltage E_f, where the voltage range between E_i and E_f encompasses the electrochemical reaction under study, as can be seen in figure 2.20 a). For the fundamental explanation of the method it is again useful

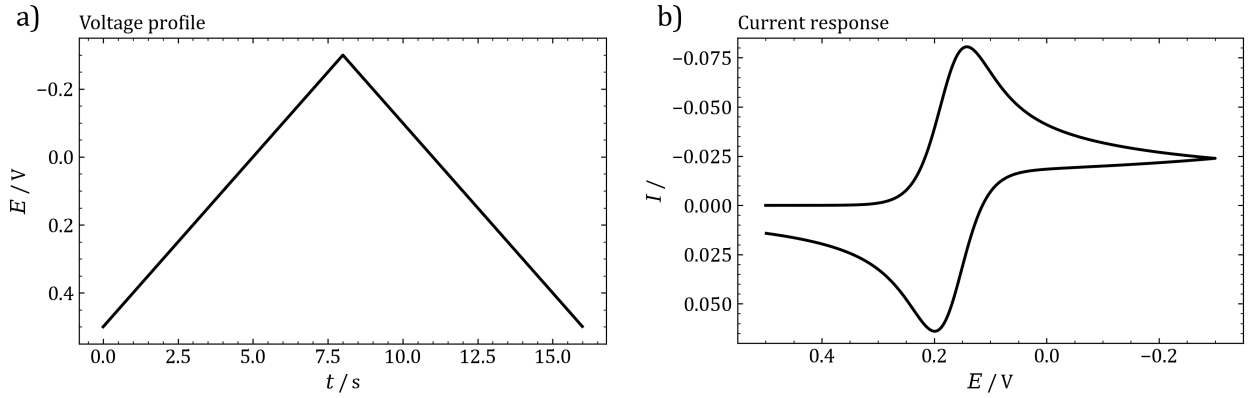

Figure 2.20.: a) Voltage applied and b) current measured during a simulated cyclovoltammetric experiment with semi-infinite diffusion at a planar electrode.

to consider the case of a general reduction reaction under conditions of semi-infinite diffusion at a planar electrode, as depicted in figure 2.20. When the experiment begins, the potential is higher than the reduction potential of the hypothetical redox couple, therefore no faradaic current is flowing. However, an electrochemical double layer is building up as soon as a voltage is applied, therefore a constant current background, dependent only on the wettable electrode area and the dielectric properties of the electrolyte is measured in a real cell, but not simulated in figure 2.20. Approaching the redox potential of the couple, the kinetics is accelerated exponentially, therefore a likewise increasing current is measured initially. As the concentration of electroactive species at the electrode surface is diminished in the course of the experiment, the supply of redox active species is maintained by diffusion and the experiment enters a diffusion-controlled regime. When kinetics finally becomes so fast that the reactant feed delivered by diffusion processes is insufficient, the current signal shows a peak, before it starts to decay towards a constant, purely diffusion-driven current. Upon reversing the potential scan in a kinetically symmetrical and totally reversible system, basically the same procedure repeats, but with the reduced species as the starting material, in a concentration, which corresponds to the amount formed during the forward scan.[35,208] The calculation of a CV curve is a non-trivial exercise and cannot be done analytically, but some fundamental relationships between the shape of the CV-curve and system-specific parameters can be pointed out. Higher diffusion coefficients generally increase the current in its value, while the electrode kinetics influences the slope of the initial current ramp and the peak position on the potential axis. A porous environment can be modelled by changing the diffusion boundary conditions from semi-infinite, with one fixed electrode surface to a

system, where the diffusion space is limited in two directions, which is then termed finite diffusion space. In this case the reactant supply is not unlimited from one side, but the electrolyte volume is restricted to the volume between the two walls, which causes the tail of the CV curve to decay faster and reach current values closer to zero.[35] The investigation of solid-state reactions by CV is somewhat different from typical, "solution-electrochemistry" for several reasons. First of all, solid state diffusion through the electrode material itself must be considered, which is usually a slow process and further depends on the dimensionality of the region in which the reaction takes place, possibly introducing another rate limiting step. Further, it is often unknown, whether the electron transfer happens as soon as the ion enters the host structure, or if the solid state diffusion occurs prior. For these reasons, the theory developed for solid/liquid electrode/electrolyte interfaces can usually not be quantitatively applied to the analysis of CV measurements on LIB and SIB anodes and CV mainly serves as a means of the identification of different processes via their respective current peaks.

Electrochemical impedance spectroscopy and DRT analysis

In (potentiodynamic) electrochemical impedance spectroscopy (EIS), a sinusoidal voltage of small amplitude is applied to the cell and the frequency is varied, typically between several tens or hundreds of kHz until down to some mHz. The cell impedance is then measured at any frequency point and presented in different types of plots. The great difference and advantage is the small perturbation imposed on the cell, as the voltage amplitude is typically below 10 mV. Therefore, the system remains in equilibrium over the course of the measurement and its integrity is hence not as affected as by methods imposing large perturbations such as galvanostatic cycling or potentiodynamic chronoamperometry.[35]
Impedance can be viewed as the generalized concept of resistance, including the Ohmic resistance as well as the frequency-dependant part in alternating current circuits. The imposed voltage E can be best represented as a vector quantity, rotating with an angular frequency ω with $\omega = 2\pi f$, and its measured value at any given time is the projection of the vector on an axis. Mathematically, this can be expressed as equation 2.6.

$$e = E \sin \omega t \tag{2.6}$$

The current will now follow the voltage signal at the same frequency, but depending on the amount and types of circuit elements, it will be shifted with respect to the potential by a phase angle Φ.

$$i = I \sin(\omega t + \Phi) \tag{2.7}$$

For resistances R, Ohm's law applies, hence for the current the relationship $I = E/R$ holds, meaning that the phase angle between current and voltage is zero in this case. A capacitance C allows alternating currents, while direct currents cannot pass. The relationship between current and voltage is given by equation 2.8.

$$i = \omega C E \sin\left(\omega t + \frac{\pi}{2}\right) \tag{2.8}$$

The term $1/\mathrm{j}\omega C$ is the capacitive impedance Z_{Cap} and describes the frequency dependent part of the impedance, caused by a capacitive element. Also it follows, that the current in a capacitance always leads the voltage by 90°. As the third element contributing to impedance, the inductance L must be mentioned, for which the relationship in equation 2.9 holds and the impedance of which can be expressed as $Z_{\mathrm{Ind}} = \mathrm{j}\omega L$, the current in a coil lags the voltage.

$$i = \frac{E}{\omega L} \sin\left(\omega t - \frac{\pi}{2}\right) \tag{2.9}$$

Voltage and current are hence linked to each other by the impedance, the sum of all contributions to cell resistance, both frequency dependent and independent. As the impact of inductive elements to cell resistance usually is negligibly small in the frequency range, relevant for EIS, the impedance is often written as in equation 2.10.[35]

$$\boldsymbol{Z}(\omega) = Z_{\mathrm{Re}} - \mathrm{j}Z_{\mathrm{Im}} \tag{2.10}$$

Information about both, the real and imaginary parts of the total cell impedance Z_{Re} and Z_{Im} are measured and recorded at each set frequency of an experiment, together with the phase angle Φ and the magnitude of the impedance $|Z|$. The most prominent way of presenting impedance data are complex plane plots, where Z_{Re} and Z_{Im} are plotted against each other. From this representation, often called Nyquist plot, one can make a first estimation about the circuit behind the impedance spectrum, but in order to obtain more detailed information, mathematical modelling of the data is necessary.

An electrochemical cell acts as a complex impedance to an applied sinusoidal perturbation, and as such can be modelled by an equivalent circuit of resistors, capacitors, and less frequently inductors, connected in series or parallel. The representation of electrochemical and interfacial processes requires the combination of circuit elements. One of the simplest cases is the series connection of a resistor R and a capacitor C in an R-C circuit, which is equiv-

alent for a conductive solution, inhibiting the current at low frequencies, when the double layer is fully charged. The impedance of such a circuit is described by equation 2.11 and the resulting complex-plane plot is depicted in figure 2.21a).[209,210]

$$Z(\omega) = R - \frac{\mathrm{j}}{\omega C} \tag{2.11}$$

If R and C are placed in parallel, an R|C circuit is obtained, describing the competition between a double-layer charging process and a resistive charge-transfer process. As the current always takes the path of the least resistance, at higher frequencies the double layer charging is dominant, while at lower ones the resistive contribution becomes prevalent. The phase angle changes from 90° to 0° during the frequency scan, and the critical frequency at which $\Phi = 45°$ is related to the time constant $\tau = RC$ via $f_C = 1/(2\pi RC)$. The impedance of a parallel R|C circuit is given as in equation 2.12. The Nyquist plot can be seen in figure 2.21b).[209,210]

$$Z(\omega) = \frac{R}{1 + (\omega RC)^2} - \frac{\mathrm{j}\omega R^2 C}{1 + (\omega RC)^2} = \frac{R}{1 + \mathrm{j}\omega RC} \tag{2.12}$$

By including a solution resistance R_{sol} in series with a parallel R|C element, one already arrives at a frequently used circuit for the treatment of a basic solution-based cell, the so called *Randles circuit*, see figure 2.21c). It simply states that all current, capacitive and resistive, must first pass through the ohmic resistance of the electrolyte and therefore explains the shift of the complex plane plot along the real axis. The impedance of the Randles circuit can be written as in equation 2.13.[209,210]

$$Z(\omega) = R_{Sol} + \frac{R}{1 + (\omega RC)^2} - \frac{\mathrm{j}\omega R^2 C}{1 + (\omega RC)^2} = R_{Sol} + \frac{R}{1 + \mathrm{j}\omega RC} \tag{2.13}$$

However, only the fewest electrochemical systems can be really described by such a simple circuitry and usually R|C elements with different time constants must be combined. They can be put in series (Maxwell circuit), in parallel (Voigt circuit), or hierarchically nested (Randles circuit), but the amount and relative contribution to the total resistance remain subject to educated guessing and trial and error iterations.[209,210]

Usually, experimental data from EIS is subjected to complex non-linear least-square fitting routines, in order to find the best-fitting model. However, doing so, one must proceed with care, as many different systems can be described by similar models. Second, the equivalent circuit developed for a certain system represents only a projection of the cell properties and components, such as interfaces, charge transfers, and diffusion steps, into a mathematically

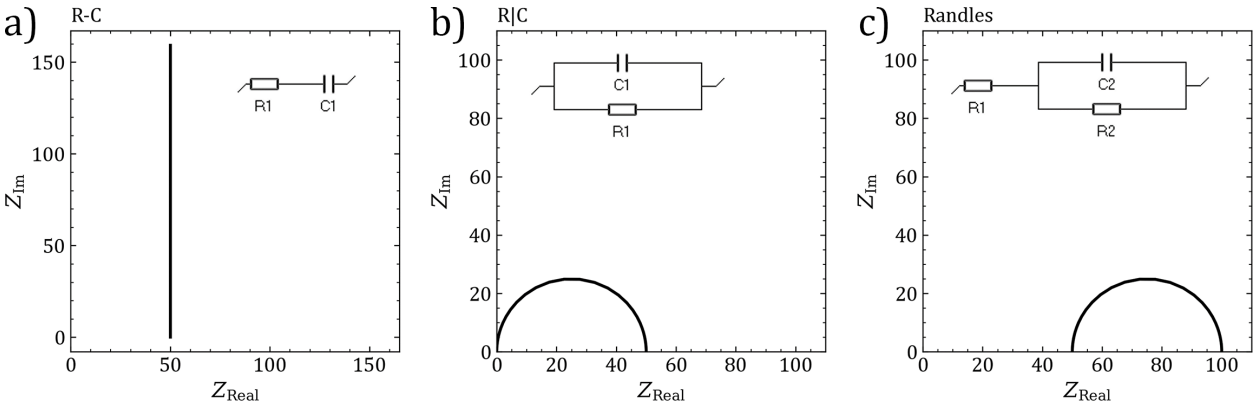

Figure 2.21.: Fundamental combinations of RC-elements and a Randles equivalent circuit. a) RC-series circuit with $C1$ =10^{-3} F and $R1$ =50 Ω, b) RC-parallel circuit with $C1$ =10^{-6} F and $R1$ =50 Ω, and Randles circuit with $C1$ =10^{-6} F, $R1$ =50 Ω, and $R2$ =50 Ω.

comprehensible model. Therefore, the assignment of processes to circuit components is possible only in the simplest cases. Finally, a priori knowledge is strictly required to set up a suitable and physically correct model for the system at hand, which is why EIS is rarely used as a first go-to method for electrochemical studies. Such information includes knowledge about the number of charge-transfer steps, an estimation of the double-layer capacity, the type of diffusion space, and the interdependence of the components. In practice, many systems cannot be fitted by ideal circuit elements and in order to obtain a "good" fit, one has to rely on distributed elements such as the constant phase element (CPE). These provide a mathematically closer fit, but are not necessarily more representative of the electrochemical system. In such cases, simply going for the best fit, without a physically reasonable model is hence basically pointless and a less-well fitting based on an understanding of the system is always preferable.[209–211] In order to determine the number of time constants or R|C circuits required to fit an impedance spectrum, the distribution of relaxation times (DRT) analysis has proven useful. Experimental impedance data is reproduced by a continuous parallel junction of R|C elements (Voigt circuit), yielding a weighting function $g(\tau)$ according to the following (DRT) integral equation 2.14.[212,213]

$$\frac{Z(\omega) - Z_\infty}{Z_0 - Z_\infty} = \int_0^\infty \frac{g(\tau)}{1 + \mathrm{j}\omega\tau} \mathrm{d}\tau = \int_{-\infty}^\infty \frac{\tau g(\tau)}{1 + \mathrm{j}\omega\tau} \mathrm{d}\ln(\tau) \tag{2.14}$$

Herein, $Z(\omega)$ is the measured impedance data, Z_∞ and Z_0 is the impedance in the two limiting cases of f approaching infinity or zero. The fraction $\frac{g(\tau)}{1+\mathrm{j}\omega\tau}\mathrm{d}\tau$ equates to the relative contribution of a R|C element with a time constant τ to the total impedance. As the function $g(\tau)$ is calculated numerically, the integral must be discretized into a finite sum.

$$\frac{Z(\omega) - Z_\infty}{Z_0 - Z_\infty} = \sum_{k=1}^{n} \frac{\gamma(\tau)}{1 + \mathrm{j}\omega\tau_k} \tag{2.15}$$

The interval of time constants $[\tau_1, \tau_n]$ must at least span over the range of frequencies covered in the EIS experiment and at the same time the number of time constants must be larger than the expected number of R|C elements in the cell. The problem is then re-formulated into matrix notation as in equation 2.16, in order to be effectively handleable by the solving algorithm.

$$\boldsymbol{z} = \boldsymbol{K}\gamma \tag{2.16}$$

The vector $\boldsymbol{z}$ contains the measured impedance data points and $\boldsymbol{K}$ is an $m \times n$ matrix, whose entries represent the impedance of the RC elements at the time constant τ_k, see equation 2.17. The number of time constants is multiplied by a constant natural number a to yield m, the number of time constants used for the calculation of the DRT.[213]

$$k_{m,n} = \frac{1}{1 + \mathrm{j}\omega_m\tau_n} \tag{2.17}$$

The vector γ is the desired distribution function. Further details regarding treatment of impedance data will be discussed in the context of the respective publication emerged within this work. Some properties and limitations of DRT analysis have yet to be pointed out. The DRT calculated in this way is based only on the assumption that the system can be described as a number of R|C elements put in series. Apart from that, it provides a model-free interpretation of measured EIS data. However, a consequence of the chosen procedure is that it is neither valid for purely capacitive ($\lim_{\omega\to\infty} \stackrel{!}{=} 0$), nor for inductive contributions ($\lim_{\omega\to 0} \stackrel{!}{=} 0$) to the impedance. Contributions from such elements must be either removed prior to DRT analysis or kept in mind during the interpretation of the results. A simulated exemplary impedance spectrum of an arbitrary circuit is shown in figure 2.22. The parameters of the two R|C elements, red and blue lines, respectively, are chosen in a way that the resulting arcs in the complex-plane plot, shown in black, coalesce into each other. The data can be deconvolved in the DRT representation two give rise to two peaks at two time constants. The DRT plot can be fitted in order to determine the polarization resistance of each respective peak, which in turn can be used to calculate the capacitances C_1 and C_2.

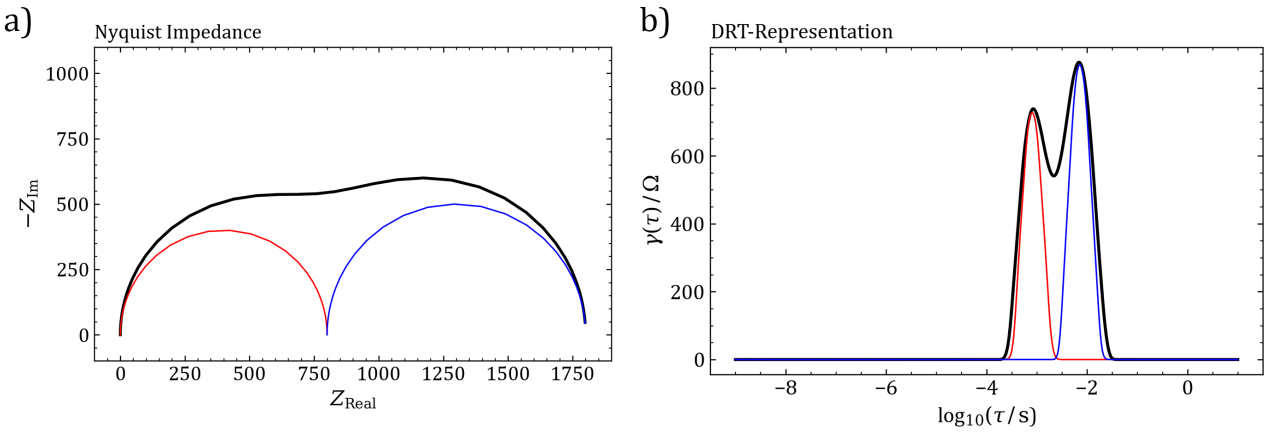

Figure 2.22.: Impedance spectrum of a circuit of two parallel RC elements in series and its DRT. R_1 =800 Ω, $C_1 = 10^{-6}$ F, R_2 =1000 Ω, $C_2 = 7 \times 10^{-6}$ F.

2.4.2. Structural analysis techniques

Gas physisorption

Gas physisorption is the physical process of enrichment of gas molecules in the vicinity of a solid surface. The forces, responsible for the interaction between gas and solid are of the Van-der-Waals type, as opposed to chemical bond formation in chemisorption. The *adsorbent* is the solid performing the process of adsorption, while the *adsorptive* is the substance being adsorbed in the gas phase. The adsorptive becomes the *adsorbate* as soon as it begins interacting with the adsorbent and enters the adsorbed state. *Adsorption* is restricted to surface interactions, while the term *absorption* is used, if the surface layer is surpassed and the bulk of the adsorbent becomes involved. Both phenomena can be addressed by the combining term *sorption*. *Desorption* is the reverse process of adsorption, when the adsorbate is released from the adsorbent surface and enters the fluid phase again. The terminology is illustrated in figure 2.23a). It is further useful to define pores by their respective diameters. All pores below 100 nm in diameter are collectively termed *nanopores*. Those pores, with diameters smaller than 2 nm are called *micropores*, those larger than 50 nm *macropores*, and pores with sizes in between are named *mesopores*.[214,215]

Gas sorption has become a widespread, if not standard method in materials laboratories for the analysis of the texture of porous solids and fine powders on the nanoscale, owing to its sensitivity and its non-destructive nature. Information about the surface area and pore volume can be derived directly from (statistical) thermodynamic considerations and density functional theory (DFT) can be used to calculate pore size distributions.[215] In contrast to

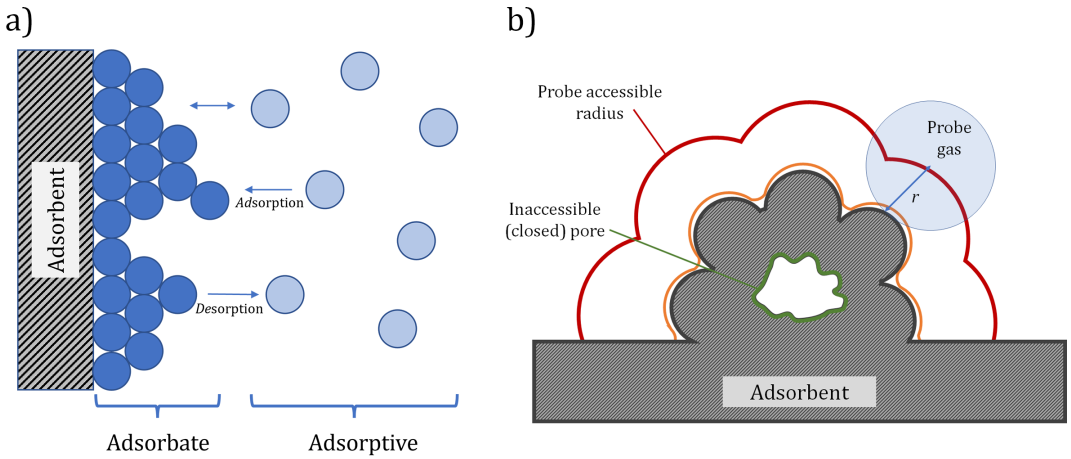

Figure 2.23.: a) Illustration of the adsorption/desorption equilibrium and of the relevant terminology. b) Adsorbent grain on a molecular level. Black line represents adsorbent grain boundary, orange line shows the Connolly surface, the surface sampled by the probe gas of radius r. Red line shows surface at distance r. After Thommes et al.[215]

other methods, like those based on X-ray scattering, in gas sorption experiments only those pores and surfaces are considered, which are accessible to the respective probe gas, regardless of how small or diffusive the gas may be. This circumstance is demonstrated in figure 2.23b). There, the probe gas obviously cannot enter the smallest crevices of the particle, hence the actual surface area is a different one than that sampled by the gas. The latter is known as the Connolly surface, defined as the area resulting from "rolling over" the sample with a sphere of the radius r, shown in orange in figure 2.23b). For example, using N_2 one can analyze pores larger than the kinetic diameter of N_2, 0.36 nm, if enough time is given for the system to reach equilibrium. Changing to CO_2 as the adsorbent, it becomes possible to study smaller pores, but closed pores, shown in green in figure 2.23b) remain restricted to any kind of gas.[215,216]

The interaction between a gas and a flat surface is the first approximation to describe the adsorption process. Probably the most prominent model and the most widely adapted method for the determination of the (mass) specific surface area (SSA) of materials was presented by Brunauer, Emmett, and Teller (BET) in 1938.[217] They extended the monolayer-adsorption model of Langmuir,[218] which frequently overestimated the surface area of a material, to a multilayer model, where a tightly-bound monolayer is continued towards the gas phase by a liquid-like phase of adsorbate, yielding the BET-equation 2.18. Herein, p/p_0 is the pressure of the adsorptive relative to the vapour pressure at the measurement temperature, n is the specific amount adsorbed and n_m is the monolayer capacity, while C is related to the monolayer adsorption enthalpy. The SSA is then determined by relating the monolayer capacity

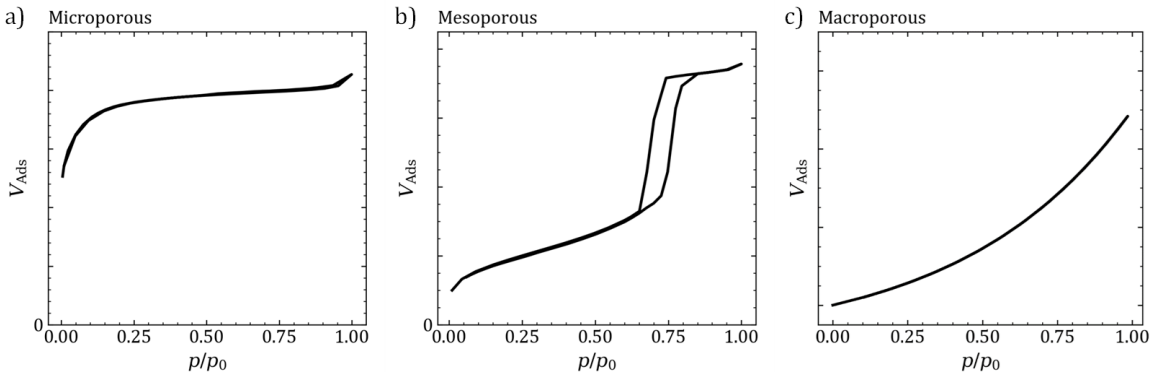

Figure 2.24.: Most important types of isotherm-shapes. a) Microporous, b) mesoporous, and c) macroporous material.

to the surface area occupied by the closely-packed adsorbate molecules.[219]

$$\frac{p(/p^0)}{n\,(p/p^0)} = \frac{1}{n_m C} + \frac{C-1}{n_m C}\left(p/p^0\right) \tag{2.18}$$

Even though this model is strictly valid only for non-porous, meso- or macroporous solids, it is widely used due to its "standard-method" character. In the presence of micropores and smaller mesopores the adsorption process significantly differs from the surface coverage process described by BET and Langmuir, and typical shapes of isotherms can be classified, depending on the pore size and geometry. Among the eight classes recommended by the IUPAC, the three possibly most important ones for carbon materials will be briefly introduced. Given a material with abundant micropores, the volume adsorbed V_{ads} will increase rapidly in the low relative pressure regime and run into a plateau for higher p/p_0, as presented in figure 2.24a). This is due to the strong interaction between the adsorbate, stabilized by two pore walls of the adsorbent. At increasing relative pressures, all available micropore volume gets filled and the adsorption takes place only at external surface area, which is often negligible compared to the micropore volume.[215,220] For a purely mesoporous material, the surface first gets covered in a monolayer of adsorbate, growing to multilayer adsorption, and finally, when the adsorbate layers are thick enough, capillary condensation occurs and the mesopore gets completely filled with liquid adsorbate. The relationship between the pore size and the relative pressure at which capillary condensation occurs is described by the Kelvin equation, equation 2.19.

$$\ln\frac{p}{p_0} = -\frac{2\gamma_l \nu^l}{r_K RT} \tag{2.19}$$

This process is subject to nucleation and growth kinetics, whereas the reverse process, the

evaporation from the pore is an equilibrium process, hence the desorption isotherm often deviates from the adsorption isotherm, giving rise to a hysteresis, which contains information about the width of the pore entrances, see figure 2.24b).[215,221] Finally, adsorption at macropores does not significantly differ from that at blank surfaces, where the multilayer becomes increasingly thick. As opposed to mesopore adsorption, the pore is too wide for capillary adsorption to occur, which is why liquefaction of the adsorbate is observed before, as can be estimated from figure 2.24c).[215] By the superposition of isotherms, calculated for all differential pore diameters and geometries from DFT, it is possible to obtain complete pore size distributions, which even allows conclusions about the pore geometry of the sample.[215,216,222–224]

Small-angle X-ray scattering

Some practical aspects of SAXS were already discussed in the context of the structural analysis of hard carbons, therefore the physical processes behind the method and the instrumentation should be emphasized here. Like in all X-ray scattering methods, in SAXS, the interaction between X-rays and the electron shell of matter is considered. At a point charge, such as for example an electron, the incident wave with the vector k_0 is scattered elastically into all directions as described by the Thomson equation. In a more macroscopic piece of matter, the radiation interacts with all present electrons, where each scattering event causes the propagation of secondary waves, and the superposition of those is measured as the intensity vs. scattering angle or scattering vector plot.[174] To calculate back, from the scattering pattern to the structure of the scattering medium is the most crucial part, but at the same time the power of SAXS. The theory behind SAXS is very broad and extends over wide fields of physics and physical chemistry. The approach used for the investigation of porous solids, such as carbonaceous materials will be discussed in further detail within the context of the respective publication evolved within this work. In order to perform a SAXS experiment, the sample is placed together with the detector in an evacuated compartment, in order to prevent scattering at gas particles, and irradiated with X-ray radiation. Here, the sample-detector distance determines the angular range, covered by the setup. The detector itself usually has a two-dimensional geometry, where the area of the incident beam is covered by a beam stop. The data obtained from laboratory-scale SAXS instruments are usually dimensionless and hence cannot provide absolute information about the sample directly. In order to obtain sample parameters like internal surface areas, pore sizes, and others in physically meaningful dimensions, a calibration procedure like the one described by Dreiss et al.[225] must be performed prior to measuring.

3. Experimental Part

Syntheses

Hexaazatriphenylene hexacarbonitrile

Hexaazatriphenylene hexacarbonitrile (HAT-CN) was prepared following the procedure of Rademacher *et al.*.[226] In a usual batch 1 eq. (5.415 g, 17.3 mmol) hexaketocyclohexane octahydrate (98 %, Thermo Fisher) and 8 eq. (15.0 g, 138.8 mmol) diaminomaleonitrile (99 % Sigma Aldrich) were dissolved in 200 ml glacial acetic acid and refluxed at 135°C for 2 h. The mixture was filtrated over a glass filter frit (porosity 1.6) and washed with 100 ml of hot glacial acetic acid. The resulting black solid was refluxed at 120°C in 81 ml of a 30 % nitric acid for another 3 h before putting the mixture onto an excess of deionized ice, to yield a precipitate over night. The product was dissolved in 300 ml acetonitrile (≥99.9 %, VWR) and refluxed at 80°C for another 2 h. The reaction mixture was filtrated and the solvent was removed from the filtrate on a rotary evaporator. The yield was 68 % (4.5 g, 11.7 mmol).

Carbon materials C-HAT-X

Carbon materials C-HAT-X were synthesized via the thermal condensation of the organic precursor HAT-CN.[227] In a typical synthesis, 1 g of the precursor was filled in a porcelain boat and placed in a horizontal tubular furnace. Under flowing N_2 or Ar atmosphere (gas purity: 99.999 %), HAT-CN was first heated to 60°C at a temperature ramp of 4°C min^{-1} and held for 30 min. For the pyrolysis step itself, the sample was heated to the target temperature of 550°C and 1000°C for 1 h at a ramp of 4°C min^{-1}. Due to the abundant evolution of side products, C-HAT-1600 was prepared from C-HAT-1000, which was transferred into a high-temperature horizontal tube furnace for a final heat treatment at 1600°C for 1 h at a heating rate of 4°C min^{-1}. The materials were denoted C-HAT-X, where X stands for the highest heat treatment temperature. The yields were 50 wt.% for C-HAT-550, 16 wt.% for C-HAT-1000, and 12 wt.% for C-HAT-1600.

Carbon/carbon nitride nanocomposites

Carbon cloths (Kynol 5092-CC, 5092-ACC10, 5092-ACC20) were supplied by Kynol Europa GmbH, Hamburg. Melamine (99 %) was purchased from Sigma Aldrich. The carbon nitride deposition process was carried out after the procedure of Giusto *et al.*.[228] In order to prepare the samples for chemical vapor deposition (CVD), the cut carbon cloths were treated in an oxygen plasma at 150 W power for 10 min at 0.5 mbar pressure, using a Harrick PDC-32G-2 plasma etcher. Plasma treated samples were titled with the suffix "Plasma". The hard carbon/carbon nitride nanocomposites were obtained by depositing polymeric carbon nitride (p-C_3N_4) on the plasma-cleaned samples in a horizontal tubular oven with two heating zones (planarGROW-3S-OS CVD System for Organic Semiconductors, by planarTECH) equipped with a 3 in. quartz tube. In a typical run, 5 g of melamine were placed in an in-house-made boat upstream to the target substrate. The carbon cloth was placed vertically to the gas stream in a quartz sample holder. The melamine was sublimed completely at 300°C and p-C_3N_4 was grown at 550°C on the target substrate. The entire process was carried out at a pressure as low as 10 Torr with N_2 as carrier gas with a flow rate of 50 sccm. After the deposition was complete, the samples were allowed to cool down naturally before collection. The mass gain after CVD was 5 % for 5092-CC, 10 % for 5092-ACC10, and 45 % for 5092-ACC20. Carbon/carbon nitride composites inherited their name from their parent carbon substrate with the suffix "C_3N_4".

Structural characterization

Gas physisorption

Gas physisorption measurements were performed on a Vapor200C gas sorption analyzer by 3P Instruments using N_2 at -196°C, Ar at -186°C, and CO_2 at 0°C as probe gasses, respectively. Prior to each experiment, the samples were degassed in vacuum at 150°C for at least 20 h. SSAs were calculated using the multipoint BET-method in a pressure range of $0.05 \leq p/p_0 \leq 0.20$ and the total pore volume was determined at $p/p_0 = 0.99$. Pore size distributions as well as SSAs and pore volumes were calculated from the adsorption branch using density functional theory. For N_2 at -196°C, the quenched-solid density functional theory (QSDFT) kernel was chosen, assuming carbon surfaces with slit/cylindrical shaped pores, for Ar at -186°C QSDFT on slit/cylindrical/sphere pores was used and for CO_2 at 0°C non-local density functional theory on carbon with slit pores was employed.

Thermal analysis

Combustive elemental analysis (EA) was carried out using a vario MICRO elemental analyzer by Elementar. Thermogravimetric analysis (TGA) was measured on a Netzsch TG-209 F1 Libra in a temperature range between room temperature and 1000°C in platinum crucibles under N_2 and synthetic air atmospheres, respectively, linearly increasing the temperature with 10°C min^{-1}.

Powder X-ray diffraction

Powder XRD patterns were recorded on a Bruker D8 powder diffractometer in Bragg-Brentano geometry in a 2Θ range of 10-70° with a step size of 0.03° using $Cu_{K\alpha}$ radiation (λ = 0.154 nm). The samples were placed horizontally on single crystal silicon sample holders.

Small-angle X-ray scattering

SAXS measurements were carried out on a Bruker Nanostar 2 machine using monochromated $Cu_{K\alpha}$ radiation with a distance from sample to detector of 28.90 cm, calibrated with a silver-behenate standard. The Vantec-2000 2D detector with 2048x2048 pixels sized 68x68 μm has a quantum efficiency of 80 % and a dark current of 5 counts per second (cps). The focal spot size of the X-ray beam has a diameter of 115 μm. The samples were ground to powders prior to measurement and filled into borosilicate capillaries with a diameter of 1.5 mm. For the data normalization, the filling density of the samples was determined, using a volume-calibrated cylinder. In order to obtain parameters in absolute dimensions, the device was calibrated using the method of Dreiss *et al.*[225] with ultrapure millipore water as primary calibration standard.

Electron microscopy and energy dispersive X-ray spectroscopy

Scanning electron microscopy (SEM) images were recorded on a Zeiss Leo Gemini 1550 microscope at 3 kV acceleration voltage and on a JEOL JSM-6510 with an acceleration voltage of 8 kV. C-HAT-X materials were sputtered with platinum or a gold/palladium alloy, in order to increase their conductivity. Energy dispersive X-ray spectroscopy (EDX) was measured on a Phenom ProX desktop SEM at 15 kV acceleration voltage. For SEM, the samples were torn into fine fibers and placed on the sample holder as-received. For EDX,

the fibres were cut and placed upright onto special aluminum-made vertical sample holders, with the freshly cut cross-section facing flat towards the optics.

Raman spectroscopy

Raman spectra of C-HAT-X materials were obtained on a Witec Raman microscope with an excitation wavelength of 532 nm at a radiation power of 3.5 mW using a Nikon (10×/0.25,∞/-WD 6.1) objective. In the case of Kynol carbon cloth samples, Raman spectroscopy was performed on a confocal inVia Raman microscope by Renishaw, using a green laser with a wavelength of 532 nm at 5 mW power, accumulating over five scans in a spectral range between 500 cm^{-1} and 3600 cm^{-1}.

Electrochemical characterization

Electrode preparation

C-HAT-X electrodes were prepared by a drop-casting method on pre-cut Cu discs. The materials were ground together with carbon black (SuperP, Alfa Aesar) as the conductive additive and a 20 mg ml^{-1} aqueous solution of sodium carboxymethylcellulose (CMC) (Sigma Aldrich, $M_W = 250.000$ Da) was added to obtain an ink with a mass ratio of 8:1:1 of active material/conductive additive/CMC. The ink was immersed into an ultrasonic bath for 1 h and stirred overnight subsequently, before 20 μl of it were dispensed over a circular Cu-foil (99.8 % purity, 0.025 mm thickness, Alfa Aesar) with a roughened surface and a diameter of 10 mm. The electrodes were dried under vacuum at 60°C before being used in sodium-ion half-cells. The area loading was approximately 1.0 mg cm^{-2}

Electrodes from Kynol carbon cloths cannot be measured directly, but have to be fabricated into powder-based electrodes by doctor blading. First, the cloths were ground to fine powders using a motorized mortar (Fritsch Pulverisette 2) for 10 min. For a typical electrode, 90 mg of the ground active material were mixed with 5 mg of a conductive carbon black (Super C65, Timical) and 125 μl of a 20 mg ml^{-1} aqueous solution of CMC, and stirred to homogeneity in an agate mortar. The resulting ink was coated onto a copper foil (99.8 % purity, 0.025 mm thickness, Alfa Aesar) using a doctor blade at 100 μm wet film thickness at a speed of 30 mm s^{-1}. The film was dried in vacuum at 70°C overnight and cut to discs of 10 mm in diameter. The area loading of 1.9-2.5 mg cm^{-2} is mainly determined by the filling density of the active material.

Cell setup

The electrochemical measurements were carried out in a two-electrode setup using Swagelok-type cells made of PTFE. A sodium metal disc of 11 mm was used as the counter electrode, against which also the potential was referenced. Whatman GF/C glass fiber filters served as the separators and were soaked with 200-300 μl of the electrolyte. The electrolyte was a 1 M solution of $NaPF_6$ in a 6:4 v/v mixture of EC and DEC. The cells were assembled in an Ar-filled glovebox with O_2 and H_2O levels below 0.1 ppm. All potentials are referred to as against Na/Na^+, unless stated otherwise.

Measurement procedures

All electrochemical measurements were carried out on an MPG-2 potentiostat by BioLogic. In order to achieve comparability with other systems, the current density was chosen with respect to the theoretical capacity of the Li-graphite anode system, where $C_{372} = 372$ mAh g^{-1}, so that 1 C corresponds to 372 mA g^{-1}.

Galvanostatic charging and discharging with lower voltage limitation was carried out as an initial assessment and in order to run-in the cell. The cell was sodiated with a current of 18.6 mA g^{-1} until a lower voltage limit of 0.002 V was reached. The current was reversed until an upper potential limit of 2.5 V and this procedure was repeated until the cell reached a steady state, usually for at least five cycles.

The maximum sodiation capacity was determined by intentionally oversodiating an already cycled-in cell and measuring the capacity at which the potential minimum is reached. This procedure was repeated with at least three cells, in order to determine an average value. The material specific sodiation capacity is current-dependent, therefore it had to be determined separately for every required current. The cells were discarded afterwards.

Galvanostatic cycling with capacity limitation was performed setting 90 % of the material-specific sodiation limit determined previously for the respective current and desodiating with an upper voltage limit of 2.5 V. Long-term stability tests were usually carried out in capacity-limited mode and the faradaic efficiency was calculated as the ratio between sodiation and desodiation capacities.

Cyclic voltammetry was measured in voltage ranges of 0.0-2.5 V and - 0.1-2.5 V at a scan rate of 0.1 mV s^{-1}.

EIS data for DRT analysis were recorded using the following routine. After five initial cycles in voltage-limited mode, the cell was fully desodiated, before applying a current pulse of C/20 for 10 min, followed by a resting period of 5 h, in order to achieve an equilibrium

state, characterized by a stable open circuit potential (OCP). An impedance spectrum was measured at 10 mV amplitude in a frequency range from 20 kHz to 10 mHz with 11 frequencies per frequency decade. The cycle of current pulse, resting period, and EIS measurement was repeated beyond sodium crystallization and performed analogously for the desodation process.

4. Results and discussion

4.1. Influence of pore structure and chemical environment on sodium storage in nitrogen-doped hard carbons

4.1.1. Motivation

Extensive parts of this section were published in the article Schutjajew et al., Small, 2021, 2006767.[229] As it was expounded in the introduction, the structural evolution, as well as the sodium and lithium storage mechanisms in carbohydrate derived hard carbons was already the subject of numerous extensive research efforts. However, these materials usually have ill-defined pore structures, as well as a varying interconnectivity between constituent atoms, aggravating the discovery of structure-property relationships. Textural limitations of these materials can be overcome partially by hydrothermal-synthetic and templating approaches, as well as by the preparation of composite materials.[186,230–235] However, even though the morphology of carbohydrate based hard carbons can be tuned in a wide range, the reaction pathway during pyrolysis remains mostly the same, restricting the possible conclusions on sodium storage mechanisms from experiments on materials from these precursors.
Therefore, the aim of the work presented in this section is the exploration of hard carbons and hard carbon-like materials derived from a wholly carbohydrate-independent starting material for the utilization as sodium-ion anode materials, in order to draw conclusions on the impact of heteroatoms, porosity, and chemical environment on the sodium storage performance. A precursor developed and well-understood recently, HAT-CN, was chosen for this purpose due to its precisely defined condensation mechanism during heat-treatment and the variety of products achievable by controlling the pyrolysis temperature. For instance, the molecule is build up solely of sp and sp^2 conjugated carbons and hence does neither contain sp^3 carbons, nor hydrogen atoms. The condensation mechanism was revealed to be a nitrile elimination/cyclization reaction.[227,236,237] HAT-CN derived materials were already

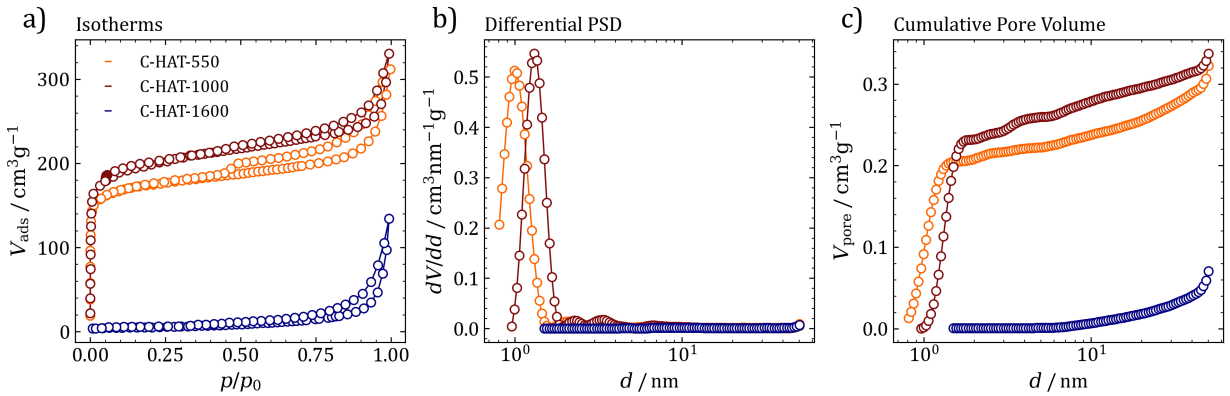

Figure 4.1.: Results of Ar-sorption experiments on C-HAT materials measured at 87 K. a) Isotherms, b) differential pore size distribution, and c) cumulative pore volumes.

proven of value for energy storage applications by Yan et al.,[238] who created composites with conductive carbon fibers by electrospinning and tested the structures under high-power conditions as sodium-ion capacitor anodes. However, due to different conditions and requirements having to be met for the successful application as battery anodes, i.e. a high energy density at relatively low currents, also the structural features and hence synthesis parameters have to be re-evaluated for the purpose of energy storage in sodium ion battery anodes. Bearing in mind the fact that in many cases significant amounts of sodium are stored below the typical cut-off potential of 0 V, the opportunity was seized to introduce a new, capacity limited charging-discharging protocol, to effectively assess the full sodiation capacity of the anode materials.

4.1.2. Structural characterization

The carbons investigated within this project are obtained from the pyrolysis of HAT-CN at temperatures of 550°C, 1000°C, and 1600°C. The latter was obtained by the post-carbonization of C-HAT-1000, for practical reasons, which is a legitimate approach in hard carbon synthesis, as the structure of carbons obtained at a certain temperature can be viewed as congealed at this particular temperature and it continues to evolve upon exceeding it.[156] At the chosen temperatures, HAT-CN yields carbons of similar particle size and shape, but utterly different porosities, carbon stacking patterns, and heteroatom contents, as will be shown by various structural characterization methods. The pore structure of the materials was analyzed by Ar sorption at 87 K and CO_2 sorption at 273 K. Ar is the preferable adsorptive for adsorbents with high heteroatom contents, as contrary to other gasses, such as N_2, it has

an isotropic charge distribution and therefore does not show specific interactions with energetically heterogeneous sites in the adsorbent.[222] Also, its boiling point is higher than that of N_2, which enables faster adsorption kinetics due to higher diffusivity, giving rise to better resolved isotherms, particularly in the low p/p_0 range.[215] In figure 4.1a), both, C-HAT-550 and C-HAT-1000 show IUPAC type I(a) isotherms, with steep uptakes in the low p/p_0 range, typical of purely microporous samples. Additionally, the type H4 hysteresis loop indicates a considerable amount of pores with narrow entrances, as it is typically observed due to the deferred evaporation of gas confined in pores with necks narrower than their mean diameter, known as pore-cavitation effect. Remarkably, this effect is less pronounced in C-HAT-1000. C-HAT-550 has a higher uptake of Ar in the low-relative pressure range with a sharp inflection at approximately $p/p_0 = 0.05$, indicating a high volume of sharply distributed, narrow micropores, which distinguishes the material against C-HAT-1000, with a less pronounced curvature at low relative pressures and consequently less precisely distributed micropores. Together with the similar total gas uptake of both materials this observation allows the conclusion that the Ar-accessible micropore volume stays constant during consecutive temperature treatment, but the diameter of micropores increases steadily. The pore size distributions (PSD) and cumulative pore volumes calculated by DFT shown in figure 4.1b) and c) confirm this picture, showing the similar total pore volumes of 0.32 $cm^3\ g^{-1}$ in C-HAT-550 and 0.33 $cm^3\ g^{-1}$ in C-HAT-1000 at mean pore diameters of 1.0 nm and 1.3 nm for the two materials, respectively. SSAs of the two materials calculated using the BET model, as well as the QSDFT method are well in line with the above model and show similar values around 700 $m^2\ g^{-1}$, as presented in table 4.1, legitimating the application of the BET theory in this case. C-HAT-1600 shows a wholly different behaviour in Ar-sorption experiments. Its isotherm can be best classified as type III and is often observed in materials with low microporosity and mainly external surface area, likewise the detected SSA, from both, BET

Table 4.1.: Results of sorption measurements with Ar at 87 K and CO_2 at 273 K and elemental composition determined by combustive CHNS analysis.

	C-HAT-550	C-HAT-1000	C-HAT-1600
$SSA_{\mathrm{BET,Ar}}$ / $m^2\ g^{-1}$	670	750	20
$SSA_{\mathrm{DFT,Ar}}$ / $m^2\ g^{-1}$	870	770	20
$V_{\mathrm{CO_2,(<0.7nm)}}$ / $cm^3\ g^{-1}$	0.17	0.18	0.13
C / wt.%	52.35	89.02	98.8
N / wt.%	35.58	6.57	0.41
H / wt.%	1.66	0.81	0.15

and DFT models, is as low as 20 m^2 g^{-1}. Results from CO_2 sorption shown in figure A.1 reveal another important and unique property of HAT-CN derived carbons. Even after heat treatment to 1600°C, the material shows a CO_2 uptake volume of 0.13 cm^3 g^{-1}, only 25 % lower than C-HAT-550 and C-HAT-1000 with 0.17 cm^3 g^{-1} and 0.18 cm^3 g^{-1}, respectively. This is remarkable in the sense that carbohydrate derived carbons usually show no open porosity at all, neither for CO_2, nor for other gasses.[198] From the physisorption data it can be concluded, that C-HAT-1600 consists of abundant, relatively large micropores with rather narrow entrances.

Combustive elemental analysis was used to obtain an overview over the heteroatom content of the bulk samples and the results are summarized in table 4.1. Containing 36 wt.% of nitrogen, C-HAT-550 can hardly be regarded as a pure carbon but rather as a nitrogen rich carbonaceous material. The nitrogen content decreases with higher temperature treatment, reaching 6.57 wt.% and 0.41 wt.% in C-HAT-1000 and C-HAT-1600, respectively. The loss of heteroatoms is a typical effect occuring during pyrolysis, while the presence of hydrogen is particularly pronounced in C-HAT-550 and is most likely to be explained by adsorbed water, as no other atoms except for carbon and nitrogen exist in the precursor.[157,227] In previous work it was already figured out that the nitrogen species in C-HAT-550 are prevalently pyrazinic, quaternary, and cyanic type, while in C-HAT-1000 the nitrogen groups are restricted to the former two types. With an amount of nitrogen as low as 0.41 wt.% after a heat treatment to 1600°C, C-HAT-1600 can be regarded as a pristine hard carbon.

From powder XRD patterns, as presented in figure A.2 (appendix), the predominantly amorphous structure of C-HAT-550 and the disordered graphitic structure of both C-HAT-1000 and C-HAT-1600 becomes evident. The XRD-pattern of C-HAT-550 shows only one broad reflex at $2\Theta = 27°$, which cannot clearly be attributed to a specific reticular plane, indicating that a graphitic framework has not yet been formed at temperatures as low as 550°C. C-HAT-1000 exhibits diffraction patterns typical of non-graphitizing carbons, consisting of two broad peaks that can be assigned to the (002) and (100) reflexes, respectively. Though the low-angle background resulting from micropore scattering may induce an error, Bragg's condition can be applied to the (002) reflex in order to identify trends in the development of the graphene interlayer distance. The value decreases from 3.8 Å in C-HAT-1000 to 3.7 Å in C-HAT-1600, but both values are well above that in ideal graphite (3.35 Å). Together with the reduced FWHM of the (002) peak, a slightly higher degree of graphitic stacking can be concluded from the XRD results.

On an atomic scale, Raman spectroscopy provides information on the binding situation of carbonaceous materials. The Raman spectra presented in figure A.3 were analyzed by

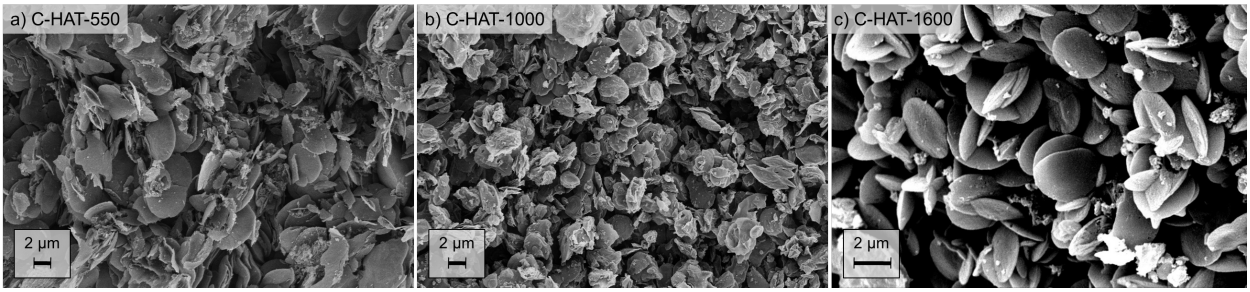

Figure 4.2.: SEM-images of C-HAT materials. a) C-HAT-550, b) C-HAT-1000, and c) C-HAT-1600.

fitting the region between 900 and 1900 cm^{-1} to a four-band model, considering the *trans*-polyacetylene (TPA), D, A-, and G-bands at approximately 1100, 1340, 1460 and 1600 cm^{-1}, respectively, following the approach of Hu et al.[239,240] The presence of TPA bands typically indicates an incomplete aromatization, while A-bands are indicative of heteroatoms and point-defects, therefore these vibrational modes are frequently found in carbonaceous materials with a high degree of disorder.[240,241] Meanwhile, the D- and G-bands are observed in disordered graphitic structures, where the former band originates from the breathing mode of carbon six rings at defective graphitic sites and the latter occurs due to in-plane bond-stretching vibrations of sp^2 hybridized carbon atoms.[242,243] In C-HAT-550 the TPA- and A-bands are dominating the Raman spectrum, indicating an almost amorphous structure and a low extent of carbonization, which is not surprising, considering the low condensation temperature and the amount of nitrogen within the framework. At higher heat treatment temperatures, the D- and G-bands have an increasing impact on the Raman spectrum of C-HAT-1000 and are the prevalent signals in the spectrum of C-HAT-1600, where the TPA-band is vanished almost completely and the A-band has only a minor contribution. A disordered graphitic structure, typical of hard carbons, can therefore be attributed to the latter two materials.

Electron microscopy allows conclusions on the morphology, particle size, and -shape of the samples under study. SEM images are depicted in figure 4.2. As it was already found in previous works and pointed out in the introduction, HAT-CN forms discoid primary particles upon pyrolysis.[227] This particle shape is kept even after being subjected to temperatures as high as 1600°C, indicating a stable, cross-linked framework formed by the condensation of HAT-CN molecules, already foreshadowing the non-graphitizing nature of the resulting carbon, with only minor, local structural rearrangements during pyrolysis. Even more, the scanning electron micrographs of C-HAT-1600 exhibit a smooth surface without smaller, shapeless fragments, visible in the two other materials.

The bright-field TEM images, shown in figure A.4 reveal a contorted structure in all three samples on a size range of several tens of nanometers, without evident differences between the materials. The constant particle morphology facilitates the investigation of structure-performance relationships and will corroborate conclusions on the impact of gas-sorption properties and heteratom contents on the sodium storage behavior.

4.1.3. Relationship between gas sorption and sodium storage

C-HAT materials were first subjected to the usual, potential-limited capacity determination procedure in a voltage range between 2.5 and 0.002 V at a low current density of 18.6 mA g^{-1}. By using such a low current it is ensured that the impact from mass-transfer or electrode polarization is minimized and a quasi-equilibrium potential-composition curve can be recorded. The first and the fifth sodiation cycle, respectively, are presented in figure 4.3, where the fifth cycle is considered representative of the material's sodiation behaviour above 0 V, as no change is observed between the sodiation curves from the fifth cycle on. In the voltage limited mode, all three materials show a capacity retention of 25 % to 34 % with respect to the first cycle. While this is rather unusual, if compared with carbohydrate-derived hard carbons obtained at temperatures of 1600°C, where higher first cycle-efficiencies are observed,[197,198] it impedes the practical applicability of C-HAT-derived materials as substantial amounts of electrolyte are consumed, effectively reducing the gravimetric capacity.
Even though the surface areas and the general pore structure of C-HAT-550 and C-HAT-1000 are very similar, C-HAT-550 exhibits almost double the absolute first cycle capacity of C-HAT-1000. This effect can clearly be ascribed to the high heteroatom content of the former material, causing an extensive amount of irreversible reactions besides the typical SEI formation due to the reduction of electrolyte, facilitated by the nitrogen sites of C-HAT-550. Further, it cannot be ruled out that the material itself is undergoing a chemical transformation upon the first cycle, and the entrapping of Na-ions must be considered, as well.[126]
The comparison of the sodiation behaviour of C-HAT-1000 and C-HAT-1600 also yields some insights into the fundamental relationship between gas sorption and sodiation properties. Both materials show similar voltage profiles in the first cycles, although their BET surface area as calculated from their Ar uptake at 87 K is fundamentally different with 750 m^2 g^{-1} for C-HAT-1000 and only 20 m^2 g^{-1} in C-HAT-1600. However, the CO_2 volume adsorbed at 1 atm is relatively high in both materials, as presented in table 4.1. This suggests that the electrolyte molecules and ions can enter pores inaccessible to adsorptives like Ar at 87 K and considering the kinetic diameters and diffusivities likely also N_2 at 77 K, rendering CO_2 at

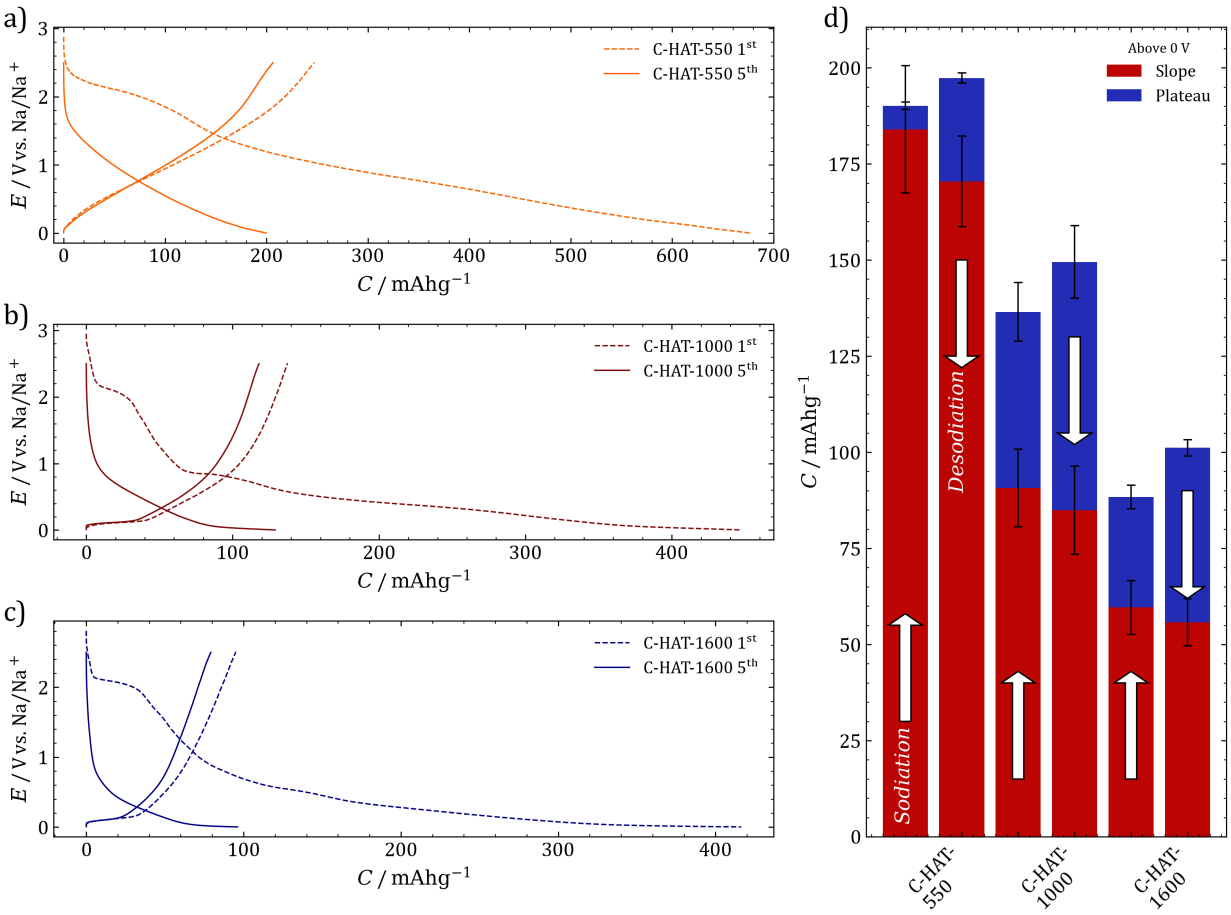

Figure 4.3.: First and fifth cycle charge-discharge curves of C-HAT materials at 18.6 mA g^{-1} with a lower voltage limit of 0 V. a) C-HAT-550, b) C-HAT-1000, and c) C-HAT-1600. d) Bar chart compares portions of sloping and plateau regions in the total capacity, respectively.

273 K a more suitable adsorptive to assess the capacity loss in the first cycle. The reason for this circumstance is not only the smaller kinetic diameter of 0.33 nm for CO_2 vs. 0.34 nm for Ar, but also the higher diffusivity at the elevated temperature at which the sorption experiment is performed, leaving the CO_2 molecules able to enter even the narrowest pores within a realistic equilibration time.[216,222] The chemical nature of the CO_2 molecule is another reason why it can serve as a model-adsorbtive to represent the first-cycle behaviour of a sodium-ion anode. Contrary to Ar, CO_2 contains an electrophilic carbon atom bound to two nucleophilic oxygen atoms, which is much more representative of the adsorption but also reactivity of the common carbonate-based electrolyte than the Ar atom with its isotropic charge distribution. The CO_2 molecule is hence able to undergo electron-donor-acceptor interactions with reactive sites in the adsorbent material, such as nitrogen and defect sites,

which are primary centers of the adsorptive energy storage as shown in the measurements on C-HAT-550 and C-HAT-1000. All together, the large capacity and therefore the profound electrochemical reactions taking place in the first cycle and the general difficulty in finding a structural descriptor for the sodium storage properties of a carbonaceous material both imply that the anode undergoes a substantial change in its chemical and its pore structure during the initial electrochemical reduction step. If for example in the case of C-HAT-550 one considers 200 mAh g^{-1} of reversible capacity and another 200 mAh g^{-1} of pure SEI formation, derived from the irreversible capacity of C-HAT-1000, attributing the remaining uptake of 300 mAh g^{-1} of charge in the first cycle to the reduction of the material itself, it would result in approximately one electrochemical reaction equivalent per 85 atomic mass units. Therefore, it is concluded that the material formed in situ is a different one than the one subjected to structural investigations before the electrochemical measurements.

In the discussion of the sodiation curves of sodium ion anodes it is often referred to sloping and plateau regions, each with their own chemical origins. In order to quantitatively distinguish between these two storage modes, without further bias as to which mechanism is responsible for the respective region, a voltage threshold of 0.1 V was chosen. Capacity between 2.5 V and 0.1 V was regarded as sloping capacity, while capacity below the threshold and the lower limit of zero volt or the onset of bulk sodium plating, respectively, was counted as plateau capacity. This approach to discriminate between slope and plateau regions is already known in literature.[197,244] The limit between the two capacity modes is chosen empirically and must be adjusted depending on the current applied due to polarization overpotentials. A possible downside that must always be considered is of course that short sloping portions below 0.1 V will be regarded as plateau even in a material with a purely sloping characteristic, like in the case of C-HAT-550. In the bar chart in figure 4.3d) the capacities of all three materials above 0 V are summarized and subdivided into slope and plateau portions. Sloping capacity is most pronounced in C-HAT-550 and diminishes with higher temperature treatment, from 170 mAh g^{-1} in C-HAT-550 to 85 mAh g^{-1} in C-HAT-1000 to finally 56 mAh g^{-1} in C-HAT-1600. A voltage plateau emerges in the case of the latter two materials, but in the voltage-limited mode, the sloping dominates the voltage profile, so that the total capacity of the material decreases within the temperature series. As already introduced, the voltage plateau often proceeds even below 0 V.

For the application of an anode material in a balanced full cell the safely utilizable capacity at a flat voltage is a more valuable information than the capacity until the rather arbitrarily chosen limit of 0 V, as the cut-off voltages are usually mainly dictated by the cathode material in a full cell. Therefore it will be shown that the capacity limited approach to determine

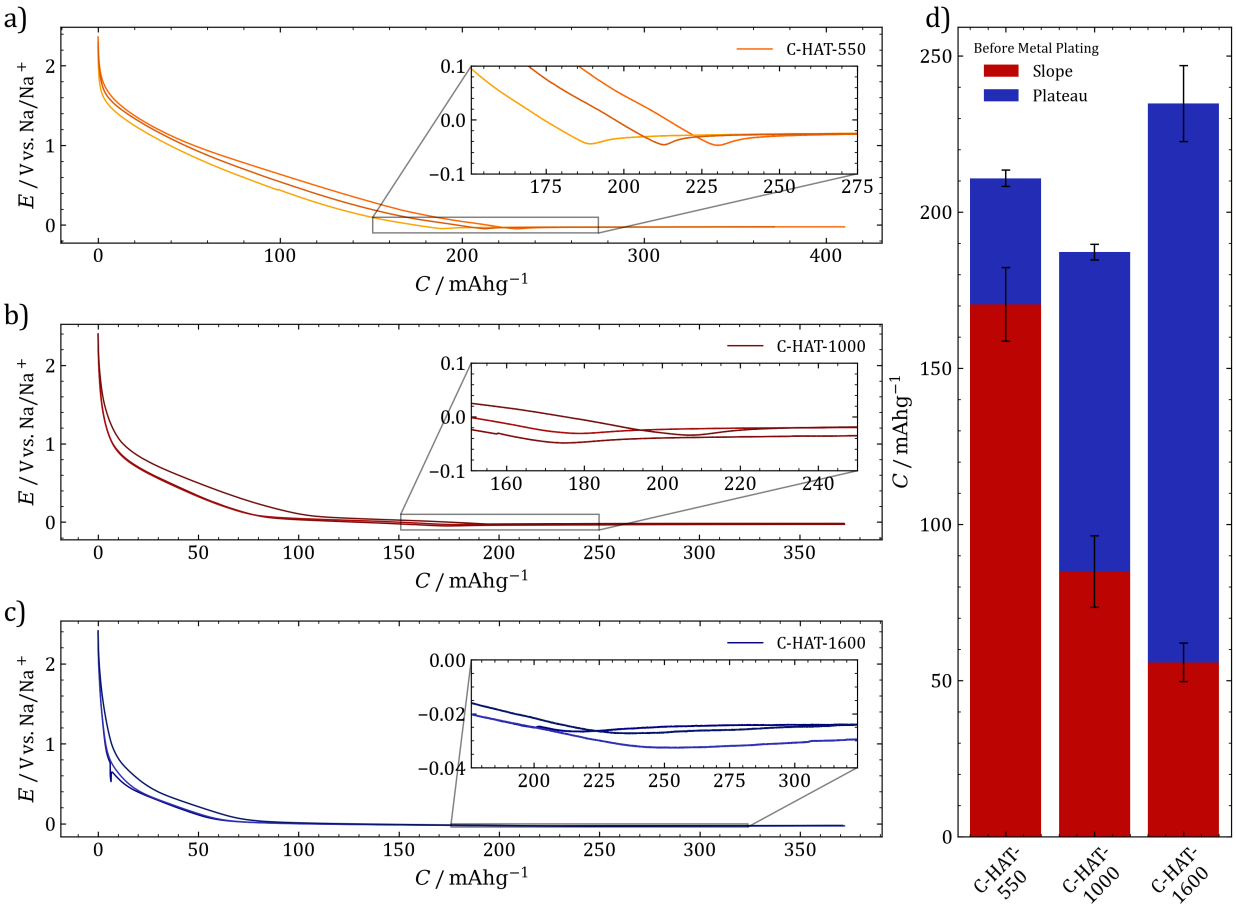

Figure 4.4.: Determination of the bulk-sodium plating capacity at 18.6 mA g^{-1} with a lower voltage limit of 0 V. a) C-HAT-550, b) C-HAT-1000, and c) C-HAT-1600. Bar chart compares portions of sloping and plateau regions in the total capacity, respectively, including capacity below 0 V.

the reversible sodiation capacity is a valuable and reproducible descriptor for an anode material, as it directly determines the material-specific property of maximum reversible sodium uptake, without being biased by setup-related errors such as uncompensated resistances and others. In figure 4.4 the voltage profiles during the oversodiation of the three materials are shown for three independent, identical cells. The inset shows a magnified view of the voltage minimum as the reversible storage mode transitions into bulk sodium deposition at the external area of carbon grains. When measuring the capacity chargeable before bulk plating occurs, $C^{\mathrm{Dip}}_{\mathrm{Sod,Tot}}$, C-HAT-550 continues its sloping characteristic until at a capacity of 200 mAh g^{-1} bulk sodium plating occurs. In C-HAT-1000 and C-HAT-1600 the sloping regions remain the same, while the voltage plateaus extend over 187 mAh g^{-1} and 235 mAh g^{-1},

respectively, if capacities at potentials below 0 V are included. The plateau region hence contributes to 55 % (102 mAh g^{-1}) and 76 % (179 mAh g^{-1}) of the capacity of the latter two materials.

The change in sodiation characteristics can only be explained by the evolution of the materials structure during the exposure to high temperatures. The structure of C-HAT-550 is comprised of abundant micropores, narrow in diameter, resulting in a high surface area. Together with a high content of nitrogen atoms, this causes a high irreversible first-cycle capacity and a considerable, reversible sloping capacity in the subsequent cycles. Even below 0 V, no plateau capacity is observed, which implies that no sodium is deposited in a quasimetallic state in this material. This can be explained by the highly polar environment established by the near-ionic charge distribution with negatively polarized nitrogen and partially positively charged carbon atoms, leading to the stabilization of single, ionic sodium species. Moreover, the formation of Na^0 requires the presence of a certain amount of carbon atoms with a defective, graphenic ordering, which can provide a similar stabilizing surrounding to the Na^0 phase like a sodium atom experiences in a sodium crystal.[196,245] Finally, the small pore size and high disorder simply cannot provide enough space to accommodate a Na^0 phase of significant lateral dimensions. In the binding situation present in C-HAT-550, the charge density is well separated between the negatively charged carbon anode and the positively charged sodium ions. At most, a minor amount of singular reduced sodium atoms is present in the fully sodiated C-HAT-550 electrode.[191]

At higher heat treatment temperatures, the material obtains a more ordered structure, closer to that of graphite, as can be observed in Raman spectroscopy, which is accompanied by the loss of nitrogen, in particular pyrazinic and cyano groups outside of the carbon framework.[227] The reduced amount of polar and amorphous regions can adsorb less sodium in an ionic state and results in the reduction of the sloping capacity in C-HAT-1000 and even more in C-HAT-1600. Instead, the as-formed expanded graphitic layers in C-HAT-1000, already similar to what is called a closed pore, but not yet wide enough, can stabilize extensive amounts of quasimetallic sodium, presumably in 2D-layers.

Judging from the chemical connectivity of carbon atoms within and between graphene layers, C-HAT-1600 can be best described as hard carbon, which inheritated the the morphology and texture from its parent materials. The results from gas sorption experiments imply that a large volume of incompletely collapsed pores with narrow entrances are present in this material, causing a high irreversible capacity in the first cycle. The Raman spectra and XRD patterns of this material indicate a more pronounced structure of turbostratically disordered and curved graphitic regions, forming Na^0-stabilizing features such as closed pores formed by

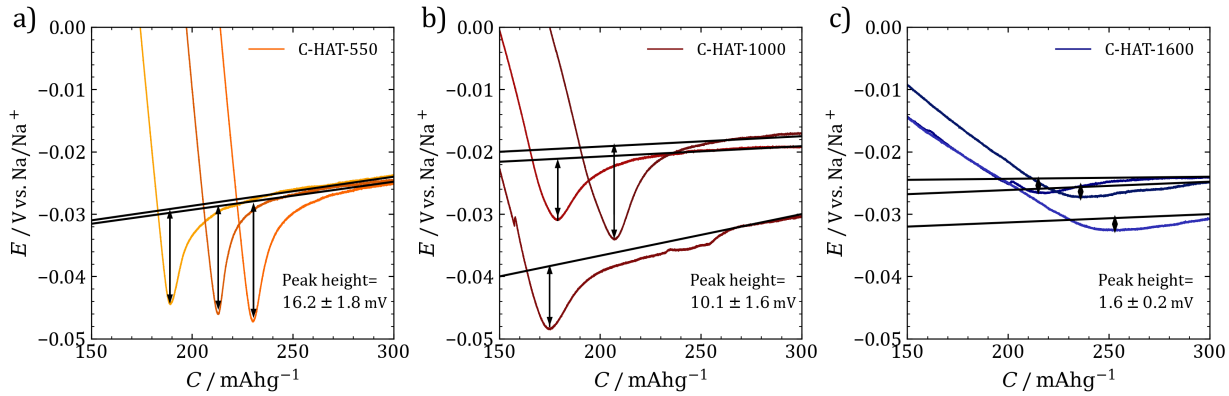

Figure 4.5.: Estimation of the width and height of the sodium crystallization peak in the charge-discharge curves of a) C-HAT-550, b) C-HAT-1000, and c) C-HAT-1600.

deviating expanded graphene layers. The formation of Na-clusters can in this case be best described by an analogy from gas physisorption in mesopores. 2D-Na^0 layers are forming at suitably defective graphene layers and where the layers are departing from each other, sodium clusters can fill the resulting voids due to processes similar to capillary condensation, finally resulting in quasimetallic Na-cluster formation. Due to the well-defined chemical nature of the newly formed two-phase structure, the potential at which this process occurs is constant and close to that of bulk sodium. However, with increasing graphene-graphene distances, i.e. larger closed pore diameters, it stands to reason that the forming Na^0 clusters become big enough that their formation stands in a competition with the bulk sodium crystal growth, rendering them indistinguishable from an energetic, and practically a voltage point of view. This circumstance is further underlined by an often overlooked feature of the charge-discharge curve, namely the width and height of the sodium crystallization peak. In an attempt to quantify this value, a baseline was drawn in the range of the sodiation curve, where sodium has already nucleated and the height of the peak was determined from the extrapolated baseline, as shown in figure 4.5. The values decrease significantly with rising heat treatment temperature from 16.2 ± 1.8 mV in C-HAT-550, to 10.1 ± 1.6 mV in C-HAT-1000, to finally 1.6 ± 0.2 mV in C-HAT-1600. On the one hand, this underlines the chemical similarity of the formed quasimetallic sodium phase to crystalline sodium, on the other hand this trend implies that extensive amounts of preformed quasimetallic sodium may serve as nucleation points for the further growth of metallic sodium crystals. As the pores of HAT-CN derived materials do not seem to close well up to 1600°C, the growth out of the pore would be impeded only by the SEI layer. Further insights into the sodiation mechanism and a distinction between the processes involved can be obtained from cyclic voltammetry. CV-measurements

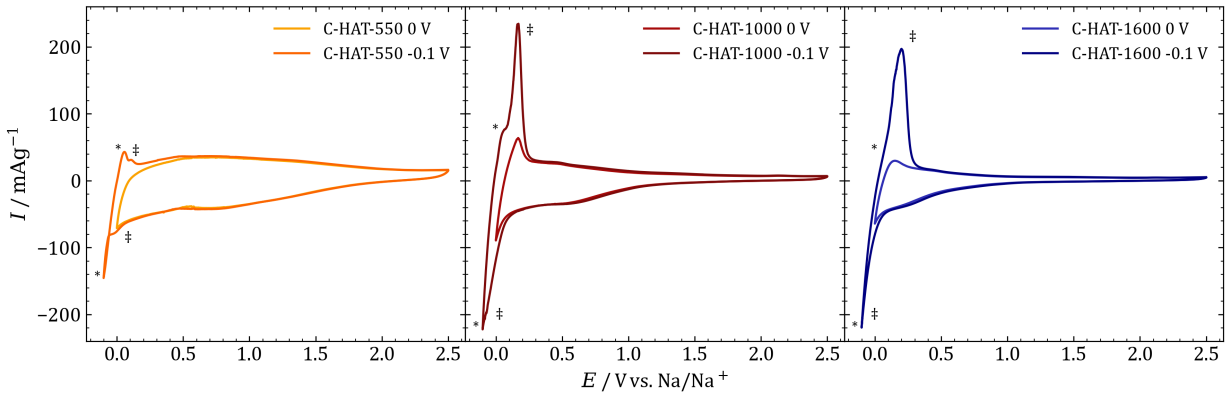

Figure 4.6.: Cyclic voltammetry measurements of C-HAT materials in voltage windows of 0.0-2.5 V and -0.1-2.5 V at scan rates of 0.1 mV s^{-1}

.

in voltage windows of 0.0-2.5 V and -0.1-2.5 V are presented in figure 4.6. In both windows, a considerable constant current portion is measured at potentials higher than approximately 0.2 V, as it is typical of capacitive charge storage processes. The onset of this signal is found to correlate well with the sloping region observed in charge-discharge curves. Approaching potentials of 0 V, an increasing cathodic current is measured in C-HAT-1000 and C-HAT-1600, with its anodic counterpart found at a potential of 0.15 V. This signal is by far not as pronounced in C-HAT-550. The lower voltage limit was extended to -0.1 V, in order to find out, whether the quasimetatallic sodium storage mode can be identified by a characteristic peak in the CV curve. While in these measurements all three electrodes show only a constantly increasing cathodic current at low voltages, the anodic scan reveals two signals, labeled with an asterisk and a double dagger, respectively, with different peak current ratios for each material. The signal labeled with an asterisk seems to continue unlimitedly and hence is attributed to the bulk sodium plating. The double dagger-labelled peak, on the other hand originates from the deposition of quasimetallic sodium in expanded graphitic interlayers and closed micropores and forms the low-voltage plateau in charge-discharge curves. The assignment is based on the voltage, but also the material, where the peak occurs most prominently. From this reasoning, it seems that reversible quasimetallic sodium storage occurs in C-HAT-550 to a minor extent, as well, if the voltage treshold of 0 V is exceeded, which can be seen from the small cathodic and anodic peaks labelled with a double dagger. Furthermore, the two signals attributed to quasimetallic storage and bulk deposition seem to coalesce with each other with increasing pyrolysis temperature. This correlates well with the finding of a reduced sodium plating overpotential in figure 4.5 and points at the similarity of

sodium plating and reversible storage, especially in materials obtained at high temperatures. In order to prove that the capacity below 0 V determined by the oversodiation method can be reversibly extracted from the material, all three samples where subjected to a galvanostatic charge-discharge experiment at a current density of C/20 with the capacity limit set to 90% of the previously measured bulk plating capacity. The materials were initially charged and discharged for 5 cycles with a voltage limit of 0 V, in order to form the SEI and stabilize the cell. The results are presented in figure A.5. In fact, in this preliminary, yet significant experiment, a fully reversible behavior was found for all three materials. However, this method was only found useful for materials exhibiting a noteworthy capacity below 0.1 V. For example for C-HAT-550, where the dip commences almost immediately below the potential of metallic sodium and only low amounts of sodium are stored in the range between 0.1 V and bulk plating, the capacity remains underutilized using this protocol.
From these measurements, C-HAT-1600 was selected for further investigations at higher current densities and long-term cycling, as it not only exhibits the highest capacity among the three samples, but also because the capacity is mainly found at constant voltages close to metallic sodium, and hence could deliver the highest energy density, if paired with and balanced against a hypothetical, constant-potential cathode. Furthermore, due to the extensive voltage plateau below 0 V, C-HAT-1600 would benefit the most from the capacity limited approach.

4.1.4. C-HAT-1600 as an SIB anode material and impact of current density

The performance of C-HAT-1600 at higher current densities as well as its long-term cycling stability were investigated. For that, the capacities of the onset of bulk sodium plating were determined additionally at C/5 and C/2. The respective measurements are shown in figure 4.7a) and the results are summarized in a bar chart in figure 4.7b). At C/5, a capacity of 200 mAh g^{-1} is still reached, while at C/2 it drops to 100 mAh g^{-1}. The plateau capacity is more affected by increasing currents than the sloping capacity, also the voltage minimum is less pronounced than at low currents, see figure 4.7b) and c). With the bulk plating capacities determined, C-HAT-1600 was cycled to 95 % of the measured capacity value for five cycles at each current density, as can be taken from figure 4.7d). The coulombic efficiency is generally higher than 99 % and the material is not negatively affected by increasing current densities. The results of long-term cycling at C/20 show coulombic efficiencies higher than 99.6 %, with a tendency to even higher values once the cell is cycled until a steady state. All in

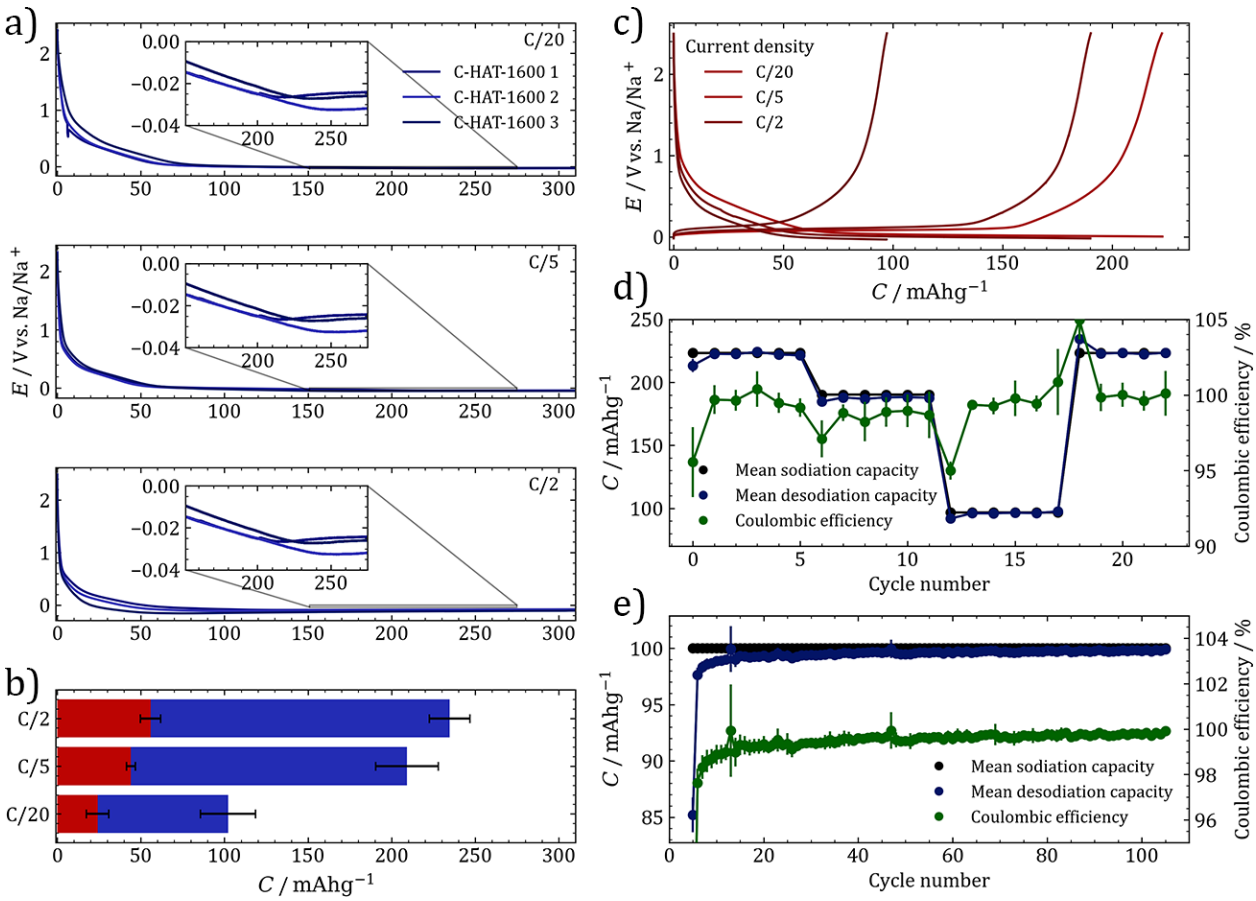

Figure 4.7.: Characterization of C-HAT-1600 as an SIB anode material. a) Determination of the bulk sodium plating capacity at current densities of C/20, C/5, and C/2. b) Bar chart summarizing slope and plateau capacities as a function of current density. c) Representative voltage profiles during cycling at different current densities. d) Capacity and coulombic efficiencies at different current densities and e) results of cycling at C/2 over 100 cycles.

all, the results demonstrate the possibility of the utilization of sodium storage mechanisms occuring close to potentials of metallic sodium deposition, even below 0 V, and the viability of the capacity limited charge and discharge protocol.

During the determination of the sodium plating capacity, an intriguing circumstance in the desodiation cycle was noticed, after the electrode was oversodiated. As it was already discussed, the potential minimum shifts towards lower capacities with increasing current densities. If the subsequent desodiation cycle, shown in figure 4.8, is considered, it becomes evident that an extensive desodiation plateau is measured after a constant portion of capacity around 50 mAh g^{-1} is desodiated at around 20 mV. The latter one is attributed to the partial stripping of the sodium metal plated irreversibly. However, the former desodiation plateau at up to 200 mV extends over 150-200 mAh g^{-1} and only weakly depends on the

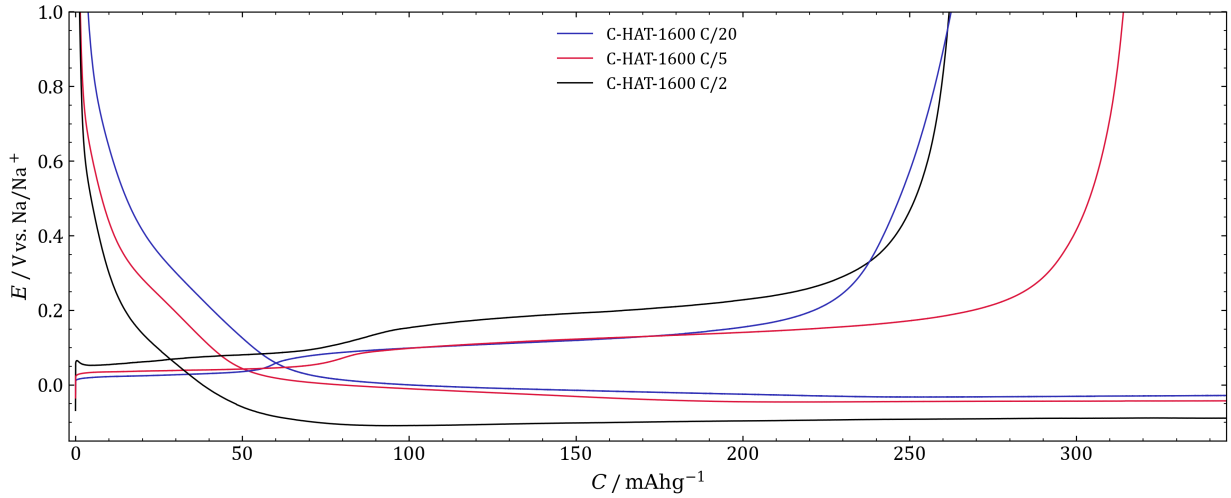

Figure 4.8.: Desodiation cycle after oversodiation of C-HAT materials at current densities of C/20, C/5, and C/2.

current density. It stands to reason that this capacity is due to the dissolution of reversibly deposited quasimetallic sodium, which could not be distinguished during the sodiation step. Hence, by relying on the sodium plating capacity in the sodiation process, the true capacity of a material is still underestimated. Further investigations on this effect shall follow in the context of a later project within this work in section 4.3.

4.1.5. Conclusion

To conclude this part of the work, a series of hard carbons and hard carbon-like materials, produced from an organic, self-templating precursor, were used to investigate the impact of pore geometry and heteroatom content on the properties of a material for sodium storage in SIB anode half cells. A capacity-limited approach was used to cycle the materials, where the maximum sodiation capacity was initially determined on a statistically relevant basis of cells. Even though the experimental effort is substantially higher, as the first cells must be sacrificed, the determined capacity value is physically more meaningful than the capacity measured until the somewhat arbitrary lower voltage limit of 0 V. It was found that only a small portion of the sodiation capacity could be utilized in the usual voltage window of 2.5-0.002 V and significant amounts of sodium were stored at potentials lower than that of metallic sodium. The amount of heteroatoms in the material was found to correlate directly with the sloping capacity, while a higher degree of ordering causes a decrease of sloping and an increase of plateau capacity. From the pore diameter and accessibility it

was concluded that in materials with existing defective graphene layers but narrow pores, the deposition takes place in 2D layers of quasimetallic sodium in a first stage at a low and constant potential. In the regions where the graphene sheets deviate from each other, forming internal cavities, such as in C-HAT-1600, the 2D layers can expand into the third dimension to form sodium clusters, well in line with the common view on the sodiation of non-graphitizing carbons in the literature. Meanwhile, the overpotential required to nucleate bulk metallic sodium is reduced with higher degrees of ordering due to high-temperature treatment of the carbons, indicating that either quasimetallic sodium can serve as nucleation point for the further growth of crystalline sodium or that the carbon material intrinsically facilitates the formation of sodium metal. However, the role of the SEI in this process is yet to be determined. A correlation between a materials behaviour in sorption experiments with different probe gasses and its electrochemical performance was also found. Generally, the accessibility of pores to electrolyte constituents during the SEI formation can be better modelled by CO_2 sorption at 273 K than with Ar or N_2 at cryogenic temperatures, which was also found in the literature.[246] The structure and performance relationships, as well as the electrochemical approaches contribute to the understanding but also to the practical application of non-graphitizing carbons in SIBs. Further analysis of the sodium storage kinetics on C-HAT-1600 will be presented in the following section.

4.2. Insights into the sodiation mechanism of hard carbons from electrochemical impedance spectroscopy

4.2.1. Motivation

Extensive parts of this section were published in the article Schutjajew et al., *Physical Chemistry Chemical Physics*, **2021** *23*, 11488-11500.[247] In the previous section, HAT-CN derived materials, in particular C-HAT-1600, were ex situ investigated structurally and their sodium storage mechanism in SIB anode half cells was studied by direct-current electrochemical methods. Most knowledge available in the literature about the sodiation mechanism of potential electrode materials is obtained either by one of the presented techniques alone or by their combination with in situ or operando electrochemistry.[14,196,248,249] Meanwhile, electrochemical impedance spectroscopy, a powerful technique, widely applied in many fields of electrochemistry, is often overlooked in the context of LIBs and SIBs.[210] The reason for the negligence of this method is likely the fact that EIS data are usually interpreted using the equivalent circuit fitting approach, which requires well-resolved impedance spectra, but also the relatively precise knowledge of all possible involved mechanistic steps during the process under study, a priori. Since the processes during the insertion and extraction of ions into a hard carbon framework are manifold, the equivalent circuit fits of impedance data for such a system would yield rather ambiguous results and the kinetic parameters obtained from such fits would be consequently devoid of any physicochemical meaning.
By calculating the DRT function from EIS data, these limitations can be overcome, as it needs no information about the studied system beforehand, in fact, the opposite is the case, as the result of a DRT analysis provides the number of R|C elements, their time constants and relative contribution to the cell impedance in a Voigt circuit arrangement. These highly valuable parameters can then be used to refine the equivalent circuit and reconstruct the impedance spectrum. Moreover, up to three processes can be resolved per frequency decade, a vast improvement if compared to Nyquist or Bode representations of EIS data, particularly important for solid-state based electrodes like LIB and SIB anodes.[250] This method has proven itself useful in solid-oxide fuel cell research,[250] and was applied to LFP cathodes and LIB full cells, as well as to porous carbon anodes in LIBs and even sodium metal anodes.[250–254] However, to the best of the author's knowledge, an investigation of non-graphitizable carbons by means of DRT analysis has not been published yet. It is therefore

the purpose of this project to obtain processable impedance data from a hard carbon sodium anode half cell and to calculate a DRT of these spectra using an optimal set of fitting parameters, in order to gain fundamental insights on the processes involved during the deposition of sodium in hard carbon anodes. In order to get a full view on the sodiation kinetics, but also to understand the reverse process, impedance spectra were measured at narrowly spaced states of charge during both the sodium insertion and extraction processes. Following the method of Schmidt et al.,[251] symmetrical sodium/sodium cells were built and measured, so that an assignment of some of the measured time constants became possible. Diffusion was found to play a major role during the sloping voltage region, but more importantly, the kinetics of the formation of a quasimetallic sodium compound during the plateau region turned out to be similar to that of bulk sodium, underlining the chemical similarity of the two species.

4.2.2. Data acquisition and processing

A solid basis of impedance data is the foundation for a reliable DRT analysis and further mechanistic conclusions and the acquisition procedure has a significant impact on the outcome of the measurements. Particularly, the absence of a direct current flow or voltage drift is important, i.e. the system must be in a chemical equilibrium during the EIS measurement. This also implies, that the amplitude of sinusoidal voltage excitation must be small enough to fulfill this criterion. In the context of this work, where a short current pulse is applied between each EIS measurement, the resting period between galvanostatic step and EIS acquisition is of crucial importance. In order to determine the optimal test conditions in terms of duration of currrent and OCV steps with respect to data linearity and reasonable experiment time, a first test run was carried out using a current pulse of 18.6 mA g^{-1} for 1 h, followed by a resting step at OCV for 3 h. In figure 4.9a), the voltage profile of one current/rest sequence is shown, and clearly, the system is driven too far out of equilibrium as can be seen by the voltage being not stabilized after the OCV period. Applying the same current density for only 10 min and allowing the system to equilibrate for 5 h, this problem can be solved. In the Nyquist plots presented in figure 4.9c) and d), the two cells also show different behaviours with higher polarization resistances in the former setup. Kramers-Kronig relationships contain information about the linearity of a measurement and basically test how well the imaginary part of the EIS data can be reproduced by the real part and vice versa.[255–258] The residual of the Kramers-Kronig transformation is low in both cases in the frequency range up to 1 mHz and obviously deviates during the, likely diffusion-driven,

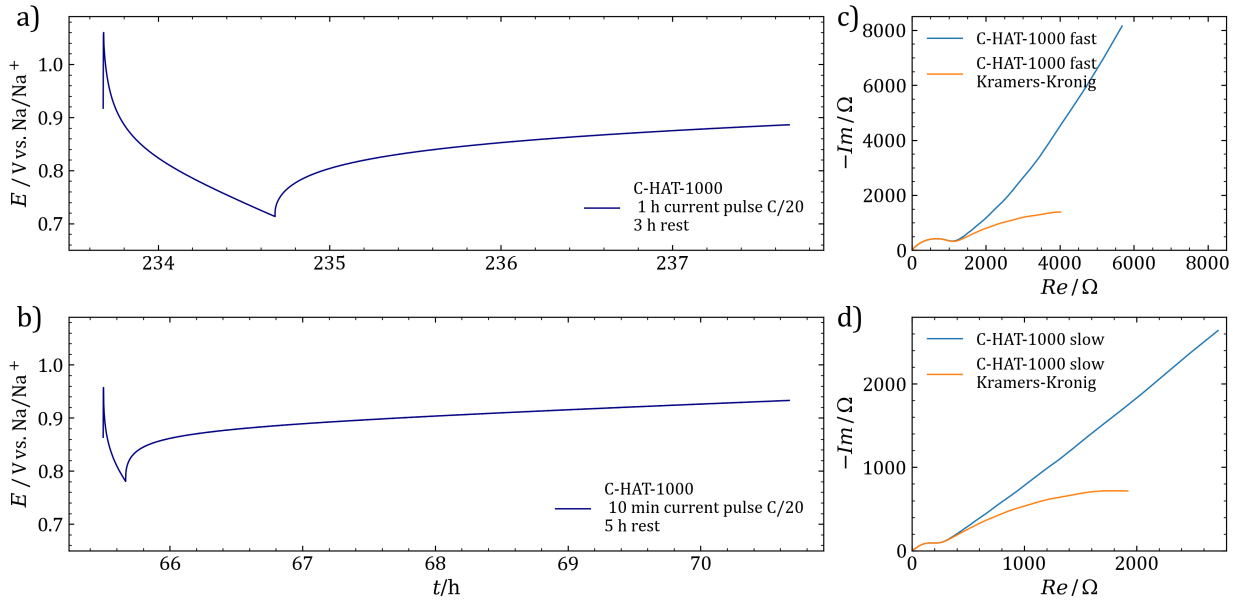

Figure 4.9.: a), b) Impact of duration of current application and resting phase on the measured EIS data on C-HAT-1000. c), d) Complex-plane plots of exemplary impedance spectra measured after one current/rest sequence with Kramers-Kronig fits.

low-frequency part of the spectra. The approach to this problem will be discussed during the treatment of data processing methods. Therefore it was decided to use the latter experimental protocol, as an extension of the equilibration time would be practically not feasible, because measuring the full sodiation plot would already now take up to one month. Also, for the further discussion, data obtained on C-HAT-1600 were chosen, as it not only shows the most distinct transitions from the charge-storage mechanisms into each other, as seen in the charge-discharge experiment, but also the sodium storage portion below 0 V can be best investigated on this material.

The basic steps of DRT data processing were already briefly introduced in the introduction section 2.4.1 and follow the method of Hahn et al.[213] The data analysis was carried out together with Dr. Tim Tichter and Jonathan Schneider. In order to set up the matrix $\boldsymbol{K}$ from equation 2.16, the resolution-enhancement factor a in equation 2.17 was set to $a = 10$, as this was a reasonable trade-off between the DRT resolution and computational time. The time constant vector was constructed from equally distributed values with logarithmic spacing between the minimum and maximum time constants τ_{min} and τ_{max}, according to

equation 4.1.

$$\begin{aligned} \tau_{min} &= 10^{\left\lfloor \left(\log_{10}\left(\frac{1}{f_{\max}}\right)\right)-b \right\rfloor} s \\ \tau_{max} &= 10^{\left\lceil \left(\log_{10}\left(\frac{1}{f_{\min}}\right)\right)+b \right\rceil} s; b = 0, 1, 2, ... \end{aligned} \tag{4.1}$$

The parameter b is used to expand the time domain outside the range of frequencies covered by the experiment, which is necessary to improve the fit at the boundaries of the measured impedance data. For this work, the parameter was chosen as $b = 3$.
Having set up the kernel matrix $\boldsymbol{K}$ and chosen the time constant domains, the DRT is calculated by solving equation 2.16 for γ.

$$\min \left\{ ||\boldsymbol{K}\gamma - z||^2 \right\} \tag{4.2}$$

This is a mathematically ill-posed problem in the definition of Hadamard, meaning that if a solution to it exists, it may be not unique or distorted by strong oscillations. Among several solutions for this problem,[250,259–262] Tikhonov regularization has proven useful in a number of publications and was applied in this work as well.[213,263–265] In this method, basically non-negative values are added at matrix positions where otherwise singularities would occur in the logarithm. Equation 4.2 is expanded by a regularization matrix $\boldsymbol{M}$ and a regularization parameter λ, as shown in equation 4.3. In this case, the identity matrix was used for regularization $\boldsymbol{M} = \boldsymbol{I}$.

$$\min \left\{ ||\boldsymbol{K}\gamma - z||^2 + \lambda ||\boldsymbol{M}||^2 \right\} \tag{4.3}$$

A non-negative least square (NNLS) solver was used, as negative values in the impedance data are physically not reasonable and not expected, which leads to some consequences on the further proceeding. First of all, inductive contributions will not be considered by the DRT, which is not a problem as no inductivity was found in the measured data. Next, the kernel matrix $\boldsymbol{K}$ must be rearranged according to equation 4.4, as complex values cannot be handled by the NNLS solver.

$$\begin{gathered} \min \left\{ ||\boldsymbol{K^*}\gamma - z^*||^2 \right\} \\ \text{with } \boldsymbol{K^*} = \Re(\boldsymbol{K}) \text{ and } z^* = \Re(z) \\ \text{and } \boldsymbol{K^*} = \Im(\boldsymbol{K}) \text{ and } z^* = \Im(z) \end{gathered} \tag{4.4}$$

Single DRTs are calculated here for the real and for the imaginary part of the impedance data, respectively. In the case of ideal, time invariant data, which obey the Kramers-Kronig

contitions over the full range of measured frequencies, it would be justified to use only one part of the spectrum. In the case of experimental data that suffer from non-linearity, as it is the case for the low-frequency part of the data being analyzed here, all available information should be used. This is done by combining the real and imaginary parts in the following matrix notation 4.5.

$$\boldsymbol{K}^* = \begin{bmatrix} \Re(\boldsymbol{K}) \\ \Im(\boldsymbol{K}) \end{bmatrix} \tag{4.5}$$

And:

$$\boldsymbol{K}^* = \begin{bmatrix} \Re(z) \\ \Im(z) \end{bmatrix} \tag{4.6}$$

The data is finally rearranged into a shape suitable for the NNLS solver in the following way 4.7, to calculate the DRT from combined real and imaginary data.

$$\min \left\{ \left|\left| \begin{bmatrix} \boldsymbol{K} \\ \lambda I \end{bmatrix} \gamma - \begin{bmatrix} z^* \\ 0 \end{bmatrix} \right|\right|^2 \right\} \equiv \min ||\boldsymbol{K}^*\gamma - z^+||^2 + \lambda||\boldsymbol{I}\gamma||^2 \tag{4.7}$$

After having set up the regularization problem, one last step remains, which is the definition of the regularization parameter λ. In equation 4.3, the first term evaluates the deviation of the fit from the experimental data, while the second expression describes the oscillations of the regression and smooths it by the amount determined by regularization parameter λ, which serves as a weighting factor.[266] A small parameter allows large oscillations and therefore may cause the appearance of artefacts, while a too high λ may smooth out too many data, leading to a loss of information. The ideal regularization parameter was determined by the method of Schlüter et al.[266] for every tenth impedance spectrum and a common parameter suitable for all spectra was found to be $\lambda = 0.1$.

4.2.3. Investigation of the sodiation process

With the data acquisition and reduction approach adapted to the present system, C-HAT-1600 was employed as the working electrode in a SIB-half cell and electrochemical impedance spectra were sampled along the entire sodiation and desodiation curve of the material. The sodiation curve and EIS data of significant regions are shown in figure 4.10 together with the DRT analysis of each of the spectra. The abscissa is plotted in a time domain in order to account for the relaxation steps. In the sodiation curve, four significantly different regions

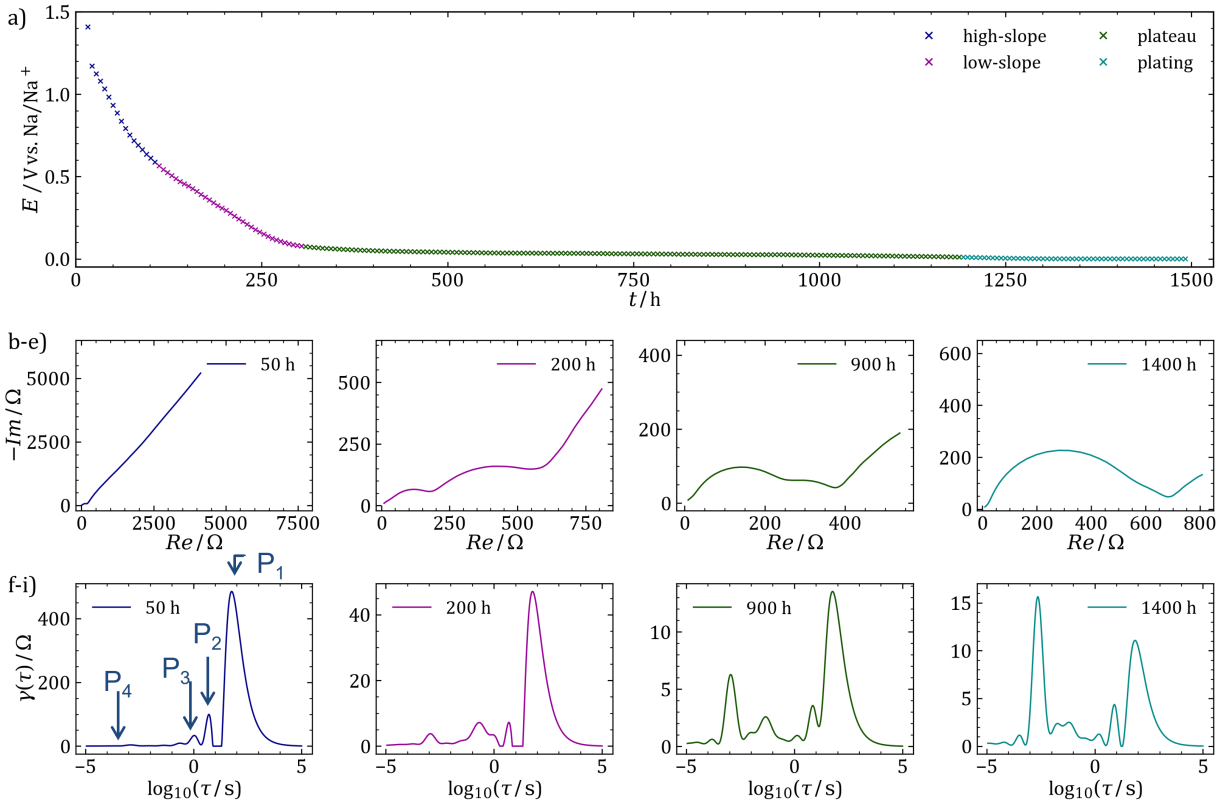

Figure 4.10.: a) Steady state sodiation profile of C-HAT-1600. Regions are color-coded with respect to the previously defined nomenclature: I) high slope, dark blue, II) low slope, purple, III) plateau, green, IV) sodium plating, cyan. b-e) Exemplary electrochemical impedance spectra at each defined sodiation stage, f-i) DRT plots corresponding to b-e).

can be recognized, namely a region with a higher slope ($0 - 100$ h, highlighted in blue), one with a lower slope ($100 - 300$ h, purple), a plateau region ($300 - 1200$ h, green), and finally a section at a constant voltage of approximately 0 V ($t > 1200$ h, cyan). Qualitatively, the impedance spectra of measurements above 0 V, presented in figure 4.10b-e), are all characterized by a semicircle with a diameter of approximately 20 Ω in diameter on the real axis. A second semicircle with a diameter decreasing at higher degrees of sodiation occurs in measurements recorded after 50 h well until the end of the sodiation plateau. The DRTs at each of the discussed SOCs are shown in figure 4.10f-i). If the fitting parameters are properly set, as it was done in preliminary experiments, every peak corresponds to an R|C element with a maximum at its characteristic time constant τ. Taking into account all other available information, it can be therefore attributed to an electrochemical polarization process. The height of $\gamma(\tau)$ can be interpreted as the contribution of the respective process to the total cell impedance at a given SOC. A most noticeable feature in all, but especially

in the spectra recorded during the sloping phase, is the ascending in the Nyquist-plots at low frequencies. This suggests the presence of diffusion processes, which seem to play an essential role in the sodiation process of C-HAT-1600 in particular, but likely also in other hard carbons. As this portion of the impedance spectrum can hardly be fitted with an R|C element, which is the basis of DRT analysis, the interpretation of such contributions will be particularly complicated. Schmidt et al.[251] presented a solution for a similar problem, which they encountered studying an LFP cathode, by modelling the low-frequency part of the EIS data with a finite-length Warburg element in series with a capacitive element and substracting this modeled data from the experimental EIS. Thereby, the authors were able to perform DRT on their data and study the electrode kinetics isolated from other influences. This is an elegant solution and definitely preferable, if it is a priori known that the mechanisms behind the EIS feature can indeed be modeled by a certain element. However, in the case of sodium storage in hard carbons, where the processes and structures involved are diffuse and not finally understood, the modeling approach should contain as little assumptions as possible in order to build an understanding based on the unbiased results. Therefore, in this work the raw impedance data was used in a first instance and subsequently the insights obtained from DRT are assigned to electrochemical processes in the cell, in order to propose a mechanism, which is built upon the results obtained, including literature knowledge on the electrode kinetics. Finally, a model is formulated, allowing the reproduction of the experimental data and the trends observed therein.

In the DRT of the impedance spectrum at the first, steeper sloping region, the main contribution to cell impedance arises due to a process denoted as P_1 with a time constant as slow as $\tau = 19$ s, as it was already expected from the qualitative analysis of the Nyquist plots. Considering the slow time constant as well as the non-closing shape of the low-frequency branch in the Nyquist plot, this process is assigned to diffusive mass transfer, presumably involving the transport of sodium ions through the SEI layer towards their respective binding sites. Two further processes, P_2 and P_3, are present in the DRTs throughout the entire SOC range, at $\tau = 2$ s and $\tau = 0.6$ s. It is reasonable to assume that at least one of the peaks is again related to sodium-ion diffusion, yet, due to the faster time constant and lower peak size, adding a lower resistance and capacitance to the cell, it probably occurs at a higher rate, presumably through the carbon material, after having passed the SEI layer. Another process, P_4 is identified at $\tau = 10^{-3}$ s. Its relative contribution to the cell impedance occurs constantly during the entire sodiation process, contrary to P_1- P_3, which show a decreasing impact on the cell impedance. Additionally considering its fast time constant, this process is assigned to the electron transfer at metallic interfaces, be it the counter electrode or Na^0

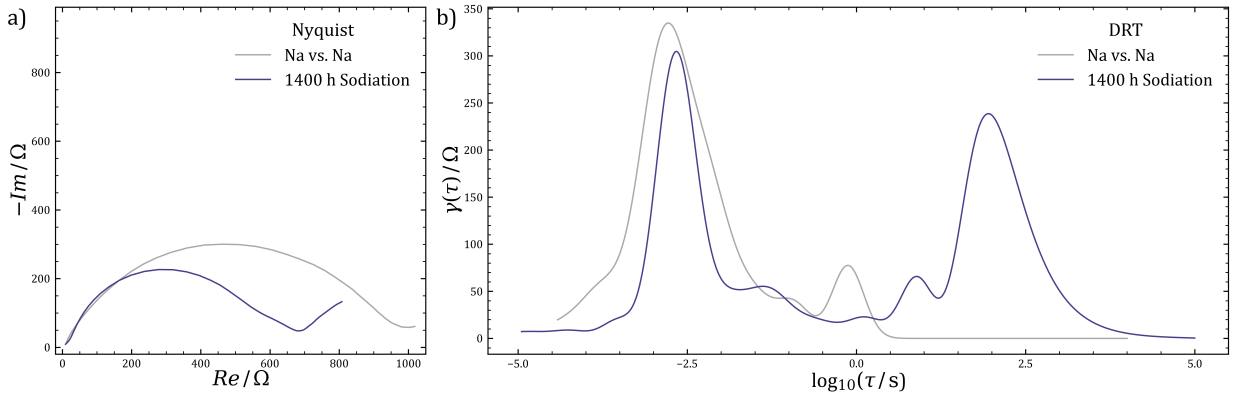

Figure 4.11.: a) Nyquist plot and b) DRT representation of the impedance of a symmetrical Na/Na cell. Data of C-HAT-1600 at 1400 h are shown for comparison.

species formed during sodiation in situ. This interpretation makes it possible to explain the doubling of the height of signal P_4 observed after 1250 h, as it occurs concomitantly with the onset of sodium plating and hence indicates the formation of metallic sodium patches on the working electrode surface, causing the process of metallic sodium deposition/dissolution to occur on both electrodes with double the impedance, consequently.

As in a two-electrode setup the total cell impedance originating from both the working and counter electrodes is measured, it is possible to assign DRT signals to electrochemical processes by comparing the half cell results with results from symmetrical Na/Na cells. It was refrained from measuring carbon/carbon cells, as this not only requires the presodiation of two C-HAT-1600 electrodes, but also introduces SOC dependent effects which would have to be studied extensively rather then provide valuable information. The resulting complex-plane plot is shown in figure 4.11 together with the DRT representation of the impedance data. Essentially, a single semi-circle is measured in the Na/Na cell and its DRT transforms into one major peak at a time constant of $\tau = 10^{-3}$ s, whereas in the C-HAT-1600/Na half cell the semicircle is accompanied by a linear tail at low-frequencies, corresponding to a time constant of $\tau = 1$ s, which is due to diffusion effects. It is therefore proven by this experiment that process P_4 indeed represents the deposition/dissolution of sodium at a metal/electrolyte interface and that the remaining peaks must be associated with effects due to the interaction of sodium and hard carbon. The remaining peaks will be assigned by monitoring the evolution of the DRT over several SOCs in a relatively high capacity-resolution. The data can be best represented and discussed in 3D waterfall plots, shown in figure 4.12b-e). The evolution of the cell's DRT over time is shown therein and it becomes clearly evident that the processes contributing to the cell impedance are highly dependent on the SOC and during

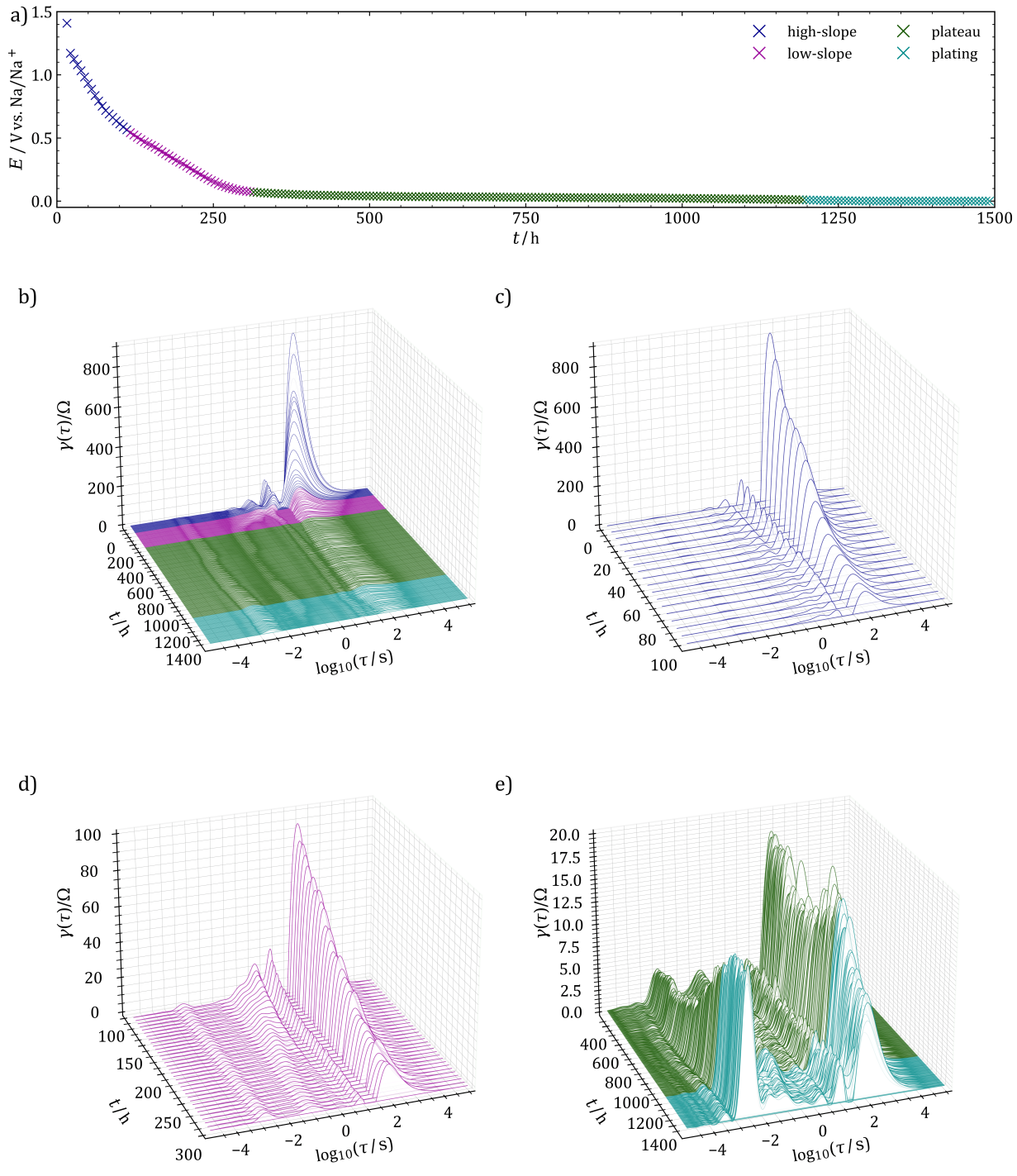

Figure 4.12.: a) Steady-state sodiation curve of C-HAT-1600. b) Waterfall plots of the DRTs during the sodiation process as a function of time. c-e) Magnified plots of the c) high-slope, d) low-slope, and e) plateau and metal plating regions.

each of the sodiation stages the DRT profile shows a characteristic shape. Therefore, the color coding introduced in figure 4.10 is adapted for the DRT-waterfall in each of the four previously defined regions of the charge-discharge curve. In the high-slope region, the main contribution to the DRT is due to the slow and pronounced processes P_1 and P_2. With increasing sodium uptake, the time constants of these peaks shift from $\tau = 19$ s and 5 s to $\tau = 16$ s and 2 s, respectively, and the peaks are reduced in height monotonously until they reach a steady state around the onset of the plateau region.
Another insightful feature resolved by DRT begins with the low-slope region and ends towards the onset of the plateau phase. While the P_1 peak continues diminishing as discussed previously, the P_2 peak begins to split in two sub-signals, one of which shows a constant relaxation time, while the other one shows a decreasing time constant. This phenomenon will be accounted for by a qualitative equivalent circuit model in a further section and can be interpreted with respect to diffusion phenomena as follows. If P_1 is indeed due to the diffusion of sodium through the SEI as it as assigned previously, then it will play a role during the entire sodiation process, as it essentially functions like a solid electrolyte and a sodium reservoir at the same time.[116] However, with increasing Na-saturation and higher electromotoric forces driving the sodium transport, the ion conductivity of the SEI will improve, hence explaining the decrease of this peak's height and its frequency shift. During the low-slope phase, the P_2 process is dominant, hence it is assigned to the storage of sodium at defective carbon sites in a one-phase solid solution-like reaction, where sodium is likely found as a cation. Furthermore, P_2 fades into the background as soon as P_3 sets in, strongly suggesting that these peaks represent the mechanisms behind sloping and plateau storage, respectively. P_3, after its occurrence at approximately 300 h, does not change substantially until the end of sodiation, neither in height nor in frequency so that it is interpreted as the electron transfer process from the defective carbon to the sodium ion, which occurs in the plateau region. The constant nature of process P_3 indicates a kinetic homogeneity of the underlying process. Considering that the diffusion related peaks did not reoccur or grow, preadsorbed sodium ions could become reduced first in this process. The plateau region therefore represents in a sense the underpotential deposition of sodium, stabilized by the surrounding carbon structure. This observation is again well in line with the common understanding of the hard carbon sodiation mechanism. Towards the end of the plateau region and the onset of bulk metal deposition, an increase in height of process P_4 can be measured, while P_3 shrinks, indicating the transition of reversible sodium storage into crystalline sodium electroplating. The detection of sodium dendrites in operating cells thereby becomes possible.

4.2.4. Investigation of the desodiation process

The desodiation was studied by the same approach with the same current density, after the cell was allowed to rest for several hours, in order to find differences and similarities to the sodiation process. In figure 4.13 the steady-state desodiation curve is shown along with characteristic impedance spectra and their DRTs, analogous to figure 4.10. Already from the duration of sodiation and desodiation at equilibrium conditions a first observation can be made regarding the reversibility and stability of the sodium structures formed inside the hard carbon. Not only the electrostripping region becomes shorter, which is not surprising, as the irreversible deposition is an intrinsic problem of electroplated metallic sodium, but also the desodiation plateau is passed through much faster for the sodium extraction than for its insertion. Unlike commonly reported charge-discharge curves, even those measured at low currents, the conduction of the experiments discussed here takes several weeks, during which the cell is held in equilibrium at nearly all SOCs, so that also potentially formed quasimetallic sodium species undergo a calendric long-term stability test. From this circumstance it is concluded that sodium species with a formal oxidation state near zero, stabilized by the hard carbon structure cannot be maintained in the cell over prolonged periods of time. Besides common self-discharge phenomena, the coalescence of small quasimetallic sodium clusters into larger metallic patches, for example by Ostwald ripening, can cause these sodium atoms to electrically disconnect from the electrode material and become unavailable for reversible energy storage. Sodium must be electrically neutral, i.e. Na^0, in order for this process to become possible. In contrast, the sloping region remains unchanged for both, forward and reverse processes, extending over 200 h. The impedance spectra for the sodium extraction process in figure 4.10b-d) are strongly resembling those observed during the insertion process, indicating that the reaction pathways are essentially the same for forward and backward reactions. This is particularly true for the mechanism during the sloping region, where the model of a negatively charged carbon framework and a cationic sodium guest species is underlined by the high reversibility of this electrochemical event. If intercalation into graphite layer interspaces was responsible for this region, it would impose strain on the material and a deterioration would be measurable alongside with a voltage hysteresis for intercalation and deintercalation. In figure 4.14, the development of the cell impedance is shown in DRT representation. Basically, the same four main peaks as in the sodiation process can be identified. The desodiation process begins with the stripping of electroplated sodium metal, dominated by process P_4, which diminishes in favor of the peak P_3, as the SOC approaches the plateau region. As after 300 h the sloping region sets in, the peaks P_1 and P_2 take over the DRT.

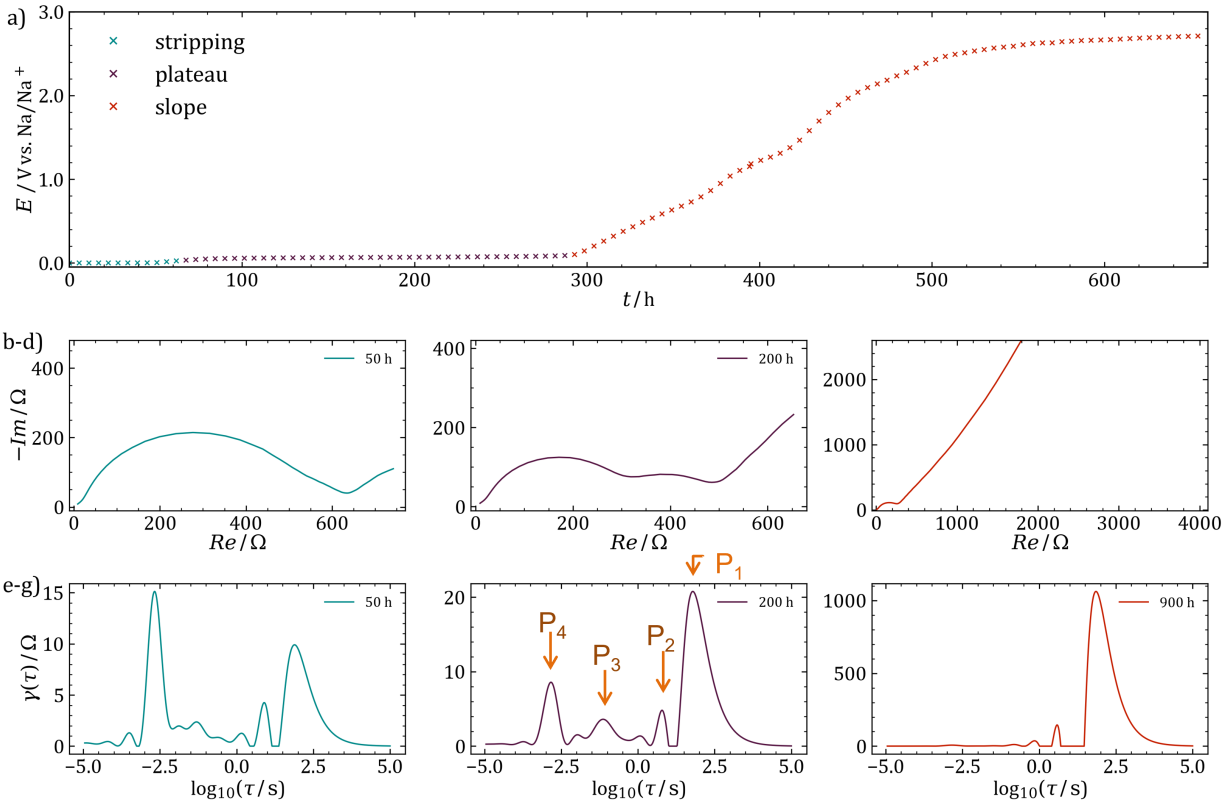

Figure 4.13.: a) Steady state desodiation profile of C-HAT-1600. Regions are color-coded as follows: I) sodium electrostripping, cyan, II) plateau, dark purple, III) slope, orange. b-d) Exemplary electrochemical impedance spectra at each defined sodiation stage, e-g) DRT plots corresponding to b-d).

A frequency shift of the two low-frequency peaks is not observed, contrary to the sodiation process.

The DRT analysis of the impedance data points out that Na diffusion through the electrolyte, SEI, as well as the carbon framework itself have a significant impact on the reaction mechanism and even constitutes the rate-determining step in the sloping region of the sodiation curve. Charge-transfer processes are even pushed into the background, indicating that the anode performance can be influenced by diffusion-relevant characteristics, such as particle size, shape, porosity and density, rather than by the chemical structure of the carbon framework itself. The importance of a well-controlled grown SEI is underlined as well, since it serves as a sodium ion reservoir for subsequents steps. The similarity of kinetics of sodiation and desodiation is pointed out by the results at hand. The method of combined EIS/DRT analysis can help to identify when the growth of a metallic sodium phase commences, which can be useful for the determination of the reversible sodium storage capacity but also for

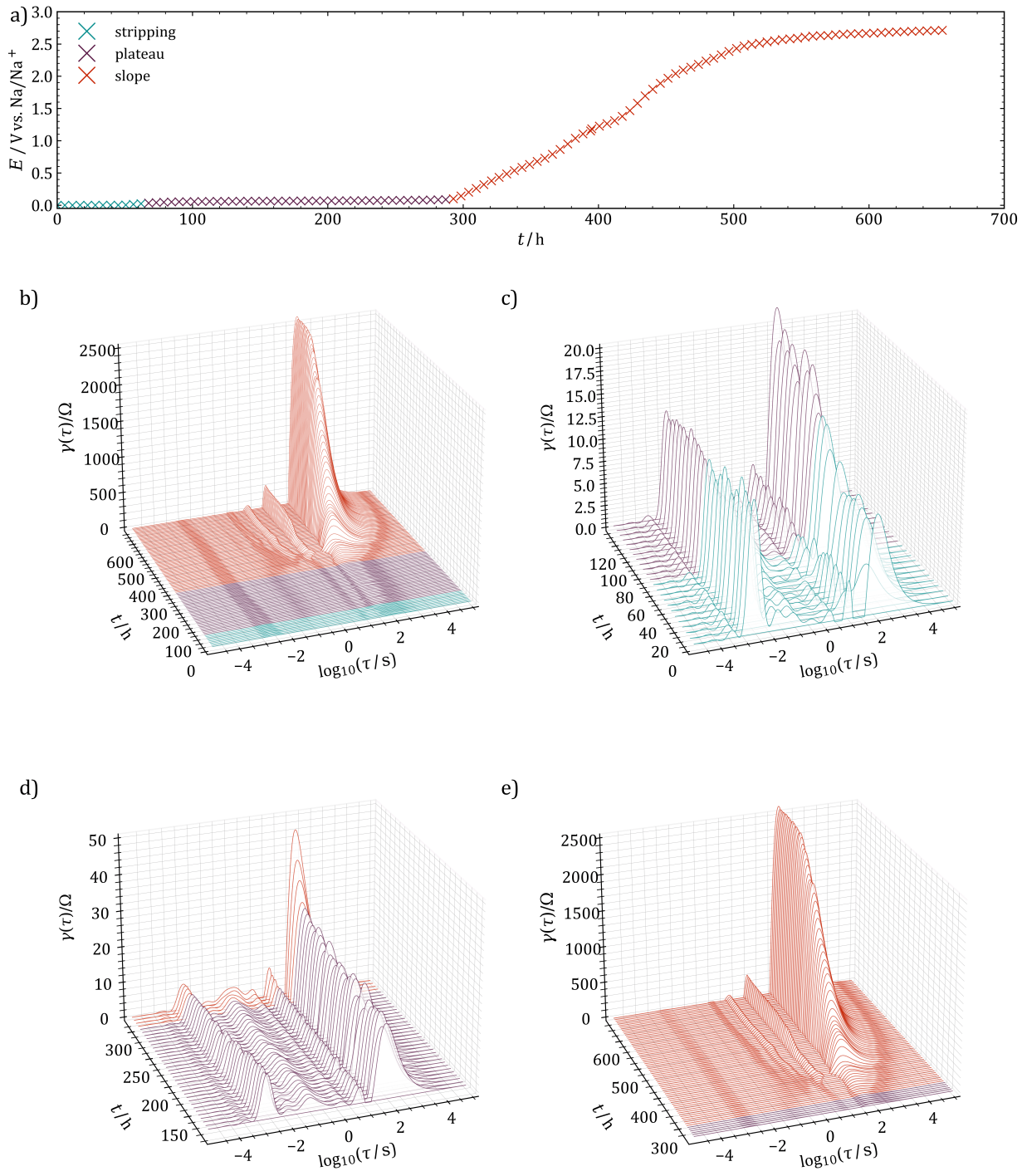

Figure 4.14.: a) Steady-state desodiation curve of C-HAT-1600. b)Waterfall plots of the DRTs during the desodiation process as a function of time. c-e) Magnified plots of the c) electrostripping, d) plateau, and e) sloping regions.

monitoring when an operating cell approaches its end of life. As no metallic sodium should be present in a functioning full cell, the detection of the characteristic sodium metal process P_4 provides a method for the destruction-free state-of-health analysis. Finally, the results are evidencing that the long-term stability of quasimetallic sodium structures may be not necessarily granted, and particularly long storage times at high states of charge are harmful for the hard carbon anode, even more than frequent cycling as was shown in the previous section. The impact of temperature and the susceptibility of different materials to underlying sodium cluster-decomposition processes must be investigated in detail.

4.2.5. Modeling upon the DRT results

In order to obtain a physically meaningful understanding about the sodiation process, the information gained from DRT must be broadcast onto a equivalent circuit model representing the single mechanistic steps. It must equally represent both the electrode kinetics as well as the mass transport phenomena involved not only on the hard carbon working but also on the sodium metal counter electrode side. The number of circuit elements required for a satisfactory fit must be kept as low es necessary, in order to prevent overfitting and to keep the model as close to the real cell as possible. The impedance data was then simulated on the basis of the proposed model, in order to be anaylzed by DRT and fitted to the DRT of experimental data. By this way the optimization of fit parameters is performed.
The equivalent circuit proposed in figure 4.15 represents one possible option to describe the sodium/hard carbon cell, fulfilling the criteria mentioned above. The sodium side is modelled by a single charge transfer resistance connected in series to a planar finite transmissive Warburg element, in order to account for the diffusion of sodium ions through the electrolyte in the separator. These two elements connected in series are in turn connected in parallel to a capacitive element, accounting for the buildup of the electrochemical double layer at the sodium metal electrode. The hard carbon side requires two series connections of a charge transfer resistance with a different Warburg element, describing the diffusion, each, as it is shown on the right hand side of the scheme depicted in figure 4.15. A capacitor connected in parallel represents the double layer forming on the carbon side. In the two series connections, the diffusion at the interface between the electrode and the electrolyte is accounted for by a planar finite transmissive Warburg element, while the diffusion of sodium ions through the carbon towards the respective storage sites is represented by a finite reflective Warburg element. The capacitor is impossible to further subdivide, as capacities in parallel generally add up to one capacity. The planar finite reflective Warburg element in principle describes

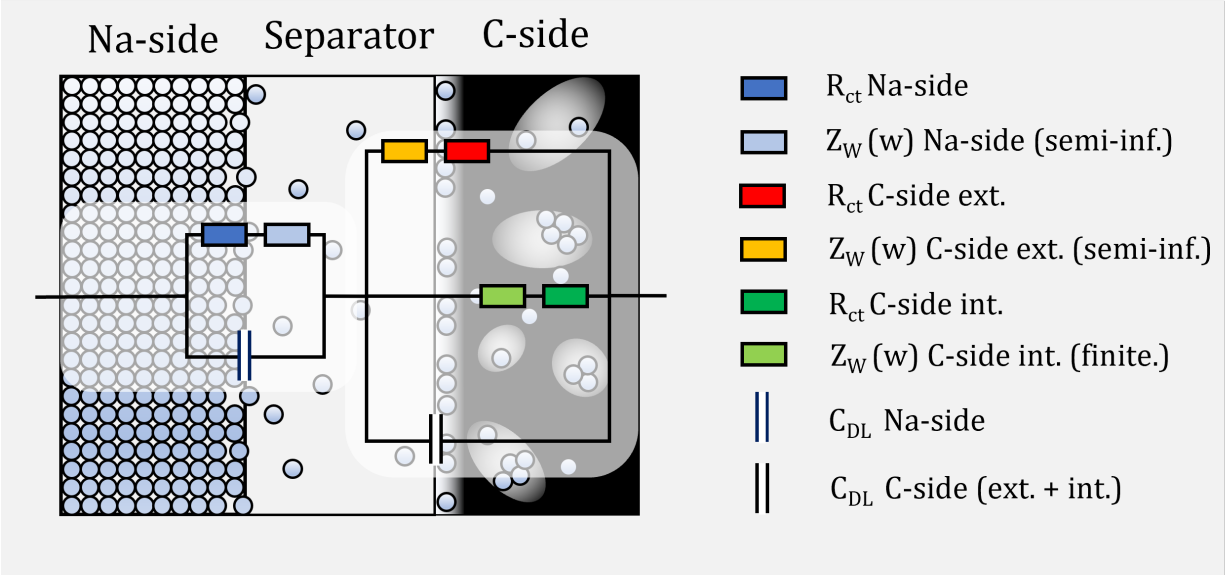

Figure 4.15.: Equivalent circuit model for the sodiation process of the C-HAT-1600/Na cell. Republished under a Creative Commons Attribution 3.0 Unported License from *Physical chemistry chemical physics*, Schutjajew et al., *23*, 11488-11500, copyright 2021.

the diffusion in a planarly confined space, such as a thin layer cell, which is not ideal for the quantitative description of a porous carbon electrode with pores of different shapes and sizes, yet it will be sufficient for a qualitative description of the mean diffusion field. Basically, the key is to account for the interrupted mass transfer within a limited diffusion domain, for which the presented Warburg element is well suited, especially if a qualitative model is sought for, as it is the case in this work. It will be shown that the kinetic and diffusion parameters required to fit the presented model to experimental data are already fairly realistic, but if one wished for a truly quantitative method, a precise picture of the pore architecture of the sodium storage-relevant inside the carbon are strictly required.
The equivalent circuit in figure 4.15 has the general impedance of Z_{tot}, as follows.

$$Z_{\mathrm{tot}} = Z_{\mathrm{Na,T}} + \frac{Z_{\mathrm{C,R}} Z_{\mathrm{C,T}}}{Z_{\mathrm{C,R}} + Z_{\mathrm{C,T}}} \tag{4.8}$$

In equation 4.8, $Z_{\mathrm{Na,T}}$ is the impedance of the sodium metal side, where T denotes the transmissive boundary, $Z_{\mathrm{C,R}}$ and $Z_{\mathrm{C,T}}$ are the impedances of the carbon side, including again a transmissive or reflective Warburg element, with indices T or R, respectively. With the faradaic resistances defined as a combination of a Warburg and a charge-transfer resistance, the individual impedances $Z_{k,l}$ (with $k, l = \mathrm{C,R;C,T;Na,T}$) can be rewritten as in equation 4.9

$$Z_{k,l} = R_{\mathrm{sol}} + \frac{1}{\frac{1}{Z_{\mathrm{Far},k,l}} + \mathrm{j}\omega C_k} \tag{4.9}$$

Here, R_{sol} is the Ohmic resistance of the entire system, C_k is its capacity and $Z_{\mathrm{Far},k,l}$ is the faradaic impedance of the respective component k. The transmissive elements are defined as in equation 4.10 and the reflective elements as in equation 4.11.

$$\begin{aligned} Z_{\mathrm{Far},k,l=\mathrm{T}} =& \frac{RT}{An^2F^2}\left(\frac{1}{\alpha}k_{\mathrm{f}}c_{\mathrm{r}} + (1-\alpha)k_{\mathrm{b}}c_{\mathrm{o}}\right) \\ &\times\left\{1 + \frac{1}{\sqrt{\mathrm{j}\omega D}}\left[k_{\mathrm{f}}\tanh\left(d\sqrt{\frac{\mathrm{j}\omega}{D}}\right) + k_{\mathrm{b}}\tanh\left(d\sqrt{\frac{\mathrm{j}\omega}{D}}\right)\right]\right\} \end{aligned} \tag{4.10}$$

$$\begin{aligned} Z_{\mathrm{Far},k,l=\mathrm{R}} =& \frac{RT}{An^2F^2}\left(\frac{1}{\alpha}k_{\mathrm{f}}c_{\mathrm{r}} + (1-\alpha)k_{\mathrm{b}}c_{\mathrm{o}}\right) \\ &\times\left\{1 + \frac{1}{\sqrt{\mathrm{j}\omega D}}\left[k_{\mathrm{f}}\coth\left(d\sqrt{\frac{\mathrm{j}\omega}{D}}\right) + k_{\mathrm{b}}\coth\left(d\sqrt{\frac{\mathrm{j}\omega}{D}}\right)\right]\right\} \end{aligned} \tag{4.11}$$

In equations 4.10 and 4.11, $\tanh(x)$ and $\coth(x)$ are the hyperbolic tangent and cotangent functions, α is the electron transfer coefficient, D is the diffusion coefficient of the electroactive species in either the electrolyte or the carbon matrix, d is the diffusion domain size, A the total electrode area, c_{r} and c_{o} are the concentrations of reduced and oxidized species, respectively, and finally k_{f} and k_{b} are the potential dependent forward and reverse reaction rate constants according to the Butler-Volmer equation, defined in equations 4.12 and 4.13.

$$k_{\mathrm{f}} = k^0 \exp\left(\frac{\alpha n F R^{\mathrm{eq}} - E^0}{RT}\right) \tag{4.12}$$

$$k_{\mathrm{b}} = k^0 \exp\left(\frac{-(1-\alpha) n F R^{\mathrm{eq}} - E^0}{RT}\right) \tag{4.13}$$

In equations 4.12 and 4.13, k^0 is the standard rate constant in units of $[k^0] = \mathrm{cm\ s^{-1}}$, n is the number of transferred electrons, while F, R, T are the respective natural constants.
Based on equations 4.8-4.13, impedance data can be simulated, carefully chosing the parameters required in mentioned formulae. Assuming physical constants from known data, spectra were calculated and the parameters were optimized iteratively by calculating DRTs of simulated data and adjusting to experimental data. The parameters obtained by this method are presented in the appendix, table A.1. The comparison of simulated DRT plots with fits of experimental data is presented in figure 4.16. The simulation fits the experimental results well, in terms of number, frequency, and height of the peaks. Furthermore,

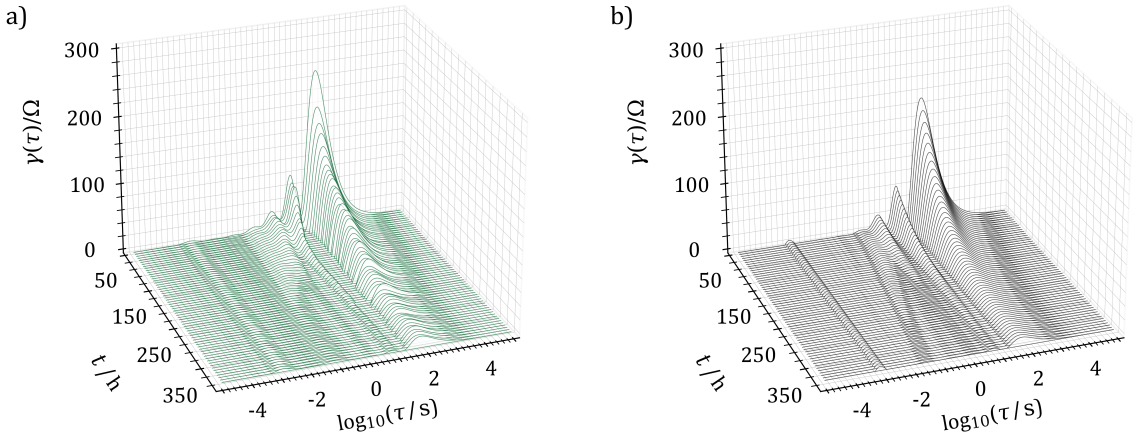

Figure 4.16.: Waterfall plots of a) experimental and b) simulated DRT data calculated between 50 h and 350 h.

it captures the shift of the signals in the time constant region around $\tau = 10$ s well, allowing an interpretation of the data regarding the sodium storage process. At the beginning of the sodiation process, where only low amounts of sodium are present inside the carbon, the faradaic impedance due to both diffusion and charge transfer processes on the carbon electrode provide overwhelming contributions to the overall impedance due to the low concentration of electroactive species within the carbon framework. As more sodium is inserted into the carbon host, likely first filling the SEI, the resistance due to this diffusion driven process occuring at low frequencies decreases progressively. Additionally, the electrode potential approaches the equilibrium reduction potential of Na/Na^+, E^0, already causing a significant change in the resulting resistance, as the potential is exponentially related to the resistance as it is shown in equations 4.10-4.13. With the increasing degree of sodiation, the carbon becomes successively occupied by sodium, after the SEI saturation is established. In order to explain the linearly changing potential of the electrode during the eponymous sloping region, it must be considered that the potential E^0 of the system responds to the degree of sodiation, whereas the Nernstian description appears insufficient, as it yields an a) too small potential drift with the present composition change, and b) this potential ramp is rather logarithmic in nature. The assumption of a composition dependent electrode potential is reasonable, if the sodiation process is considered as a non-equilibrium one-phase phase transition, with a distinct E^0 associated with each Na/C ratio. Thereby, a linear voltage decay can be achieved in the simulations. However, as a rather major deviation from the assumptions, it must be stated that in order to reproduce the experimental frequency shift of

the peak, a sodium concentration inside the carbon about three orders of magnitude smaller than that calculated from Faraday's second law must be assumed. If this result is accurate, it indicates that not all of the reversibly stored sodium is participating in the formation of a Na/C solid solution and other mechanisms must be considered to account for the full sodiation curve, especially towards the end of the sloping voltage region.
The experimentally measured splitting of the $\tau = 10$ s peak and its frequency shift could also be reproduced by this model, by introducing the parallel connection of reflective and transmissive Warburg elements on the carbon side. Both elements will show the same kinetics regarding the charge transfer process, while their diffusive contributions will behave inherently different. The increasing degree of sodiation drives the potential closer to E^0, which causes both resistances to decrease and the resulting DRT to decay. In the model, as soon as the reflective diffusion part starts to limit the reaction, it will proceed increasingly via the transmissive branch, which is the point at which peak splitting sets in. With a higher SOC, the E^0 of the working electrode approaches that of Na/Na^+, causing also the reflective branch on the carbon side to strive towards the remaining transmissive side on the sodium side, which explains the frequency shift. Also, from this results it follows that the modelling of the plateau region would require the invocation of another equivalent circuit with different processes involved or at least the extension of the present one, as driving this model further and further would simply result in a convergence at the symmetrical Na/Na cell.

4.2.6. Conclusion

In this section, EIS combined with DRT analysis was established as a highly insightful method for the investigation of hard carbon anodes in SIBs. Impedance spectra were acquired during several SOCs and the amount and relative contributions of the involved processes were extracted, revealing that sodiation and desodiation essentially proceed via the same pathway. Diffusion was found to be a major contribution to cell impedance and a rate-determining process, especially during sloping regions, suggesting tuning of the particle and pore geometry as key approaches for the optimization of electrode performance. The onset of metallic sodium plating could be followed by this method, rendering it viable for operando state of health monitoring. By using the generated insights to set up a representative equivalent circuit, experimental data during the sloping phase could be qualitatively reproduced, allowing conclusions on the mechanistic origins of sloping and plateau phases. With a more precise view on the carbon structure, the diffusion domains could be possibly modelled more precisely, allowing a quantitative derivation of physicochemical parameters.

4.3. Preparation of hard carbon/carbon nitride nanocomposites to reveal the impact of open and closed porosity on sodium storage

4.3.1. Motivation

Extensive parts of this section were published in the article Schutjajew et al., *Carbon* **2021** *185*, 697-708.[267] So far, efforts have been undertaken to extend the knowledge on sodium storage, by observing trends in homologous carbon materials and developing methods for the investigation of energy storage kinetics. In this section, a synthetic method towards closed-porous materials as well as an extension of the established capacity limited charge-discharge protocol will be introduced and discussed in detail.

The preparation of non-graphitizing carbons with abundant closed pores generally is subject to chance and usually is accomplished by treating precursors at different pyrolysis temperatures, in order to optimize the charge storage characteristics.[14,52,197] This is of course related to the projected application of SIBs as large-scale, sustainable means of energy storage, but also to the inherent difficulty in obtaining, but also analyzing closed porous materials and proving the presence of such structures. Hence, only few articles where published on the directed synthesis of internally porous materials, to the best of the author's knowledge.[244,268,269] In principle, two methods for the synthesis of such materials can be thought of. The first one is to select a precursor or a set of precursors, templates, or porogens in a way that the product develops the desired porosity, while the second approach is to deposit a coating layer on a regular, open porous material in a post-synthetic step. The latter method potentially requires more synthetic effort but offers the opportunity to precisely control the pore size, geometry, and volume of the open porous precursor, e.g. by gas sorption methods, and compare its sodium storage capabilities with its closed porous analogue. Also, the bonding pattern between the carbons within the framework could be tuned independently of the coating layer. The ideal coating layer shares properties with an artificial SEI layer, i.e. it should be permeable for sodium ions, but not for other electrolyte constituents, such as anions, solvent molecules, and additives, be electrically insulating but at the same time conduct sodium ions well. Electrical insulation is useful in order to prevent the decomposition of electrolyte and support the formation of a mechanically and electrically stable SEI, however is not a necessary criterion for a coating agent. Polymeric carbon nitride (p-C_3N_4) is well suited for this purpose due to its thermal and chemical stability,

mechanical flexibility and durability, and tunable electrical and ionic conductivity.[270,271] A particularly favorable method to coat p-C_3N_4 on different materials, is based on chemical vapor deposition with melamine as starting material, as reported e.g. by Giusto et al.[272,273] This approach results in particularly thin and homogeneous layers on planar supports, while porous materials were not investigated yet, despite its prospect for the production of closed porous carbon materials. The aim of this work was therefore, to explore the CVD process mentioned above for the deposition of p-C_3N_4 on a porous substrate, to optimize the experimental conditions to guarantee a homogeneous result, and finally to achieve the transformation of open porous into closed porous hard carbon materials. For that, it is crucial to investigate the deposition mode, i.e. whether the p-C_3N_4 deposition occured in a layer above the pores, within the pores, or if the pores were completely filled out with p-C_3N_4 at all, which was carried out by a combined application of gas sorption and SAXS techniques.

4.3.2. Preparation and structural characterization of hard carbon/carbon nitride nanocomposites

The carbon substrates selected for the investigation in this work were carbon cloths in different degrees of chemical activation and hence different average pore sizes and diameters.[274] The carbon cloths are manufactured from phenol-formaldehyde resins, which are polymerized, spun, and subsequently woven, before being finally subjected to a high-temperature treatment, not further stated by the manufacturer, but probably higher than 1600°C, as after an additional heat treatment in the laboratory furnace at this temperature caused neither a mass loss, nor a change in sodium storage characteristics. Afterwards they are activated in a CO_2 or H_2O activation process until the desired porosity is reached.[274] These resins are cross-linked and therefore thermosetting polymers, rendering them suitable hard carbon precursors.[14] For this work, cloth types of different porosities were selected, namely the unactivated model CC-5092, moderately activated ACC10-5092, and finally the highly activated ACC20-5092, which will be referred to by the first part of their title (CC, ACC-10, ACC-20) throughout the rest of this work.

While chemical activation offers only very limited options for tuning the porosity and essentially only yields micropores of slightly different diameters and volumes, the free-standing property of the selected cloths was the crucial factor for their appearance in this study, as in the present stationary CVD oven a powder could not be coated homogeneously from all directions, while placing a sheet of carbon upright in the stream resulted in the desired result, as can be seen in N_2 sorption isotherms at 77 K in figure 4.17a). There, about 150 mg of a

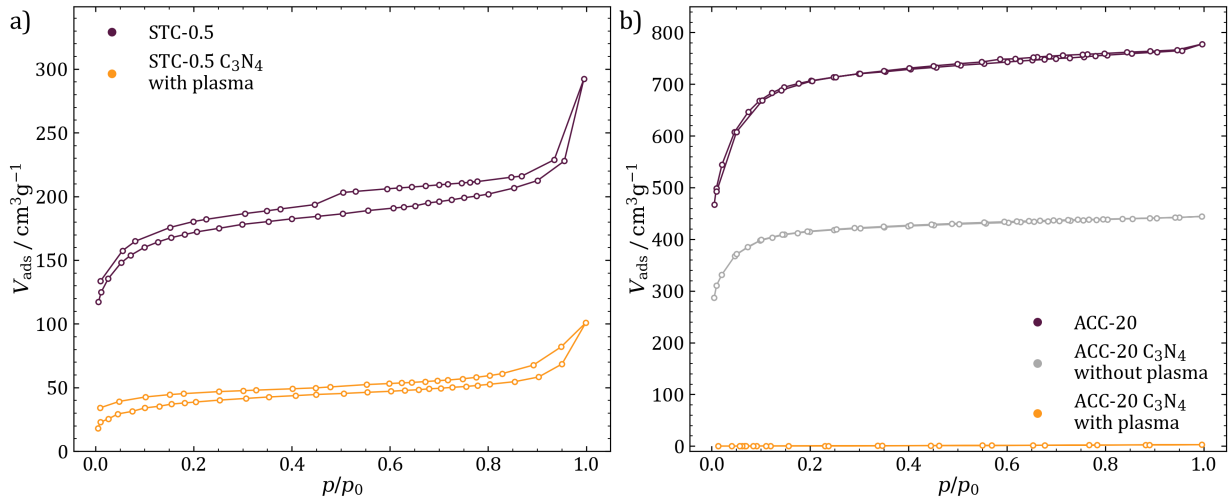

Figure 4.17.: Isotherms of intermediate materials during the optimization of process conditions. a) Microporous hard carbon powder before and after CVD and plasma etching. b) Kynol ACC-20 before and after CVD with and without prior plasma etching.

plasma-pretreated microporous hard carbon powder was placed on a flat, shallow porcelain crucible in the CVD oven, spread out to a thin layer and even though a substantial reduction of adsorbed gas volume and SSA from 830 m^2 g^{-1} to 180 m^2 g^{-1} was achieved, the pores could apparently not be closed completely. On the other hand, the impact and the importance of plasma etching is demonstrated in figure 4.17b), where N_2 sorption isotherms at 77 K are shown for an untreated ACC-20, and two p-C_3N_4 coated samples are shown, one with and one without plasma pretreatment, respectively. Evidently, only after the carbon surface was etched and made reactive towards the CVD gas stream, the full extent of the pore structure was available for p-C_3N_4 deposition. The surface area develops from over 3000 m^2 g^{-1} for ACC-20 to still 2000 m^2 g^{-1} in the p-C_3N_4 composite without plasma etching, to less than 20 m^2 g^{-1} in the plasma etched and CVD treated sample. Therefore, the preparation of the carbon surface became a mandatory step in the synthesis of carbon/p-C_3N_4 nanocomposites, where the conditions of etching were selected in a way that the nanostructure of the carbon was not altered by burning off the carbon skeleton.[275]

First insights on the elemental composition and thereby the amount of deposited p-C_3N_4 can be obtained from thermogravimetric analysis (TGA) under both N_2 and synthetic air atmospheres, shown in figure 4.18. Under N_2 atmosphere, only a minor mass loss below 5 % is observed for untreated as well as plasma-etched samples below 1000°C, while p-C_3N_4 nanocomposites show two distinct mass loss processes, one below 100°C and one at 550°C. The former is clearly associated with the evaporation of asorbed gasses and water, while the

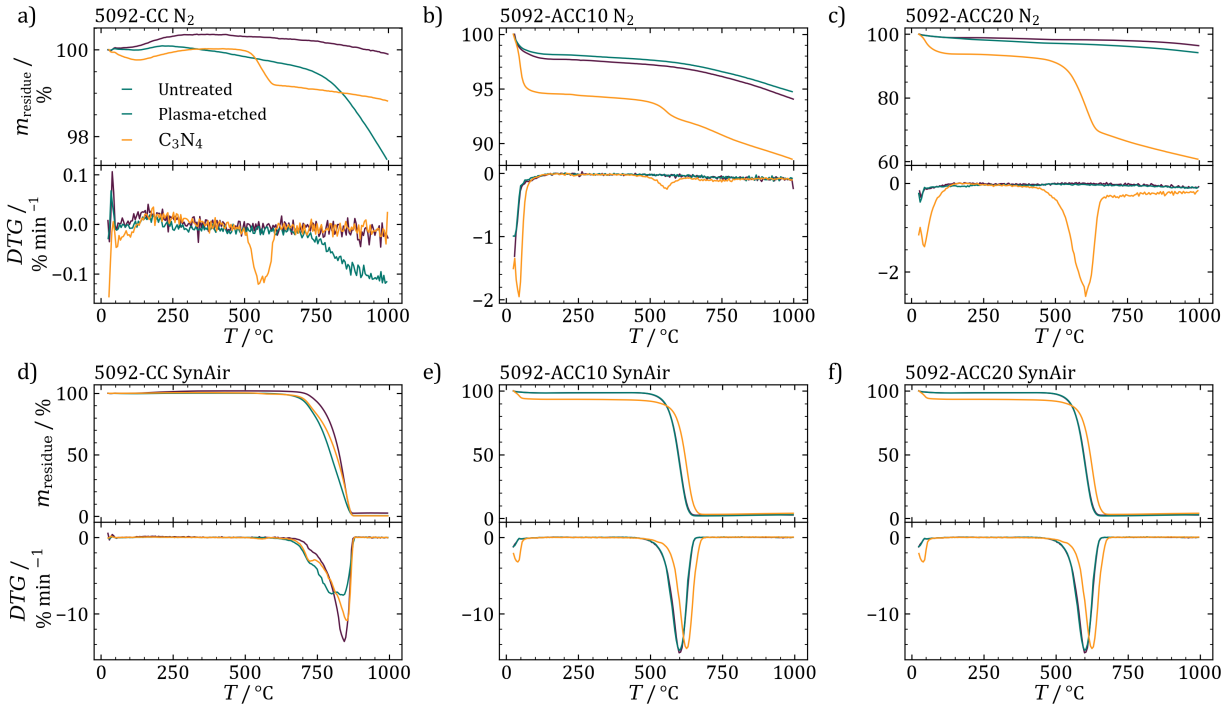

Figure 4.18.: TGAs of carbon materials and their nanocomposites under a-c) N_2 and d-f) synthetic air. Upper panels show the relative residual mass loss, lower panels show the differential mass loss.

latter peak is due to the onset of thermal decomposition of p-C_3N_4, where Kynol CC-C_3N_4 loses about 1 %, ACC-10-C_3N_4 2 %, and ACC-20-C_3N_4 25 % of their initial masses. However, the thermal decomposition of p-C_3N_4 is not finished at 550°C, but rather continues an equilibrium reaction with different gaseous intermediates until higher temperatures, which is manifested in a constant decline in mass at temperatures up to 1000°C. Together with the elemental analysis results, presented in table A.2, the mass loss at 1000°C can serve as a convenient indicator for the gravimetric amount of p-C_3N_4 deposited, considering that nitrogen constitutes 39 wt.% of the formula weight of ideal C_3N_4. For ACC-20, 20.95 wt.% of nitrogen are found from EA, which corresponds to 34.92 wt.% of ideal carbon nitride. This is less than the mass loss observed at 1000°C, but can be explained by the fact that p-C_3N_4 usually does not reach the ideal formula, but rather an excess of carbon is found. Thereby, the results from thermal analysis are in good accord with each other. TGA under synthetic air atmosphere reveals one main combustion peak for all of the investigated samples, with the difference that the DTG mass loss peak occurs shifted to higher temperatures by about 50°C in p-C_3N_4 coated samples. The absence of a second peak for the p-C_3N_4 phase and the identical FWHM of the signal indicates the homogenous composite structure of the prepared

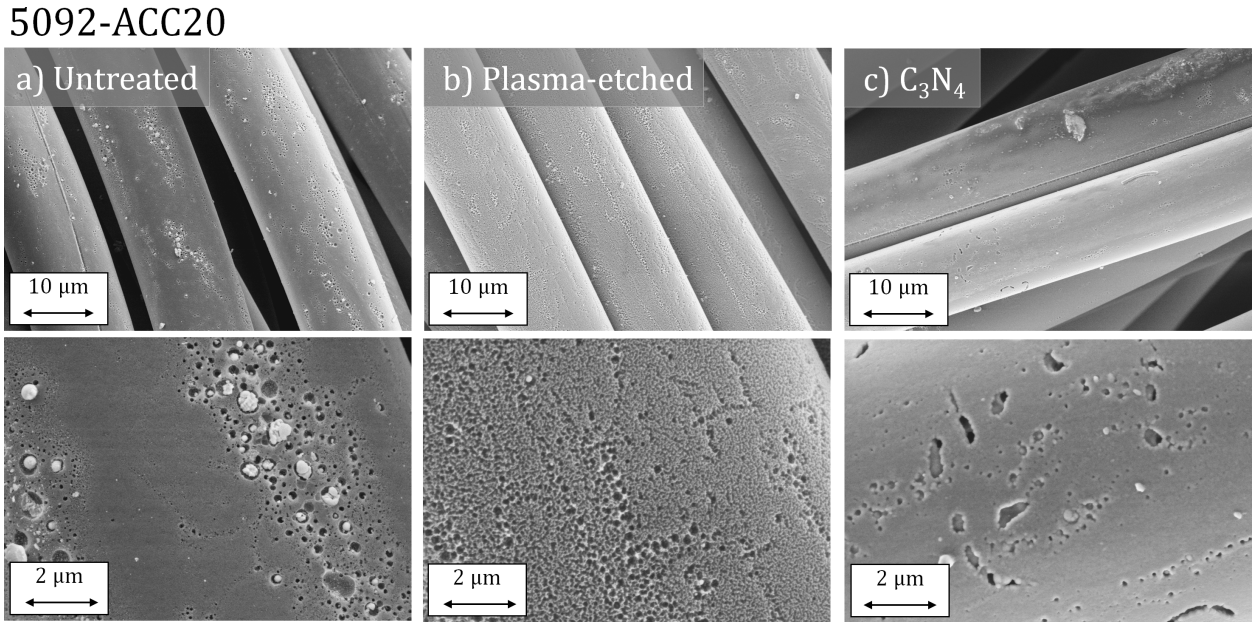

Figure 4.19.: SEM images of Kynol ACC-20 and derived materials. a) Untreated fibers, b) plasma-etched samples, and c) p-C_3N_4 nanocomposites.

materials. An additional interesting feature of Kynol CC and derived samples is the exceptionally high decomposition onset temperature of 650°C, which is due to the high degree of order and lack of defects in the sample, as will be further seen in Raman spectra.
Scanning electron micrographs, shown exemplary for ACC-20 in figure 4.19 provide insights about the evolution of the morphology of the materials from pristine, over plasma-etched, to finally p-C_3N_4 composited samples. SEM images of other samples can be found in the appendix, figures A.6 and A.7. The fibrous structure is clearly seen in the images, with single carbon strands of about 10 μm in diameter, but especially on the higher magnification scale of the untreated carbons, single adsorbed particles can be perceived at the fibers, with a generally rather inhomogeneous surface. A part of the effect of plasma etching lies in the removal of such foreign particles and the general roughening of the surface, making the bulk of the fiber accessible to reactive gases in the CVD. Finally, after CVD a compact, smooth layer is found on top of the carbons in the SEM images, which is the freshly grown phase of p-C_3N_4. Similar trends are found also for the other two materials. The SEM investigations are consolidated by additional energy dispersive X-ray (EDX) spectroscopy, shown in figure 4.20, where cross sections of the single carbon strands were prepared and EDX spectra were measured along the cross sections in order to identify the amount and distribution mainly of nitrogen and carbon. The EDX linescan shows an amount of nitrogen as high as 20 wt.%, even for the unactivated Kynol CC, which according to the more reliable EA

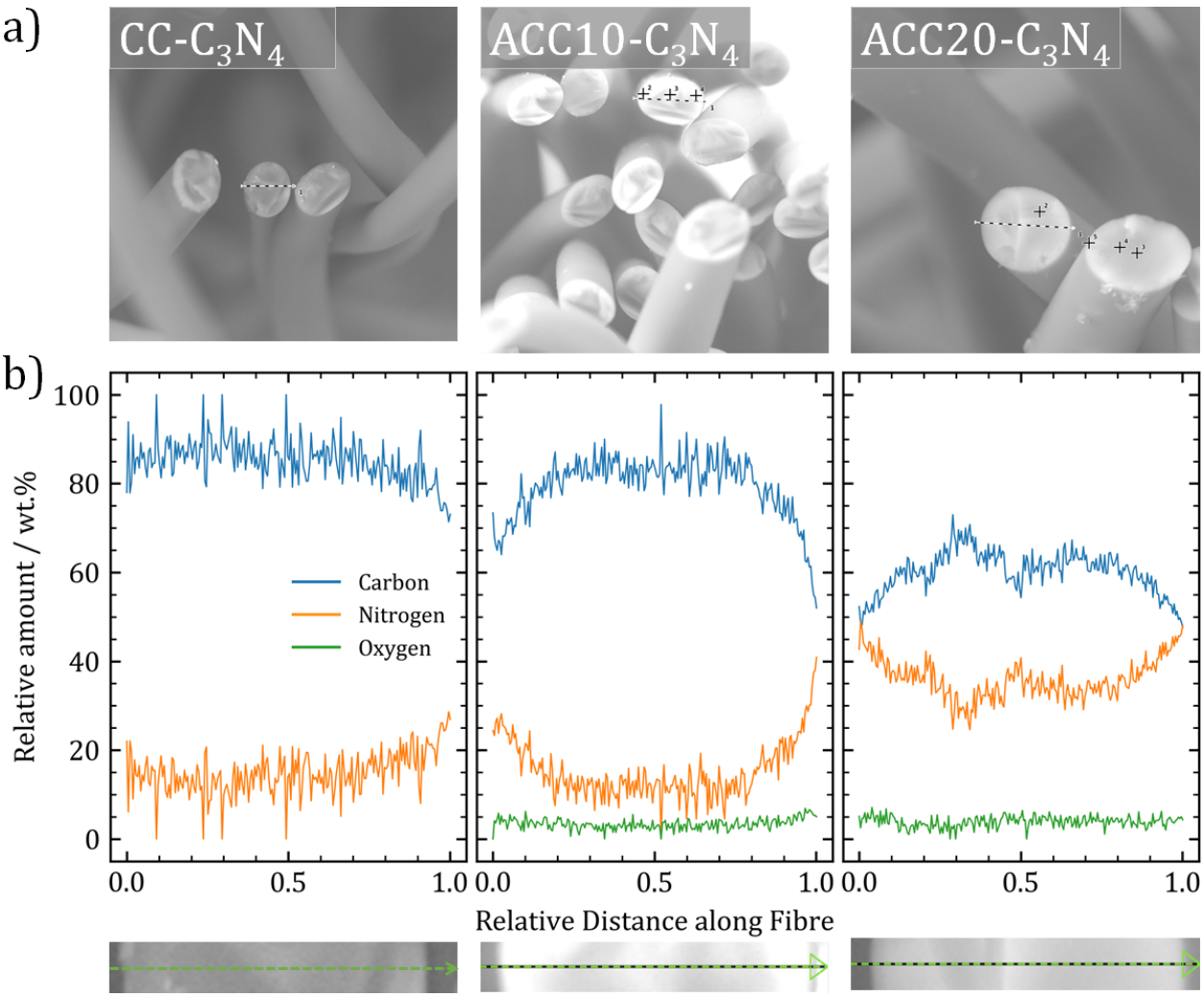

Figure 4.20.: a) SEM images and b) EDX linescans of the carbon/p-C_3N_4 nanocomposites with enlarged region where the EDX scan was measured.

should contain near to no nitrogen at all. This can be explained and accepted by the well known fact that of course nitrogen and carbon are both light elements and as such difficult to distinguish from each other. Therefore, the value of 20 wt.% is seen as a baseline and the results from EDX are generally regarded as more qualitative. However, the main point of these measurements is the fact that with a higher activation degree of the carbon substrate the nitrogen content increases, primarily in the outer bounds of the material, for ACC-10-C_3N_4, but also in the fiber center for ACC-20-C_3N_4. This can be explained by referring to the pore diameter, which is certainly too narrow in ACC-10 for the pores to be reached by C-N species in the CVD, where the process of diffusion stands in direct competition to reacting-off at one of the pore walls. In the pore system of ACC-10, the latter process appar-

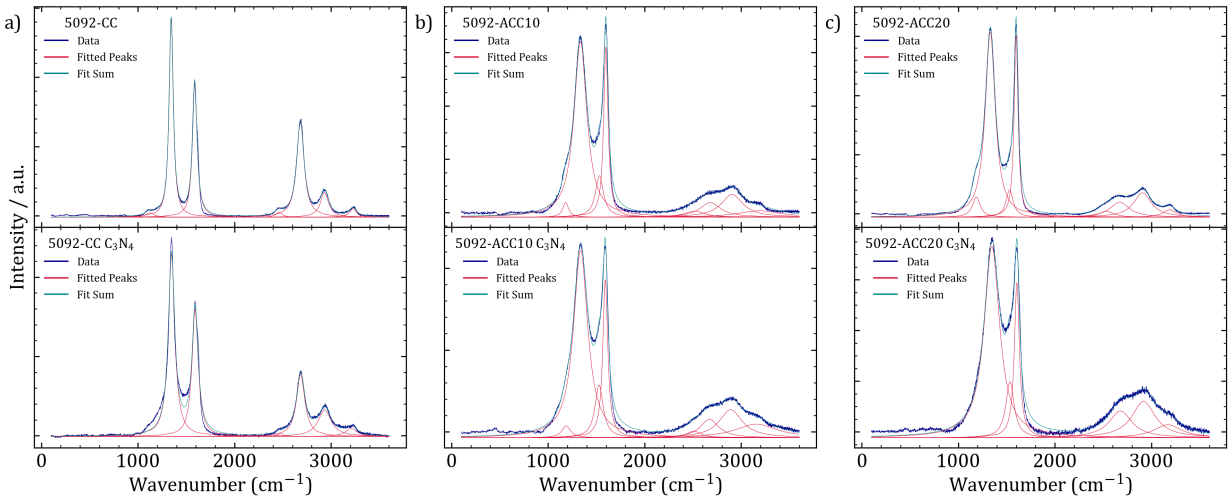

Figure 4.21.: Background-corrected Raman spectra of untreated materials, upper panel, and p-C_3N_4 composites, lower panel. Fitted bands and fit sum added for comparison of fit quality.

ently happens earlier, leaving the smaller pores on the inside blank, while the pore system of ACC-20 is completely filled by the p-C_3N_4. This already in parts yields an answer to the question for the deposition mode of p-C_3N_4, which will be further confirmed by sorption and SAXS experiments at a later stage.

First, the evolution of binding patterns of the materials, with the chemical activation but also after the formation of carbon/p-C_3N_4 composites will be investigated by Raman spectroscopy. The Raman spectra were fit to the same four-band model as the C-HAT-X spectra[239] and are presented in figure 4.21 and in figure A.8a-c) for the plasma-etched samples, respectively. A comparison of the pristine samples with the plasma-cleaned ones reveals that the pretreatment step indeed does not alter the chemical nature of the carbon, even though Raman is a surface specific technique and the changes that the 10 min treatment in oxygen plasma introduces are rather surface based. In all of the samples, the D- and G-bands at 1340 cm^{-1} and 1600 cm^{-1} are particularly strong and even their overtones between 2500 and 3000 cm^{-1} are measured.[242] The overtones are assigned to the 2D4-band at 2476 cm^{-1}, the 2D1-band at 2685 cm^{-1}, 2D1+G-band at 2935 cm^{-1}, and the 2D2 band at 3250 cm^{-1}.[276] Finally, the TPA- and A-bands contribute to the spectra to varying extents, where they are particularly weak in unactivated Kynol CC-derived samples, but become more influential in the spectra of activated carbons ACC-10 and ACC-20. The dominating D- and G-bands in Kynol CC and its descendant carbons together with the practical absence of TPA and A-bands and the sharply defined overtones indicate a relatively high

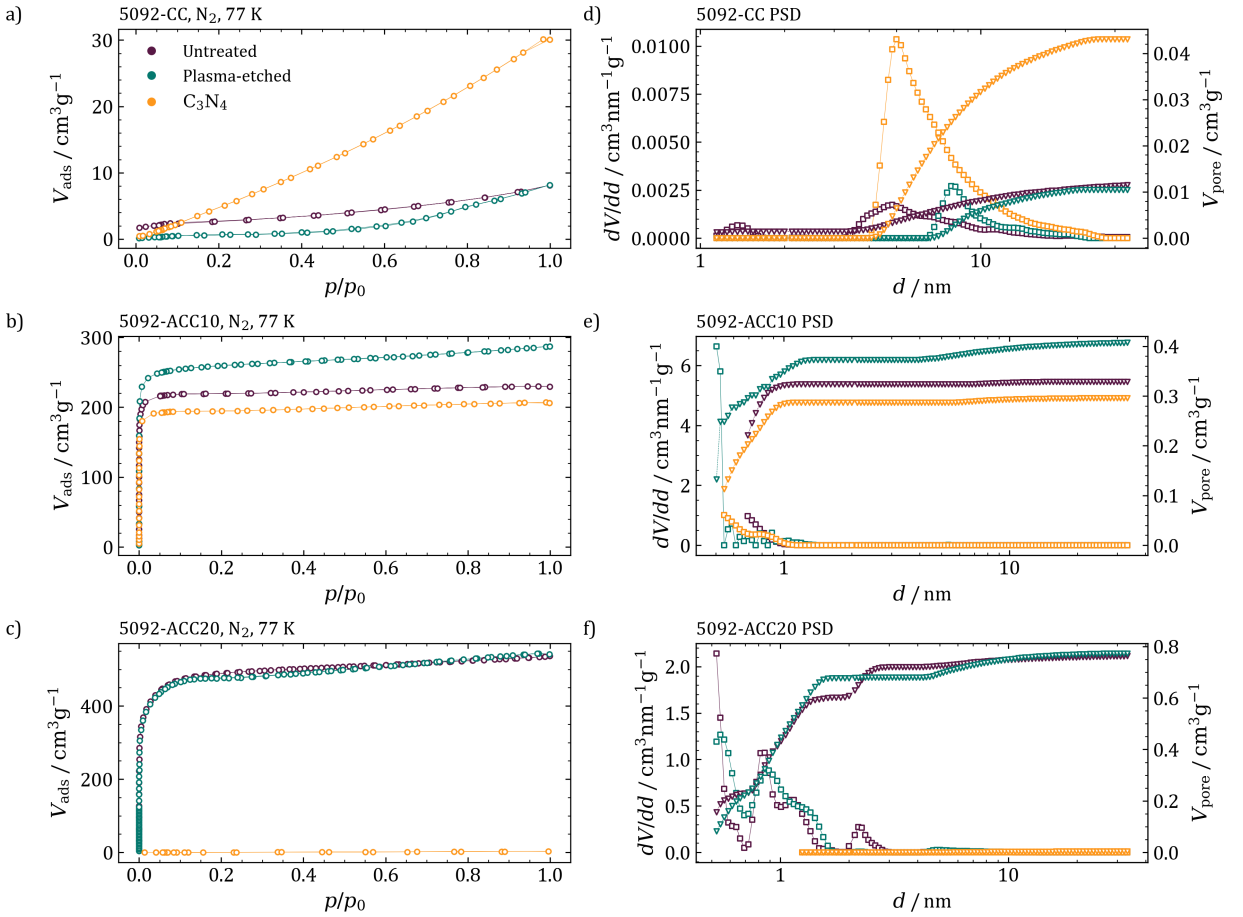

Figure 4.22.: Results of N_2 sorption experiments at 77 K for carbon/p-C_3N_4 composites. a-c) Isotherms, d-f) pore size distributions calculated from a QSDFT kernel for slit/cylindrical pores using the adsorption branch of the isotherm.

degree of ordering with rather low amounts of point defects, such as heteroatoms or sp^3 carbons. The chemical activation with CO_2 introduces such defects, as it basically makes use of the Boudouard equilibrium to generate porosity, in the course of which defects such as vacancies and dangling bonds are introduced.[157,158] Therefore, TPA- and A-bands emerge and the overtone signals broaden in ACC-samples. The deposition of p-C_3N_4 also increases the height of particularly the A-bands.[239,243,277]

The pore structure can be quite comprehensively studied by a combination of gas sorption and SAXS, where the former gives information on the gas-accessible porosity, while the latter detects all scattering density contrasts of the sample due to both, closed and open pores. Nitrogen sorption isotherms at 77 K are presented in figure 4.22a-c), the respective differential and cumulative PSD plots are shown in figure 4.22d-f). All Kynol CC derived

carbons shows a type II isotherm with low gas uptake, indicating the presence of unrestricted monolayer-multilayer adsorption, which describes the non-porous but fibrous structure of the material.[215] After plasma etching, the gas uptake is shifted to higher relative pressures, while the total gas uptake stays the same. The Kynol CC/p-C_3N_4 composite shows no inflection point and a linearly increasing gas uptake, with higher volumes adsorbed at saturation pressure, which indicates the impeded interaction with the adsorbent surface and the beginning clustering around sites in the adsorbent of higher affinity, which is readily explained by the presence of polarizing nitrogen groups of the carbon nitride at the surface.[215] However, the surface area of each of the materials is lower than 24 m^2 g^{-1}, as calculated from DFT, summarized in table A.3. The ACC-10 related carbons show type I isotherms with sharp inflections in the low relative pressure region, indicating the presence of narrowly distributed pores of small diameters, which is investigated in detail by DFT pore size distributions, shown in figure 4.22e). The majority of pore volume is due to pores narrower than 1 nm, where roughly 1000 m^2 g^{-1} of surface area are present before and after plasma etching. In the p-C_3N_4 composite, the surface area drops only slightly to 805 m^2 g^{-1}, where particularly the narrowest pores below 0.9 nm in diameter are disappearing. This fraction of pores must be covered at the entrance by a layer ov p-C_3N_4, while larger pores are yet too small to be entered by p-C_3N_4, but also too big for their entrances to be bridged by the p-C_3N_4-phase, indicating that this treshold value of coatable distances between two adjacent carbon fragments is around 0.9 nm. If pore diameters narrower than those reachable by N_2 at 77 K are considered, e.g. in CO_2 sorption experiments in figure A.9b), a very similar trend is observed, however, due to the abundant heteroatoms the pore size distributions of such materials are not reliable enough to draw conclusions about the treshold diameter from them. Yet, the similarity of N_2 and CO_2 results indicates that the CN-oligomers present in the CVD atmosphere are larger than the pores accessible to both probe gasses. The greatest changes due to the deposition of p-C_3N_4 were observed in ACC-20 carbons. Before and after plasma etching essentially the same isotherm is measured, however, after CVD the surface area drops from 2000 m^2 g^{-1} to only 2-4 m^2 g^{-1}, depending on the calculation method. This indicates a by far higher degree of pore filling by p-C_3N_4, however, not all of the N_2 accessible pore volume of 0.761 cm^3 g^{-1} is occupied by carbon nitride, as this would correspond to a mass gain of 150 %, which is not the case. This can be easily explained by the larger diameter of the reactive gasses in the CVD, as well as by the fact that after a certain free path length the CN-oligomer is bound to react with the pore wall and deposit, meaning that deposition temperature should have a substantial impact on the CVD product.[271,278] The analysis of sorption data therefore not only nicely underlines the possibility to visualize the progessing of nitrogen into the carbon

fiber bulk by EDX mapping of fiber cross sections, but also indicates the possible formation of closed pores in ACC-10-C_3N_4, as only there the particularly important narrow pores close to the fiber surface could be successfully made inaccessible to N_2 contrary to ACC-20-C_3N_4, where a dense, impermeable layer was deposited into the outer several micrometers of the fiber bulk, rendering them inactive for any kind of useful energy storage, as will be shown in a later section.

In order to analyze the SAXS patterns of the materials, the model-free approach of Schiller and Mering[180] and Perret and Ruland[181,182,279,280] was used. The mathematical treatment was followed as outlined by Härk et al.[184,281] and Jafta et al.[282] and proceeded in close collaboration with Dr. Eneli Härk from the Helmholtz Zentrum Berlin. The relevant equations will be summarized in the following. First the SAXS patterns were calibrated to absolute scattering units and normalized to their filling density ρ_{app} in the capillaries.

$$\frac{d\Sigma_{\mathrm{m}}}{d\Omega}(q) = \frac{1}{\rho_{\mathrm{app}} V}\frac{d\sigma}{d\Omega}(q) \tag{4.14}$$

The macroscopic scattering cross section $d\Sigma_{\mathrm{m}}/d\Omega(q)$ is a superposition of two statistically independent scattering contributions, of which $d\Sigma_{\mathrm{pores}}/d\Omega(q)$ is due to the scattering at the interface between carbon and vacuum, i.e. at pores, and $d\Sigma_{\mathrm{fluct}}/d\Omega(q)$ arises from fluctuations due to lateral imperfections and finite size of the carbon regions. A constant background C is observed due to general density fluctuations in an amorphous phase, as in equation 4.15.

$$\frac{d\Sigma_{\mathrm{m}}}{d\Omega}(q) = \frac{d\Sigma_{\mathrm{pores}}}{d\Omega}(q) + \frac{d\Sigma_{\mathrm{fluct}}}{d\Omega}(q) + C \tag{4.15}$$

The fluctuation scattering was removed and the data for a two phase system was further considered, for samples containing p-C_3N_4 a mass-weighted and previously measured p-C_3N_4 scattering pattern $d\Sigma_{\mathrm{m}}/d\Omega\,[C_3N_4]$ was subtracted from the data for the total material $d\Sigma_{\mathrm{m}}/d\Omega\,[\mathrm{Kynol/C_3N_+C_3N_4}]$ according to equation 4.16.

$$\frac{d\Sigma_{\mathrm{m}}}{d\Omega}\left[\mathrm{Kynol/C_3N_4 + C_3N_4}\right](q) = \frac{d\Sigma_{\mathrm{m}}}{d\Omega}\left[\mathrm{Kynol/C_3N_4}\right](q) + \frac{d\Sigma_{\mathrm{m}}}{d\Omega}\left[\mathrm{C_3N_4}\right] \tag{4.16}$$

The fluctuation term can further be described as in equation 4.17 with B_{fl} as the scattering contribution of the carbon phase and l_{R} is the degree of lateral correlation.

$$\frac{d\Sigma_{\mathrm{fluct}}}{d\Omega}(q) = \frac{B_{\mathrm{fl}} l_{\mathrm{R}}^2 (18 + l_{\mathrm{R}}^2 q^2)}{9 + l_{\mathrm{R}}^2 q^2} \tag{4.17}$$

By combining equations 4.15 and 4.17 it is possible to determine B_{fl} at high q from a modified Porod law, equation 4.18, where P_{m} is the Porod constant and L is the structural length

scale.

$$\frac{d\Sigma_{\mathrm{m}}}{d\Omega}(q) \xrightarrow[qL>>1]{} \frac{(2\pi)^4 P_{\mathrm{m}}}{q^4} + \frac{B_{\mathrm{fl}}}{q^2} + C \tag{4.18}$$

After the subtraction of the B_{fl} term, all scattering curves show an asymptotic behaviour proportional to q^{-4}, as can be seen in figure A.10. Further, the Porod constant is linked to the inner surface area SSA_{SAXS} and allows the calculation of all surface area related to the scattering contrast between carbon and vacuum, according to equation 4.19, where $\Delta\rho$ is the scattering contrast of carbon against that of the vacuum, calculated from natural constants and the skeleton density of carbon ρ_{sk}.

$$\begin{aligned} P_{\mathrm{m}} &= \frac{\Delta\rho^2}{(2\pi)^3} SSA_{\mathrm{SAXS}} \\ \Delta\rho &= \frac{N_{\mathrm{A}}\rho_{\mathrm{sk}} r_{\mathrm{e}} Z}{M_{\mathrm{C}}} \end{aligned} \tag{4.19}$$

Additionally, the porosity Φ can be calculated from the following integral over the pore scattering term in equation 4.20, with the invariant Q_{m}, and $\rho_{\mathrm{fiber}} = \rho_{\mathrm{sk}}(1-\Phi)$.

$$Q_{\mathrm{m}} = \frac{1}{(2\pi)^3} \int_0^\infty \frac{d\Sigma_{\mathrm{pores}}}{d\Omega}(q) 4\pi q^2 dq = \frac{\Delta\rho^2}{\rho_{\mathrm{fiber}}} \Phi(1-\Phi) \tag{4.20}$$

From the invariant Q_{m} and the Porod constant P_{m} the mean length of the pores $\langle l_{\mathrm{pore}} \rangle$ and the pore walls $\langle l_{\mathrm{solid}} \rangle$ are related to the chord length l_{p} via equation 4.21.

$$\langle l_{\mathrm{Pore}} \rangle = \frac{l_{\mathrm{p}}}{1-\Phi}; \langle l_{\mathrm{solid}} \rangle = \frac{l_{\mathrm{p}}}{\Phi} \tag{4.21}$$

Finally, the degree of disorder (DoD) is calculated according to equation 4.22, where a_3 is the distance between two carbon layers in a graphite lattice, corresponding to $a_3 = d_{002} = 0.335$ nm.

$$\frac{B_{\mathrm{fl}}\Phi}{2\pi a_3 Q_{\mathrm{m}}} = \frac{\langle \Delta^2 a_3 \rangle}{\langle a_3 \rangle^2} + \frac{\langle \Delta^2 l_{\mathrm{R}} \rangle}{\langle \mathrm{R} \rangle^2} \tag{4.22}$$

All samples show high SSAs in the SAXS experiments, which is particularly interesting in the case of Kynol CC samples, where nearly no gas accessible porosity was observed. The SAXS-surface areas in the case of the activated carbons are rather similar to the values measured from N_2 sorption, indicating that all present surface area is of gas accessible nature in untreated ACC-10 and ACC-20 carbons. The SAXS surface area decreases from 1000 m^2g^{-1} in Kynol CC to 800 m^2g^{-1} in Kynol ACC-10, together with an increase in wall-thickness,

indicating a rearrangement of carbon atoms due to activation towards more disordered structures, as shown by Raman spectra and the DoDs of the materials. The transformation from ordered, internally porous to typical activated carbons is also manifested in the contribution due to lateral imperfections B_{fl}, which constantly increases with activation. However, the effect of plasma etching is low on the SAXS-derived parameters as well, while changes due to the deposition of p-C_3N_4 can indeed be measured. Except for the decrease in SSA, which closely follows the trend from gas sorption, imperfections and defects are removed, as indicated by a lower DoD in p-C_3N_4 composited samples. Therefore, an annealing effect of CVD on activated carbon materials is concluded, which could improve the electronic conductivity at the direct interface between sodium deposited at low potentials and the electrode surface. Kratky plots shown in figure A.11 furthermore reveal that the largest pores are found in unactivated Kynol CC, with diameters >2 nm, and the size of these pores only decreases with further activation. Also, the deposition of p-C_3N_4 influences the material ACC-20 the most, as the surface area due to smaller pores significantly vanishes.

4.3.3. Electrochemical sodium storage in open and closed pores

After the thorough clarification of the structures of carbons and composites, the samples were subjected to an initial characterization by charge-discharge experiments at low currents of 18.6 mA g^{-1}, to investigate the impact of open and closed pores, but also the addition of a carbon nitride phase on the sodium storage properties. As it was shown that no significant differences in the structure of plasma-etched samples are observed, also no impact on the sodium storage is to be expected, hence these carbons where disregarded in the following. As already expected from the results on open microporous samples in the previous section 4.1, ACC-10 and ACC-20 exhibit a low sloping capacity of less than 100 mAh g^{-1} in the measurements above 0 V, after showing a high irreversible capacity >200 mAh g^{-1} in the first cycle. In the oversodiation cycle, these materials behave similar to microporous C-HAT-550, almost immediately beginning to plate sodium as soon as the potential limit of 0 V is alleviated. On the other hand, Kynol-CC derived carbons and composites have lower first-cycle capacities, but also their capacity above 0 V is reduced as compared to the activated samples. However, as these carbons are oversodiated, no clear dip occurs. This effect is even more pronounced than in the C-HAT-X series. Even more, during the desodiation following the excess sodium insertion and plating, a plateau between 100 mV and 300 mV occurs, as it was described in section 4.1.4 and in figure 4.8 for C-HAT-1600. Again, this plateau occurs at a distinct, higher voltage than the stripping of deposited metallic sodium, and is observed

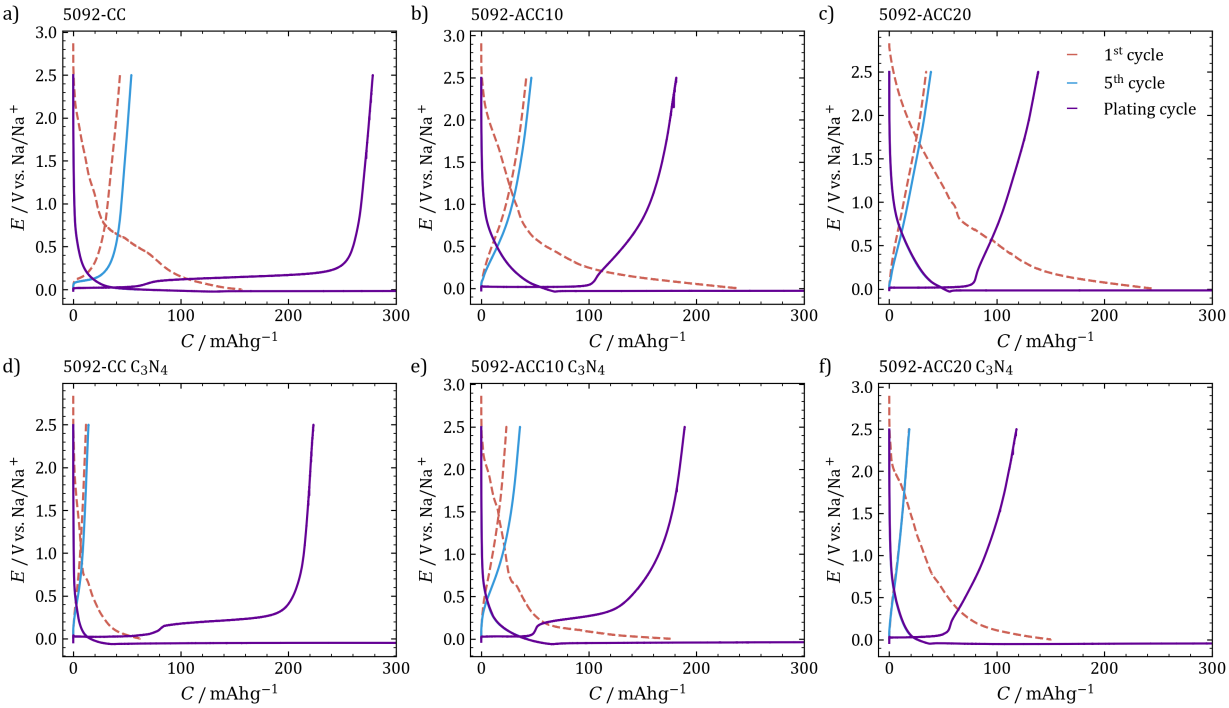

Figure 4.23.: Galvanostatic charge-/discharge curves of Kynol carbons and composites recorded at 18.6 mA g^{-1}. Dashed red line shows first cycle with SEI formation, light blue line shows fifth cycle with 0.002 V as lower voltage limit, purple line recorded during oversodiation.

only in samples, where closed pores are suspected from the structural characterization data, i.e. in Kynol-CC, CC-C_3N_4, and ACC-10-C_3N_4. This underlines the importance of closed pores within the carbon framework, which cannot be entered by electrolyte, in contrast to their open pendants, rendering the former as suitable stabilization sizes for quasimetallic sodium, depositing at constant, low potentials. The absence of the distinct sodium plating onset is hypothesized to be due to the large size of internal pores, especially in Kynol CC related samples, where the energetic barrier for sodium cluster nucleation is similar to that of crystalline sodium, leading to a coalescence of the two signals. All carbon nitride coated samples show a significantly reduced first cycle capacity with respect to the pristine carbons, typically by 50-100 mAh g^{-1}.This can be ascribed to the reduced conductivity σ, as can be compared in table A.5, where σ is lower by at least one order of magnitude in carbon/p-C_3N_4 nanocomposites. This indicates that the p-C_3N_4 layer is impermeable for electrolyte molecules and ions and that the potential at the outer bounds of the composite grains is indeed reduced by the insulating nature of p-C_3N_4. The generally reduced surface area after CVD likely contributes to this effect, as well. However, in Kynol CC-C_3N_4, the introduced

carbon nitride species unfortunately also negatively affects the plateau capacity, just as in ACC-20-C_3N_4 the sloping capacity is reduced. While in the latter sample the reduction can be explained by the displacement of mass by electrochemically inactive carbon nitride, the reason for the deterioration of capacity in Kynol CC remains unclear. In ACC-10-C_3N_4, the greatest difference before and after CVD can be perceived, where the nanocomposite shows a broadened peak below 0 V, as opposed to the sharp sodium plating onset in pristine ACC-10. During the desodiation also a voltage plateau at approximately 300 mV is measured in this sample. Quantitatively, ACC-10-C_3N_4 shows a total capacity of 137±2 mAh g^{-1}, of which 54±6 mAh g^{-1} are found at a constant potential below 0 V, compared to a total capacity of 76 mAh g^{-1} in untreated ACC-10. Apparently, the CVD process with carbon nitride is suitable to cover a certain extent of narrower pores and thereby transform them into closed pores, suitable for the stabilization of quasimetallic sodium clusters. Additional information is gained from CV experiments in voltage windows of 0.0-2.5 V and -0.1-2.5 V, respectively, shown in figure A.12. The peaks attributed to SEI formation reactions at 2.1 V and 0.4 V[109,283,284] are present in all samples, particularly in ACC-10 and ACC-20, but generally are smaller in height in p-C_3N_4-coated materials. During the cathodic scan, a first current begins to flow below 1 V and increases seemingly exponentially when approaching 0 V, which is reversed in a smooth peak in the anodic scan, yielding very similar CV curves for all of the samples between 2.5 and 0.0 V. After extending the lower voltage limit to -0.1 V, no new signals are measured in the cathodic scan, similar to the observation in the oversodiation cycle in charge-discharge experiments, however in the anodic scan the peak at 0.2 V is significantly higher in these measurements. In samples without distinct voltage plateau, only a small sharp oxidative signal occurs at 0 V, presumingly due to metallic sodium stripping. As similar observations were made in section 4.1, the general validity of the approach and of the deducted conclusions on sodium storage below 0 V is demonstrated. In the next step, the charging and discharging protocol from section 4.1 will be extended, by determining the maximum sodiation capacity not anymore from the dip capacity in the sodiation step, but rather from the amount of sodium reversibly extracted in the desodiation plateau following oversodiation, proving the reversible nature of the sodium species formed therein. Quantitatively, the capacity limit is determined as the capacity measured between 100 mV and 2.5 V in the desodiation cycle directly after the oversodiation. In order to account for experimental errors, the determination was repeated three times and the limit was set to only 90 % of the determined value. Only samples exhibiting considerable voltage plateaus were measured here. The exact capacity values are summarized in table A.6 and the resulting exemplary charge-discharge curves as well as cycling performance and coulombic

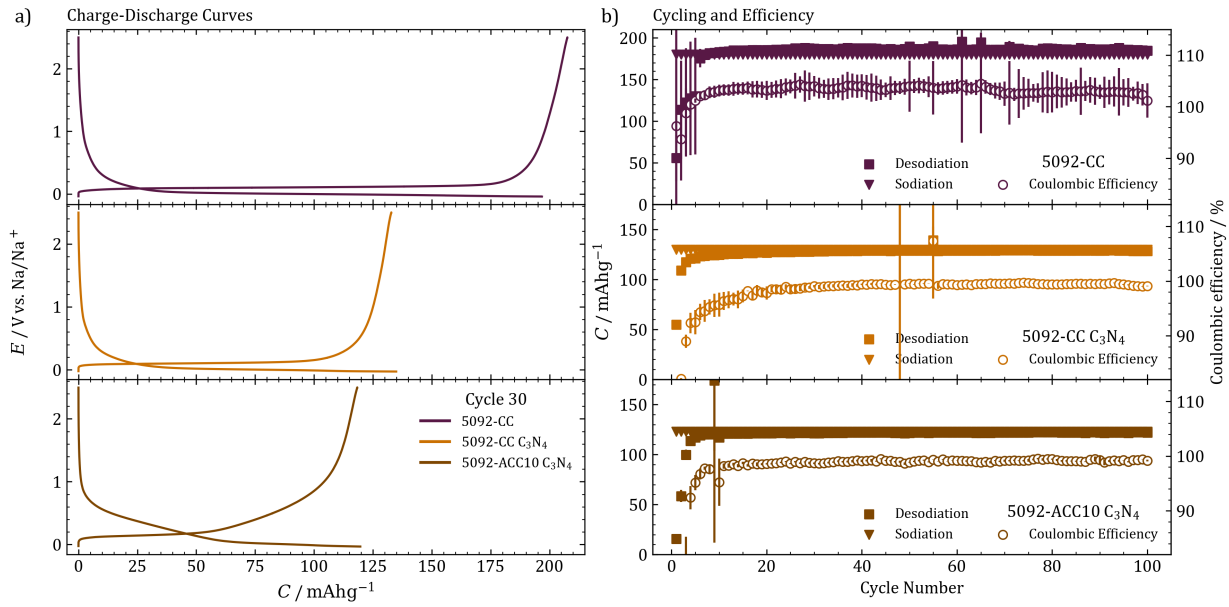

Figure 4.24.: a) Capacity-limited galvanostatic charge-/discharge curves of Kynol carbons and composites recorded at 18.6 mA g^{-1} using the capacity limit previously determined from desodiation cycles. b) Results of cycling over 100 cycles at 18.6 mA g^{-1}.

efficiency is plotted in figure 4.24. The majority of capacity of Kynol CC, namely 87 % of its 200 mAh g^{-1}, are measured at a constant potential plateau below 0 V. The practical absence of a sloping region is both remarkable and beneficial for the energy density in the full cell application, and leaves space for oversizing in order to account for a safety buffer. The samples withstand 100 cycles at C/20 without further problems and without sodium dendrite growth, as shown in figure A.13. The first cycle efficiency loss is also re-evaluated in the light of these results, where for example in Kynol CC the first cycle capacity is 240 mAh g^{-1}, while the reversible sodiation capacity is as high as 222 mAh g^{-1}, and 200 mAh g^{-1} if only 90 % of the capacity are used. Hence, a loss in capacity of only 17 % is observed in Kynol CC, where the values for the other two carbons are similar. The key to this transformation is the fact that small pores in the center of the ACC-10 fibers are inaccessible to the reactive gases in the CVD oven, leaving them necessarily coated by the p-C_3N_4 layer grown on their tops, whereby they can be effectively regarded as closed, i.e. reachable to sodium ions only by mechanisms of solid state diffusion, without their respective solvation shells. Hypothetically, an ideal substrate for this CVD process would therefore be a fibrous, hollow material, with pores in the shell maximally as narrow as approximately 0.9 nm, the previously assumed treshold value for closable pores. Thereby, sodium could deposit in confined spaces inside of the structure, allowing reversible and safe long-term operation.

4.3.4. Conclusion

In this section, hard carbon/p-C_3N_4 nanocomposites were prepared by CVD of p-C_3N_4 on hard carbon cloth precursors of different porosities, which were then utilized as the negative electrodes in SIB anode half cells. The broad and systematic range of pore systems in the samples encompassed closed as well as open micropores. Furthermore, the influence of wall thickness, carbon ordering and micropore size on sodium storage could be effectively studied on these samples. The porosity has a substantial impact on the outcome of CVD. While externally non-porous samples will obtain a homogeneous thin layer coating of p-C_3N_4, with increasing pore width the penetration of the pore system by carbon nitride increases. The reactive CN-oligomers were found to be larger in size than the kinetic diameter of both, the N_2 and the CO_2 molecules, so that the critical pore diameter below which pores are inaccessible is located around 0.9 nm. By a combination of SAXS and gas sorption it was determined that a rearrangement of the carbon framework itself takes place during CO_2 activation, and high gas-inaccessible SSA is transformed nearly entirely into open porosity. Apart for the filling of certain pore regions, p-C_3N_4 causes an annealing of defective carbon structures. High plateau capacities were measured by an advanced charging and discharging approach only in internally porous samples, among which ACC-10-C_3N_4 takes a special place, as it contains artificially introduced closed pores, changing its sodium storage characteristics from a purely sloping voltage profile in the pristine sample to a profile containing a plateau region. Furthermore, a reduction of the extent of SEI formation was achieved in carbon/p-C_3N_4 nanocomposites by reducing both, the conductivity and the SSA of the samples. Considering the aspect of changing the voltage profile during sodiation from sloping to a low voltage plateau storage, this rather simple and scalable approach could be adapted for practical applications.

5. Conclusion and Outlook

The SIB constitutes a viable and sustainable alternative to follow up the current LIB technology. However, the hard carbon anode side suffers from relatively low capacities and at the same time imposes concerns due to considerable amounts of electrolyte consumed in the first cycle so that it remains limiting for the charge stored and thereby the achievable energy density. Sodium is stored in the hard carbon in two mechanisms, seamlessly transitioning into each other, the first one yielding a sloping voltage region in a range of approximately 0.1-2.0 V vs. Na/Na^+ due to adsorption of Na^+ ions to high-energy sites, while the second one occurs at a low and constant potential of approximately 0.1 V vs. Na/Na^+ due to sodium clusters forming inside of closed pore structures of the carbon. In order to increase energy density and efficiency of hard carbon SIB anodes, the sodium storage mechanism has to be understood in more detail, using both, suitable analysis techniques and synthetic approaches towards closed porous materials.

In this work, first a comprehensive and systematic study of structure and property relationships is presented on a homologous series of hard carbons and hard carbon-like materials with varying porosities, nitrogen contents, and degrees of ordering. Correlations between gas sorption, surface chemistry and sodium storage are established, particularly effects of pore closure on first-cycle capacity loss and the shape of the voltage profile are observed. The plateau region was found to develop with reducing pore accessibility, confirming the model of quasimetallic sodium depositing in preferentially closed HC pores at constant low potentials. Most importantly, it is shown that in this type of carbons a significant, if not major share of capacity is found at potentials lower than that of metallic sodium, leading to the development of a capacity-limited cycling approach, capable of measuring the material-specific sodiation capacity more accurately than in common voltage limited galvanostatic experiments. These results show that already state-of-the-art materials could potentially be exploited to store higher amounts of sodium, improving the overall energy density simply by adjusting the operation conditions.

The second part of this thesis deals with the investigation of elementary mechanistic steps occuring during the electrochemical insertion and extraction of sodium in a hard carbon elec-

trode, by performing DRT analysis on EIS data obtained at different cell SOCs to determine the amount and relative contribution of electrochemical processes occuring. Diffusion was found to play a major role in the sodiation mechanism, by far outweighing charge-transfer effects, especially during sloping capacity regions. Specific processes with characteristic time constants were also found responsible for the plateau and sodium plating phases, respectively. The approach was finally validated by establishing a qualitative model and reproducing the experimental data. Therefore, the presented method allows the non-destructive investigation of the onset of the respective sodium storage processes. It can not only be applied in materials research and screening, but with a more precise understanding of the carbon structure could also be used to obtain quantitative kinetic data. This could facilitate materials development and allow new mechanistic insights on sodium storage, without the need for coupling with other techniques. Another practically relevant application of the developed method can be also imagined in the detection of metallic sodium in full cells, which has the potential to improve operational safety of battery devices.

Finally, a CVD method was employed to prepare hard carbon/p-C_3N_4 composites, which allows the transformation of open porous materials into closed porous ones. This allows the direct study of the impact of pore closure on pore systems of similar geometries. The materials' structure was thoroughly investigated by a set of physical characterization methods and the treshold pore size above which p-C_3N_4 begins to grow inside the pore was approximated. Closed porous materials, were again shown to store sodium at a low-voltage plateau, but most importantly, the post-synthetically closed porous samples exhibited the same sodium storage mechanism as the intrinsically closed porous ones. This demonstrates the viability of this method for the preparation of advanced electrode materials. A reduction of the extent of SEI growth was additionally measured on all p-C_3N_4 coated samples, rendering the method even suitable for the synthesis of artificial SEI-layers to increase the materials' coulombic efficiency. Mechanistic investigations, using methods like in situ SAXS or NMR on samples prepared by this method could provide insightful results on the contribution of closed pores to sodium storage.

All together, this work constitutes a comprehensive study of the sodium storage mechanism in different hard carbon-related materials, together with electrochemical approaches for their investigation, which exceed the commonly applied techniques. By combining the insights gained with a novel synthetic method for the preparation of closed porous materials, it serves the purpose of extending the understanding of processes involved in hard carbon sodium storage and revealing ways to optimize the parameters required for sodium storage at high energy densities.

Bibliography

[1] M. Duren, *Understanding the Bigger Energy Picture - DESERTEC and Beyond*, **2017**, pp. 1–1080.

[2] Z. Yang, J. Zhang, M. C. Kintner-Meyer, X. Lu, D. Choi, J. P. Lemmon, J. Liu, *Chemical Reviews* **2011**, *111*, 3577–3613.

[3] C. A. Powell, B. D. Morreale, *MRS Bulletin* **2008**, *33*, 309–315.

[4] V. Smil, *Energy Transitions: Global and National Perspectives*, 2nd ed., Praeger, **2017**.

[5] BP, bp Statistical Review of World Energy 2020, tech. rep., **2020**.

[6] K. W. Thoning, A. M. Crotwell, J. W. Mund, Atmospheric Carbon Dioxide Dry Air Mole Fractions from continuous measurements at Mauna Loa, Hawaii, Barrow, Alaska, American Samoa and South Pole, tech. rep., **2021**.

[7] M. Sterner, F. Bauer, F. Crotogino, F. Eckert, C. von Olshausen, D. Teichmann, M. Thema, *Chemische Energiespeicher*, **2017**, pp. 327–493.

[8] A. Bauer, J. Song, S. Vail, W. Pan, J. Barker, Y. Lu, *Advanced Energy Materials* **2018**, *8*, 1–13.

[9] B. Dunn, H. Kamath, J. M. Tarascon, *Science* **2011**, *334*, 928–935.

[10] J. Liu, *Advanced Functional Materials* **2013**, *23*, 924–928.

[11] K. Turcheniuk, D. Bondarev, V. Singhal, G. Yushin, *Nature* **2018**, *559*, 467–471.

[12] C. Delmas, *Advanced Energy Materials* **2018**, *8*, 1–9.

[13] J. Y. Hwang, S. T. Myung, Y. K. Sun, *Chemical Society Reviews* **2017**, *46*, 3529–3614.

[14] D. Saurel, B. Orayech, B. Xiao, D. Carriazo, X. Li, T. Rojo, *Advanced Energy Materials* **2018**, *8*, 1703268.

[15] D. Saurel, J. Segalini, M. Jauregui, A. Pendashteh, B. Daffos, P. Simon, M. Casas-Cabanas, *Energy Storage Materials* **2019**, *21*, 162–173.

[16] D. A. Stevens, J. R. Dahn, *Journal of The Electrochemical Society* **2000**, *147*, 4428.

[17] D. A. Stevens, J. R. Dahn, *Journal of The Electrochemical Society* **2000**, *147*, 1271.

[18] D. A. Stevens, J. R. Dahn, *Journal of The Electrochemical Society* **2001**, *148*, A803.

[19] F. Chevallier, M. Letellier, M. Morcrette, J. M. Tarascon, E. Frackowiak, J. N. Rouzaud, F. Béguin, *Electrochemical and Solid-State Letters* **2003**, *6*, A225–A228.

[20] D. Larcher, J. M. Tarascon, *Nature Chemistry* **2015**, *7*, 19–29.

[21] T. F. Stocker, D. Qin, G.-K. Plattner, M. Tignor, S. K. Allen, J. Boschung, A. Nauels, Y. Xia, V. Bex, P. M. Midgley, Summary for Policymakers, tech. rep., Cambridge, New York, **2013**.

[22] I. Loladze, *Trends in Ecology and Evolution* **2002**, *17*, 457–461.

[23] I. Loladze, J. M. Nolan, L. H. Ziska, A. R. Knobbe, *Molecular Nutrition and Food Research* **2019**, *63*, 1–9.

[24] R. J. Lowe, G. M. Huebner, T. Oreszczyn, *Building Services Engineering Research and Technology* **2018**, *39*, 698–711.

[25] A. H. Philips, *Nature* **1882**, *27*, 127–127.

[26] S. Arrhenius, *Philosophical Magazine and Journal of Science* **1896**, *41*, 237–276.

[27] I. Brkic, United Nations. Economic Commission for Europe, *Pathways to sustainable energy : accelerating energy transition in the UNECE region. Vol. 41*, **2020**, p. 47.

[28] V. Wesselak, T. Schabbach, T. Link, J. Fischer, *Handbuch Regenerative Energietechnik*, **2017**.

[29] A. Markandya, P. Wilkinson, *Lancet* **2007**, *370*, 979–990.

[30] B. K. Sovacool, R. Andersen, S. Sorensen, K. Sorensen, V. Tienda, A. Vainorius, O. M. Schirach, F. Bjørn-Thygesen, *Journal of Cleaner Production* **2016**, *112*, 3952–3965.

[31] R. Turconi, A. Boldrin, T. Astrup, *Renewable and Sustainable Energy Reviews* **2013**, *28*, 555–565.

[32] M. Pehl, A. Arvesen, F. Humpenöder, A. Popp, E. G. Hertwich, G. Luderer, *Nature Energy* **2017**, *2*, 939–945.

[33] T. Klaus, V. Carla, W. Kathrin, L. Harry, K. Müschen, *2050: 100% Erneuerbarer Strom*, **2010**.

[34] N. S. Lewis, *MRS Bulletin* **2007**, *32*, 808–820.

[35] A. J. Bard, L. R. Faulkner, *Electrochemical Methods: Fundamentals and Applications*, 2nd ed., John Wiley & Sons, Inc., New York, NY, **2001**.

[36] P. Atkins, J. de Paula, *Physical Chemistry*, 8th ed., (Ed.: W. Freeman), Oxford University Press, Oxford, **2006**, p. 1072.

[37] L. Medenbach, P. Adelhelm, *Topics in Current Chemistry* **2017**, *375*, 1–25.

[38] C. Wadia, P. Albertus, V. Srinivasan, *Journal of Power Sources* **2011**, *196*, 1593–1598.

[39] A. Yoshino, *Angewandte Chemie - International Edition* **2012**, *51*, 5798–5800.

[40] Y. Nishi, *The Chemical Record* **2001**, *1*, 406–413.

[41] D. Guerard, A. Herold, *Carbon* **1975**, *13*, 337–345.

[42] R. Yazami, P. Touzain, *Journal of Power Sources* **1983**, *9*, 365–371.

[43] R. E. Franklin, *Acta Crystallographica* **1951**, *4*, 253–261.

[44] N. Yabuuchi, K. Kubota, M. Dahbi, S. Komaba, *Chemical Reviews* **2014**, *114*, 11636–11682.

[45] G. H. Newman, L. P. Klemann, *Journal of The Electrochemical Society* **1980**, *127*, 2097–2099.

[46] K. M. Abraham, *Solid State Ionics* **1982**, *7*, 199–212.

[47] L. W. Shacklette, T. R. Jow, L. Townsend, *Journal of The Electrochemical Society* **1988**, *135*, 2669–2674.

[48] K. Kubota, N. Yabuuchi, H. Yoshida, M. Dahbi, S. Komaba, *MRS Bulletin* **2014**, *39*, 416–422.

[49] M. M. Doeff, Y. Ma, S. J. Visco, L. C. De Jonghe, *Journal of The Electrochemical Society* **1993**, *140*, L169–L170.

[50] T. R. Jow, L. W. Shacklette, M. Maxfield, D. Vernick, *Proceedings - The Electrochemical Society* **1987**, *87-1*, 314–324.

[51] Y. Ma, M. M. Doeff, S. J. Visco, L. C. De Jonghe, *Journal of The Electrochemical Society* **1993**, *140*, 2726–2733.

[52] J. R. Dahn, T. Zheng, Y. Liu, J. S. Xue, *Science* **1995**, *270*, 590–593.

[53] K. Kubota, S. Komaba, *Journal of The Electrochemical Society* **2015**, *162*, A2538–A2550.

[54] T. Hosaka, K. Kubota, A. S. Hameed, S. Komaba, *Chemical Reviews* **2020**, *120*, 6358–6466.

[55] Y. Li, Y. Lu, P. Adelhelm, M. M. Titirici, Y. S. Hu, *Chemical Society Reviews* **2019**, *48*, 4655–4687.

[56] E. Irisarri, A. Ponrouch, M. R. Palacin, *Journal of The Electrochemical Society* **2015**, *162*, A2476–A2482.

[57] R. Korthauer, *Lithium-ion batteries: Basics and applications*, **2018**, pp. 1–413.

[58] P. Adelhelm, P. Hartmann, C. L. Bender, M. Busche, C. Eufinger, J. Janek, *Beilstein Journal of Nanotechnology* **2015**, *6*, 1016–1055.

[59] S. Muench, A. Wild, C. Friebe, B. Häupler, T. Janoschka, U. S. Schubert, *Chemical Reviews* **2016**, *116*, 9438–9484.

[60] E. Castillo-Martínez, J. Carretero-González, M. Armand, *Angewandte Chemie* **2014**, *126*, 5445–5449.

[61] H. Wang, Y.-I. Jang, B. Huang, D. R. Sadoway, Y.-M. Chiang, *Journal of The Electrochemical Society* **1999**, *146*, 473–480.

[62] T. Ohzuku, R. J. Brodd, *Journal of Power Sources* **2007**, *174*, 449–456.

[63] G. Wang, M. Lindsay, M. Ionescu, D. Bradhurst, S. Dou, H. Liu, *Journal of Power Sources* **2001**, *97-98*, 298–302.

[64] J. Molenda, J. Marzec, *Functional Materials Letters* **2009**, *02*, 1–7.

[65] G. G. Amatucci, J. M. Tarascon, L. C. Klein, *Solid State Ionics* **1996**, *83*, 167–173.

[66] H. Breuer, *dtv-Atlas Chemie*, 9th ed., dtv Verlagsgesellschaft, München, **2000**.

[67] K. B. Shedd, Cobalt, tech. rep., United States Geological Survey, National Minerals Information Center, **2021**.

[68] J. R. Dahn, C. A. Michal, *Solid State Ion.* **1990**, *44*, 87–97.

[69] C. Pouillerie, L. Croguennec, P. Biensan, P. Willmann, C. Delmas, *Journal of The Electrochemical Society* **2000**, *147*, 2061.

[70] A. Rougier, P. Gravereau, C. Delmas, *Journal of The Electrochemical Society* **1996**, *143*, 1168–1175.

[71] S. K. Mishra, G. Ceder, *Physical Review B - Condensed Matter and Materials Physics* **1999**, *59*, 6120–6130.

[72] A. R. Armstrong, P. G. Bruce, *ChemInform* **2010**, *27*, 499–500.

[73] C. H. Chen, J. Liu, M. E. Stoll, G. Henriksen, D. R. Vissers, K. Amine, *Journal of Power Sources* **2004**, *128*, 278–285.

[74] W. S. Yoon, Y. Paik, X. Q. Yang, M. Balasubramanian, J. McBreen, C. P. Grey, *Electrochemical and Solid-State Letters* **2002**, *5*, 9–13.

[75] L. Wang, J. Li, X. He, W. Pu, C. Wan, C. Jiang, *Journal of Solid State Electrochemistry* **2009**, *13*, 1157–1164.

[76] O. K. Park, Y. Cho, S. Lee, H. C. Yoo, H. K. Song, J. Cho, *Energy and Environmental Science* **2011**, *4*, 1621–1633.

[77] M. M. Thackeray, Y. Shao-Horn, A. J. Kahaian, K. D. Kepler, E. Skinner, J. T. Vaughey, S. A. Hackney, *Electrochemical and Solid-State Letters* **1998**, *1*, 7–9.

[78] Y. Shin, A. Manthiram, *Journal of The Electrochemical Society* **2004**, *151*, A204.

[79] G. Ceder, A. Van Der Ven, *Electrochimica Acta* **1999**, *45*, 131–150.

[80] M. M. Thackeray, A. de Kock, M. H. Rossouw, D. Liles, R. Bittihn, D. Hoge, *Journal of The Electrochemical Society* **1992**, *139*, 363–366.

[81] B. Deng, H. Nakamura, M. Yoshio, *Journal of Power Sources* **2008**, *180*, 864–868.

[82] G. Q. Liu, L. Wen, Y. M. Liu, *Journal of Solid State Electrochemistry* **2010**, *14*, 2191–2202.

[83] A. K. Padhi, K. S. Nanjundaswamy, J. B. Goodenough, *Journal of The Electrochemical Society* **1997**, *144*, 1188–1194.

[84] B. Kang, G. Ceder, *Nature* **2009**, *458*, 190–193.

[85] B. Kang, G. Ceder, *Journal of The Electrochemical Society* **2010**, *157*, A808.

[86] N. Ravet, Y. Chouinard, J. F. Magnan, S. Besner, M. Gauthier, M. Armand, *Journal of Power Sources* **2001**, *97-98*, 503–507.

[87] T. Drezen, N.-H. Kwon, P. Bowen, I. Teerlinck, M. Isono, I. Exnar, *Journal of Power Sources* **2007**, *174*, 949–953.

[88] J. Dewulf, G. Van der Vorst, K. Denturck, H. Van Langenhove, W. Ghyoot, J. Tytgat, K. Vandeputte, *Resources Conservation and Recycling* **2010**, *54*, 229–234.

[89] F. Cerdas, P. Titscher, N. Bognar, R. Schmuch, M. Winter, A. Kwade, C. Herrmann, *Energies* **2018**, *11*, DOI 10.3390/en11010150.

[90] P. K. Nayak, L. Yang, W. Brehm, P. Adelhelm, *Angewandte Chemie - International Edition* **2018**, *57*, 102–120.

[91] Y. Yamada, Y. Iriyama, T. Abe, Z. Ogumi, *Langmuir* **2009**, *25*, 12766–12770.

[92] Y. Yamada, Y. Koyama, T. Abe, Z. Ogumi, *Journal of Physical Chemistry C* **2009**, *113*, 8948–8953.

[93] K. Kuratani, N. Uemura, H. Senoh, H. T. Takeshita, T. Kiyobayashi, *Journal of Power Sources* **2013**, *223*, 175–182.

[94] Y. You, A. Manthiram, *Advanced Energy Materials* **2018**, *8*, 1–11.

[95] X. Xiang, K. Zhang, J. Chen, *Advanced Materials* **2015**, *27*, 5343–5364.

[96] H. Yoshida, N. Yabuuchi, S. Komaba, *Electrochemistry Communications* **2013**, *34*, 60–63.

[97] N. Yabuuchi, H. Yoshida, S. Komaba, *Electrochemistry* **2012**, *80*, 716–719.

[98] K. Zaghib, J. Trottier, P. Hovington, F. Brochu, A. Guerfi, A. Mauger, C. M. Julien, *Journal of Power Sources* **2011**, *196*, 9612–9617.

[99] M. Avdeev, Z. Mohamed, C. D. Ling, J. Lu, M. Tamaru, A. Yamada, P. Barpanda, *Inorganic Chemistry* **2013**, *52*, 8685–8693.

[100] J. B. Goodenough, H. Y.-p. Hong, J. A. Kafalas, *Materials Research Bulletin* **1976**, *5*, 77843.

[101] J. Gaubicher, C. Wurm, G. Goward, C. Masquelier, L. Nazar, *Chemistry of Materials* **2000**, *12*, 3240–3242.

[102] K. Saravanan, C. W. Mason, A. Rudola, K. H. Wong, P. Balaya, *Advanced Energy Materials* **2013**, *3*, 444–450.

[103] G. He, L. F. Nazar, *ACS Energy Letters* **2017**, *2*, 1122–1127.

[104] Y. Lu, L. Wang, J. Cheng, J. B. Goodenough, *Chemical Communications* **2012**, *48*, 6544–6546.

[105] H. W. Lee, R. Y. Wang, M. Pasta, S. W. Lee, N. Liu, Y. Cui, *Nature Communications* **2014**, *5*, 1–6.

[106] A. Ponrouch, D. Monti, A. Boschin, B. Steen, P. Johansson, M. R. Palacín, *Journal of Materials Chemistry A* **2015**, *3*, 22–42.

[107] C. Bommier, X. Ji, *Small* **2018**, *14*, 1–20.

[108] L. Otaegui, E. Goikolea, F. Aguesse, M. Armand, T. Rojo, G. Singh, *Journal of Power Sources* **2015**, *297*, 168–173.

[109] G. G. Eshetu, S. Grugeon, H. Kim, S. Jeong, L. Wu, G. Gachot, S. Laruelle, M. Armand, S. Passerini, *ChemSusChem* **2016**, *9*, 462–471.

[110] H. Che, S. Chen, Y. Xie, H. Wang, K. Amine, X. Z. Liao, Z. F. Ma, *Energy and Environmental Science* **2017**, *10*, 1075–1101.

[111] A. V. Cresce, S. M. Russell, O. Borodin, J. A. Allen, M. A. Schroeder, M. Dai, J. Peng, M. P. Gobet, S. G. Greenbaum, R. E. Rogers, K. Xu, *Physical Chemistry Chemical Physics* **2017**, *19*, 574–586.

[112] B. Jache, P. Adelhelm, *Angewandte Chemie - International Edition* **2014**, *53*, 10169–10173.

[113] C. Ding, T. Nohira, R. Hagiwara, K. Matsumoto, Y. Okamoto, A. Fukunaga, S. Sakai, K. Nitta, S. Inazawa, *Journal of Power Sources* **2014**, *269*, 124–128.

[114] J.-J. Kim, K. Yoon, I. Park, K. Kang, *Small Methods* **2017**, *1*, 1700219.

[115] K. Xu, *Chemical Reviews* **2014**, *114*, 11503–11618.

[116] E. Peled, *Journal of The Electrochemical Society* **1979**, *126*, 2047–2051.

[117] S. Komaba, W. Murata, T. Ishikawa, N. Yabuuchi, T. Ozeki, T. Nakayama, A. Ogata, K. Gotoh, K. Fujiwara, *Advanced Functional Materials* **2011**, *21*, 3859–3867.

[118] V. A. Oltean, B. Philippe, S. Renault, R. Félix Duarte, H. Rensmo, D. Brandell, *Chemistry of Materials* **2016**, *28*, 8742–8751.

[119] R. Mogensen, D. Brandell, R. Younesi, *ACS Energy Letters* **2016**, *1*, 1173–1178.

[120] F. A. Soto, P. Yan, M. H. Engelhard, A. Marzouk, C. Wang, G. Xu, Z. Chen, K. Amine, J. Liu, V. L. Sprenkle, F. El-Mellouhi, P. B. Balbuena, X. Li, *Advanced Materials* **2017**, *29*, 1606860.

[121] R. Mogensen, J. Maibach, W. R. Brant, D. Brandell, R. Younesi, *Electrochimica Acta* **2017**, *245*, 696–704.

[122] M. Winter, *J. Electrochem. Soc* **1998**.

[123] F. Béguin, F. Chevallier, C. Vix-Guterl, S. Saadallah, V. Bertagna, J. N. Rouzaud, E. Frackowiak, *Carbon* **2005**, *43*, 2160–2167.

[124] W. Luo, C. Bommier, Z. Jian, X. Li, R. Carter, S. Vail, Y. Lu, J. J. Lee, X. Ji, *ACS Applied Materials and Interfaces* **2015**, *7*, 2626–2631.

[125] C. Bommier, W. Luo, W. Y. Gao, A. Greaney, S. Ma, X. Ji, *Carbon* **2014**, *76*, 165–174.

[126] E. M. Lotfabad, P. Kalisvaart, A. Kohandehghan, D. Karpuzov, D. Mitlin, *Journal of Materials Chemistry A* **2014**, *2*, 19685–19695.

[127] W. Liu, P. Liu, D. Mitlin, *Advanced Energy Materials* **2020**, *10*, 2002297.

[128] C. Natarajan, H. Fujimoto, K. Tokumitsu, A. Mabuchi, T. Kasuh, *Carbon* **2001**, *39*, 1409–1413.

[129] F. Béguin, F. Chevallier, C. Vix, S. Saadallah, J. N. Rouzaud, E. Frackowiak, *Journal of Physics and Chemistry of Solids* **2004**, *65*, 211–217.

[130] H. Liu, X. B. Cheng, Z. Jin, R. Zhang, G. Wang, L. Q. Chen, Q. B. Liu, J. Q. Huang, Q. Zhang, *EnergyChem* **2019**, *1*, 100003.

[131] T. Perveen, M. Siddiq, N. Shahzad, R. Ihsan, A. Ahmad, M. I. Shahzad, *Renewable and Sustainable Energy Reviews* **2020**, *119*, 109549.

[132] G. N. Zhu, Y. G. Wang, Y. Y. Xia, *Energy and Environmental Science* **2012**, *5*, 6652–6667.

[133] S. Guo, J. Yi, Y. Sun, H. Zhou, *Energy and Environmental Science* **2016**, *9*, 2978–3006.

[134] K. T. Kim, G. Ali, K. Y. Chung, C. S. Yoon, H. Yashiro, Y. K. Sun, J. Lu, K. Amine, S. T. Myung, *Nano Letters* **2014**, *14*, 416–422.

[135] B. Babu, P. Simon, A. Balducci, *Advanced Energy Materials* **2020**, *10*, 2001128.

[136] A. Maazaz, C. Delmas, P. Hagenmuller, *Journal of Inclusion Phenomena* **1983**, *1*, 45–51.

[137] L. Zhao, H. L. Pan, Y. S. Hu, H. Li, L. Q. Chen, *Chinese Physics B* **2012**, *21*, 028201.

[138] J. C. Pérez-Flores, A. Kuhn, F. García-Alvarado, *Journal of Power Sources* **2011**, *196*, 1378–1385.

[139] A. Rudola, K. Saravanan, S. Devaraj, H. Gong, P. Balaya, *Chemical Communications* **2013**, *49*, 7451–7453.

[140] M. M. Doeff, J. Cabana, M. Shirpour, *Journal of Inorganic and Organometallic Polymers and Materials* **2014**, *24*, 5–14.

[141] X. Wang, G. Pawar, Y. Li, X. Ren, M. Zhang, B. Lu, A. Banerjee, P. Liu, E. J. Dufek, J.-G. Zhang, J. Xiao, J. Liu, Y. S. Meng, B. Liaw, **2019**, *19*, 1339–1345.

[142] W. J. Zhang, *Journal of Power Sources* **2011**, *196*, 877–885.

[143] C. J. Wen, R. A. Huggins, *Journal of Solid State Chemistry* **1981**, *37*, 271–278.

[144] M. N. Obrovac, L. Christensen, *Electrochemical and Solid-State Letters* **2004**, *7*, DOI 10.1149/1.1652421.

[145] A. Franco Gonzalez, N. H. Yang, R. S. Liu, *Journal of Physical Chemistry C* **2017**, *121*, 27775–27787.

[146] C. H. Lim, T. Y. Huang, P. S. Shao, J. H. Chien, Y. T. Weng, H. F. Huang, B. J. Hwang, N. L. Wu, *Electrochimica Acta* **2016**, *211*, 265–272.

[147] S. C. Jung, D. S. Jung, J. W. Choi, Y. K. Han, *Journal of Physical Chemistry Letters* **2014**, *5*, 1283–1288.

[148] C.-M. Park, H.-J. Sohn, *Journal of The Electrochemical Society* **2010**, *157*, A46.

[149] A. Darwiche, C. Marino, M. T. Sougrati, B. Fraisse, L. Stievano, L. Monconduit, *Journal of the American Chemical Society* **2012**, *134*, 20805–20811.

[150] L. Wang, J. Światowska, S. Dai, M. Cao, Z. Zhong, Y. Shen, M. Wang, *Materials Today Energy* **2019**, *11*, 46–60.

[151] K. P. Hembram, H. Jung, B. C. Yeo, S. J. Pai, S. Kim, K. R. Lee, S. S. Han, *Journal of Physical Chemistry C* **2015**, *119*, 15041–15046.

[152] W. M. Zhang, J. S. Hu, Y. G. Guo, S. F. Zheng, L. S. Zhong, W. G. Song, L. J. Wan, *Advanced Materials* **2008**, *20*, 1160–1165.

[153] L. Wang, Y. Lu, J. Liu, M. Xu, J. Cheng, D. Zhang, J. B. Goodenough, *Angewandte Chemie - International Edition* **2013**, *52*, 1964–1967.

[154] L. Li, Y. Zheng, S. Zhang, J. Yang, Z. Shao, Z. Guo, *Energy and Environmental Science* **2018**, *11*, 2310–2340.

[155] M. D. Bhatt, J. Y. Lee, *International Journal of Hydrogen Energy* **2019**, *44*, 10852–10905.

[156] X. Dou, I. Hasa, D. Saurel, C. Vaalma, L. Wu, D. Buchholz, D. Bresser, S. Komaba, S. Passerini, *Materials Today* **2019**, *23*, 87–104.

[157] F. Rodrguez-Reinoso in *Handbook of Porous Solids*, *Vol. 3*, Wiley-VCH Verlag GmbH, Weinheim, Germany, **2002**, pp. 1766–1827.

[158] J. W. Patrick, S. Hanson in *Handbook of Porous Solids*, *Vol. 3*, Wiley-VCH Verlag GmbH, Weinheim, Germany, **2002**, pp. 1900–1922.

[159] B. Zhang, C. M. Ghimbeu, C. Laberty, C. Vix-Guterl, J. M. Tarascon, *Advanced Energy Materials* **2016**, *6*, 1–9.

[160] E. R. Buiel, A. E. George, J. R. Dahn, *Carbon* **1999**, *37*, 1399–1407.

[161] P. J. Harris, *International Materials Reviews* **1997**, *42*, 206–218.

[162] F. C. Cowlard, J. C. Lewis, *Journal of Materials Science* **1967**, *2*, 507–512.

[163] S. Mrozowski, *Physical Review* **1952**, *86*, 1056–1056.

[164] P. W. Anderson, *Physical Review* **1958**, *109*, 1492–1505.

[165] H. Marsh, F. Rodríguez-Reinoso, *Activated Carbon*, **2006**, pp. 143–242.

[166] R. E. Franklin, *Proceedings of the Royal Society of London. Series A. Mathematical and Physical Sciences* **1951**, *209*, 196–218.

[167] J. J. Kipling, J. N. Sherwood, P. V. Shooter, N. R. Thompson, *Carbon* **1964**, *1*, 321–328.

[168] H. Yamamoto, S. Muratsubaki, K. Kubota, M. Fukunishi, H. Watanabe, J. Kim, S. Komaba, *Journal of Materials Chemistry A* **2018**, *6*, 16844–16848.

[169] B. E. Warren, *Physical Review* **1941**, *59*, 693–698.

[170] R. E. Franklin, *Acta Crystallographica* **1950**, *3*, 107–121.

[171] A. Gibaud, J. S. Xue, J. R. Dahn, *Carbon* **1996**, *34*, 499–503.

[172] G. Porod in *Small angle X-ray scattering*, (Eds.: O. Glatter, O. Kratky), Academic Press, **1982**.

[173] G. Porod, *Kolloid-Zeitschrift* **1951**, *124*, 83–114.

[174] L. A. Feigin, D. I. Svergun, *Structure Analysis by Small-Angle X-Ray and Neutron Scattering*, (Ed.: G. W. Taylor), Springer US, New York, NY, **1987**.

[175] J. R. Dahn, W. Xing, Y. Gao, *Carbon* **1997**, *35*, 825–830.

[176] R. Dash, J. Chmiola, G. Yushin, Y. Gogotsi, G. Laudisio, J. Singer, J. Fischer, S. Kucheyev, *Carbon* **2006**, *44*, 2489–2497.

[177] R. Morita, K. Gotoh, K. Kubota, S. Komaba, K. Hashi, T. Shimizu, H. Ishida, *Carbon* **2019**, *145*, 712–715.

[178] A. P. Terzyk, S. Furmaniak, P. J. Harris, P. A. Gauden, J. Włoch, P. Kowalczyk, G. Rychlicki, *Physical Chemistry Chemical Physics* **2007**, *9*, 5919–5927.

[179] L. L. Ban, D. Crawford, H. Marsh, *Journal of Applied Crystallography* **1975**, *8*, 415–420.

[180] J. Mering, C. Schiller, *Comptes rendus de l'Académie des sciences* **1967**, 247–250.

[181] R. Perret, W. Ruland, *Journal of Applied Crystallography* **1968**, *1*, 308–313.

[182] W. Ruland, *Carbon* **2001**, *39*, 323–324.

[183] E. Härk, A. Petzold, G. Goerigk, M. Ballauff, B. Kent, U. Keiderling, R. Palm, I. Vaas, E. Lust, *Microporous and Mesoporous Materials* **2019**, *275*, 139–146.

[184] E. Härk, A. Petzold, G. Goerigk, S. Risse, I. Tallo, R. Härmas, E. Lust, M. Ballauff, *Carbon* **2019**, *146*, 284–292.

[185] S. J. Townsend, T. J. Lenosky, D. A. Muller, C. S. Nichols, V. Elser, *Physical Review Letters* **1992**, *69*, 921–924.

[186] A. C. Jensen, E. Olsson, H. Au, H. Alptekin, Z. Yang, S. Cottrell, K. Yokoyama, Q. Cai, M. M. Titirici, A. J. Drew, *Journal of Materials Chemistry A* **2020**, *8*, 743–749.

[187] H. Alptekin, H. Au, A. C. Jensen, E. Olsson, M. Goktas, T. F. Headen, P. Adelhelm, Q. Cai, A. J. Drew, M.-M. Titirici, *ACS Applied Energy Materials* **2020**, *3*, 9918–9927.

[188] K. Kubota, S. Shimadzu, N. Yabuuchi, S. Tominaka, S. Shiraishi, M. Abreu-Sepulveda, A. Manivannan, K. Gotoh, M. Fukunishi, M. Dahbi, S. Komaba, *Chemistry of Materials* **2020**, *32*, 2961–2977.

[189] K. Gotoh, T. Yamakami, I. Nishimura, H. Kometani, H. Ando, K. Hashi, T. Shimizu, H. Ishida, *Journal of Materials Chemistry A* **2020**, *8*, 14472–14481.

[190] Z. Li, C. Bommier, Z. S. Chong, Z. Jian, T. W. Surta, X. Wang, Z. Xing, J. C. Neuefeind, W. F. Stickle, M. Dolgos, P. A. Greaney, X. Ji, *Advanced Energy Materials* **2017**, *7*, 1–10.

[191] J. M. Stratford, P. K. Allan, O. Pecher, P. A. Chater, C. P. Grey, *Chemical Communications* **2016**, *52*, 12430–12433.

[192] S. Qiu, L. Xiao, M. L. Sushko, K. S. Han, Y. Shao, M. Yan, X. Liang, L. Mai, J. Feng, Y. Cao, X. Ai, H. Yang, J. Liu, *Advanced Energy Materials* **2017**, *7*, 1700403.

[193] R. Morita, K. Gotoh, M. Fukunishi, K. Kubota, S. Komaba, N. Nishimura, T. Yumura, K. Deguchi, S. Ohki, T. Shimizu, H. Ishida, *Journal of Materials Chemistry A* **2016**, *4*, 13183–13193.

[194] M. B. Armand in *Materials for Advanced Batteries*, (Eds.: D. W. Murphy, J. Broadhead, B. C. H. Steele), Plenum Press, New York, NY, **1980**, Chapter Intercalat, pp. 145–162.

[195] A. Anani, R. A. Huggins, *Journal of Power Sources* **1992**, *38*, 351–362.

[196] C. Bommier, T. W. Surta, M. Dolgos, X. Ji, *Nano Letters* **2015**, *15*, 5888–5892.

[197] Y. Morikawa, S.-i. Nishimura, R.-i. Hashimoto, M. Ohnuma, A. Yamada, *Advanced Energy Materials* **2020**, *10*, 1903176.

[198] C. Matei Ghimbeu, J. Górka, V. Simone, L. Simonin, S. Martinet, C. Vix-Guterl, *Nano Energy* **2018**, *44*, 327–335.

[199] K. Gotoh, *Batteries & Supercaps* **2021**, 1–13.

[200] M. Letellier, F. Chevallier, F. Béguin, *Journal of Physics and Chemistry of Solids* **2006**, *67*, 1228–1232.

[201] S. Łoś, M. Letellier, P. Azaïs, L. Duclaux, *Journal of Physics and Chemistry of Solids* **2006**, *67*, 1182–1185.

[202] K. Gotoh, M. Maeda, A. Nagai, A. Goto, M. Tansho, K. Hashi, T. Shimizu, H. Ishida, *Journal of Power Sources* **2006**, *162*, 1322–1328.

[203] H. Fujimoto, A. Mabuchi, K. Tokumitsu, N. Chinnasamy, T. Kasuh, *Journal of Power Sources* **2011**, *196*, 1365–1370.

[204] R. Alcántara, P. Lavela, G. F. Ortiz, J. L. Tirado, *Electrochemical and Solid-State Letters* **2005**, *8*, A222.

[205] K. Gotoh, T. Ishikawa, S. Shimadzu, N. Yabuuchi, S. Komaba, K. Takeda, A. Goto, K. Deguchi, S. Ohki, K. Hashi, T. Shimizu, H. Ishida, *Journal of Power Sources* **2013**, *225*, 137–140.

[206] A. I. Freytag, A. D. Pauric, S. A. Krachkovskiy, G. R. Goward, *Journal of the American Chemical Society* **2019**, *141*, 13758–13761.

[207] Y. Zheng, Y. Lu, X. Qi, Y. Wang, L. Mu, Y. Li, Q. Ma, J. Li, Y. S. Hu, *Energy Storage Materials* **2019**, *18*, 269–279.

[208] J. Heinze, *Angewandte Chemie International Edition in English* **1984**, *23*, 831–847.

[209] V. F. Lvovich, *Impedance Spectroscopy*, John Wiley & Sons, Inc., Hoboken, NJ, USA, **2012**, p. 353.

[210] A. Lasia, *Electrochemical Impedance Spectroscopy and its Applications*, 1st ed., Springer New York, New York, NY, **2014**.

[211] *Impedance Spectroscopy*, (Eds.: E. Barsoukov, J. R. Macdonald), Wiley, New Jersey, **2005**.

[212] T. H. Wan, M. Saccoccio, C. Chen, F. Ciucci, *Electrochimica Acta* **2015**, *184*, 483–499.

[213] M. Hahn, S. Schindler, L.-C. Triebs, M. A. Danzer, *Batteries* **2019**, *5*, 43.

[214] K. S. W. Sing, *Pure and Applied Chemistry* **1985**, *57*, 603–619.

[215] M. Thommes, K. Kaneko, A. V. Neimark, J. P. Olivier, F. Rodriguez-Reinoso, J. Rouquerol, K. S. Sing, *Pure and Applied Chemistry* **2015**, *87*, 1051–1069.

[216] N. Mehio, S. Dai, D.-e. Jiang, *The Journal of Physical Chemistry A* **2014**, *118*, 1150–1154.

[217] S. Brunauer, P. H. Emmett, E. Teller, *Journal of the American Chemical Society* **1938**, *60*, 309–319.

[218] I. Langmuir, *Journal of the American Chemical Society* **1919**, *40*, 1361–1403.

[219] K. S. Sing, *Assessment of Surface Area by Gas Adsorption*, 2nd ed., Elsevier Ltd., **2013**, pp. 237–268.

[220] K. S. Sing, F. Rouquerol, P. Llewellyn, J. Rouquerol, *Adsorption by Powders and Porous Solids: Principles Methodology and Applications: Second Edition* **2013**, 303–320.

[221] K. S. Sing, F. Rouquerol, J. Rouquerol, P. Llewellyn, *Assessment of Mesoporosity*, *Vol. 270*, **2013**, pp. 269–302.

[222] J. Silvestre-Albero, A. Silvestre-Albero, F. Rodríguez-Reinoso, M. Thommes, *Carbon* **2012**, *50*, 3128–3133.

[223] J. Silvestre-Albero, A. M. Silvestre-Albero, P. L. Llewellyn, F. Rodríguez-Reinoso, *Journal of Physical Chemistry C* **2013**, *117*, 16885–16889.

[224] G. Y. Gor, M. Thommes, K. A. Cychosz, A. V. Neimark, *Carbon* **2012**, *50*, 1583–1590.

[225] C. A. Dreiss, K. S. Jack, A. P. Parker, *Journal of Applied Crystallography* **2006**, *39*, 32–38.

[226] J. T. Rademacher, K. Kanakarajan, A. W. Czarnik, *Synthesis* **1994**, *1994*, 378–380.

[227] R. Walczak, B. Kurpil, A. Savateev, T. Heil, J. Schmidt, Q. Qin, M. Antonietti, M. Oschatz, *Angewandte Chemie - International Edition* **2018**, *57*, 10765–10770.

[228] P. Giusto, B. Kumru, J. Zhang, R. Rothe, M. Antonietti, **2020**, *32*, 7284–7291.

[229] K. Schutjajew, J. Pampel, W. Zhang, M. Antonietti, M. Oschatz, *Small* **2021**, 2006767.

[230] M. Sevilla, A. B. Fuertes, *Carbon* **2009**, *47*, 2281–2289.

[231] M. M. Titirici, A. Thomas, S. H. Yu, J. O. Müller, M. Antonietti, *Chemistry of Materials* **2007**, *19*, 4205–4212.

[232] S. Wenzel, T. Hara, J. Janek, P. Adelhelm, *Energy and Environmental Science* **2011**, *4*, 3342–3345.

[233] Z. Li, J. Ding, D. Mitlin, *Accounts of Chemical Research* **2015**, *48*, 1657–1665.

[234] X. Zhou, X. Zhu, X. Liu, Y. Xu, Y. Liu, Z. Dai, J. Bao, *Journal of Physical Chemistry C* **2014**, *118*, 22426–22431.

[235] M. S. Balogun, Y. Luo, W. Qiu, P. Liu, Y. Tong, *Carbon* **2016**, *98*, 162–178.

[236] J. L. Segura, R. Juárez, M. Ramos, C. Seoane, *Chemical Society Reviews* **2015**, *44*, 6850–6885.

[237] X. Y. Yan, M. D. Lin, S. T. Zheng, T. G. Zhan, X. Zhang, K. D. Zhang, X. Zhao, *Tetrahedron Letters* **2018**, *59*, 592–604.

[238] R. Yan, M. Antonietti, M. Oschatz, *Advanced Energy Materials* **2018**, *8*, 1–12.

[239] C. Hu, S. Sedghi, A. Silvestre-Albero, G. G. Andersson, A. Sharma, P. Pendleton, F. Rodríguez-Reinoso, K. Kaneko, M. J. Biggs, *Carbon* **2015**, *85*, 147–158.

[240] M. W. Smith, I. Dallmeyer, T. J. Johnson, C. S. Brauer, J. S. McEwen, J. F. Espinal, M. Garcia-Perez, *Carbon* **2016**, *100*, 678–692.

[241] A. C. Forse, C. Merlet, P. K. Allan, E. K. Humphreys, J. M. Griffin, M. Aslan, M. Zeiger, V. Presser, Y. Gogotsi, C. P. Grey, *Chemistry of Materials* **2015**, *27*, 6848–6857.

[242] A. C. Ferrari, J. Robertson, *Physical Review B* **2000**, *61*, 14095–14107.

[243] A. C. Ferrari, J. Robertson, *Physical Review B - Condensed Matter and Materials Physics* **2001**, *64*, 1–13.

[244] F. Xu, Y. Qiu, H. Han, G. Jiang, R. Zhao, E. Zhang, H. Li, H. Wang, S. Kaskel, *Carbon* **2020**, *159*, 140–148.

[245] P. C. Tsai, S. C. Chung, S. K. Lin, A. Yamada, *Journal of Materials Chemistry A* **2015**, *3*, 9763–9768.

[246] Y. Matsukawa, F. Linsenmann, M. A. Plass, G. Hasegawa, K. Hayashi, T.-P. Fellinger, *Beilstein J. Nanotechnol* **2020**, *2020*, 1217–1229.

[247] K. Schutjajew, T. Tichter, J. Schneider, M. Antonietti, C. Roth, M. Oschatz, *Physical Chemistry Chemical Physics* **2021**, *23*, 11488–11500.

[248] K. Kubota, S. Shimadzu, N. Yabuuchi, S. Tominaka, S. Shiraishi, M. Abreu-Sepulveda, A. Manivannan, K. Gotoh, M. Fukunishi, M. Dahbi, S. Komaba, *Chemistry of Materials* **2020**, *32*, 2961–2977.

[249] F. Xie, Z. Xu, Z. Guo, M.-M. Titirici, *Progress in Energy* **2020**, *2*, 042002.

[250] H. Schichlein, A. C. Müller, M. Voigts, A. Krügel, E. Ivers-Tiffée, *Journal of Applied Electrochemistry* **2002**, *32*, 875–882.

[251] J. P. Schmidt, T. Chrobak, M. Ender, J. Illig, D. Klotz, E. Ivers-Tiffée, *Journal of Power Sources* **2011**, *196*, 5342–5348.

[252] J. P. Schmidt, P. Berg, M. Schönleber, A. Weber, E. Ivers-Tiffée, *Journal of Power Sources* **2013**, *221*, 70–77.

[253] M. Hahn, A. Schiela, P. Mößle, F. Katzer, M. A. Danzer, *Journal of Power Sources* **2020**, *477*, 228672.

[254] M. Mandl, J. Becherer, D. Kramer, R. Mönig, T. Diemant, R. J. Behm, M. Hahn, O. Böse, M. A. Danzer, *Electrochimica Acta* **2020**, *354*, 136698.

[255] V. A. Tyagay, G. Y. Kolbasov, *Elektrokhimiya* **1972**, *8*, 59.

[256] R. L. Van Meirhaeghe, E. C. Dutoit, F. Cardon, W. P. Gomes, *Electrochimica Acta* **1975**, *20*, 995–999.

[257] J. P. Diard, P. Landaud, J. M. Canut, B. L. Gorrec, C. Montella, *Electrochimica Acta* **1994**, *39*, 2585–2590.

[258] A. Sadkowski, M. Dolata, J.-P. Diard, *Journal of The Electrochemical Society* **2004**, *151*, E20.

[259] A. D. Franklin, H. J. De Bruin, *Physica Status Solidi (a)* **1983**, *75*, 647–656.

[260] T. Hörlin, *Solid State Ionics* **1998**, *107*, 241–253.

[261] A. B. Tesler, D. R. Lewin, S. Baltianski, Y. Tsur, *Journal of Electroceramics* **2010**, *24*, 245–260.

[262] S. Hershkovitz, S. Baltianski, Y. Tsur, *Solid State Ionics* **2011**, *188*, 104–109.

[263] M. Saccoccio, T. H. Wan, C. Chen, F. Ciucci, *Electrochimica Acta* **2014**, *147*, 470–482.

[264] Y. Zhang, Y. Chen, M. Yan, F. Chen, *Journal of Power Sources* **2015**, *283*, 464–477.

[265] Y. Zhang, Y. Chen, M. Li, M. Yan, M. Ni, C. Xia, *Journal of Power Sources* **2016**, *308*, 1–6.

[266] N. Schlüter, S. Ernst, U. Schröder, *ChemElectroChem* **2019**, *6*, 6027–6037.

[267] K. Schutjajew, P. Giusto, E. Härk, M. Oschatz, *Carbon* **2021**, *185*, 697–708.

[268] F. Xu, H. Han, Y. Qiu, E. Zhang, H. Repich, C. Qu, H. Yu, H. Wang, S. Kaskel, *Carbon* **2020**, *167*, 896–905.

[269] A. Kamiyama, K. Kubota, D. Igarashi, Y. Youn, Y. Tateyama, H. Ando, K. Gotoh, S. Komaba, *Angewandte Chemie - International Edition* **2020**, 1–8.

[270] Y. Wang, X. Wang, M. Antonietti, *Angewandte Chemie - International Edition* **2012**, *51*, 68–89.

[271] A. Thomas, A. Fischer, F. Goettmann, M. Antonietti, J.-O. Müller, R. Schlögl, J. M. Carlsson, *Journal of Materials Chemistry* **2008**, *18*, 4893.

[272] P. Giusto, H. Arazoe, D. Cruz, P. Lova, T. Heil, T. Aida, M. Antonietti, *Journal of the American Chemical Society* **2020**, *142*, 20883–20891.

[273] P. Giusto, D. Cruz, T. Heil, H. Arazoe, P. Lova, T. Aida, D. Comoretto, M. Patrini, M. Antonietti, *Advanced Materials* **2020**, *32*, 1908140.

[274] J. S. Hayes in Air and Waste Management Association, 95th Annual Conference and Exhibition, Baltimore, MD, **2002**, pp. 1–19.

[275] A. B. García, A. Martínez-Alonso, C. A. Leon Y Leon, J. M. Tascón, *Fuel* **1998**, *77*, 613–624.

[276] M. Pawlyta, J. N. Rouzaud, S. Duber, *Carbon* **2015**, *84*, 479–490.

[277] Z. Y. Chen, J. P. Zhao, T. Yano, T. Ooie, *Applied Physics A: Materials Science and Processing* **2002**, *74*, 213–216.

[278] M. E. Alf, A. Asatekin, M. C. Barr, S. H. Baxamusa, H. Chelawat, G. Ozaydin-Ince, C. D. Petruczok, R. Sreenivasan, W. E. Tenhaeff, N. J. Trujillo, S. Vaddiraju, J. Xu, K. K. Gleason, *Advanced Materials* **2010**, *22*, 1993–2027.

[279] R. Perret, W. Ruland, *Journal of Applied Crystallography* **1972**, *5*, 183–187.

[280] W. Ruland, *Advanced Materials* **1990**, *2*, 528–536.

[281] E. Härk, N. Kardjilov, A. Hilger, A. Petzold, S. Risse, I. Vaas, G. Goerigk, C. Jafta, M. Ballauff, E. Lust, *ECS Transactions* **2017**, *77*, 1133–1144.

[282] C. J. Jafta, A. Petzold, S. Risse, D. Clemens, D. Wallacher, G. Goerigk, M. Ballauff, *Carbon* **2017**, *123*, 440–447.

[283] I. A. Shkrob, Y. Zhu, T. W. Marin, D. Abraham, *Journal of Physical Chemistry C* **2013**, *117*, 19255–19269.

[284] C. Peschel, F. Horsthemke, M. Leißing, S. Wiemers-Meyer, J. Henschel, M. Winter, S. Nowak, *Batteries & Supercaps* **2020**, *3*, 1183–1192.

A. Appendix

A.1. Supplementary tables and figures

Influence of pore structure and chemical environment on sodium storage in nitrogen-doped hard carbons

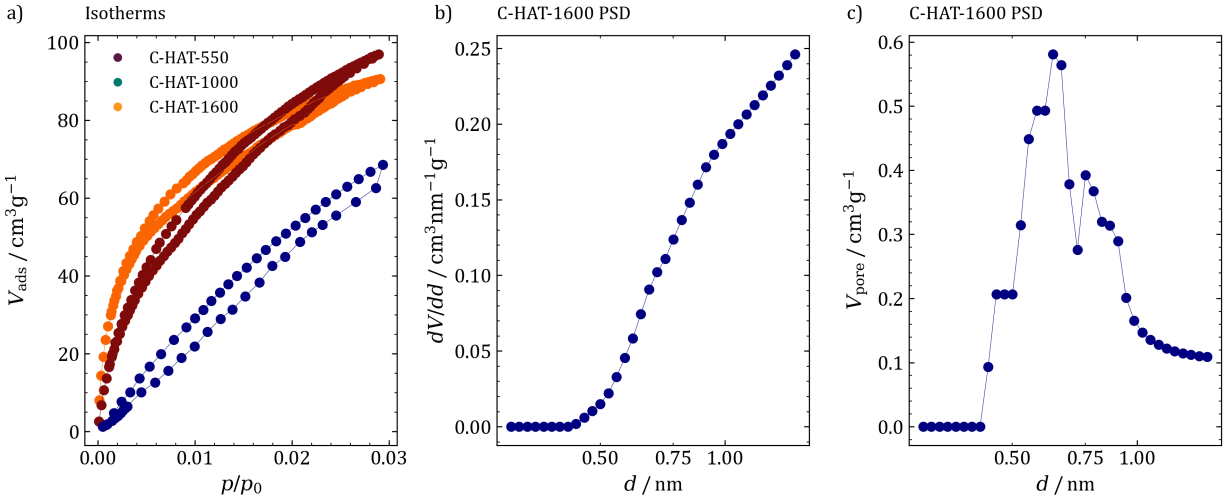

Figure A.1.: CO_2 isotherms of C-HAT-X materials measured at 273 K and PSD of C-HAT-1600 calculated from NLDFT.

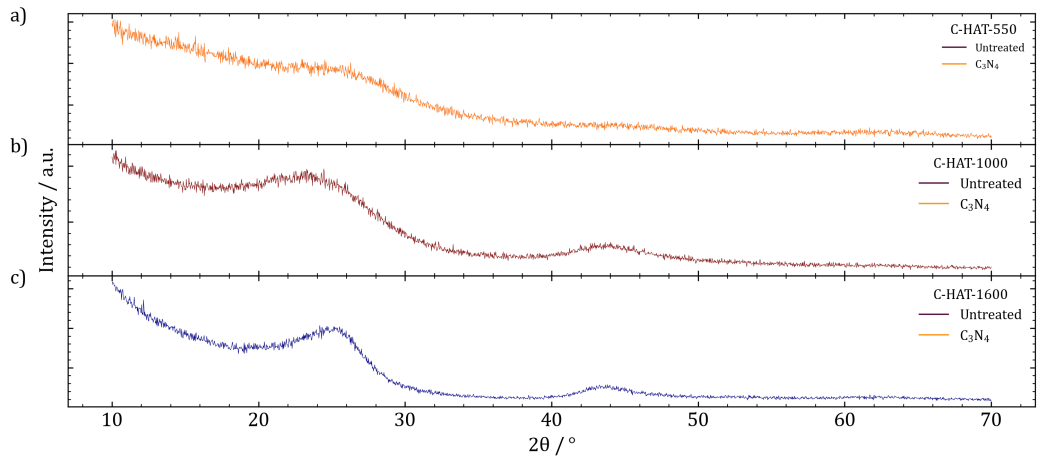

Figure A.2.: XRD-patterns of C-HAT-X materials. a) C-HAT-550, b) C-HAT-1000, c) C-HAT-1600.

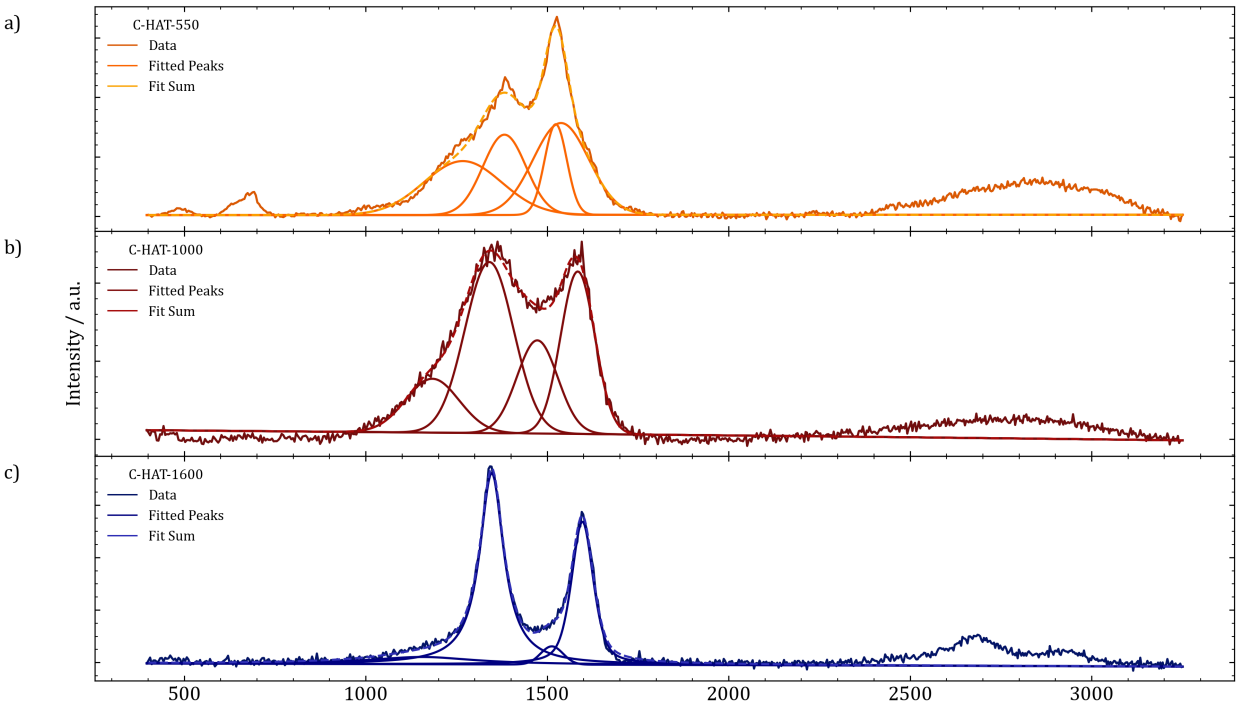

Figure A.3.: Raman spectra of C-HAT-X materials. Fitted peaks in lighter shade of the respective color, fit sum in dashed lines.

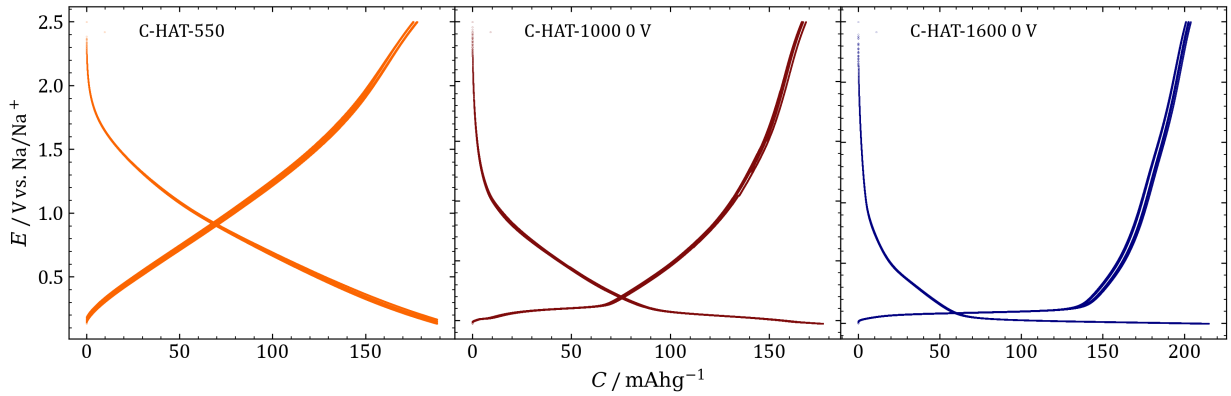

Figure A.5.: Capacity limited galvanostatic charge discharge curves of C-HAT-materials at $I = 18.6$ mAh g^{-1} with a limit of 90 % of the determined bulk plating capacity.

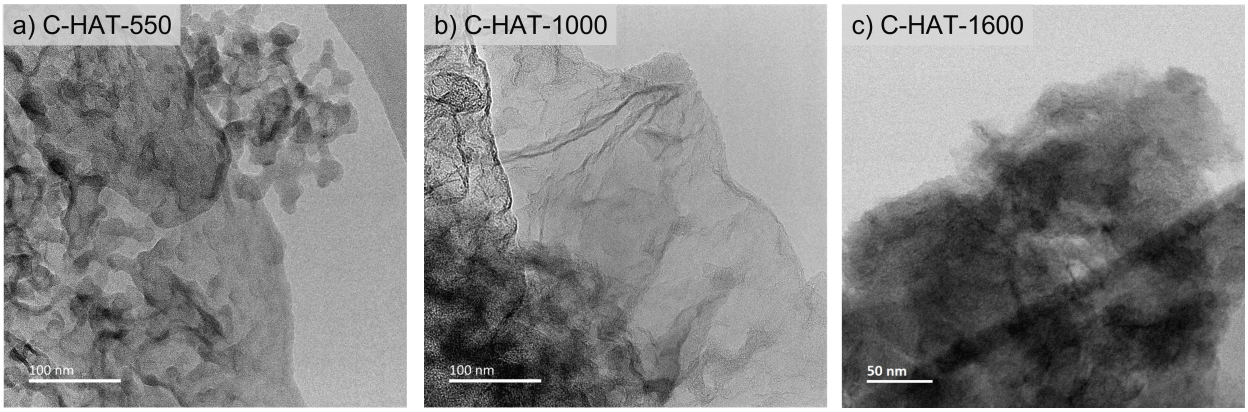

Figure A.4.: Bright-field TEM-images of C-HAT materials. a) C-HAT-550, b) C-HAT-1000, and c) C-HAT-1600.

Insights into the sodiation mechanism of hard carbons from electrochemical impedance spectroscopy

Table A.1.: Parameters employed for the simulation of impedance data.

Name	Physical meaning	Value
NUMMM	Number of spectra	60
E-Eqs	Number of potentials E^{eq}	np.linspace (0.25,0.1, NUMMM)
NUMMM2	-	0
FreqLoww	Lowest frequency used	0.01 Hz
FreqUpp	Highest frequency used	2×10^{-4} Hz
FreqNumm	Number of log-spaced frequencies	70
Tot_Drift	Voltage drift (artificial)	0.00 V
kzeroC	k_C^0	4×10^{-7} cm s^{-1}
kzeroNa	k_{Na}^0	2×10^{-7} cm s^{-1}
kzeroNaC	k_C^0	4×10^{-7} cm s^{-1}
D_Sep	Diffusion coefficient of Na in electrolyte, $D_{Na,T}$	4×10^{-13} cm^2s^{-1}
D_C	Diffusion coefficient of Na in carbon, $D_{C,T}$	1×10^{-9} cm^2s^{-1}
SepThickn	Separator thickness	0.026 cm
DiffDom_C	Length of diffusion domain in carbon, d_R	3.5×10^{-4} cm
A_Na	Active area of sodium counter electrode, A_{Na}	0.78 cm^2
A_C	Active area of carbon working electrode, A_{Na}	5000 cm^2
Cap_C_in	Capacity of internal double layer $C_{C,R}$	5×10^{-4} F
Cap_C_ext	Capacity of external double layer $C_{C,T}$	5×10^{-4} F
Cap_Na	Capacity of sodium double layer $C_{Na,T}$	1×10^{-5} F
c_Na_in_Na	Concentration of sodium in sodium	0.042 mol cm^3
c_Na_in_C	Concentration of sodium in carbon	3.5×10^{-5}mol cm^3

Preparation of carbon/carbon nitride nanocomposites for sodium ion anodes

Table A.2.: Elemental analyses of Kynols and p-C_3N_4 nanocomposites.

Sample	N / wt.%	C / wt.%	H / wt.%	S / wt.%
CC	0.11	100.44	0.11	0.03
CC-Plasma	0.16	99.23	0.36	0.09
CC-C_3N_4	0.64	98.4	0.10	0.03
ACC-10	0.19	93.64	0.90	0.05
ACC-10-Plasma	0.16	93.72	1.09	0.05
ACC-10-C_3N_4	5.13	84.03	1.40	0.04
ACC-20	0.24	92.76	1.46	0.08
ACC-20-Plasma	0.26	94.96	1.12	0.04
ACC-20-C_3N_4	20.95	64.32	1.83	0.10

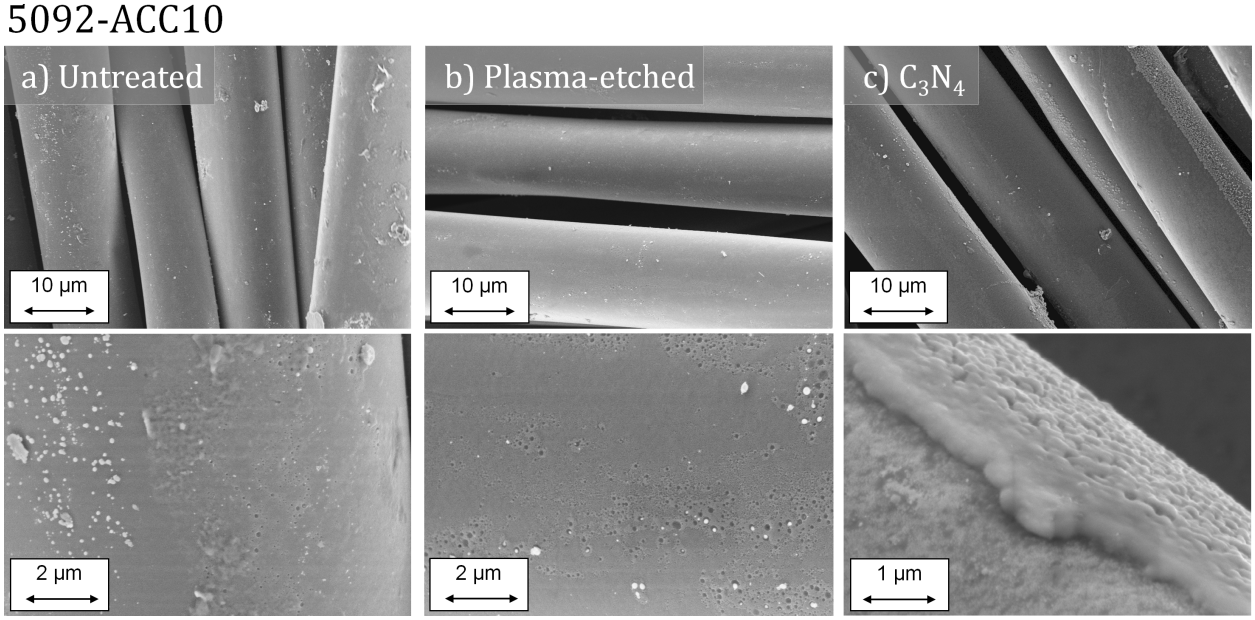

Figure A.6.: SEM images of Kynol ACC-10 and derived materials. a) Untreated fibers, b) plasma-etched samples, and c) p-C_3N_4 nanocomposites.

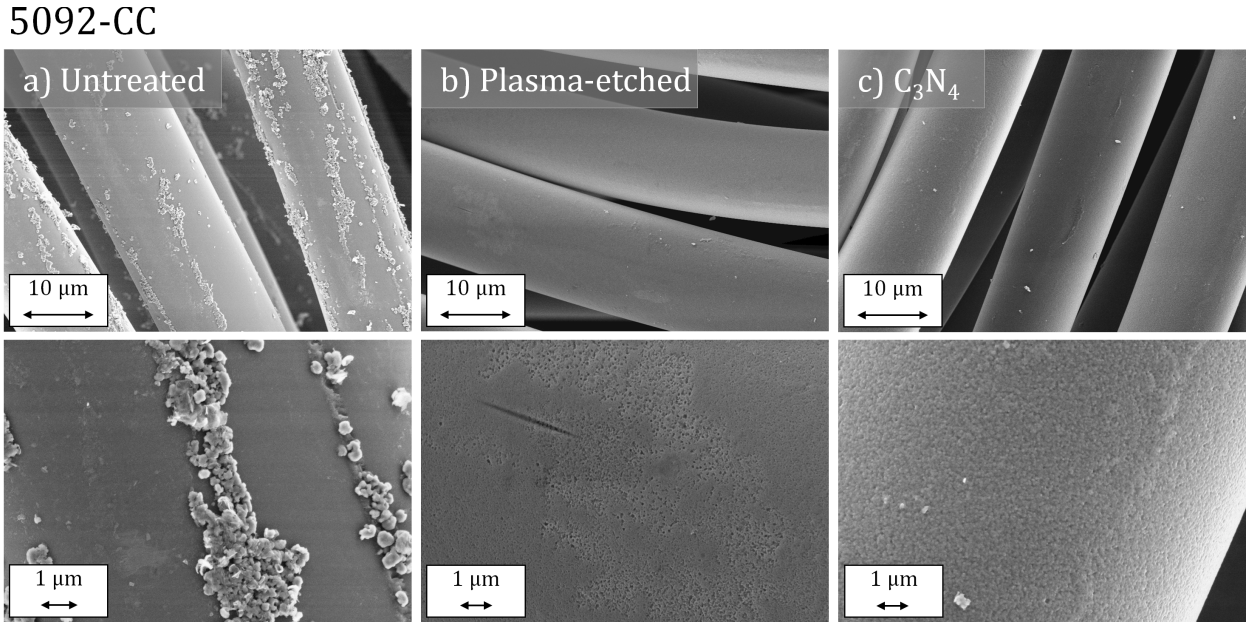

Figure A.7.: SEM images of Kynol CC and derived materials. a) Untreated fibers, b) plasma-etched samples, and c) p-C_3N_4 nanocomposites.

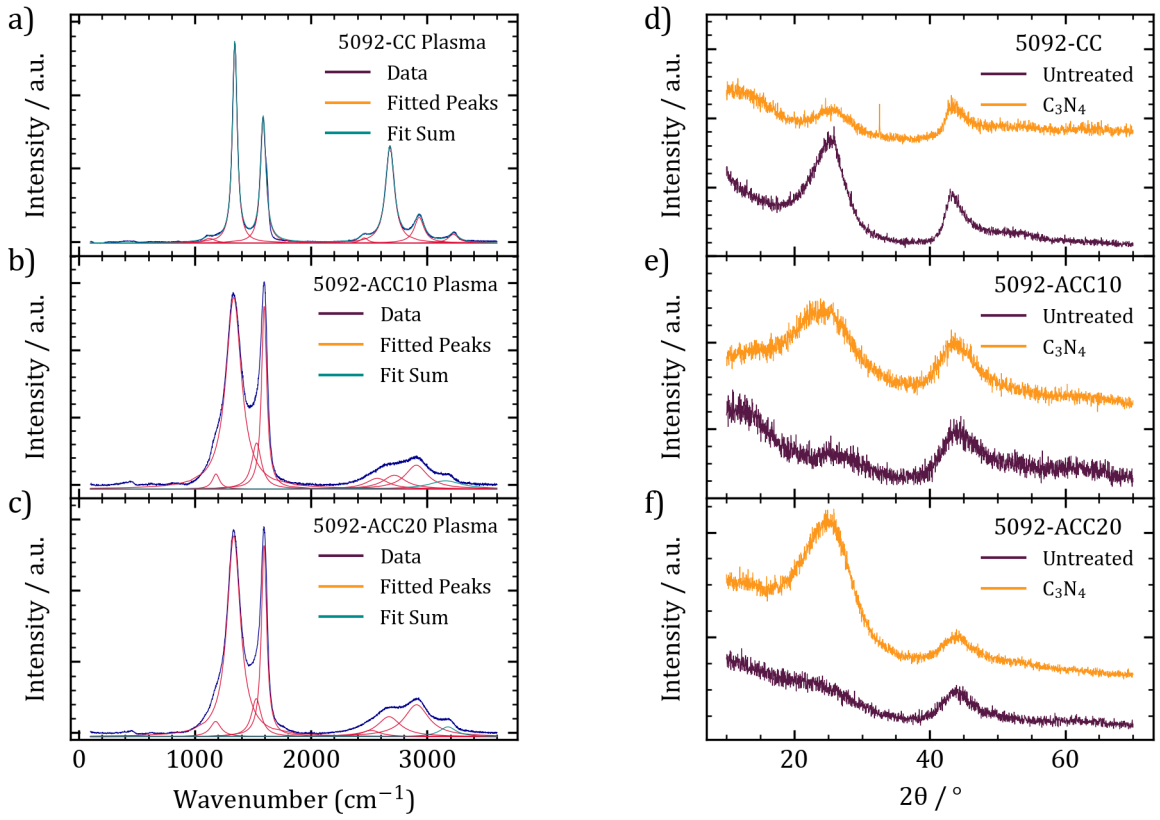

Figure A.8.: a-c) Background-corrected Raman spectra of plasma-etched carbons. Fitted bands and fit sum added for comparison of fit quality. d-f) XRD patterns of materials.

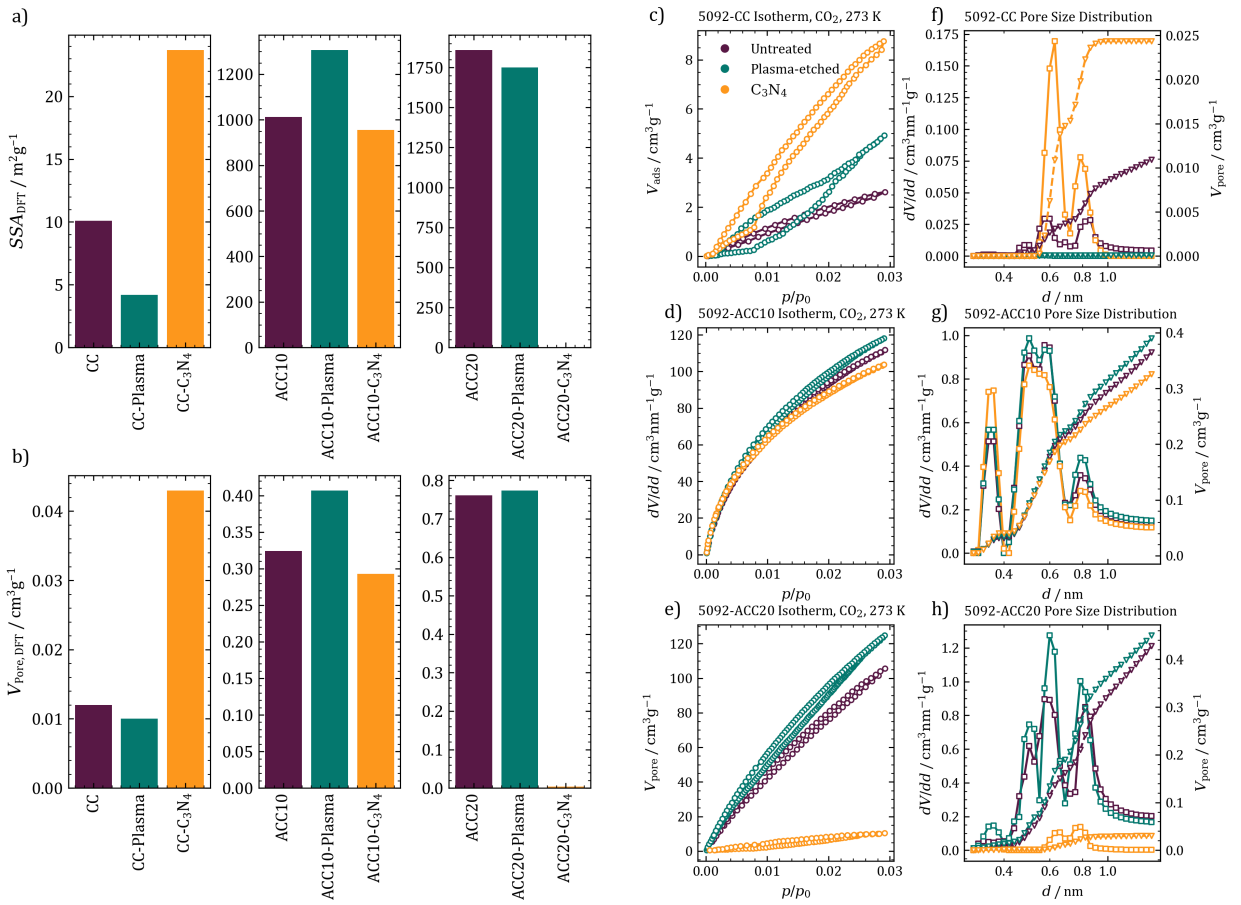

Figure A.9.: a-b) Surface areas and pore volumes from BET and DFT models. c-e) Results of CO_2 sorption experiments at 273 K for carbons and carbon/p-C_3N_4 composites. c-e) Isotherms, f-h) pore size distributions calculated from a NLDFT kernel for using the adsorption branch of the isotherm.

Table A.3.: SSAs and total pore volumes of carbons and carbon/p-C_3N_4 nanocomposites. SSAs are determined by the multipoint BET method as well as form QSDFT on slit/cylindrical pores at the adsorption branch of N_2 sorption isotherms at 77 K. Total pore volume was determined from DFT and directly from the isotherm at p/p_0 =0.99.

Sample	SSA_{BET} / $m^2\ g^{-1}$	SSA_{DFT} / $m^2\ g^{-1}$	$V_{\mathrm{Pore,DFT}}$ / $cm^3\ g^{-1}$	$V_{\mathrm{Pore,Isotherm}}$ / $cm^3\ g^{-1}$	I_D/I_G
CC	9	10	0.012	0.013	1.45
CC-Plasma	3	3	0.010	0.013	1.62
CC-C_3N_4	49	24	0.043	0.047	1.43
ACC-10	897	1012	0.324	0.355	1.05
ACC-10-Plasma	1037	1307	0.407	0.444	1.04
ACC-10-C_3N_4	805	956	0.293	0.319	1.19
ACC-20	1900	1860	0.761	0.830	1.02
ACC-20-Plasma	1880	1750	0.774	0.837	1.05
ACC-20-C_3N_4	4	2	0.004	0.004	1.24

Table A.4.: Material characteristics of Kynols obtained by SAXS. Fluctuation contribution B_{fl}, Porod constant P_{m}, invariant Q_{m}, porosity Φ, lateral correlation length l_{R}, number-average chord length l_{p}, weight-average chord length l_{c}, mean chord lengths of pore and solid, $\langle l_{\mathrm{pore}} \rangle$ and $\langle l_{\mathrm{solid}} \rangle$, degree of disorder, DoD

Value	CC	CC-Plasma	CC-C_3N_4	ACC10	ACC10-Plasma	ACC10-C_3N_4	ACC20	ACC20-Plasma	ACC20-C_3N_4
B_{fl} / $\mathrm{cm^2 g^{-1} nm^{-2}}$	10.55 ±0.05	10.27 ±0.03	10.15 ±0.30	26.90 ±0.86	20.40 ±0.62	10.55 ±0.65	36.20 ±0.12	43.00 ±0.54	3.98 ±0.24
C / $\mathrm{cm^2 g^{-1}}$	0	0	0.031 ±0.004	0	0	0.113 0.008	0	0	0.153 0.003
P_{m} / $\mathrm{cm^2 g^{-1} nm^{-4}}$	0.12 ±0.001	0.168 ±0.003	0.149 ±0.001	0.092 ±0.011	0.095 ±0.007	0.087 ±0.008	0.203 ±0.003	0.239 ±0.017	0.093 ±0.002
SSA_{SAXS} / $\mathrm{m^2\ g^{-1}}$	1064 ±107	1450 ±147	1283 ±129	794 ±122	825 ±103	747 ±100	1753 ±177	2061 ±253	804 ±83
Q_{m} / $\mathrm{cm^2 g^{-1} nm^{-3}}$	7.683 ±0.157	8.592 ±0.203	9.790 ±0.157	4.17 ±0.33	3.88 ±0.27	3.24 ±0.28	8.422 ±0.191	9.423 ±0.425	6.351 ±0.177
Φ	0.53 ±0.03	0.59 ±0.03	0.68 ±0.04	0.29 ±0.03	0.27 ±0.02	0.23 ±0.02	0.58 ±0.03	0.65 ±0.04	0.44 ±0.03
l_{R} / nm	4.0 ±0.1	5.0 ±0.1	9.0 ±0.2	0.80 ±0.07	1.1 ±0.1	2.0 ±0.2	0.95 ±0.05	1.2 ±0.1	>10
l_{c} / 1.44 nm	1.42 ±0.04	1.45 ±0.06	1.26 ±0.03	0.84 ±0.20	1.08 ±0.18	0.92 ±0.25	0.87 ±0.05	1.86 ±0.12	±0.06
l_{p} / 1.00 nm	0.82 ±0.02	1.06 ±0.02	0.73 ±0.01	0.65 ±0.10	0.60 ±0.06	0.67 ±0.07	0.64 ±0.02	1.10 ±0.05	±0.04
$\langle l_{\mathrm{pore}} \rangle$ / nm	2.16 ±0.12	2.05 ±0.14	3.32 ±0.21	1.03 ±0.20	0.89 ±0.12	0.78 ±0.13	1.6 ±0.08	1.85 ±0.32	1.97 ±0.16
$\langle l_{\mathrm{solid}} \rangle$ / nm	1.88 ±0.11	1.37 ±0.09	1.56 ±0.09	2.51 ±0.42	2.42 ±0.32	2.67 ±0.43	1.14 ±0.07	0.97 ±0.10	2.50 ±0.17
$l_{\mathrm{c}}/l_{\mathrm{p}}$	1.43 ±0.05	1.73 ±0.08	1.37 ±0.04	1.72 ±0.37	1.30 ±0.30	1.78 ±0.49	1.37 ±0.09	1.37 ±0.22	1.69 ±0.08
DoD	0.35 ±0.02	0.34 ±0.02	0.335 ±0.02	0.89 ±0.12	0.67 ±0.08	0.35 ±0.05	1.19 ±0.07	1.42 ±0.11	0.13 ±0.01
ρ_{app}	0.67	0.67	0.50	0.57	0.57	0.50	0.354	0.354	0.509

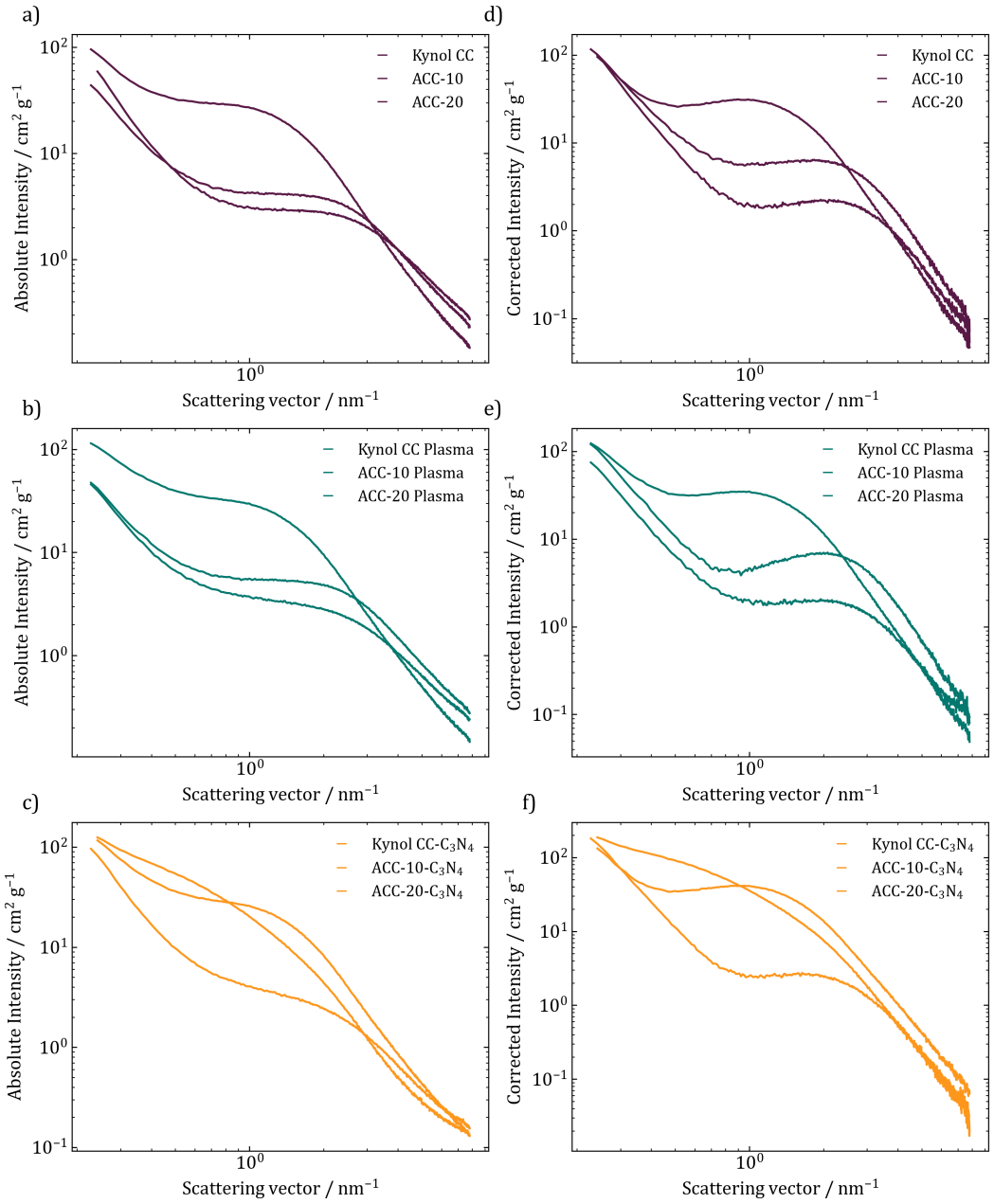

Figure A.10.: Normalized and corrected SAXS curves of Kynol materials.

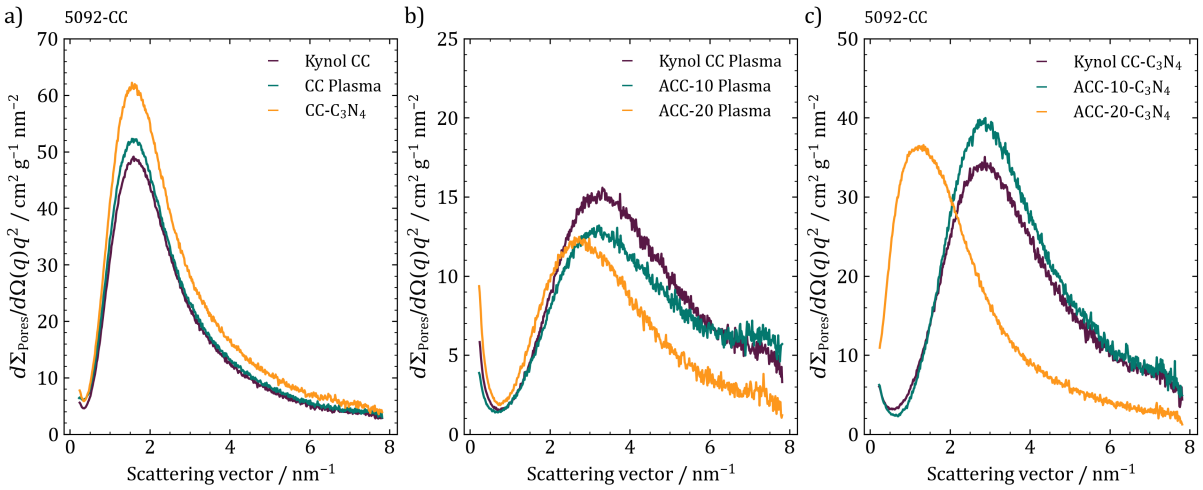

Figure A.11.: Kratky plots of the scattering data.

Table A.5.: Electrical conductivities of the Kynol carbons and their p-C_3N_4 composites measured in a four-probe setup.

Sample	σ / S m^{-1}
CC	3685±5
CC-Plasma	2274±3
CC-C_3N_4	0.080±0.001
ACC-10	266±1
ACC-10-Plasma	280±1
ACC-10-C_3N_4	20±1
ACC-20	195±1
ACC-20-Plasma	109±1
ACC-20-C_3N_4	0.8±1

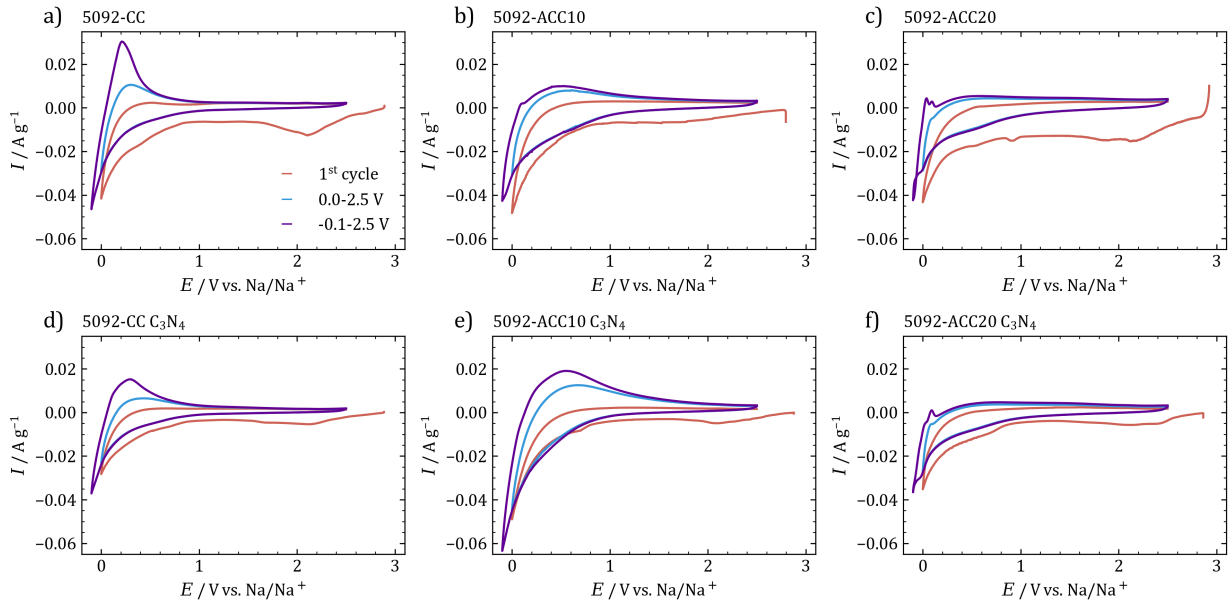

Figure A.12.: CV curves of Kynol carbons and nanocomposites at 2 mV s^{-1}. Red curve shows first cycle, light blue shows measurements in a voltage range of 0.0-2.5 V, dark blue lines recorded in a voltage range between -0.1-2.5 V.

Table A.6.: Reversible desodiation capacity $C_{\mathrm{Des,rev}}$ of the Kynol carbons and their p-C_3N_4 composites.

Sample	90 of $C_{\mathrm{Des,rev}}$ / mAh g^{-1}	Plateau of $C_{\mathrm{Des,rev}}$ / mAh g^{-1}
CC	199.7±4.9	173.7±2.9
CC-C_3N_4	145.3±1.8	113.3±3.1
ACC-10	75.7±4.2	12.0±1.3
ACC-10-C_3N_4	137.3±1.1	54.0±6.0
ACC-20	57.0±1.3	5.7±0.9
ACC-20-C_3N_4	59.3±6.9	5.0±0.7

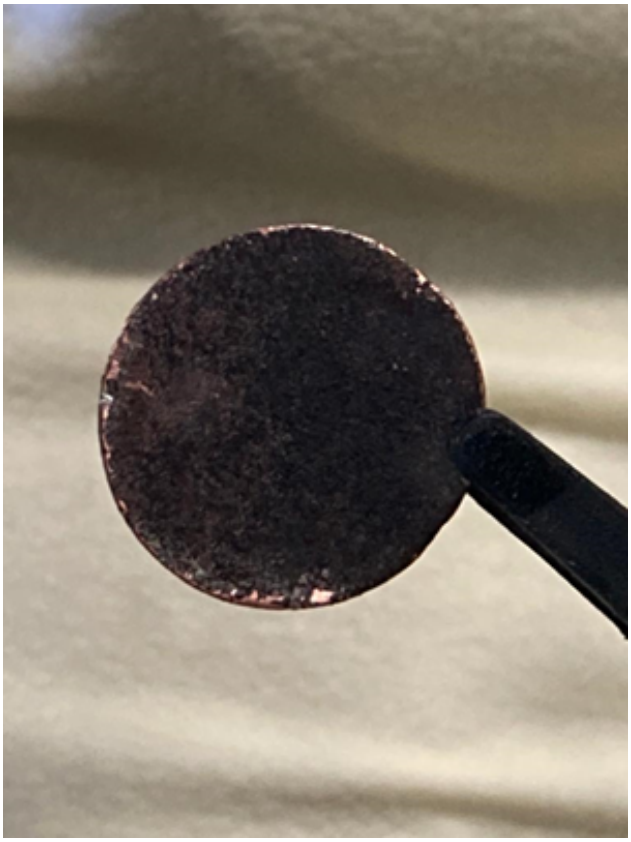

Figure A.13.: Photograph of an electrode of Kynol CC after 100 cycles. No metallic sodium can be seen, neither in the electrode, nor in the separator (not shown).

A.2. Abbreviations and Variables

Abbreviations

BMS	Battery Management System
BET	Brunauer, Emmet, Teller
CMC	Carboxymethyl cellulose
CV	Cyclic voltammetry
DEC	Diethyl Carbonate
DFT	Density Functional Theory
DMC	Dimethyl Carbonate
DRT	Distribution of Relaxation Times
EA	Elemental Analysis
EDX	Energy dispersive X-ray (spectroscopy)
EES	Electrochemical Energy Storage
EC	Ethylene Carbonate
EIS	Electrochemical Impedance Spectroscopy
FEC	Fluoroethylene Carbonate
FSI	$[N(FSO_2)_2]^-$
HC	Hard Carbon
LIB	Lithium Ion Battery
LCO	Lithium Cobalt Oxide
LFP	Lithium Iron Phosphate
LNO	Lithium Nickel Oxide
LMO	Lithium Manganese Oxide
NCA	Cobalt Aluminium Oxide

Abbreviations

NMC	Nickel Manganese Cobalt Oxide
NMR	Nuclear magnetic resonance
OTf	$[CF_3SO_3]^-$
PC	Propylene Carbonate
PXRD	Powder X-ray Diffraction
RFB	Redox Flow Battery
RTIL	Room-temperature ionic liquid
SAXS	Small-angle X-ray scattering
SEI	Solid Electrolyte Interphase
SEM	Scanning Electron Microscopy
SIB	Sodium Ion Battery
TEM	Tunnel Electron Microscopy
TFSI	$[N(CF_3SO_2)_2]^-$
TGA	Thermogravimetric Analysis
VC	Vinylene Carbonate
XRD	(Powder) X-ray diffraction

Variables

Name	Symbol	Unit
Power	P	W
Energy	W	J, Wh
Current	I	A
Charge	Q, C as in capacity	C, mAh g^{-1}
Time	t	h, min, s
Number of electrons	z_e	number
Faraday's constant	$F = 96485$	C mol^{-1}
Gibbs' free energy	$\Delta_R G$	J mol^{-1}
Gibbs' free energy under standard conditions	$\Delta_R G^0$	J mol^{-1}
Ideal gas constant	$R = 8.3144$	J $mol^{-1}K^{-1}$
Absolute temperature	T	K
(Electrical/electrochemical) Potential	E	V
Mass specific surface area	SSA	m^2g^{-1}
Angular frequency	$\omega = 2\pi f$	$s^{-1} \equiv$ Hz
Ohmic resistance	R	Ω
Capacity	C	F
Inductance	L	H
Impedance	Z	Ω
Relative pressure	p/p_0	dimensionless

A.3. Eigenständigkeitserklärung

Die vorliegende Dissertation wurde von mir im Zeitraum zwischen Januar 2019 und Oktober 2021 eigenständig unter der Anleitung von Prof. Dr. Martin Oschatz am Max-Planck-Institut für Kolloid- und Grenzflächenforschung angefertigt.
Hiermit versichere ich, dass ich die vorliegende Arbeit selbständig verfasst habe. Ich versichere, dass ich keine anderen als die angegebenen Quellen benutzt und alle wörtlich oder sinngemäß aus anderen Werken übernommenen Aussagen als solche gekennzeichnet habe, und dass die eingereichte Arbeit weder vollständig noch in wesentlichen Teilen Gegenstand eines anderen Prüfungsverfahrens gewesen ist.

Potsdam, den 14.10.2021
Ort, Datum

Unterzeichner

A.4. List of Publications

As a main author

1. K. Schutjajew, J. Pampel, W. Zhang, M. Antonietti, M. Oschatz, *Influence of Pore Architecture and Chemical Structure on the Sodium Storage in Nitrogen-Doped Hard Carbons*, Small, **2021**, 2006767. DOI: 10.1002/smll.202006767

2. K. Schutjajew, T. Tichter, J. Schneider, M. Antonietti, C. Roth, M. Oschatz, *Insights into the sodiation mechanism of hard carbon-like materials from electrochemical impedance spectroscopy*, Physical Chemistry Chemical Physics, **2021** *23*, 11488-11500. DOI: 10.1039/D1CP00610J

3. K. Schutjajew, P. Giusto, E. Härk, M. Oschatz, *Preparation of hard carbon/carbon nitride nanocomposites by chemical vapor deposition to reveal the impact of open and closed porosity on sodium storage*, Carbon, **2021** *185*, 697-708. DOI: 10.1016/j.carbon.2021.09.051

As a coauthor

1. M. Gebhard, T. Tichter, D. Franzen, M. C. Paulisch, K. Schutjajew, T. Turek, I. Manke, C. Roth, *Improvement of oxygen-depolarized cathodes in highly alkaline media by electrospinning of poly (vinylidene fluoride) barrier layers*, ChemElectroChem, **2020**, *7*, 830-837. DOI: 10.1002/celc.201902115

2. I. K. Ilic, K. Schutjajew, W. Zhang, M. Oschatz, *Sodium storage with high plateau capacity in nitrogen doped carbon derived from melamine–terephthalaldehyde polymers*, Journal of Materials Chemistry A, **2021**, *9*, 8711-8720. DOI: 10.1039/D0TA10960F

3. J. Hwang, W. Zhang, S. Youk, K. Schutjajew, M. Oschatz, *Understanding Structure–Property Relationships under Experimental Conditions for the Optimization of Lithium-Ion Capacitor Anodes based on All-Carbon-Composite Materials*, Energy Technology, **2021**, *9*, 2001054. DOI: 10.1002/ente.202001054

4. I. K. Ilic, K. Schutjajew, W. Zhang, M. Oschatz, *Changes of porosity of hard carbons during mechanical treatment and the relevance for sodium-ion anodes*, **2022**, *186*, 55-63. DOI: 10.1016/j.carbon.2021.09.063